Alabeos y Truncamientos de los Discos Estelares de Galaxias de Perfil

Ana Guijarro Román
Universidad de Granada
Programa de Doctorado "FÍSICA" (121.99.1)

30 de Mayo de 2012

Editor: Editorial de la Universidad de Granada
Autor: Ana Guijarro Román
D.L.: GR 724-2013
ISBN: 978-84-9028-439-1

Memoria de Tesis doctoral presentada por Ana Guijarro Román como parte de los requisitos para optar al grado académico de Doctor en Ciencias de la Universidad de Granada. Esta tesis contiene los resultados obtenidos en investigaciones llevadas a cabo en el Departamento de Física Teórica y del Cosmos bajo la dirección de los Profesores Eduardo Battaner López, Estrella Florido Navío y Jorge Jiménez Vicente.

La Doctoranda:
Ana Guijarro Román

El Director:
Eduardo Battaner López

La Directora:
Estrella Florido Navío

El Director:
Jorge Jiménez Vicente

La doctoranda Ana Guijarro Román y los directores de tesis Profesores Eduardo Battaner López, Estrella Florido Navío y Jorge Jiménez Vicente. Garantizamos, al firmar esta tesis doctoral, que el trabajo ha sido realizado por la doctorando bajo la dirección de los directores de la tesis y hasta donde nuestro conocimiento alcanza, en la realización del trabajo, se han respetado los derechos de otros autores a ser citados, cuando se han utilizado sus resultados o publicaciones.

Fdo.:
La Doctoranda:
Ana Guijarro Román

Fdo.:
El Director:
Eduardo Battaner López

Fdo.:
La Directora:
Estrella Florido Navío

Fdo.:
El Director:
Jorge Jiménez Vicente

Granada, 30 de Mayo de 2012

Esta tesis doctoral consiste en el reagrupamiento en una memoria de trabajos de investigación publicados por la doctoranda en medios científicos relevantes e internacionales en el ámbito de conocimiento de Astronomía y Astrofísica. El factor de impacto (FI) de las publicaciones presentadas está incluido en primer cuartil en la relación de revistas del ámbito de la especialidad y referenciadas en la última relación publicada por el Journal Citation Reports (SCI y/o SSCI), ver Tabla 1.

Los directores de tesis Profesores Eduardo Battaner López, Estrella Florido Navío y Jorge Jiménez Vicente, como coautores de las publicaciones presentadas en esta tesis declaramos que todos los artículos que configuran la tesis doctoral están publicados con fecha posterior a la obtención del título de licenciatura de la doctoranda y no han sido utilizados ni se utilizarán en ninguna tesis. Certificamos que la aportación científica de la doctoranda ha sido esencial. Ha llevado una gran parte de la carga en la labor de reducción y un claro liderazgo en la fase de discusión, interpretación y publicación de resultados. Además aceptamos e informamos de la idoneidad de la presentación de la tesis bajo esta modalidad porque los resultados se han publicado en la revista europea de astrofísica por excelencia: Astronomy and Astrophysics. Esta revista es gratis para los investigadores españoles debido a la cuota de participación (25000 euros anuales) gestionada por la Comisión Nacional de Astronomía. Al utilizar este procedimiento, los resultados están avalados por el estricto sistema de *"Referees"* que garantizan el rigor y la innovación de la tesis. Los artículos no tratan de temas dispersos sino agrupados en una estrecha especificación. La coherencia de los temas tratados se justifica con una introducción que aglutina y armoniza los artículos.

La doctoranda Ana Guijarro Román respeta los derechos de propiedad intelectual relativos a la difusión de los artículos utilizados en esta tesis doctoral.

Fdo. Los Directores:

Eduardo Battaner López Estrella Florido Navío Jorge Jiménez Vicente

Granada, 30 de Mayo de 2012

Tabla 1: Datos obtenidos del Journal Citation Reports ,SCI y/o SSCI, *(http://admin-apps.webofknowledge.com/JCR/JCR?PointOfEntry=Home&SID=V2LaiNApKbdBi9iInpL).*
Las citas son las totales de la revista y la posición global de dicha revista dentro de la categoría de la Astronomía y Astrofísica, con respecto al número de citas totales.

Revista	AÑO	ISSN	Factor de Impacto	Citas Totales	Clasificación Global
ASTRONOMY & ASTROPHYSICS	2001	1432-0746	2.281	41039	2
ASTRONOMY & ASTROPHYSICS	2003	0004-6361	3.843	63021	2
ASTRONOMY & ASTROPHYSICS	2006	0004-6361	3.971	70537	3
ASTRONOMY & ASTROPHYSICS	2007	0004-6361	4.259	76647	3
ASTRONOMY & ASTROPHYSICS	2010	0004-6361	4.425	89787	3

Prólogo

En esta Tesis vamos a estudiar e identificar la morfología y estructura que presentan los discos estelares de las galaxias espirales en sus zonas más externas. En particular nos centraremos en EL TRUNCAMIENTO Y EL ALABEO de estos discos. Para ello hemos elegido galaxias espirales vistas de perfil y observaciones en las longitudes de onda del visible y del infrarrojo cercano.

La distribución estelar de los discos de las galaxias espirales queda descrita con el brillo superficial a lo largo del radio galáctico. Este brillo sigue de forma general un modelo exponencial (de Vaucouleurs 1958 y Freeman 1970). Lo interesante es que, a grandes radios, este perfil de brillo deja de ser exponencial para decrecer de forma rápida hasta alcanzar un radio de truncamiento, R_t, donde el disco termina. Este rasgo morfológico fue descubierto por van der Kruit (1979) y ha sido muy estudiado por otros autores. En nuestra Galaxia, a pesar de que es más difícil la observación, también se ha detectado el truncamiento del disco. Por ejemplo Habing (1988) lo encontró a $R_t = 9.5$ kpc, Robin, Creze y Mohan (1992) a 14 kpc y Ruphy et al. (1996) a 15 kpc. A pesar de que los estudios realizados constatan que es un fenómeno muy general, y se han propuesto varias hipótesis para explicarlo, hacen falta más observaciones que permitan restringirlas. En esta tesis, hemos estudiado el truncamiento de los discos estelares de las galaxias espirales con observaciones en infrarrojo cercano (NIR) de galaxias vistas de perfil. Así, nuestros datos no estarán tan afectados por la extinción y mostrarán la distribución estelar mejor que los datos en el visible. Téngase presente que es la componente estelar la que se trunca, no el disco gaseoso, que parece extenderse hasta radios mucho mayores. Los truncamientos pueden observarse tanto en galaxias de cara (Pohlen et al. 2002), en galaxias de inclinación intermedia (Erwin, Pohlen y Beckman 2008), como en galaxias de perfil (Barteldrees y Dettmar 1994, de Grijs, Kregel y Wesson 2001, Florido et al. 2001, Pohlen 2001, Kregel, van der Kruit y de Grijs 2002). Si se pretende encontrar el perfil de brillo superficial radial, en el primer y segundo caso debemos realizar una integración en azimut. En el tercer caso, para galaxias vistas completamente de perfil debemos realizar una desproyección. Todos los estudios pueden ser complementarios. Nosotros hemos preferido centrarnos en el caso de las galaxias de perfil. Es posible que existan diferencias intrínsecas del truncamiento entre las regiones visibles e infrarrojas del espectro, puesto que nos indican diferentes tipos de población estelar. Por tanto, en ocasiones hemos recurrido también a observaciones en el visible con objeto de cuantificar estas diferencias.

La mayoría de las galaxias espirales, incluida la nuestra, tienen el disco alabeado (desviación suave y moderada en la dirección perpendicular al disco) tanto en la componente extendida del gas neutro, observada a partir del HI con la línea de 21 cm (Sancisi 1976, Bosma 1981, Briggs 1990, García-Ruiz, Sancisi y Kuijken 2002b), como en el disco estelar observado en el visible (Sánchez-Saavedra, Battaner y Florido 1990, Florido et al. 1991, Reshetnikov y Combes 1998, Ann y Park 2006). A partir de observaciones en la línea de 21 cm en nuestra propia Galaxia, Burke (1957) y Kerr (1957) detectaron por primera vez que el disco de una galaxia estaba alabeado. El alabeo plantea el problema de su origen y de su mantenimiento. Nuevamente, se precisan observaciones para restringir el variado número de hipótesis teóricas alternativas propuestas. Véanse, por ejemplo, los trabajos de recopilación de Binney (1992), Battaner et al. (1997) y van der Kruit (2007). Es, por tanto, el alabeo de los discos estelares el segundo fenómeno que queremos investigar en esta tesis. Para ello utilizamos datos muy profundos observados en el rango visible y en el infrarrojo. Son datos que se complementan y que pueden dar información sobre diferentes aspectos de la misma estructura. El alabeo es un fenómeno muy común, y su estudio es importante para comprender la dinámica de la periferia de las galaxias.

Es muy interesante investigar el alabeo en muestras de galaxias de perfil observadas en diferentes

filtros, y estudiar la posible relación entre las dos estructuras dinámicas estudiadas, el truncamiento y el alabeo. Ambas ocurren en los bordes de los discos, donde la gravedad deja de ser dominante, y podemos estudiar la influencia del campo magnético en la formación de estas estructuras.

Todos los datos obtenidos en los diferentes observatorios pertenecen a galaxias muy brillantes y cercanas nunca antes observadas en infrarrojo cercano, por lo que aunque estos datos están siendo utilizados sobre todo para estudiar el truncamiento y el alabeo, pueden ser utilizados para estudiar otros rasgos tales como la distribución de la capa de polvo en las galaxias, las corrugaciones, etc.

En el capítulo 1 haremos una breve introducción histórica y describiremos en qué consisten estos fenómenos que queremos estudiar. Presentamos la muestra elegida en el capítulo 2, explicando los procesos de reducción y análisis de datos utilizados. Dedicamos el capítulo 3 y el 4 al estudio más detallado de truncamientos y alabeos en estas galaxias. Para ello incluimos los resultados en artículos ya publicados en revistas internacionales. En el siguiente capítulo hacemos una breve exposición de la teoría magnética que puede explicar ambos fenómenos. Posteriormente mostramos los resultados y conclusiones.

Índice general

Capítulo 1

Introducción

1.1. Introducción histórica

En la publicación *"On the Construction of the Heavens"* de William Herschel (Herschel 1785) podemos admirar el primer modelo de una galaxia, la nuestra, la Vía Láctea. Contando cuidadosamente las estrellas del cielo, Sir William Herschel calculó cómo sería la distribución de estrellas en el "Sistema Sideral" (el término galaxia aún no era conocido) con el Sistema Solar en el centro. Es una imagen impresionante que ya muestra la parte más destacada que tienen las galaxias espirales: su disco. En 1845 William Parsons descubrió la estructura espiral de los "Universos Isla", que era como se empezaron a llamar las galaxias. Su famoso dibujo de M51 es el primer esquema que tenemos de una galaxia espiral. Años después Jacobus Kapteyn volvió a estudiar la distribución de estrellas en la Vía Láctea (Kapteyn 1922) reafirmando la forma de disco, pero colocando de nuevo al Sol cerca de su centro e ignorando la existencia de la absorción interestelar. La importancia del disco y el desarrollo de la estructura espiral fueron la base para el sistema de clasificación de galaxias que John Reynolds y Edwin Hubble expusieron en 1936 y que todavía es usado en nuestros días: la Secuencia de Hubble.

Eggen, Lynden-Bell y Sandage (1962) desarrollaron la primera teoría moderna de la formación de nuestra galaxia (conocida como ELS, por sus iniciales) basada en el colapso monolítico simple de una gran nube de gas relativamente rápido ($\sim$ 0.5 Giga-años), donde primero se forma el halo y después el disco. Fue mejorada por Searle y Zinn (1978) al incluir en esa nube de gas inicial fragmentos de unas $10^{6-8}\mathrm{M}_{\odot}$ donde ya existieran cúmulos globulares y estrellas ya formadas. Así se podrían explicar las diferencias de la evolución química entre el disco y el bulbo de las galaxias. La estructura tan definida de la galaxia NGC 7814 llevó a van der Kruit y Searle (1982b) a reafirmar lo anterior deduciendo que hubo dos épocas discretas de formación estelar en esa galaxia, una antes y otra después de la virialización del esferoide (bulbo) y la formación del disco.

La hipótesis de los halos de materia oscura por White y Rees (1978) y la formación jerárquica de estructuras por Tinsley y Larson (1977) ayudaron a entender mejor cómo se formaron, además de cómo se establecieron las propiedades de las galaxias. En los últimos años, la observación de barras, estructura espiral y otras subestructuras ha llevado a reafirmar el modelo de evolución secular interna para el desarrollo de los discos (Kormendy 2007).

Con observaciones de M33, Patterson en su tesis (1940) describió por primera vez la naturaleza exponencial de la distribución de brillo superficial con el radio de las galaxias y de Vaucouleurs en 1958 estableció el disco exponencial como descripción universal de la distribución radial de luz en los discos galácticos:

$$\mathrm{I(R)} \propto \exp(-\mathrm{R}/\mathrm{h_R}) \tag{1.1}$$

donde h_R es el parámetro de longitud de escala radial, con un valor comprendido entre 1 y 10 kpc.

En 1970 Freeman examinó con detalle la naturaleza exponencial de esta distribución, reafirmándola y encontrando además que la mayoría de las galaxias espirales tenían un brillo superficial central extrapolado, μ_0, con una notable constancia aparente de 21.65 $mag/arcsec^2$ en

el filtro B, siendo la desviación estándar de 0.30. Es un resultado que aún prevalece para las galaxias espirales, aunque hoy sabemos que es un efecto de selección, pues esta "ley" se determinó para un tipo de galaxias con un brillo superficial determinado, ni muy débiles porque no se detectarían, ni muy brillantes porque no las hay. El estudio de la distribución del brillo superficial fue completado por van der Kruit y Searle (1981a, 1981b, 1982a, 1982b) con las observaciones de la distribución vertical de la luminosidad en galaxias vistas de perfil. Estos autores obtuvieron que esa distribución se puede aproximar también a una exponencial con una escala de altura h_z que sorprendentemente no depende del radio galactocéntrico, es decir que el espesor de los discos sería independiente del radio; o en todo caso, parece aumentar, dando lugar a un ensanchamiento radial del disco (*flaring*).

1.2. Discos estelares

La distribución radial de brillo superficial en los discos se puede aproximar a una exponencial (ver Ecuación 1.1). Al hacer este ajuste obtenemos dos parámetros que dependen de la banda fotométrica: h_R e I_0. Una extensión de este modelo es lo que actualmente muchos autores están utilizando, el conocido como perfil de Sérsic (1963):

$$I(R) = I_0 exp\left(\left(\frac{R}{h_R}\right)^{-1/n}\right) \tag{1.2}$$

donde n es el índice de Sérsic.

Las galaxias con disco poseen además un bulbo central que en general tiene forma elíptica, aunque como indica Peletier (2008), no podemos simplificar las características de estas concentraciones de luz en el centro de las galaxias. Los bulbos pueden tener una barra interna, presentar forma elíptica, de "caja", o de "cacahuete" (en inglés *boxy o peanut*) e incluso ajustarse a perfiles exponenciales que típicamente asociamos con discos.

El disco puede tener una estructura espiral muy pronunciada y una banda de polvo que complica las observaciones. Y por supuesto, la distribución del disco tiene un espesor que se puede modelar como primera aproximación considerando un disco isotermo (Camm 1950). De manera general la distribución de brillo superficial se puede escribir como (van der Kruit 1988):

$$I(R, z) = I(0, 0) exp(-R/h_R) sech^{2/n}\left(\frac{nz}{2h_z}\right) \tag{1.3}$$

donde n es un índice que cuando toma el valor n=1 describiría la distribución isoterma $I(z) \propto sech^2(z/z_0)$ con $z_0 = 2h_z$, cuando toma el valor de n=2 tendríamos $I(z) \propto sech(z/h_z)$ y si $n = \infty$ describiría la distribución exponencial $I(z) \propto exp(-z/h_z)$. Ajustes en las bandas infrarrojas I y K' de de Grijs, Peletier y van der Kruit (1997) dan como resultado que $2/n = 0.54 \pm 0.20$.

Muchas galaxias espirales, incluida la nuestra, tienen una segunda componente en el disco; el llamado disco grueso que rodea al disco estrecho. Estos discos (Burstein 1979) están formados por población muy vieja.

Estudiando las galaxias que se ven de perfil queda patente que los discos son muy planos, al menos en las partes más internas. El hecho de que los discos de las galaxias sean planos lo vemos en todos sus componentes, en las estrellas, el polvo y el gas que los forman. Las partes más externas de los discos estelares presentan deformaciones tales como los alabeos. En esta tesis investigamos qué ocurre en las partes más externas de los discos estelares, las desviaciones de la distribución de brillo superficial exponencial extrapolada o TRUNCAMIENTOS y las desviaciones respecto al plano o ALABEOS.

1.3. Truncamientos

Según la primera descripción por van der Kruit (1979), el brillo de la galaxia no continúa indefinidamente, sino que se acaba a un determinado radio $R_t \approx (3.6 \pm 0.8)h_R$. Van der Kruit y Searle (1981a) hicieron un estudio más detallado con fotometría superficial de 4 galaxias muy brillantes vistas de perfil, confirmando la presencia de estos truncamientos, aunque la separación de la exponencial hasta alcanzar el truncamiento era gradual. En Florido et al. (2006), y como

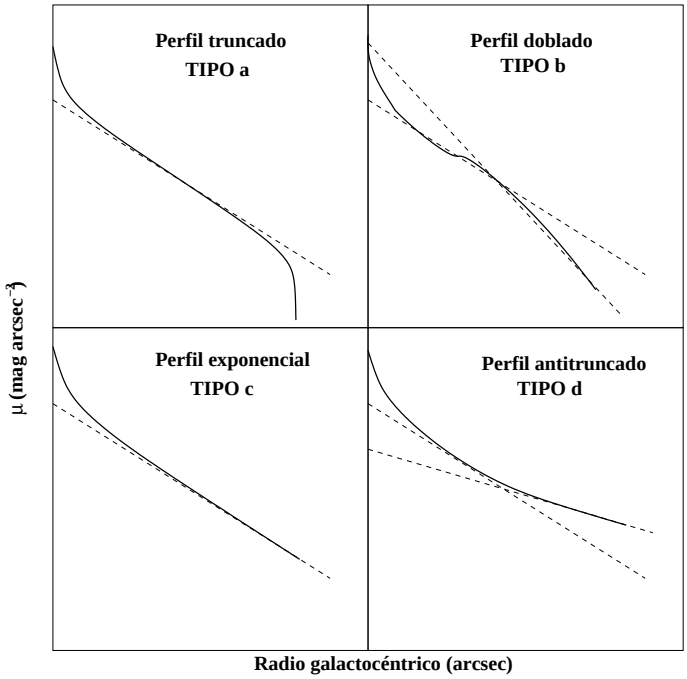

Figura 1.1: Tipos de perfiles radiales.

parte de esta tesis, obtuvimos los perfiles de brillo de galaxias de perfil después de un proceso de desproyección. Usamos datos en el infrarrojo cercano que mostraron que la distribución estelar del disco se truncaba completamente de manera relativamente suave, de acuerdo con el modelo tradicional de van der Kruit y Searle.

No obstante, algunas galaxias no presentan truncamiento, otras presentan un cambio de pendiente y otras un antitruncamiento (ver la Figura 1.1 y el artículo de Erwin et al. 2008). Pérez (2004) mostró que los perfiles radiales de las galaxias jóvenes a $z \sim 1$ se ajustaban mejor a dobles exponenciales, es decir, perfiles con cambio de pendiente. Por tanto, es posible que el fenómeno del truncamiento presente una variedad de formas, por lo que su estudio observacional se hace más necesario. Es posible incluso que los distintos tipos de perfiles radiales no sean excluyentes. Por ejemplo, tras un antitruncamiento pudiera tener lugar un truncamiento completo.

En nuestra galaxia, Ruphy et al. (1996), identificaron el truncamiento del disco estelar a un radio galactocéntrico de 14-15 kpc que coincide con la determinación obtenida $\mathrm{R}_t \approx (3.6 \pm 0.8)\mathrm{h_R}$, pues según Kent, Dame y Fazio (1991) h_R en la Vía Láctea es de 3.5-5.5 kpc (diferente al 2.1 ± 0.3 medido en el infrarrojo cercano, Porcel et al. 1998). El brillo superficial al que ocurren los truncamientos está un poco por encima del nivel del cielo oscuro, unos 26 $mag/arcsec^2$ en el filtro B, por lo que es más difícil detectarlos en galaxias que no están de perfil.

Hay varios modelos que intentan explicar el truncamiento del disco estelar de las galaxias. El primero es de Larson (1976) que tomaba el truncamiento como la extensión en ese momento de un disco que crece añadiendo material del exterior. Con este modelo se explicaría el gradiente de edad que se observa a lo largo de los discos (de Jong 1996). Otros modelos, como el de Kennicutt (1989), justifican el truncamiento proponiendo un umbral en la formación estelar cuando la densidad superficial del gas cae por debajo de cierto valor. Pero se ha detectado formación estelar más allá del radio de truncamiento de la Vía Láctea (Kobayashi y Tokunaga 2000 y otros autores) y de otras galaxias (Lequeux y Guélin 1996). Si hay formación estelar, ¿dónde están las estrellas? Van der Kruit (2001) presenta otra teoría con los resultados obtenidos en 3 galaxias donde el truncamiento coincide con una disminución bastante brusca de la velocidad de rotación. Esto se justificaría con una disminución real en la distribución radial de la densidad total, gaseosa y estelar. La región de truncamiento se corresponde con la del máximo momento angular del disco, que podría ser el mismo que tendría la protogalaxia si en el colapso de la misma se conservara el momento angular (Fall y Efstathiou 1980).

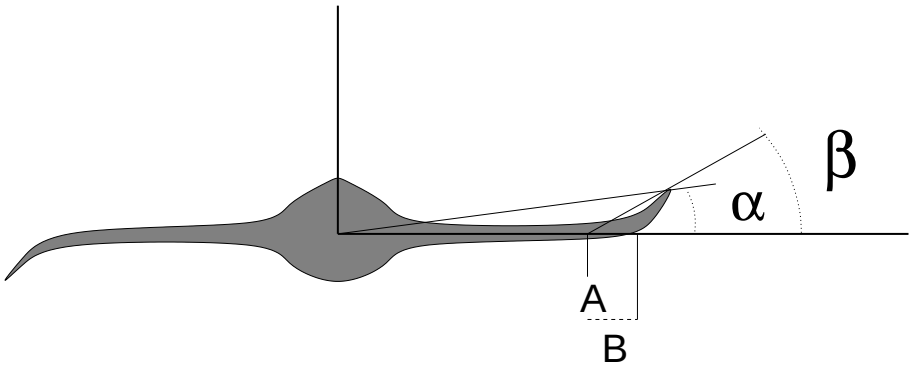

Figura 1.2: Parametrización del alabeo: A es el radio al que empieza el alabeo, B es la distancia en la que el alabeo alcalza la dirección asintótica, α es el ángulo formado entre la línea que conecta el centro de la galaxia y el punto más lejano detectado y el eje mayor del disco de la galaxia, y β es el ángulo entre la línea trazada desde A hasta el punto más lejano detectado y el eje mayor del disco de la galaxia. La tangente de β es la pendiente asintótica que llamamos C.

En el modelo de Battaner, Florido y Jiménez-Vicente (2002) el campo magnético es el causante del truncamiento. La fuerza magnética actúa sobre el gas ionizado y desaparece al formarse las estrellas. Al desaparecer esta fuerza hacia adentro, las estrellas recién formadas se moverían a órbitas más externas o incluso escaparían de la galaxia, produciendo un truncamiento del disco estelar. Erwin, Beckman y Pohlen (2005) introdujeron por primera vez el término antitruncamiento, que sería cuando al disco estelar se le pueden ajustar dos exponenciales, en vez de una, pero con una longitud de escala radial externa mayor que la longitud de escala radial interna. Esto también se podría explicar con el modelo magnético, pues esta segunda exponencial o parte del disco más externa, se correspondería con las estrellas recién formadas que han migrado a órbitas más externas pero no han escapado de la galaxia.

1.4. Alabeos

El disco de las galaxias espirales en la parte interna es plano y delgado. En cambio, en las partes externas las desviaciones se hacen mayores y con frecuencia tienen forma de signo integral (Figura 1.2). Esto es el alabeo. En algunas ocasiones es muy pronunciado, como en la galaxia ESO510-G13 (Figura 1.3). El alabeo en las galaxias se conoce desde hace medio siglo, cuando Burke (1957) y Kerr (1957) lo descubrieron en nuestra Galaxia con el hidrógeno neutro.

Distintos estudios (Sánchez-Saavedra, Battaner y Florido 1990, Florido et al. 1991, de Grijs 1997, Reshetnikov y Combes 1998, Reshetnikov et al. 2002) indican que la mayoría, si no todos los discos estelares de las galaxias presentan alabeos en sus partes externas. El alabeo se presenta en todas las componentes del disco: el disco gaseoso, la capa de polvo y el disco estelar. Un resultado muy interesante es el obtenido por Reylé et al. (2009) en el que gracias al mapeado de gran escala en infrarrojo cercano, 2MASS, son capaces de estudiar las partes más externas del plano galáctico de nuestra Galaxia, obteniendo la forma del alabeo estelar. Al compararlo con estudios anteriores encuentran que es asimétrico, parecido a las observaciones en HI, pero con una pendiente significativamente más pequeña que la del alabeo gaseoso. Además lo comparan con el alabeo en la capa de polvo observando que dicho alabeo tiene una pendiente intermedia entre el gaseoso y el estelar. Florido et al. (1991) ya hicieron esta apreciación en otras galaxias observadas a cuatro longitudes de onda. Por tanto, de estos y otros estudios, se deduce que la amplitud en el alabeo estelar es siempre bastante más pequeña que la observada en HI. ¿Por qué ocurren estas diferencias?

Los modelos que intentan explicar esta estructura son varios. Entre ellos están los que lo justifican debido a interacciones con otras galaxias (Kerr 1957, Hunter y Toomre 1969, Weinberg 1998, Weinberg y Blitz 2006, y otros), dejando sin explicación los sistemas aislados, y los que lo explican como resultado de la adición de material gaseoso externo con momento angular desalineado

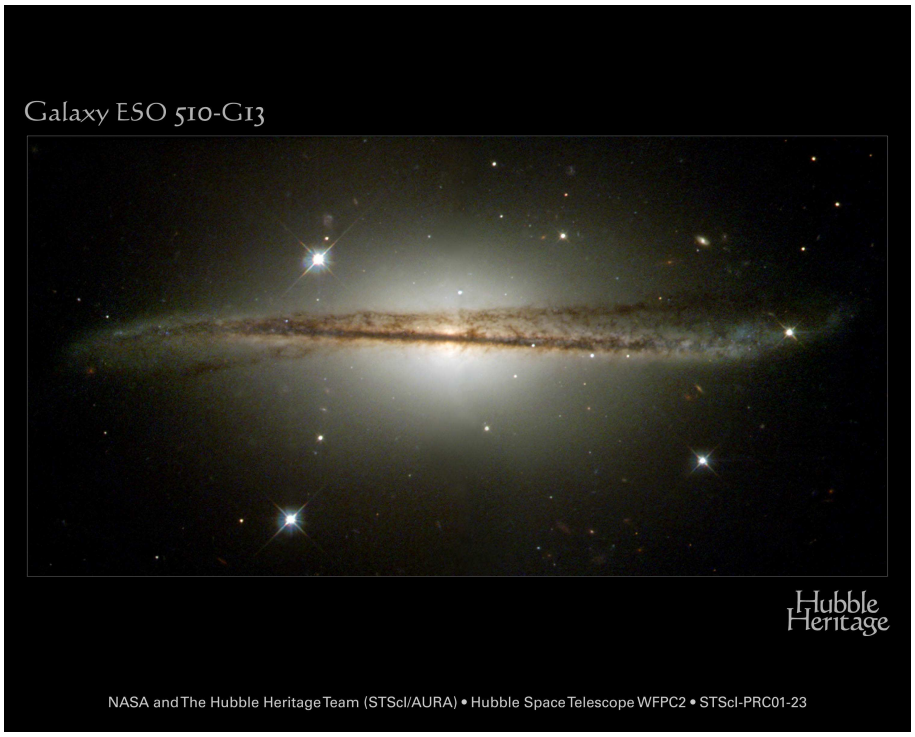

Figura 1.3: Galaxia espiral alabeada.

con respecto al disco principal (Kahn y Woltjer 1959, López-Corredoira, Betancort-Rijo y Beckman 2002, y otros). Van der Kruit (2001) relaciona el alabeo en HI con el truncamiento en el disco estelar, obteniendo que el alabeo comienza de manera muy brusca y muy cercano al truncamiento del disco y además en una zona donde se detecta una caída significativa en la velocidad de rotación. Esto último sugiere una discontinuidad en la distribución de la masa del disco. Además van der Kruit propone, con estas observaciones y resultados, que el disco interior plano y el disco exterior alabeado son distintas componentes con distintas historias de formación: el disco interior se formaría inicialmente en un proceso monolítico y rápido y el externo y alabeado se formaría más tarde como resultado de la caída de gas hacia el disco con momento angular con diferente orientación.

También se ha propuesto que el campo magnético puede ser un agente externo que induciría el alabeo, afectando más al gas ionizado que a las estrellas (Battaner, Florido y Sánchez-Saavedra 1990). Esta teoría predeciría un alabeo diferente según la población observada: el polvo y el gas estarían más alabeados que las estrellas. Las estrellas nuevas (mostradas en los filtros del visible) seguirían en un principio la distribución del polvo y gas del que han nacido, por lo que mostrarían un alabeo más pronunciado que las estrellas más viejas (más luminosas en el infrarrojo).

Un campo magnético externo con una dirección de unos 45^o con respecto al plano de la galaxia es óptimo para producir el alabeo. Se necesita una intensidad de campo del orden de unos 10^{-8} a 10^{-6} Gauss. Ya se conoce que el campo intergaláctico es del orden de 1 a 3 μG al menos (ver, por ejemplo, Kronberg 1994). En las partes más externas del disco de las galaxias, la fuerza gravitatoria es relativamente pequeña, por lo que el campo magnético intergaláctico puede influir de una manera decisiva en la dinámica del gas. Las líneas del campo magnético están congeladas con el gas del disco galáctico (es decir, el flujo magnético que atraviesa una determinada superficie es constante). El campo magnético intergaláctico tiene una distribución regular dentro de un grupo de galaxias, por lo que se esperaría una orientación similar en las galaxias que pertenecen a un mismo grupo. Este efecto fue investigado por Zurita y Battaner (1997) en el Grupo Local encontrando un alineamiento bastante significativo. También fue observado por Battaner, Florido y Sánchez-Saavedra en 1990 y Garrido et al. (1993) en otros grupos de galaxias.

Capítulo 2

Muestra y Reducción

2.1. Muestra de galaxias

2.1.1. Muestra de galaxias del Norte

Para el estudio del truncamiento disponemos de observaciones de alta sensibilidad que se realizaron con la cámara infrarroja CAIN del Telescopio Carlos Sánchez de Izaña, Tenerife. En total son 14 galaxias espirales observadas con los filtros J, H y K_S. En todas las campañas se tomaron estrellas estándares de calibración de catálogos infrarrojos para calibrar nuestras imágenes. La cámara infrarroja CAIN consta de un mosaico de 256x256 elementos fotoeléctricos de HgCdTe con sensibilidad en el rango 1-2,5 micras (NICMOS *array*). CAIN dispone de dos ópticas diferentes. Una de ellas, estrecha, corresponde a 0,39 segundos de arco por píxel y un campo de visión equivalente a 100x100 segundos de arco. La otra, ancha, con 1,00 segundos de arco por píxel y un campo de visión de 256x256 segundos de arco que es la que nosotros hemos usado.

La selección de las galaxias del Hemisferio Norte se hizo a partir de la base de datos LEDA (*Lyon-Meudon Extragalactic Database, http://leda.univ-lyon1.fr*) con tres criterios fundamentales:

- i (inclinación) = 90^o, es decir, galaxias de perfil.
- $D_{25}(B) \leq 4.0$', así el tamaño proyectado de las galaxias, o diámetro óptico medido con la isofota de $\mu_B = 25\ mag/arcsec^2$, es menor de 4 minutos de arco y se ajusta al campo de visión, FOV, de la cámara que vamos a utilizar para su observación.
- Tipo morfológico de Sa a Sd.

Después de esta primera selección, las 101 galaxias que cumplían estas condiciones, fueron examinadas usando las placas ya digitalizadas del *Digitized Sky Survey* obtenidas con el telescopio Schmidt del *Palomar Observatory Sky Survey (POSS)* que pertenece al *Space Telescope Science Institute (STScI)*. De este modo eliminamos las galaxias que podían estar perturbadas o interactuando con otras (en total 2), las que presentan demasiadas estrellas de la Vía Láctea, sobre todo en las partes más externas de las galaxias (6 galaxias), las muy débiles en brillo (6 galaxias) y las que no estuvieran claramente de perfil (33 galaxias). De este modo, nos quedamos con 54 galaxias de las que observamos 14 (ver Tabla 2.1) elegidas por tener mayor rango de visibilidad en la época de las observaciones. La meteorología nos impidió observar más objetos.

No podemos descartar un sesgo en estos criterios de selección, pero es bastante improbable ya que no hemos usado otros parámetros físicos y la elección final de galaxias resulta aleatoria. Esta muestra la observamos en 4 campañas: en Octubre de 2001, Marzo de 2002, Octubre-Noviembre 2002 y en Marzo de 2003.

2.1.2. Muestra de galaxias del Sur

Para el estudio del alabeo se seleccionó una muestra de 20 galaxias observadas ya en el visible en los filtros B,V e I (por de Grijs 1998), y se observaron en la banda infrarroja K_S con la cámara

Tabla 2.1: Propiedades básicas de las galaxias del Hemisferio Norte obtenidas de la base de datos *HyperLeda (http://leda.univ-lyon1.fr).*

Nombre de la Galaxia (1)	RA hh:mm:ss.s (2)	Dec gg:mm:ss (3)	Tipo de Hubble (4)	cz km/s (5)	$\log D_{25}$ (6)	M_{abs} (7)	v_{rot} km/s (8)	PA (grados) (9)
NGC 522	01:24:45.9	09:59:40.5	4.1±0.4	2738±23	1.38±0.03	-20.53	169.1	33.0
NGC 684	01:50:14.0	27:38:44.2	3.0±0.4	3535±4	1.47±0.05	-21.53	223.2	89.7
MGC-01-05-047	01:52:49.0	-03:26:48.6	5.0±0.5	5008±12	1.51±0.02	-21.77	247.7	160.4
NGC 781	02:00:09.0	12:39:21.5	0.6±2.0	3488±31	1.17±0.06	-20.87		12.6
NGC 2654	08:49:11.9	60:13:13.9	2.0±0.3	1349±3	1.65±0.03	-20.09	188.0	63.0
UGC 4906	09:17:39.9	52:59:34.3	1.1±0.6	2277±10	1.28±0.05	-20.26	176.2	58.8
NGC 2862	09:24:55.1	26:46:29.0	3.9±1.0	4098±5	1.42±0.03	-21.44	281.1	114.0
NGC 3279	10:34:42.6	11:11:50.7	6.4±0.8	1394±4	1.39±0.03	-19.27	155.9	152.3
NGC 3501	11:02:47.4	17:59:22.6	5.9±0.5	1131±7	1.63±0.03	-19.05	133.6	27.6
NGC 4013	11:58:31.5	43:56:50.9	3.1±0.5	836±3	1.69±0.02	-19.47	181.7	53.4
NGC 4217	12:15:50.8	47:05:30.8	3.1±0.4	1029±5	1.74±0.03	-19.96	187.6	49.0
NGC 5981	15:37:53.6	59:23:30.9	4.2±0.5	2529±9	1.44±0.05	-20.61	251.1	140.0
NGC 6504	17:56:05.7	33:12:31.7	1.0±2.0	4645±40	1.26±0.07	-22.28		94.5
NGC 6835	19:54:33.1	-12:34:02.5	1.1±0.7	1604±10	1.44±0.05	-19.55	65.9	70.0

(1) nombre de la galaxia; (2) and (3) coordenadas (J2000.0); (4) tipo morfológico; (5) velocidad radial heliocéntrica; (6) logaritmo de la proyección del eje mayor de la galaxia en la isofota 25 $mag/arcsec^2$ en la banda B, en log de 0.1 $arcmin$; (7) magnitud absoluta en la banda B; (8) velocidad máxima de rotación en la línea de 21-cm, corregida por la inclinación; (9) ángulo de posición del eje mayor sobre el cielo.

CIRIM del Telescopio Ritchey-Chretien del Observatorio de Cerro Tololo, Chile.

Para que nuestras conclusiones no estén sesgadas por el tipo de galaxias elegidas, las 20 galaxias analizadas fueron seleccionadas de una muestra estadísticamente completa aunque limitada en diámetro, de galaxias con disco vistas de perfil del *Surface Photometry Catalogue of the ESO-Uppsala Galaxies* (ESO-LV, Lauberts-Vallentijn 1989). Este catálogo contiene un gran número de galaxias que han sido seleccionadas y parametrizadas de un modo uniforme. Primero se seleccionaron las galaxias con una declinación $\delta \leq$ -17.5°, excluyendo el área del ecuador Galáctico $|b| < 15°$ para no tener muchas estrellas de nuestra Galaxia en la imagen. Dentro de esos criterios, seleccionamos las que tiene las siguientes propiedades:

- Galaxias aisladas o sin vecinas significativas a una distancia menor o igual a cinco veces sus diámetros ópticos, así que en principio no están interaccionando con otras y no están perturbadas.
- $D_{25}(B) \geq 2.2$', es decir, con un diámetro óptico (medido con la isofota de $\mu_B = 25$ $mag/arcsec^2$, brillo superficial en el azul) mayor de 2.2 minutos de arco.
- i (inclinación) $> 87^o$, esto nos asegura que vemos la galaxia prácticamente de perfil y podemos identificar mejor el alabeo. Esta inclinación se determina asumiendo el criterio $(b/a)_0 = 0.11$ (de Grijs 1998), donde b/a es la proporción observada de ejes. Esta condición podría dejar fuera las galaxias de tipo temprano con bulbos prominentes que deberían estar presentes en la discusión sobre el fenómeno de alabeos. En cambio, usando este enfoque, intentamos evitar la confusión entre brazos espirales, corrugaciones y alabeos.
- Tipo morfológico dentro del rango S0 a Sd, es decir, galaxias espirales y lenticulares.

La única restricción externa impuesta a esta muestra, es que fueran observables en la época del año en el que se realizaron las observaciones, desde Chile. Las propiedades básicas de estas galaxias aparecen en la Tabla 2.2.

Esta muestra fue observada por R. de Grijs en:

Tabla 2.2: Parámetros globales de las galaxias obtenidos del Catálogo ESO-LV (Lauberts & Valentijn 1989).

Galaxia	RA(J2000.0) (hh:mm:ss.s)	Dec(J2000.0) (gg:mm:ss)	Tipo de Hubble	a/b (relación de ejes)	$D_{25}(B)$ (arcsec)	B mag (total)	$B-R$ (tot) (mag)	Velocidad Radial (km s^{-1})	PA (grados) (N→E)
ESO026-G06	20:48:28.3	−78:04:09	6.7±1	9.3	134.9	15.48±0.30	+1.37	2323[1)]	76.0
ESO033-G22	05:31:41.8	−73:44:58	6.8±1	12.5	131.8	15.56±0.19	+0.86	3932[1)]	170.0
ESO142-G24	19:35:42.3	−57:31:10	6.6±1	8.4	237.1	14.03±0.24	+1.30	2027[1)]	6.0
ESO157-G18	04:17:54.4	−55:56:04	6.5±1	6.6	186.2	13.90±0.48	+0.96	1139	18.0
ESO201-G22	04:09:00.4	−48:43:36	4.8±1	7.3	151.4	14.73±0.32	···	4014	59.0
ESO202-G35	04:32:15.6	−49:40:31	3.4±1	6.2	184.1	13.38±0.31	+1.06	1856	133.0
ESO235-G53	21:05:10.4	−47:47:17	3.0±0	6.0	153.1	14.53±0.26	+1.85	5110	49.0
ESO240-G11	23:37:49.3	−47:43:34	4.7±1	10.0	331.1	13.05±0.21	+1.35	2817	129.0
ESO288-G25	21:59:17.6	−43:52:02	4.2±1	6.5	153.1	13.97±0.21	+1.30	2484	53.0
ESO311-G12	07:47:34.2	−41:27:07	0.1±1	6.4	251.2	12.83±0.28	+1.69	848[1)]	14.0
ESO340-G08	20:17:11.0	−40:55:22	6.0±1	24.0	192.8	15.45±0.20	+0.95	3004[1)]	34.0
ESO340-G09	20:17:20.2	−38:40:29	7.0±1	9.0	160.3	14.52±0.27	···	2546	98.0
ESO358-G26	03:35:30.8	−34:26:49	−1.6±2	4.2	153.1	12.90±0.40	+1.19	1660	84.0
ESO358-G29	03:36:31.4	−35:17:38	−2.0±1	3.9	153.1	12.47±0.18	+1.45	1740	139.2
ESO416-G25	02:48:41.3	−31:32:09	3.2±1	6.0	141.3	14.68±0.25	+1.38	4992	31.0
ESO460-G31	19:44:21.2	−27:24:22	4.8±1	9.5	154.9	15.15±0.21	···	5352[1)]	92.0
ESO487-G02	05:21:48.6	−23:48:45	3.9±1	7.5	199.5	13.62±0.26	+1.35	2088[1)]	60.0
ESO531-G22	21:40:29.5	−26:31:40	4.5±1	8.7	154.2	13.94±0.35	···	3639[1)]	8.0
ESO555-G36	06:07:41.5	−19:54:54	5.5±1	11.5	139.6	15.60±0.58	+1.62	···	146.0
ESO564-G27	09:11:54.3	−20:07:04	6.1±1	14.0	278.6	14.39±0.90	+1.36	2178	168.0

[1)] Velocidades Heliocéntricas radiales obtenidas de Mathewson et al. (1992).

-**Infrarrojo Cercano** con el telescopio de 1.5 metros Ritchey-Chretien, del Observatorio Inter-American Cerro Tololo (CTIO) del 22 al 27 de Octubre de 1998 (Prop0020), equipado con la cámara *Cerro Tololo Infrared IMager* (CIRIM), que tiene un detector NICMOS3 de HgCdTe 256x256 píxeles, con una escala de 1.16"/px. Estas medidas fueron tomadas con el filtro K_{short} ($\equiv K_S$) de $\lambda_{eff} = 2.15$ μm (Wainscoat & Cowie 1992). Se utilizó este filtro, porque el cielo es un poco menos brillante que en K, cuya $\lambda_{eff} = 2.20$ μm; por ejemplo, el cielo en UKIRT, Hawaii, es 13.5 $mag/arcsec^2$ en K_S y 13 $mag/arcsec^2$ en K ([1]), y la extinción es prácticamente la misma, en torno a 0.11 $mag/airmass$.

-**Visible**, las medidas vienen de dos telescopios del Observatorio Europeo del Sur (ESO): el telescopio de 1.54 metros danés, equipado con un CCD TEK 1081x1040 píxeles, con una escala de 0.36"/px, en los filtros B y V de Johnson, y con el i de Thuan & Gunn, y el telescopio de 0.92 metros holandés, con un CCD TEK de 512x512 píxeles y una escala de 0.44"/px en los filtros B, V y R de Johnson, y con el i de Thuan & Gunn. Estos datos ya reducidos fueron proporcionados por R. de Grijs (ver su tesis, de Grijs 1997). Por homogeneidad, el filtro i de Thuan & Gunn es llamado I, pero no debe confundirse con el I de Johnson que aunque es parecido i-I = 0.816 - 0.081 (R-I) (Thim et al. 2004), es un sistema fotométrico diferente que fue diseñado para evitar contaminación de las líneas de Hg de las ciudades, y las líneas del [OI] del cielo (Thuan y Gunn 1976).

2.2. Reducción de los datos en infrarrojo

El rango espectral del infrarrojo cercano (longitud de onda λ entre 1 y 5 μm), es el más adecuado para estudiar la distribución de poblaciones estelares mayoritarias en los discos y bulbos, a la vez que minimiza los efectos de la extinción interna (la absorción, en magnitudes, en el filtro K es el 10 % de la que es en la banda V, $A_K / A_V \sim 0.1$). Además la emisión en el infrarrojo cercano traza mejor la población estelar vieja de las galaxias, uno de nuestros objetivos. Por esta razón se ha escogido este rango, complementario al visible, para realizar las observaciones de una muestra de galaxias espirales de perfil, y así poder estudiar estructuras del disco estelar de estas galaxias.

Hemos hecho la reducción de estos datos con paquetes especiales de tratamiento de datos infrarrojos, donde la correcta sustracción del cielo y las estrellas de nuestra Galaxia que aparecen en primer plano en la imagen es especialmente importante.

2.2.1. Fotometría superficial de galaxias

Analizando la distribución del brillo superficial de las galaxias que se obtiene directamente de un telescopio, podemos estudiar su morfología y estructura. Pero para ello hay que tener en cuenta el brillo del cielo, cuyo nivel nunca es cero y el brillo que se pierde al atravesar la atmósfera terrestre, que no es completamente transparente.

Necesitamos un valor de brillo superficial que nos permita estudiar los truncamientos y los alabeos de las galaxias. Tenemos que ser capaces de medir la parte más externa de la galaxia, la cual tiene un brillo por debajo de 26 $mag/arcsec^2$ en la banda B. Esto es el 6 % del brillo del cielo ($\mu_B \sim 23$ $mag/arcsec^2$): $\frac{10^{-26/2.5}}{10^{-23/2.5}} \cdot 100$, por lo que en el proceso de reducción, la medida del brillo del cielo debe ser determinada con extrema precaución. Esto se acentúa más cuando estamos trabajando en el rango del infrarrojo, donde el cielo nocturno es más brillante: (B - V) = 0.9 ó μ_K = 13 $mag/arcsec^2$.

Además, un factor importante a tener en cuenta cuando se trabaja con datos dentro de la banda del infrarrojo, es que el nivel de cielo (de fondo) puede cambiar significativamente en escala de minutos, tanto en espacio (minutos de arco) como en tiempo (120 segundos), y es unas 10^4 veces más brillante que las regiones externas de las galaxias en las que estamos interesados. Por lo tanto, al hacer las observaciones es fundamental obtener tantas imágenes de cielo como de los objetos (galaxias), para que la posterior sustracción del cielo sea lo más precisa posible. En este caso, se tomaron imágenes de cielo y objeto alternativamente, con el mismo tiempo de exposición y separadas espacialmente unos 5 minutos de arco. Debido al alto brillo del cielo de fondo en el infrarrojo, los tiempo de exposición deben ser cortos, para no saturar la cámara y estar dentro del régimen lineal de la misma.

[1] `http://www.jach.hawaii.edu/UKIRT/instruments/uist/imaging/imaging.html`

Todo esto hace que en la reducción de los datos, el proceso de aplanado del campo *flatfielding*, sustracción del cielo y posterior combinación de las distintas imágenes para obtener el resultado final, se realice con especial cuidado para no introducir errores sistemáticos. Una sustracción incorrecta del cielo, puede hacer que su nivel contribuya al brillo de la galaxia a grandes radios, si se infraestima, o que exista un radio de truncamiento ficticio, a partir del cual no hay material luminoso, si se sobreestima.

2.2.2. REDUCE

Para obtener la fotometría superficial de las galaxias en infrarrojo, utilizamos un paquete de reducción y análisis de datos llamado *REDUCE* y desarrollado por R.F. Peletier. *REDUCE* trabaja dentro del *software IRAF* ("Image Reduction and Analysis Facility"que es un paquete de programas desarrollado por el *National Optical Astronomy Observatories (NOAO)* en Tucson, Arizona) y está especialmente preparado para tratar datos muy profundos de imagenes con nivel de fondo alto. Mostramos un esquema del proceso de reducción en la Figura 2.1. Los programas borran las estrellas de nuestra Vía Láctea que aparecen en las imágenes del cielo. Una vez limpias se usan para sustraer el cielo a las imágenes donde tenemos los objetos que se han tomado adyacentes en tiempo.

Para calibrar las observaciones y conocer la magnitud que medimos en los objetos, se observaron un número de estrellas estándares de calibración del catálogo de *SAAO/ESO/ISO Faint Standard Stars* (Carter y Meadows, 1995) y del catálogo de *UKIRT Faint Standard Stars* (Casali y Hawarden, 1992). Se ha usado la corrección de Wainscoat y Cowie (1992) para transformar las medidas en K_S con las establecidas en la banda K. Estas estrellas se tomaron al menos tres veces por noche con diferentes masas de aire, por lo que se pudo calcular la extinción atmosférica existente en las noches fotométricas de observación con bastante precisión:

$$\mu_{obs} = \mu_{real} - \mathrm{ZP} - \mathrm{Ext} \cdot \mathrm{X} - \mathrm{C} \cdot (\mathrm{J} - \mathrm{K}) \tag{2.1}$$

$$\mu_{obs} = -2.5 \log_{10} \frac{\text{cuentas}}{\text{segundos} \cdot \text{escala}^2} \tag{2.2}$$

donde μ_{obs} es la magnitud medida por segundo, μ_{real} es la magnitud real por segundo, ZP es el punto de referencia del telescopio, es decir, es la magnitud aparente que debe tener una estrella para dar 1 cuenta por segundo en la cámara, Ext es el coeficiente de extinción atmosférico por masa de aire, X es la masa de aire medida durante la observación, C es el coeficiente de correción de color y (J-K) es el color, tomado de Peletier y Balcells (1996). La escala en este detector es 1.16"/px. Los cálculos fueron desarrollados dentro de *IRAF* con un total de 21 estrellas estándares, y con los siguientes resultados:

ZP = 19.831 ± 0.016 $mag/arcsec^2$
Ext = -0.12 ± 0.02 $mag/(airmass \cdot arcsec^2)$
C = -0.14 ± 0.05 $mag/arcsec^2$

Así pudimos comprobar, sustituyendo en la Ecuación 2.1, que son observaciones muy profundas que alcanza un brillo superficial de 24 - 24.5 $mag/arcsec^2$ en K_S a una sigma, que se corresponde en la banda azul (B) con 28.5, lo que quiere decir que medimos zonas muy débiles en intensidad. La resolución que tenemos está limitada al tamaño de pixel de la cámara, que es de 1.16"/px.

Con *REDUCE* conseguimos reducir el ruido electrónico correlado que introducía la cámara utilizada en el Telescopio Carlos Sánchez, CAIN y obtener unos resultados que nos permitieron realizar la investigación sobre truncamientos estelares.

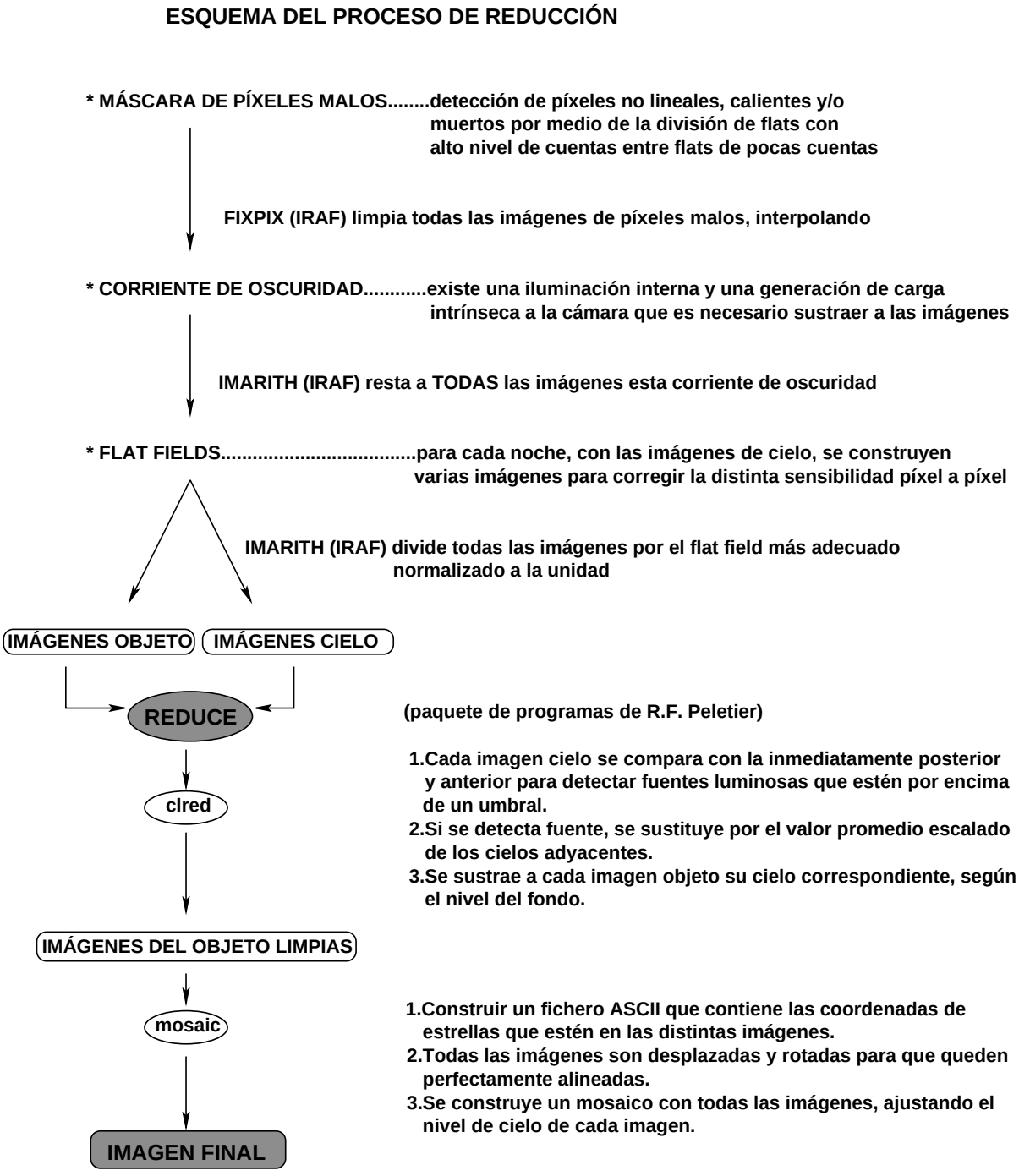

Figura 2.1: Esquema del proceso de reducción.

Capítulo 3

Truncamientos

En el presente capítulo hacemos un breve resumen y adjuntamos 4 artículos internacionales de la revista *Astronomy & Astrophysics* en los que hemos publicado el trabajo realizado sobre este tema.

3.1. Introducción

Como dijimos en la introducción general, el truncamiento de los discos estelares fue descubierto por van der Kruit (1979), describiéndolo más tarde (van der Kruit y Searle 1981a) como un límite relativamente brusco en la distribución de brillo superficial, a partir del cuál no se detectaba emisión de la galaxia aunque se aumentara el tiempo de exposición. Lo llamó radio de truncamiento (*cut-off*), R_t, y midió que ocurría a un radio de 3 a 5 longitudes de escala radial, h_R. Kregel, van der Kruit y de Grijs (2002) concluyen que el truncamiento es evidente en el 60 % de sus 34 galaxias de perfil y que por tanto es una estructura muy común en las galaxias. A pesar de todos los trabajos que se han hecho (Barteldrees y Dettmar 1994, de Grijs, Kregel y Wesson 2001, Pohlen et al. 2004, Erwin, Beckman y Pohlen 2005, Pohlen y Trujillo 2006, y otros autores), aún son necesarias más observaciones a distintas longitudes de onda que describan este fenómeno y nos ayuden a discernir si los perfiles radiales tienen un truncamiento real o un radio de corte que separa la parte interna y la externa del disco de la galaxia. Las hipótesis propuestas para explicar esta estructura tampoco son definitivas.

El brillo superficial de las galaxias de disco a grandes radios se puede ajustar a una ley exponencial del tipo:

$$\mathrm{I(R) = I_0 exp(-R/h_R)} \tag{3.1}$$

donde h_R es la escala radial del disco. Las desviaciones de este perfil se suelen explicar como contaminaciones debidas a otras componentes, como es el caso de la contribución en la parte más interna del disco por un bulbo elíptico que obedece a la ley de de Vaucouleurs:

$$\mathrm{I(R) = I_e exp\left\{-7.67\left[(R/R_e)^{1/4} - 1\right]\right\}} \tag{3.2}$$

donde R_e es el radio efectivo, o radio que encierra la mitad de la luz del sistema, y donde I_e es el brillo superficial a $R = R_e$. Este brillo que proviene del bulbo no es completamente nulo, incluso en las zonas más externas de las galaxias.

Esta descomposición disco-bulbo se puede hacer de un modo más fiable ajustando modelos en dos dimensiones a la fotometría superficial, como el de van der Kruit y Searle (1981b):

$$\mathrm{I(R,z) = \begin{cases} I_0 e^{-R/h_R} sech^2(z/2h_z) & R < R_t \\ 0 & R > R_t \end{cases}} \tag{3.3}$$

donde (R,z) son coordenadas cilíndricas que definen los ejes de simetría del modelo, e I_0, h_R, h_z y R_t son parámetros con valor constante. Van der Kruit y Searle (1981a) encontraron que no había

dependencia de h_z, espesor característico del disco, con el radio R y que a $R = R_t$ el perfil muestra una mayor pendiente, de tal forma que en menos de 1 kpc el brillo superficial termina cayendo 4 magnitudes por debajo del nivel estimado del cielo.

Wainscoat, Freeman y Hyland (1989) propusieron otro modelo para determinar la distribución de la luz en galaxias de perfil, a partir de fotometría en el infrarrojo cercano para evitar el problema con la banda de polvo. Así, para la galaxia IC 2531, determinaron la existencia de tres componentes: un disco viejo rojo, con (B - V) = 0.78, un disco joven azul con (B - V) = -0.04, y una capa de polvo. Para las tres componentes asumieron una distribución exponencial que puede expresarse de la forma general:

$$D(R,z) = \begin{cases} D_0 e^{-R/h_R - |z|/h_z} & R < R_t \\ 0 & R > R_t \end{cases} \tag{3.4}$$

donde D es la distribución de la intensidad para el disco viejo y el joven y la distribución de la absorción para la capa de polvo. El mejor ajuste al modelo se obtiene con los parámetros $h_R = 6.4$ kpc y $R_t = 4h_R$. El disco viejo tiene $h_z = h_R/12$, el joven $h_z = h_R/96$ (es más delgado) y la capa de polvo $h_z = h_R/48$; la densidad de luminosidad D_0 ($\equiv$ I(0,0)) es la misma para los dos discos estelares, pero para la capa de polvo la absorción o extinción sería $D_0 \equiv A_V = 1.6$ mag kpc^{-1} y $D_0 \equiv A_K = 0.18$ mag kpc^{-1}.

En 1979 Burstein concluyó que además del disco y el bulbo existía un disco grueso cuya distribución de intensidad se podía expresar con la ecuación (3.4), pero con $h_z \sim 1$ kpc. Este disco grueso empezaría a dominar sobre el disco delgado a $\mu_B \simeq 23.5\ mag/arcsec^2$. Este fenómeno se ha detectado en muchas pero no en todas las galaxias disco, ya sean S0 o espirales. En muchos casos es difícil distinguir entre disco grueso y bulbo prominente, o simplemente el disco no sigue un perfil vertical exponencial, por lo que la interpretación física de este fenómeno aún está por aclarar.

Analizando el gradiente de color en las galaxias disco vemos que, en general, en la zona dominada por el bulbo los colores son los esperados en una galaxia elíptica. Avanzando a radios mayores nos encontramos que las estrellas jóvenes cobran protagonismo, el índice de color muestra un progresivo azulamiento del disco. Este gradiente de color se puede deber a gradientes en el grado de extinción interna por polvo, a gradientes en la edad media de las estrellas o a gradientes en la metalicidad. Estas causas se pueden dar de manera conjunta o individual dependiendo de cada galaxia, e incluso hay perfiles de color que no muestran este comportamiento sistemático.

Para las galaxias de disco, la tarea de deducir su forma en tres dimensiones a partir de la proyección, es complicada debido a la presencia de polvo que hace que no sean transparentes, sobre todo en algunas longitudes de onda. Para galaxias de este tipo, vistas de perfil, es muy importante tener en cuenta que la luz de las estrellas que nos llega ha atravesado regiones del medio interestelar ricas en polvo, absorbiendo y dispersando gran parte de la misma. Otro dato a tener en cuenta es si la distribución de ese polvo en el disco se encuentra en una capa, o si se confina en pequeños cúmulos, alrededor de estrellas luminosas. Para intentar evadir estos problemas, se trabaja a longitudes de onda dentro del infrarrojo cercano (< 1250 nm), donde la absorción por polvo es considerablemente menos importante que en visible. La luz azul (longitud de onda en torno a 400-500 nm) tiene más absorción y dispersión que la luz roja (~ 1000 nm).

3.1.1. Tipos de perfiles radiales

Freeman (1970) examinó con detalle la naturaleza exponencial de los perfiles de brillo superficial radial de los discos estelares de las galaxias e hizo la primera clasificación, dividiéndolos en dos de los tipos que hoy conocemos: tipo c o exponencial y tipo b o doble exponencial. Erwin, Beckman y Pohlen (2005) fueron capaces de llegar a niveles de brillo superficial más débiles μ_R = 27-28 $mag/arcsec^2$ e identificaron un nuevo tipo que denominaron perfil antitruncado (tipo d). Junto al perfil truncado descubierto por van der Kruit (1979), tendríamos la siguiente clasificación (en la introducción presentamos un esquema en la Figura 1.1):

* Tipo a o perfil truncado: es el perfil, en la mayoría de los casos exponencial, que a grandes radios termina o se "trunca" de forma brusca o gradual en una region de unos pocos kiloparsecs trazando una "curva de truncamiento". El radio galactocéntrico a partir del cual la densidad estelar se anula se llama radio de truncamiento o R_t.

** Tipo b o perfil doblado *break*: es aquel en el que a partir de un radio que llamamos de corte, el perfil se ajusta a otra exponencial de mayor pendiente que la exponencial interna. En este caso no hay un truncamiento real o completo del perfil, sino una clara división del disco en interno y externo, presentando este último una escala radial menor que el interno. Pérez (2004) mostró que las galaxias jóvenes a $z \sim 1$ podían considerarse de este tipo al concluir en su estudio que los perfiles radiales se ajustaban mejor a perfiles de doble exponencial.

*** Tipo c o perfil exponencial: Perfil que se ajusta a una exponencial hasta el límite crítico, a partir del cual el nivel de brillo es indetectable, confundiéndose con el ruido del fondo de cielo.

**** Tipo d o perfil antitruncado: Perfil parecido al tipo b, con un radio de corte a partir del cual, también de una forma brusca o gradual, la pendiente cambia siendo menos inclinada que la de la exponencial inicial.

Podemos encontrar otras clasificaciones como por ejemplo la que aparece en Pohlen et al. (2007).

3.1.2. Modelos teóricos de truncamiento

Los modelos propuestos para explicar el origen de los truncamientos son:

1) Magnético: propuesto por Battaner, Florido y Jiménez-Vicente (2002) y basado en el modelo magnético que explica la curva de rotación alta y plana (Nelson 1988, Battaner et al. 1992) en el cual la fuerza magnética que actúa sobre el gas ionizado desaparecería al formarse las estrellas y estas se moverían a órbitas más externas o incluso escaparían de la galaxia. Cuando el disco se ha formado presenta una estructura donde las fuerzas que actúan sobre el gas están en equilibrio: gravedad y fuerza magnética frente a la fuerza centrífuga. Si se forman estrellas de este gas, la fuerza magnética deja de actuar y la gravedad no es capaz de retener a las estrellas recién formadas que pueden escaparse a radios más lejanos, produciendo un perfil antitruncado, o escapar completamente, lo que provocaría un truncamiento real en el disco estelar.

2) Colapso: Van der Kruit (2001) presenta otra teoría donde el truncamiento coincide con una clara disminución de la velocidad de rotación. Esto se justificaría con una disminución real en la distribución radial de la densidad total, gaseosa y estelar. La región de truncamiento se corresponde con la del máximo momento angular del disco, que podría ser el mismo que tendría la protogalaxia si en el colapso de la misma se conservara el momento angular (Fall y Efstathiou 1980). Esto implicaría que el material gaseoso que existe más allá del radio de truncamiento del disco estelar ha sido acretado en fases más tardías de la evolución galaáctica (Broeils y Rhee 1997). El hecho de que el alabeo del disco gaseoso empiece a un radio cercano al radio de truncamiento (van der Kruit 2001), quedaría justificado en cierto modo por esta teoría.

3) Umbral: Otros investigadores, como Kennicutt (1989), justifican el truncamiento encontrando a ese radio un umbral en la formación estelar cuando la densidad superficial del gas cae por debajo de cierto valor. Pero hay formación estelar más allá del radio de truncamiento. Por ejemplo en la Vía Láctea Kobayashi y Tokunaga (2000) demostraron que existían estrellas muy jóvenes recién formadas asociadas a una nube molecular que dista del centro galáctico unos 15-19 kpc, siendo el radio de truncamiento de nuestra Galaxia de unos 14-15 kpc (Ruphy et al. 1996). Y es que decrece exponencialmente la densidad de nubes moleculares, pero no la densidad dentro de ellas, que parece que es constante y por tanto capaz de seguir formando estrellas. Por tanto, las pocas nubes moleculares que existan fuera del radio de truncamiento, siguen siendo capaces de formar estrellas. Esto es un problema, porque hay formación estelar, pero no hay estrellas. Además con el descubrimiento de van der Kruit (2001) de una bajada en la velocidad de rotación en torno al radio de truncamiento justificaría una disminución en la densidad, pero no debida al umbral que proponen Kennicutt (1989) y otros autores. En cambio, el modelo del umbral predice que las galaxias de bajo brillo superficial tendrían una proporción $\mathrm{R}_t/\mathrm{h}_R$ menor, relación que se ha demostrado en esta tesis y en la tesis de Kregel (2003). El modelo del colapso estaría en contra de esta observación porque predice que la relación es constante para todas las galaxias.

4) Acreción: El primer modelo que se propuso es de Larson (1976) que tomaba el truncamiento como la extensión en ese momento de un disco que crece añadiendo material del exterior. Con este modelo se explicaría el gradiente de edad que se observa a lo largo de los discos (de Jong 1996). Además justificaría que hubiera formación estelar fuera del radio de truncamiento pero no estrellas, ya que estas serían muy jóvenes, masivas y calientes y observables en el rango del ultravioleta.

3.2. Observaciones

El objetivo en esta parte de la tesis es estudiar el truncamiento de los discos estelares de las galaxias, y para ello necesitamos obtener observaciones muy profundas de los objetos (por debajo de 26 $mag/arcsec^2$ en la banda B). En este trabajo destacamos que hemos usado datos a longitudes de onda del infrarrojo cercano frente a los datos en el visible, donde se han realizado la mayoría de los estudios. Esto hace que la extinción por polvo se minimice y podamos detectar mejor el disco estelar. Además utilizamos galaxias vistas de perfil para trazar los perfiles radiales hasta radios que serían inobservables en las galaxias vistas de cara, en las que prodría no alcanzarse la región de truncamiento. En total hemos observado 14 galaxias espirales vistas de perfil con la cámara CAIN del 1.5m TCS, de Tenerife, que permite realizar observaciones de objetos extensos con resultados óptimos. El TCS es un telescopio especialmente diseñado para la observación en infrarrojo con instrumentación criogénica, materiales con mínima emisión térmica, contaminación de fondo controlada por "cold stop" y localizado en un lugar especialmente seco.

Como dijimos en el capítulo 2, el cielo en infrarrojo cercano es muy brillante y variable, lo que obliga a que los datos tomados a estas longitudes de onda sean muy numerosos, del orden de 100 ficheros por galaxia. La secuencia que seguimos para observar es la clásica: alternancia entre exposiciones de objeto y cielo (Obj_1-Sky_1-Sky_2-Obj_2-Obj_1-Sky_3-Sky_4-Obj_2) donde Obj_1 y Obj_2 son las exposiciones de la galaxia desplazadas la 2 de la 1 unos 15" al Norte y al Este, y Sky_x son las exposiciones del cielo que están tomadas a x =1: 600" al Oeste de Obj_1, x =2: 900" al Oeste, x =3: 600" al Este de Obj_2 y x =2: 900" al Este. Cada exposición es un fichero (un cubo) de 120 segundos: 24 imágenes individuales de 5 segundos cada una para los filtros H y K_S y 4 imágenes individuales de 30 segundos para el filtro J. En total tenemos unos 48 minutos de exposición en el objeto y 48 minutos en el cielo. Para la reducción hemos diseñando *scripts* o secuencias de comandos dentro del paquete de reducción y procesado de análisis de imágenes IRAF (desarrollado en el *National Optical Astronomy Observatories* (NOAO) en Tucson, Arizona), para realizar las tareas que de otra forma, y debido a la gran cantidad de ficheros, llevarían demasiado tiempo. Para corregir de *flatfield*, substraer el cielo y alinear el conjunto de imagenes de una galaxia para luego sumarlas, hemos usado el paquete de reducción desarrollado por R.F. Peletier, REDUCE, que funciona dentro de IRAF (ver Figura 2.1).

Los resultados se calibraron con estrellas estándares del catálogo de UKIRT (Casali y Hawarden 1992) y con estos datos trazamos los mapas de isofotas de todas las galaxias en los diferentes filtros del infrarrojo cercano J, H y K_S.

3.3. Análisis de los datos

Lo primero que hacemos con las galaxias de perfil ya reducidas y calibradas es rotarlas para que el eje mayor quede horizontal. De esta manera, los perfiles a lo largo del eje X son perfiles proyectados del disco a lo largo del radio galactocéntrico. Es necesario desproyectar la distribución de brillo superficial $I(\vec{R})$ que medimos a cada radio proyectado R para obtener la densidad de luminosidad en tres dimensiones $j(\vec{r})$, que representa la estructura real de las galaxias. Para ello hemos utilizado un método numérico de inversión, frente al método analítico descrito por Binney y Tremaine (1987) que se basa en la integral de Abell (ver Apéndice A al final del capítulo). Hemos probado, no obstante, a hacer la desproyección de los perfiles con el método analítico de Binney y Tremaine (1987) obteniendo los mismos resultados (Figura 3.1).

3.3.1. Método numérico de inversión

Con el método numérico necesitamos asumir extinción despreciable y axisimetría. Cumplimos la hipótesis de extinción despreciable porque las observaciones en infrarrojo están menos afectadas por la banda de polvo. Podemos asumir axisimetría también porque en nuestras galaxias de perfil los dos lados del disco son similares. Lo importante es que no asumimos ningún modelo de galaxia. El método consiste en dividir el disco de la galaxia en anillos de anchura constante Δr dentro de los cuales la emisividad en la dirección del observador es constante (Figura 3.2). Esa emisión por unidad de volumen en la dirección del observador, l_i, es la cantidad que nosotros queremos obtener por el método de inversión a partir de I, que es el brillo superficial que tenemos de las

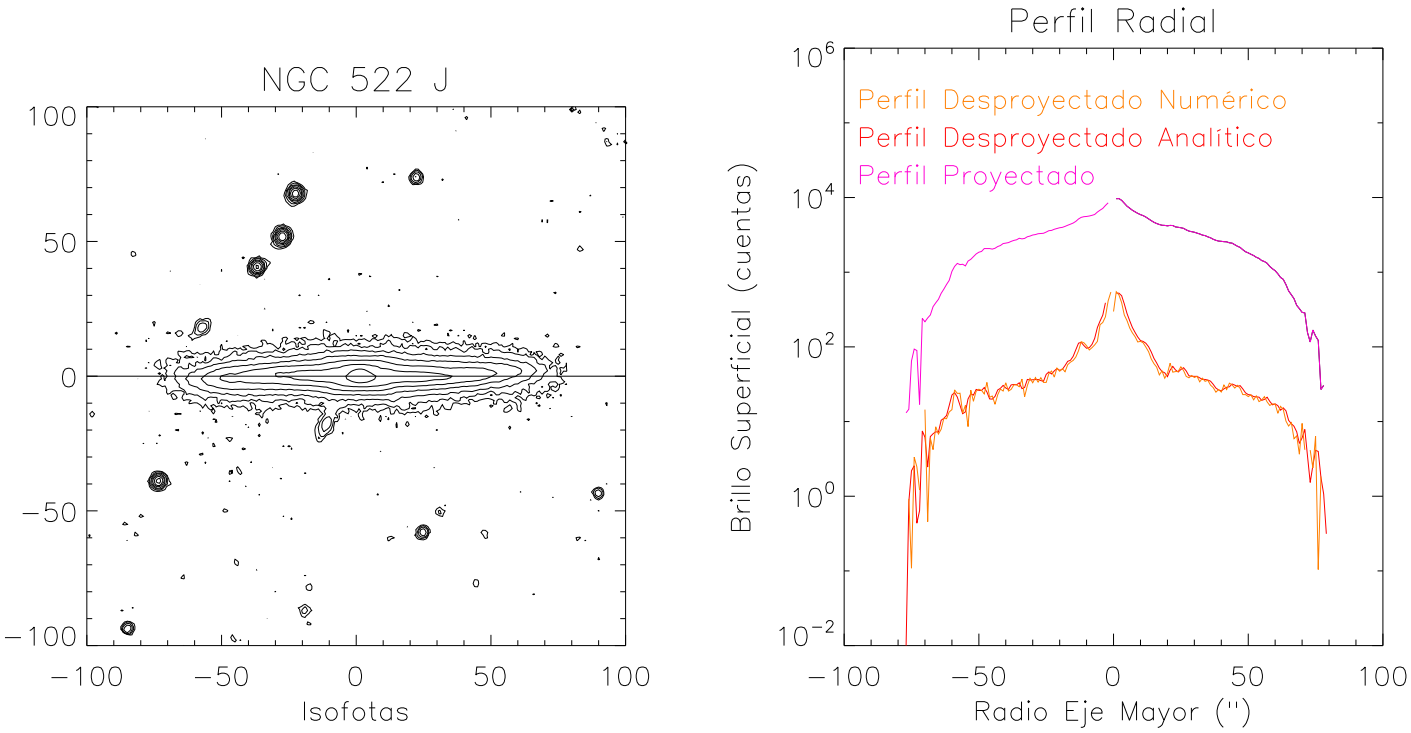

Figura 3.1: Izquierda: Mapa de contornos de NGC 522 en el filtro J. La distancia entre isofotas es equidistante con un paso de $+0.75\ mag/arcsec^2$ empezando en $20.6\ mag/arcsec^2$ (= 3 veces el nivel de ruido). Derecha: Comparación entre los métodos de desproyección analítico y numérico.

observaciones. Para cada radio, a la integral de I contribuyen varios anillos y con diferente área A_{ki}, de tal forma que $I_k = 2\sum_i A_{ki} l_i$. Una vez calculado l_i, si lo integramos en la dirección vertical z, obtendríamos el brillo superficial de la galaxia si la viéramos de cara. k es el orden de píxel desde el centro de la galaxia hasta el borde, que hemos observado a z = 0. i denota los diferentes anillos en los que puedo dividir el disco de la galaxia. Con la Figura 3.2 vemos que las áreas son:

$$A_{ki} = \int_{(k-1/2)\Delta}^{(k+1/2)\Delta} \left((i+1/2)^2\Delta^2 - x^2\right)^{1/2} dx - \int_{(k-1/2)\Delta}^{(k+1/2)\Delta} \left((i-1/2)^2\Delta^2 - x^2\right)^{1/2} dx \tag{3.5}$$

donde Δ es el tamaño del píxel. Teniendo en cuenta que:

$$\int \left(a^2 - x^2\right)^{1/2} dx = \frac{1}{2}\left[x\left(a^2 - x^2\right)^{1/2} + a^2 \sin^{-1}\frac{x}{\mid a \mid}\right] \tag{3.6}$$

Obtenemos:

$$\begin{aligned} 2A_{ki} = \ & \Delta^2 \Bigg(\left(k+\tfrac{1}{2}\right)\left(\left(i+\tfrac{1}{2}\right)^2 - \left(k+\tfrac{1}{2}\right)^2\right)^{1/2} - \left(k-\tfrac{1}{2}\right)\left(\left(i+\tfrac{1}{2}\right)^2 - \left(k-\tfrac{1}{2}\right)^2\right)^{1/2} \\ & \underline{-\left(k+\tfrac{1}{2}\right)\left(\left(i-\tfrac{1}{2}\right)^2 - \left(k+\tfrac{1}{2}\right)^2\right)^{1/2}} + \underline{\left(k-\tfrac{1}{2}\right)\left(\left(i-\tfrac{1}{2}\right)^2 - \left(k-\tfrac{1}{2}\right)^2\right)^{1/2}} \\ & + \left(i+\tfrac{1}{2}\right)^2 \sin^{-1}\tfrac{k+1/2}{i+1/2} - \left(i+\tfrac{1}{2}\right)^2 \sin^{-1}\tfrac{k-1/2}{i+1/2} \\ & \underline{-\left(i-\tfrac{1}{2}\right)^2 \sin^{-1}\tfrac{k+1/2}{i-1/2}} + \underline{\left(i-\tfrac{1}{2}\right)^2 \sin^{-1}\tfrac{k-1/2}{i-1/2}} \Bigg) \end{aligned} \tag{3.7}$$

las partes de la ecuación subrayadas _____ no se calculan cuando $i = k$. En todos los casos $i \geq k$. Para $k = N$ siendo N el último punto que podemos medir cuando la señal del fondo

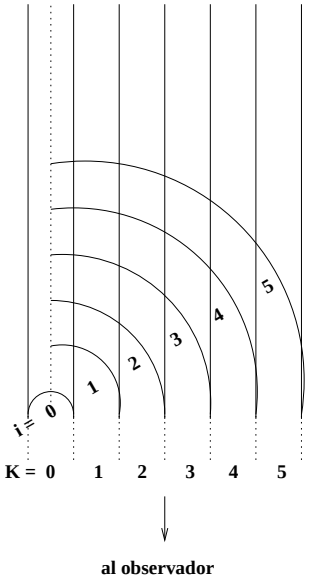

Figura 3.2: Esquema del método numérico de inversión, donde i es el subíndice para denotar los anillos del disco y k para denotar la distancia radial de la galaxia vista de perfil.

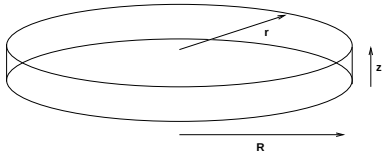

Figura 3.3: Parámetros del disco.

(a 3σ) y de la galaxia son indistinguibles, tenemos que $I_N = 2A_{NN}l_N$ y por tanto $l_N = I_N/2A_{NN}$. En general:

$$l_k = \frac{I_k - 2\Sigma_{i=k+1}^{N} A_{ki}l_i}{2A_{kk}} \tag{3.8}$$

es decir, podemos calcular l_k conociendo l_m con $m > k$. Vamos calculando desde los límites externos de la galaxia $k = N$ hasta el interior cuando $k = 0$. Repetimos este proceso para cada z y así calculamos el brillo superficial desproyectado (de la galaxia como si estuviera de cara) integrando l_{iz} sobre z con Δz en torno a los 10-30 segundos de arco.

El paso de desproyectar para cada z y luego integrar es completamente intercambiable con integrar en z y luego desproyectar: a partir de I(R,z), brillo superficial de la galaxia de perfil obtenemos I(r) que es el brillo superficial de la galaxia de cara (ver la Figura 3.3). Tomamos el tamaño del píxel como la unidad. Si sumamos en z y luego desproyectamos tenemos I(R) = Σ_zI(R,z) y obtenemos I(r)= $\frac{I(R)}{A(r,R)}$. Si desproyectamos y luego sumamos en z tenemos $l(r,z)$ con $l(r,z) = \frac{I(R,z)}{A(r,R)}$ y sumamos en z:

$$I(r) = \Sigma_z l(r,z) = \Sigma_z \frac{I(R,z)}{A(r,R)} = \frac{1}{A(r,R)}\Sigma_z I(R,z) = \frac{1}{A(r,R)}I(R)$$

Obteniendo exactamente el mismo resultado.

Con este método se estima que el error que cometemos es del orden de 0.03 mag.

En la Figura 3.4 representamos un ejemplo de perfil radial desproyectado y comparamos el perfil original con el proyectado para comprobar la bondad del método de desproyección utilizado. En la gráfica se representan los perfiles radiales, sumados en z. Son la media de los dos semiejes. Así se obtiene el perfil original (línea rosa continua). El perfil desproyectado es el obtenido con nuestro método numérico, y es también con el promedio de los dos semiejes (línea naranja de puntos). El perfil proyectado para hacer la comprobación es simplemente la integral desde R hasta

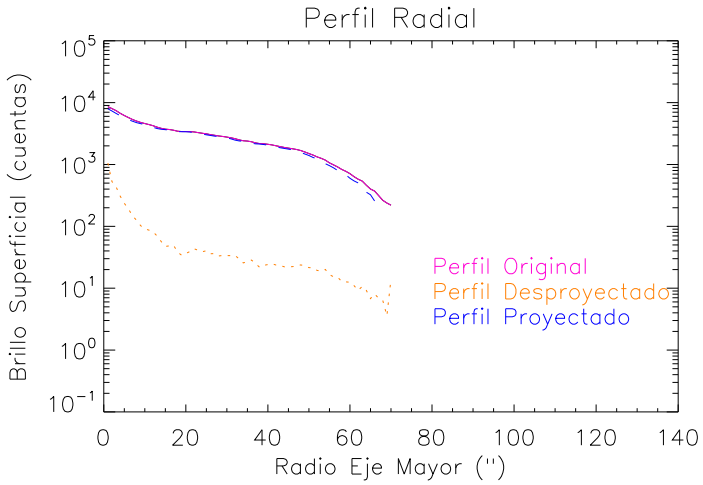

Figura 3.4: En la gráfica se representan los perfiles radiales, sumados en z: línea contínua para el perfil original, discontinua para el perfil proyectado y puntos para el desproyectado.

infinito de la densidad de luminosidad por r dividido entre la raiz cuadrada de r^2-R^2, es decir el brillo superficial a cada radio proyectado. Se representa con la línea discontinua azul.

De esta forma obtenemos los perfiles radiales de los discos estelares de las galaxias desproyectados, con la ventaja de llegar a radios galactocéntricos que para galaxias vistas de cara y con igual nivel de ruido de fondo serían inobservables. Alcanzamos valores de 20-23 $mag/arcsec^2$ en el filtro J y 19-21 $mag/arcsec^2$ en el filtro K_S, que corresponde a un brillo superficial en galaxias de cara de 25-26 $mag/arcsec^2$ en J y 24-25 $mag/arcsec^2$ en K_S. En estos perfiles claramente destaca el bulbo, el disco cuasi-exponencial y en algunos casos el anillo. Tambien observamos el truncamiento con tal detalle que se puede estudiar esta región con una precisión muy pocas veces alcanzada.

3.3.2. Curva de truncamiento

Otra importante aportación ha sido definir una curva de truncamiento T(R) = μ(R) - μ_D(R), donde μ(R) es el brillo superficial observado y μ_D(R) es el brillo superficial exponencial. Es decir, a partir de la Ecuación 3.1, tenemos que μ_D(R) = μ_0+ (1.086/h_R)R (donde μ_0 = μ(R = 0)). Esta curva define qué ocurre en la problemática región del truncamiento de una manera cuantificada. Así, T(R_t) = ∞, con R_t el radio de truncamiento. Además se puede ajustar con una función de tres parámetros:

$$T = \frac{a}{(R_t - R)^n} \tag{3.9}$$

así cuando R = R_t, T = ∞, lo que significa que el truncamiento es completo. a es una constante y n es un exponente obtenido por ajuste con valor cercano a la unidad.

Mostramos también distintas maneras de describir el fenómeno del truncamiento (o de los perfiles radiales descritos en la Sección 3.1.1) a partir de la forma de la curva de truncamiento:

* Tipo a: Truncamiento, suave: las galaxias terminan truncándose de una manera gradual y completa en una región de unos pocos kiloparsecs (ver Florido et al. 2001), o brusco: van der Kruit y Searle (1981a,b) interpretaron este tipo de perfiles en las galaxias vistas de perfil, que se traduciría en un truncamiento suave en galaxias de cara.

** Tipo b: Los perfiles radiales están compuestos de dos regiones separadas por un radio de corte. Cada región se puede ajustar a una exponencial con diferente pendiente. En este caso no habría un verdadero truncamiento (ver Pohlen et al. 2004).

*** Tipo c: Curva de truncamiento plana, es decir, galaxias sin truncamiento ni cambio de pendiente en la exponencial ajustada, sería el perfil de Freeman (1970).

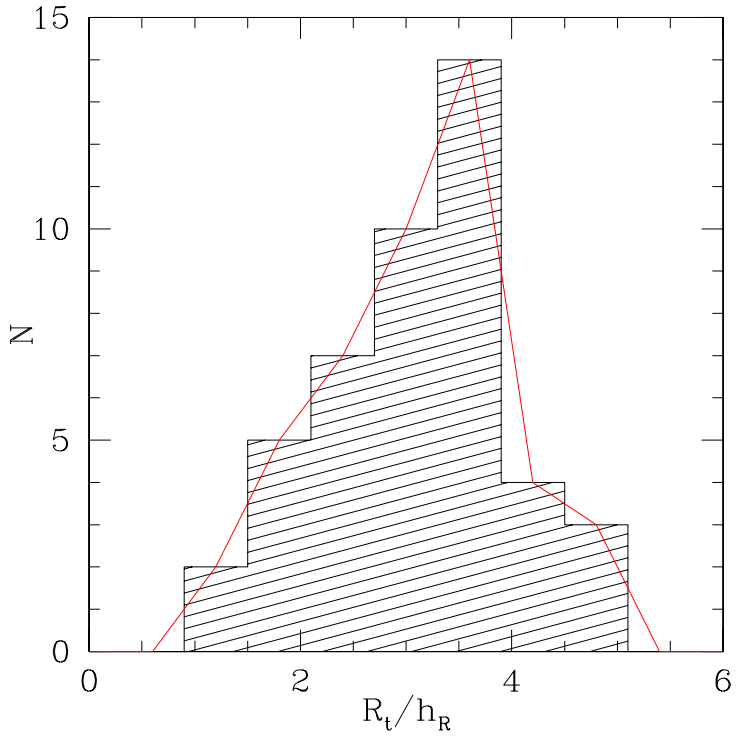

Figura 3.5: Histograma R_t/h_R para todos los filtros y galaxias observadas.

**** Tipo d: Curva de truncamiento parecida al tipo b, con un radio de corte a partir del cual, la pendiente cambia y pasa a tener una inclinación menor que la de la pendiente inicial. Es el "antitruncamiento".

3.4. Resultados

1) Hemos observado en infrarrojo cercano 14 galaxias espirales vistas de perfil, 10 están truncadas y 4 no muestran ningún tipo de truncamiento dentro de los límites de las observaciones (J $<$ 24-25 $mag/arcsec^2$). El truncamiento observado es gradual y completo en una región de unos pocos kiloparsecs.

2) Encontramos un valor medio de radio de truncamiento (ver Figura 3.5) de $R_t = (3.6\pm0.8)h_R$, un poco más bajo pero acorde con lo encontrado por otros investigadores como van der Kruit y Searle (1982a) que obtienen $R_t = (4.2\pm0.5)h_R$ o Barteldrees y Dettmar (1994) con $R_t = (3.7\pm1.0)h_R$. En nuestro trabajo, tenemos datos de galaxias de perfil en infrarrojo cercano donde la extinción y los efectos de la inclinación afectan menos que en el rango del visible, donde se puede estar infraestimando este valor.

3) Detectamos algunas diferencias entre el R_t que obtenemos para los distintos filtros (ver Figura 3.6), así que podemos decir que encontramos dependencia de color en él para algunas galaxias. En general, el radio de truncamiento es menor para las longitudes de onda mayores, lo que podría interpretarse como que el disco de población más vieja se trunca antes que el de las estrellas recién nacidas. La longitud de escala radial h_R depende de la longitud de onda (de Jong 1996) por lo que el estudio de la dependencia del color del radio de truncamiento se debe hacer con R_t y no con R_t/h_R.

4) Obtenemos un buen ajuste de la curva de truncamiento mediante la expresión:

$$T \propto \frac{a}{R_t - R} \tag{3.10}$$

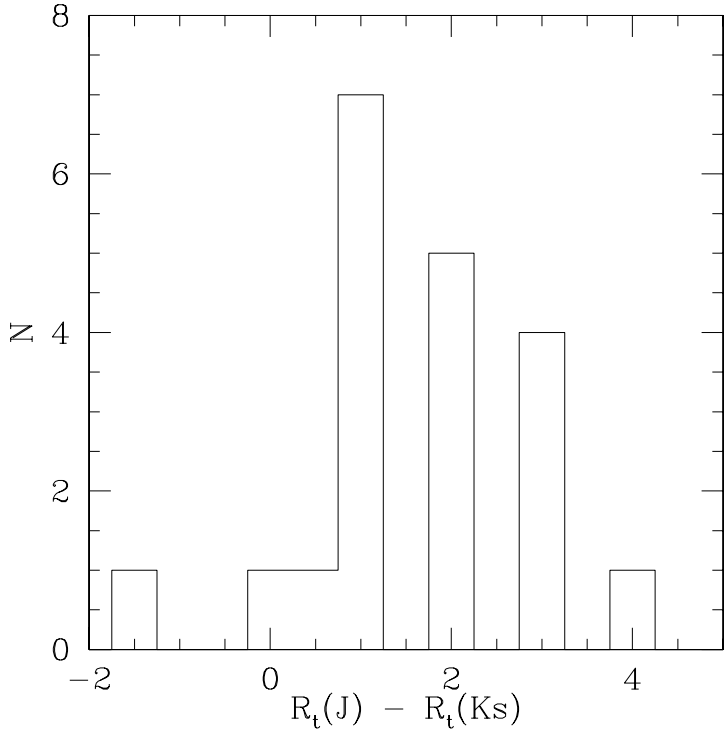

Figura 3.6: Diferencia entre R_t para el filtro J y R_t para el filtro K_S.

con a cercano a la unidad. Los perfiles que hemos obtenido se ajustan a una curva de truncamiento suave de Tipo a. Las curvas de truncamiento que obtenemos de la misma galaxia vista de perfil y desproyectada, de cara, son diferentes, pero el radio de truncamiento es el mismo.

5) En el caso del estudio individual de la galaxia NGC 6504 podemos concluir que ninguno de los perfiles obtenidos en las cuatro bandas observadas V, J, H y K_S, se ajusta a un perfil de doble exponencial, todos muestran truncamiento real. En particular en el perfil radial en la banda V este se muestra a partir de 28.5 $mag/arcsec^2$ que, extrapolando, ocurre a un $R_t(V) = 85$ *arcsec*. En las bandas del infrarrojo cercano los perfiles radiales muestran tambien truncamiento, que ocurre a $R_t(K_S) = 74$ *arcsec*, es decir una diferencia de 3.3 kpc.

6) Aunque nuestra estadística es pobre, podemos sugerir que el truncamiento afecta principalmente a galaxias espirales de tipo tardío (Schwarzkopf y Dettmar (2000) también econtraron esta tendencia) y que, como ya encontró Pohlen et al. (2004), el radio de truncamiento aumenta con la velocidad de rotación máxima de la forma: $R_t \propto V_m^c$, con c del orden de 1.5. Teniendo en cuenta la relación de Tully-Fisher, esto nos lleva a que R_t es mayor para galaxias más brillantes, que es el resultado que obtenemos cuando relacionamos el radio de truncamiento con la magnitud absoluta en la banda B.

7) Hemos encontrado una clara correlación entre R_t y h_R: las galaxias más extendidas tienen radios de truncamiento mayores y R_t/h_R es proporcional al brillo superficial central. Ambas relaciones fueron encontradas también por Kregel (2003).

3.5. Conclusiones

Es un hecho que en todas las galaxias el disco estelar es menos extenso que el disco gaseoso. Queda demostrado que esta característica no podemos atribuirla a los límites de sensibilidad de los telescopios ópticos actuales ni a un efecto de la proyección en galaxias de perfil. Hay un mecanismo

físico que produce que el disco estelar se termine, y de nuestras observaciones se deduce que para 2/3 de las galaxias el truncamiento es real, ya sea de forma suave o brusca. Para investigar el truncamiento de los discos estelares es obvio que las observaciones en el rango del infrarrojo cercano son las mejores. A estas longitudes de onda las estrellas más viejas se pueden trazar mejor ya que la gran parte de su flujo se emite en infrarrojo cercano, a la vez que se minimizan los efectos de la extinción interna mostrando mejor la distribución estelar real. La formación estelar reciente más allá del truncamiento tiene influencia en las observaciones en el visible, pero muy poca en el rango del infrarrojo.

El hecho de que los perfiles radiales observados en el rango del visible se ajusten mejor por un perfil con dos exponenciales, es compatible con que en infrarrojo exista un truncamiento gradual. Las estrellas recién formadas podrían escaparse. Si la velocidad de escape es aproximadamente igual a la velocidad de rotación, del orden de 100 km s^{-1}, y si el espacio que recorren es del orden de 10 kpc, el tiempo de escape podría ser del orden de 10^8 años, un tiempo que diferenciaría claramente las estrellas viejas de las recién formadas.

Con el método de inversión utilizado para desproyectar los perfiles podemos utilizar galaxias vistas de perfil y así alcanzar radios galactocéntricos que de otra forma serían inobservables. Es un proceso crítico para confirmar que el truncamiento del disco estelar en las galaxias no es debido a la proyección del disco al verlo de perfil.

El principal problema para comparar los resultados de esta tesis con los diferentes estudios que se han hecho sobre este tema, es que se han realizado a diferentes longitudes de onda, en galaxias de perfil y de cara y usando métodos de desproyección diferentes, por lo que la comparación es muy dependiente del método y la reducción. Así que, para hacer una comparación homogénea y completa, hemos escogido una galaxia disco vista de perfil, NGC 6504, que hemos observado en infrarrojo cercano y en el visible alcanzando las partes más externas y débiles del disco. Hemos desproyectado con el mismo método y hemos confirmado que hay truncamiento en todos los filtros con diferencias en el radio de truncamiento, siendo menor para las longitudes de onda mayores.

Son necesarias más observaciones, pero con los resultados obtenidos (y mostrados en la Sección anterior) se pueden poner restricciones a los modelos teóricos propuestos. Estas teorías tienen que explicar los resultados que hemos encontrado con los datos en infrarrojo cercano:

1. El truncamiento afecta principalmente a galaxias espirales de tipo tardío.

2. El radio de truncamiento es menor para las longitudes de onda mayores, aumenta con la velocidad de rotación máxima y es mayor para galaxias más brillantes.

3. Las galaxias más extendidas tienen radios de truncamiento mayores.

4. R_t/h_R es proporcional al brillo superficial central.

El módelo magnético de Battaner, Florido y Jiménez-Vicente (2002) es una teoría que además de explicar la velocidad de rotación de las galaxias, explica el truncamiento y el antitruncamiento. En el capítulo 5 explicaremos la relación entre el campo magnético y el truncamiento.

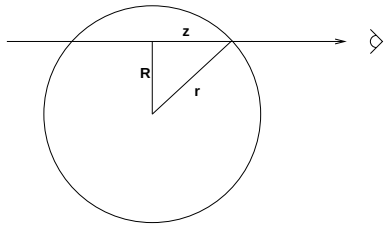

Figura 3.7: Proyección de la densidad de luminosidad a lo largo de la línea de visión

3.6. Apéndice A: Método analítico de inversión

Binney y Tremaine (1987) describen un método analítico de inversión. La densidad de luminosidad $j(\vec{r})$ y el brillo superficial $I(\vec{R})$ están relacionados por la fórmula (ver Figura 3.7):

$$I(R) = \int_{-\infty}^{\infty} j(r)dz = 2\int_{R}^{\infty} \frac{j(r)rdr}{\sqrt{r^2 - R^2}} \tag{3.11}$$

$$\begin{array}{c} r^2 = R^2 + z^2 \\ \frac{dz}{dr} = \frac{r}{\sqrt{r^2 - R^2}} \end{array} \tag{3.12}$$

Esto es una ecuación integral de Abel que pasamos a resolver con el siguiente cambio de variable:
$R^2 = x \Rightarrow dx = 2RdR$
$I(R) \Rightarrow f(x)$
$r^2 = t \Rightarrow dt = 2rdr$
$j(r) \Rightarrow g(t)$

Así tenemos:

$$f(x) = \int_{x}^{\infty} \frac{g(t)dt}{\sqrt{t - x}} \tag{3.13}$$

que es una ecuación integral lineal que resolvemos multiplicando ambos lados por $\frac{dx}{(u-x)^{1-(1/2)}}$ e integramos con respecto a x desde 0 a u:

$$\int_0^u \frac{f(x)dx}{(u-x)^{1-(1/2)}} = \int_0^u \frac{dx}{(u-x)^{1-(1/2)}} \int_x^{\infty} \frac{g(t)dt}{(t-x)^{(1/2)}} \tag{3.14}$$

$$\int_0^u \frac{f(x)dx}{(u-x)^{1-(1/2)}} = \int_0^u g(t)dt \int_t^u \frac{dx}{(u-x)^{1-(1/2)}(x-t)^{(1/2)}} \tag{3.15}$$

con el cambio de variable $y = \frac{u-x}{u-t}$ y teniendo en cuenta que

$$\int_0^1 \frac{du}{u^{\alpha}(1-u)^{1-\alpha}} = \frac{\pi}{sen\alpha\pi} \qquad \text{para} \qquad 0 < \alpha < 1 \tag{3.16}$$

obtenemos

$$\int_0^u \frac{f(x)dx}{(u-x)^{1-(1/2)}} = \int_0^u g(t)dt \int_0^1 \frac{dy}{y^{1-(1/2)}(1-y)^{(1/2)}} = \int_0^u g(t)dt \frac{\pi}{sen(1/2)\pi} \tag{3.17}$$

diferenciamos respecto a u y cambiamos u a t:

$$g(t) = \frac{sen(1/2)\pi}{\pi} \frac{d}{dt} \left[\int_0^t \frac{f(x)dx}{(t-x)^{1-(1/2)}} \right] \tag{3.18}$$

como no podemos diferenciar bajo el signo de integración porque creamos una integral divergente, integramos por partes:

$$f(x) = u \rightarrow \frac{df}{dx}dx = du; \quad \frac{dx}{(t-x)^{1-(1/2)}} = dv \rightarrow \frac{-(t-x)^{(1/2)}}{(1/2)} = v \tag{3.19}$$

y, ahora sí, diferenciamos bajo el signo de integral, obteniendo el resultado final:

$$g(t) = \frac{sen\alpha\pi}{\pi}\left[\int_0^t \frac{df}{dx}\frac{dx}{(t-x)^{1-\alpha}} + \frac{f(0)}{t^{1-\alpha}}\right] \tag{3.20}$$

$$j(r) = -\frac{1}{\pi}\int_r^\infty \frac{dI}{dR}\frac{dR}{\sqrt{R^2 - r^2}} \tag{3.21}$$

Esta solución tan sólo es útil si I(R) es una función suave no muy contaminada por el ruido. Tomando j(r) de forma analíticamente simple, el perfil de brillo superficial viene dado por:

$$I(R) = \frac{I_0}{1 + (R/r_0)^2} \Leftrightarrow j(r) = \frac{j_0}{[1 + (r/r_0)^2]^{3/2}} \tag{3.22}$$

donde $I_0 = 2r_0 j_0$.

Este perfil de brillo superficial es conocido como Ley de Hubble Modificada. En ella vemos que $I \propto R^{-2}$ para $R \gg r_0$, mientras que $j \propto r^{-3}$ para $r \gg r_0$.

3.7. Artículos

3.7.1. Near infrared observations of the truncation of stellar disks

Florido, E., Battaner, E., Guijarro, A., Garzón, F., Jiménez-Vicente, J. 2001, A&A, 378, 82

3.7.2. Truncated stellar disks in the near infrared. I. Observations

Florido, E., Battaner, E., Guijarro, A., Garzón, F., Castillo-Morales, A. 2006a, A&A, 455, 467

3.7.3. Truncated stellar disks in the near infrared. II. Statistical properties and interpretation

Florido, E., Battaner, E., Guijarro, A., Garzón, F., Castillo-Morales, A. 2006b, A&A, 455, 475

3.7.4. The truncation of the stellar disc of NGC 6504

Florido, E., Battaner, E., Zurita, A., Guijarro, A. 2007, A&A, 472, L39

Capítulo 4

Alabeos

En este capítulo presentamos el trabajo realizado sobre el alabeo en galaxias espirales, que ha sido publicado en 2 artículos en la revista *Astronomy & Astrophysics*.

4.1. Introducción

Los estudios realizados sobre el alabeo, ya sea en la componente extendida del gas neutro (HI) (Sancisi 1976, Bosma 1981, Briggs 1990, García-Ruiz, Sancisi y Kuijken 2002b), como en el disco estelar observado en el visible (Sánchez-Saavedra, Battaner y Florido 1990, Florido et al. 1991, Reshetnikov y Combes 1998, Ann y Park 2006) indican que la mayoría de las galaxias espirales, incluida la nuestra, tienen el disco alabeado. Burke (1957) y Kerr (1957) detectaron por primera vez que el disco de una galaxia estaba alabeado a partir de observaciones en la línea de 21 cm en nuestra propia Galaxia.

Normalmente el alabeo del disco gaseoso empieza a radios galactocéntricos donde el disco en el visible es ya muy débil. Para detectar más claramente los alabeos se escogen galaxias de perfil, aunque hay observaciones del alabeo en galaxias con inclinación intermedia, en las cuales se detecta a partir de la información cinemática del disco (observando el campo de velocidades en el plano galáctico), como es el caso de M83 (Rogstad, Lockhart y Wright 1974), NGC 5033, NGC 5055, NGC 2841 y NGC 7331 (Bosma 1978), M31 (Brinks y Burton 1984), y M33 (Corbelli, Schneider y Salpeter 1989). García-Ruiz, Sancisi y Kuijken (2002b), analizando sus observaciones en HI, encontraron que todas las galaxias vistas de perfil que tenían un disco extenso en HI con respecto a la componente en el visible estaban alabeadas. Briggs (1990) concluye, a partir de una pequeña muestra de galaxias alabeadas, que el alabeo de la capa de gas se desarrolla entre el radio al cual el brillo superficial en la banda B es $\mu_{\rm B} = 25\ mag/arcsec^2$ y el radio de Holmberg, $R_{\rm Ho}$, en el cual $\mu_{\rm B} = 26.5\ mag/arcsec^2$.

Reshetnikov et al. (2002) observaron que los alabeos en los discos estelares eran también muy frecuentes en el pasado (con una frecuencia de galaxias alabeadas de 2/3), presentando incluso mayor magnitud de alabeo en galaxias a $z \approx 1$.

Ann y Park (2006) encontraron que el 73 % de un total de 325 galaxias que pertenecían a una muestra bien definida de galaxias de perfil ($a/b > 9.5$, donde a/b es la relación entre los ejes mayor y menor a $\mu_{\rm B} = 25\ mag/arcsec^2$) mostraban alabeos en el visible. Reylé et al. (2009) han encontrado que en nuestra Galaxia existe alabeo en el disco estelar, en el de gas y en la componente de polvo, y que todos son asimétricos y caracterizados por una línea de nodos similar. Pero el alabeo del gas, en HI, es más fuerte que el alabeo de la banda de polvo, y el alabeo estelar es significativamente menor (un factor ≈ 2). Estos autores concluyen con esta comparación que los distintos componentes (gas, polvo y estrellas) de las galaxias reaccionan de manera diferente a las fuerzas que originan el alabeo.

Aún no se conoce el origen del alabeo, ni tampoco por qué se mantiene con el tiempo. Que sea un fenónmeno tan común nos indica que debe persistir largo tiempo (Sparke y Casertano 1988); algo debe mantener el alabeo para que una vez creado el campo gravitatorio o la rotación diferencial

del disco no lo destruyan. Los numerosos mecanismos que han sido propuestos y explorados no han dado todavía una respuesta definitiva y satisfactoria (ver, por ejemplo, los trabajos de recopilación de Binney 1992, Battaner et al. 1997 y van der Kruit 2007). Las teorías más importantes que se han propuesto para explicar este fenómeno son:

- Kerr (1957), Weinberg (1998), Weinberg y Blitz (2006), y otros autores han sugerido que los alabeos pueden ser el resultado de las interacciones de marea de la galaxia con una galaxia satélite o vecina. Pero esta hipótesis no explicaría los alabeos de las galaxias aisladas (Sancisi 1976, Tubbs y Sanders 1979, Sparke 1984) ni el de nuestra Galaxia. García-Ruiz, Kuijken y Dubinski (2002a) demostraron que el alabeo de la Vía Láctea no se podía producir por la interacción con las Nubes de Magallanes.

- Es muy interesante considerar la posibilidad de que sea el medio intergaláctico el que juegue el papel importante en la formación del alabeo, pues el movimiento de las galaxias dentro del gas intergaláctico podría generar distintas presiones y deformar los bordes de los discos (Kahn y Woltjer 1959, López-Corredoira, Betancort-Rijo y Beckman 2002, Sánchez-Salcedo 2006).

- Hunter y Toomre (1969) y Dekel y Shlosman (1983) propusieron que el alabeo de nuestra Galaxia era el resultado de oscilaciones en el disco, ya sean provocadas por la interacción con otra galaxia en el pasado o debidas a que el disco se encuentra alojado en un halo no esférico (achatado) de materia oscura. Sparke y Casertano (1988) mostraron cómo algunos modos de oscilación discreta podían incluso sobrevivir en el tiempo. Sin embargo, esta teoría no está exenta de problemas. Por ejemplo, Binney (1991) mostró que de esa forma el halo debería responder al desalineamiento con el disco alineándose de nuevo, destruyendo así el alabeo en unos pocos periodos orbitales.

- El modelo de Ostriker y Binney (1989) se basa en la idea de que las galaxias están tomando (acrecentando) material del medio intergaláctico y dicho material hace cambiar el momento angular del halo en su parte externa. Esa parte ejercería un momento de fuerzas sobre su parte interna y sobre el disco, de tal forma que la parte interna del disco (donde la densidad superficial es alta) seguiría plana debido a la autogravitación pero la externa se deformaría formando el alabeo. Este modelo explicaría el hecho observado de que el núcleo del disco de la Vía Láctea esté inclinado con una coincidencia con la línea de nodos del alabeo externo del disco.

- Otro modelo es el del acoplamiento no lineal entre una onda espiral y dos ondas de alabeo, introducido por Masset y Tagger (1997), de tal forma que la onda espiral (linealmente inestable y alimentada de energía y momento angular por la parte central del disco) alimente contínuamente a las de alabeo. La eficiencia de este mecanismo es demasiado débil en todo el disco estelar, excepto en el borde, cerca de la resonancia externa de Lindblad, donde la energía de la onda espiral se convertiría casi completamente en dos ondas de alabeo: una transmitida (hacia afuera), que sería el alabeo y otra reflejada (hacia adentro), que se observaría como una corrugación del disco.

- Battaner, Florido y Sánchez-Saavedra (1990) explican los alabeos como resultado del campo magnético intergaláctico, el cual actuaría distorsionando directamente la distribución del gas. El sistema estelar se alabearía indirectamente ya que las estrellas se forman en el gas que estaría alabeado. Según esta teoría, se debería observar alguna diferencia entre el alabeo de las estrellas recién formadas y el de las estrellas viejas. Así, si obtenemos una diferencia en el alabeo a diferentes longitudes de onda nos daría una clave importante. Incluso, según este modelo, las galaxias pobres en gas como las S0 no deberían mostrar alabeos.

El alabeo puede ser la respuesta natural del disco externo a una serie de estímulos, y podría ser que el mecanismo responsable no fuera necesariamente el mismo para cada galaxia. En cualquier caso, la observación de galaxias de perfil puede contribuir a determinar definitivamente cuál es el escenario dominante.

4.2. Catálogo de alabeos

En Sánchez-Saavedra, Battaner y Florido (1990) se realizó un cartografiado del cielo del Hemisferio Norte a partir de las placas del *Palomar Observatory Sky Survey* en el que se demostró por primera vez que la frecuencia del alabeo del disco estelar es alta (en torno al 60 % de las observadas). Como parte de esta Tesis, hemos repetido el cartografiado pero con galaxias del Hemisferio Sur.

A partir de la base de datos LEDA (*Lyon–Meudon Extragalactic Database*, www-obs.univ-lyon1.fr) seleccionamos 276 galaxias que cumplen con los siguientes requisitos:

- $log(\mathrm{r25}) > 0.60$, donde $log(\mathrm{r25})$ es el logaritmo decimal de la razón eje mayor/menor de las galaxias medidos en la isofota de 25 $mag/arcsec^2$ de la banda B,
- $B_t < 14.5$, donde B_t es la magnitud total aparente,
- declinación $< 0°$,
- tipo morfológico entre -2.5 y 7 (para tener galaxias lenticulares y espirales).

Estas galaxias fueron analizadas con las placas del DSS (*Digitized Sky Survey*) y de manera visual se detectaron 150 galaxias alabeadas. Consideramos alabeados los discos con un ángulo de alabeo *wa*, medido desde el centro de la galaxia hasta el último punto observado con respecto al plano galáctico, mayor de 4°.

Como resultado de este análisis podemos concluir que, si se tiene en cuenta que los alabeos sólo se pueden detectar si su orientación (proyección) es favorable y no está en la línea de visión, la mayoría (si no todas) las galaxias espirales están alabeadas. Hay que resaltar además un resultado muy importante, y es que en el estudio se han incluido 38 galaxias S0 con el resultado de que en ninguna de ellas se encontró alabeo. Para galaxias espirales, en cambio, la frecuencia y el grado de alabeo parece ser independiente del tipo morfológico. La principal diferencia entre las galaxias espirales y las S0 es la carencia de gas en estas últimas, así que parece que es el gas un ingrediente importante para la formación de alabeos.

4.3. Observaciones

A continuación (Guijarro et al. 2010) vamos a describir la nueva aportación que hacemos en este campo: el estudio de los alabeos galácticos con datos muy profundos en cuatro filtros, tres en la banda visible y uno en el infrarrojo cercano. Hasta el año 2009 tan solo se habían usado datos en el infrarrojo para estudiar el alabeo en nuestra Galaxia (Djorgovski y Sosin 1989, Reylé et al. 2009). Saha, de Jong y Holwerda (2009) publicaron por primera vez observaciones en el infrarrojo (a $\lambda = 4.5$ μm) con el satélite *Spitzer/IRAC* de 24 galaxias espirales de perfil para analizar el alabeo del disco estelar. En esta tesis es la primera vez que se han usado los datos en el infrarrojo cercano (a $\lambda = 2.15$ μm) para estudiar alabeos. Estas observaciones son esenciales para trazar la distribución de masa de las estrellas, pues a las longitudes de onda del infrarrojo ($1 < \lambda < 5\mu$m) la extinción por polvo se minimiza. Además la emisión en el infrarrojo cercano traza mejor la población estelar vieja de las galaxias, uno de nuestros objetivos. Por lo tanto, estas longitudes de onda suministran una información esencial y complementaria a los datos en el visible para el estudio de los alabeos estelares.

4.3.1. Análisis de los datos

Para extraer los parámetros de las galaxias de un modo consistente, primero modificamos las imágenes reducidas de cada una de ellas en los cuatro filtros, B, V, I y K_S, para que tengan la misma escala y estén alineadas, utilizando para esto último las estrellas del fondo y el centro de las galaxias. Hay que tener en cuenta que cada banda observada nos muestra distinta morfología de la galaxia debido a que la extinción del polvo y el tipo de población estelar es diferente para cada filtro. Uno de los problemas que se tuvo que tratar con especial cuidado fue la sustracción de las estrellas de fondo para evitar que su luminosidad contaminara la de las galaxias. Para ello se construyó una máscara en cada uno de los filtros y con la suma de todas se hizo una máscara

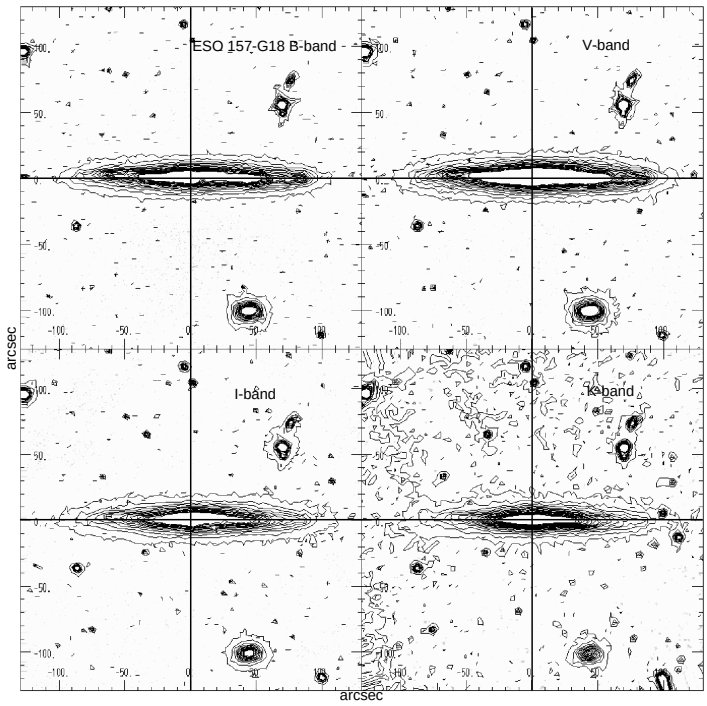

Figura 4.1: Mapa de isofotas de la galaxia ESO157-G18 en los cuatro filtros analizados. El contorno más débil se corresponde con un nivel de cuentas de 3σ sobre el fondo del cielo y el más brillante, con 75σ. Son en total 15 contornos, en escala lineal y suavizados en 4 píxeles.

general que se pasó a todas las imágenes. Las imagenes han sido previamente rotadas (plano de la galaxia en el eje X) por un método iterativo, que toma como base el ángulo de posición PA del catálogo ESO-LV, y ajusta una línea recta a la parte central de la galaxia. Con este método el ángulo de posición se determina con un error de 0.1 grados. Como ejemplo de los resultados obtenidos, en la Figura 4.1 se muestra las líneas de igual brillo superficial, o isofotas, de la galaxia ESO157-G18.

Para caracterizar el alabeo definimos la curva de alabeo, que es la curva que indica la posición de máxima intensidad a lo largo del eje perpendicular (z) al plano del disco como función del radio galactocéntrico (R) cuando la galaxia es proyectada en el plano del cielo. El alabeo se muestra como una desviación de la curva de alabeo respecto del plano de simetría. Para determinar esta curva, tanto en visible como en infrarrojo, hemos desarrollado varios métodos:

- Calculando el máximo para cada corte en la dirección perpendicular del plano de la galaxia. Es un método que utilizamos al principio del estudio como una primera aproximación y del que luego prescindimos pues es demasiado sensible, ruidoso y muy confuso a la hora de discriminar pequeñas estrellas que pueden aparecer en el fondo.

- Con el primer momento. Método que calcula la posición media pesada con la intensidad para cada corte en la dirección perpendicular del plano de la galaxia de perfil: $\overline{j} \equiv ypos(i) = \sum_j j \cdot I(i,j) / \sum_j I(1,j)$. Este método fue el elegido pues era mejor y más fiable que el anterior. Con él analizamos todas las galaxias hasta que comprobamos que era muy dependiente de la posición de la banda de polvo (sobre todo en las longitudes de onda más azules), del tamaño del segmento a analizar en cada corte perpendicular, de la existencia de píxeles brillantes lejos del centro (por ejemplo debidos a las estrellas de nuestra Galaxia) y a las máscaras estrellas.

- Ajustando Gaussianas a los perfiles verticales. Con este método, si los puntos centrales del disco de la galaxia están distorsionados por la banda de polvo, el resultado está menos afectado gracias a la propia simetría del disco. Es el método que hemos usado para calcular la curva de alabeo con un resultado menos ruidoso y más fiable y completamente independiente del tamaño del segmento a analizar en cada corte perpendicular.

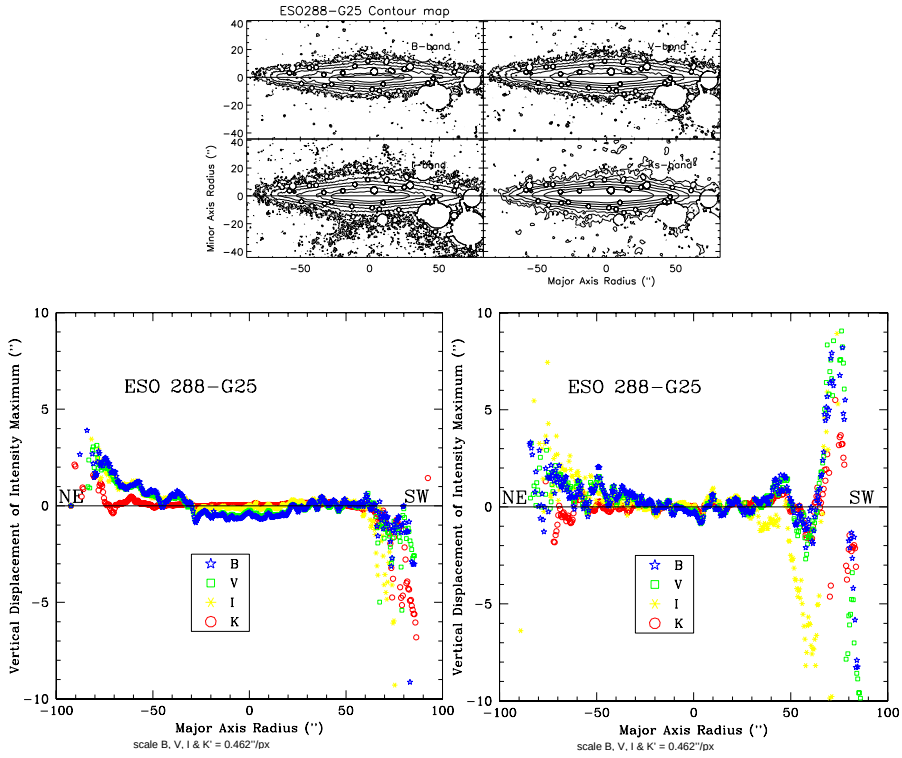

Figura 4.2: Arriba: Mapa de isofotas de la galaxia ESO288-G25 en los cuatro filtros analizados. El contorno más débil se corresponde con un nivel de cuentas de 3σ sobre el fondo del cielo aumentado en escala lineal con un paso de $+0.75$ $mag/arcsec^2$. Abajo-Izquierda: Curvas de alabeos para los cuatro filtros calculadas ajustando Gaussianas a los perfiles verticales. Abajo-Derecha: Curvas de alabeos para los cuatro filtros calculadas con el primer momento.

Mostramos una comparación de estos dos últimos métodos para la galaxia ESO 288-G25 en la Figura 4.2, donde claramente se muestran como las curvas de alabeo calculadas para los cuatro filtros ajustando Gaussianas (gráfica de la izquierda) son menos ruidosas que las ajustadas calculando el primer momento (gráfica de la derecha) y muestran mayor influencia de las estrellas del campo.

4.3.2. Curva de Alabeo extraída del ajuste de Gaussianas

Para ello se utilizó una modificación del programa *gaussfit.pro* dentro del paquete de programación *IDL*, que tiene como entrada la imagen de cada una de las galaxias en los 4 filtros. Sólo se tomaron para el cálculo los datos cuya intensidad era mayor de 3σ, donde:

$$\sigma = \sqrt{\sigma_{sys}^2 + \sigma_{std}^2} \tag{4.1}$$

donde σ_{sys} es el ruido o error sistemático (variación o gradiente en el nivel de cuentas en la imagen) y σ_{std} es el error estadístico o desviación estándar (ruido en cada píxel).

La curva de alabeo se obtiene uniendo los puntos que tienen una barra de error menor de 0.5 *arcsec*.

Para cuantificar y realizar estudios estadísticos es conveniente definir algunos parámetros de alabeo. Para galaxias de perfil, el sistema de coordenadas más adecuado es el que corresponde a

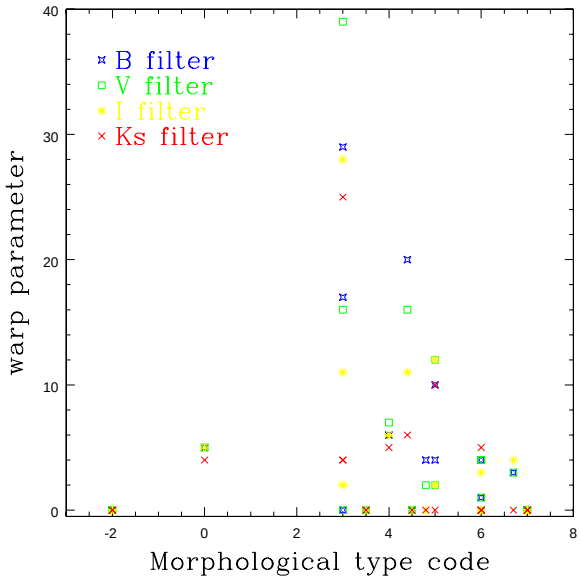

Figura 4.3: Valor absoluto del parámetro de alabeo ω que indica el grado o fuerza del alabeo frente al tipo morfológico.

las dos direcciones contenidas en el plano del cielo: x es la coordenada en la dirección del eje mayor de la galaxia e y la coordenada en la dirección del eje de rotación, con el origen de ambas en el centro de la galaxia. De Jiménez-Vicente et al. (1997) tomamos el parámetro de alabeo ω:

$$\omega = \frac{1}{L^3} \int_{-L/2}^{+L/2} xy \mathrm{d}x, \tag{4.2}$$

donde L es el tamaño de la galaxia que medimos a 3σ sobre el fondo del cielo. El valor absoluto de este parámetro mide la intensidad del alabeo.

Para las galaxias que muestran un disco apreciablemente alabeado hemos ajustado una curva teórica de alabeo para parametrizar los resultados y describir geométricamente este fenómeno. Hemos ajustado una simplificación de la curva de alabeo teórica de Jiménez-Vicente et al. (1997):

$$y = \begin{cases} 0 & |x| < |A| \\ C(x - A) & |x| \geq |A| \end{cases} \tag{4.3}$$

Esta función reproduce razonablemente la forma del alabeo: es plana hasta cierto punto A, donde empieza a desviarse del plano de simetría hasta alcanzar una dirección asintótica, con una pendiente C.

4.4. Resultados

1) En la primera parte de este capítulo, con el catálogo de galaxias del Hemisferio Sur, obtenemos que 150 de 250 galaxias espirales están alabeadas. En la segunda parte con una muestra mucho menor, que 13 de 20 están alabeadas. Por lo que concluimos que la frecuencia de alabeos es muy alta, el 60 %, dato comparable al encontrado por otros autores y que indica la universalidad de este fenómeno. Teniendo en cuenta que algunas orientaciones del alabeo impiden su detección observacional, podemos afirmar que la mayoría de las galaxias espirales, si no todas, están alabeadas. El alabeo en el visible es menos perceptible que en el gas, pero la frecuencia es la misma.

2) El alabeo no depende del tipo morfológico, está presente en todos los tipos de galaxias espirales. La única excepción es para las galaxias S0 donde el alabeo es nulo.

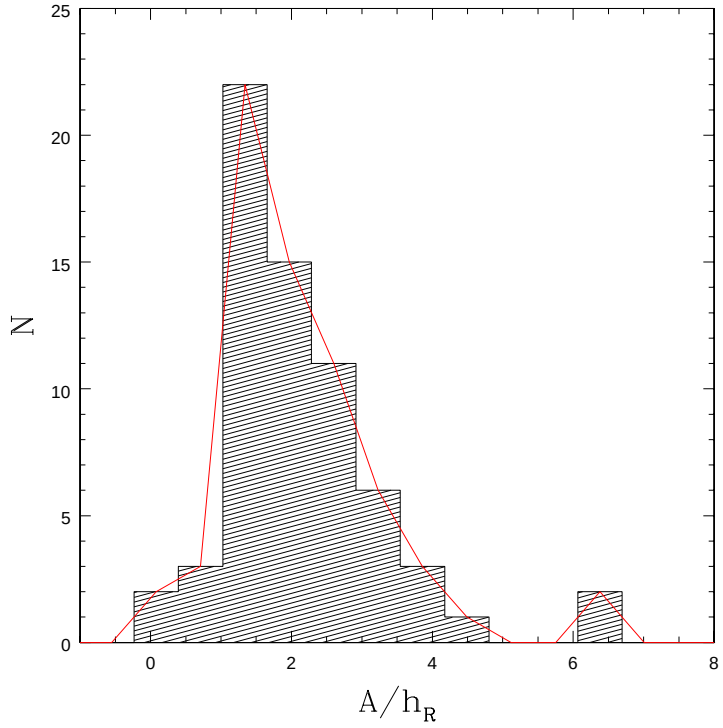

Figura 4.4: Histograma A/h_R para todos los filtros y galaxias alabeadas, donde A es el radio al que comienza el alabeo y h_R la escala de longitud radial

3) El grado de alabeo, medido con el valor absoluto del parámetro ω, también es independiente del tipo morfológico (Figura 4.3).

4) Encontramos un valor medio del radio al que comienza el alabeo para todos los filtros (ver Figura 4.4) de $A \sim 2.16$ h_R. Es un valor más bajo que el estimado por Sparke y Casertano (1988) con datos en el visible de $A \sim 5h_R$- $3h_R$. Hemos tomado h_R (escala de longitud radial) de de Grijs (1997). Aunque la determinación del radio al que empieza exactamente el alabeo tiene una incertidumbre intrínseca por definición, sí que podemos concluir según nuestros resultados, que el alabeo comienza a radios menores que el truncamiento, sin existir un sesgo natural que provoque esta situación: en la Figura 4.5 podemos ver que el radio de alabeo es menor al de truncamiento de modo que no tenemos valores mayores no porque no podamos verlos al truncarse el disco, sino que realmente no existen.

5) Podemos comparar los resultados obtenidos con los diferentes filtros utilizados, obteniendo que de las 13 galaxias alabeadas, 5 muestran la misma curva de alabeo en los 4 filtros, 1 está alabeada en los 4 filtros pero el grado de alabeo es menor en la banda infrarroja (ω(B) = -20±6, ω(V) = -16±4, ω(I) = -11±4, $\omega(K_S)$ = -6±2), otra está alabeada en V, I y K_S y las 6 restantes presentan alabeos en los 3 filtros del visible pero no en el del infrarrojo cercano.

6) El radio al cual empieza el alabeo, A, es aproximadamente igual a 0.8 R_t (ver Figura 4.6). R_t es el radio de truncamiento que Kregel, van der Kruit y de Grijs (2002) obtuvieron en el estudio que hicieron sobre truncamientos con la misma muestra de galaxias que nosotros. Van der Kruit (2007) encontró que el alabeo para HI empieza a aproximadamente 1.2 R_t. Esta diferencia, de ser confirmada (hay que tener en cuenta la baja resolución de los datos en HI), pudiera indicar que el alabeo estelar empieza siempre antes que el del disco gaseoso.

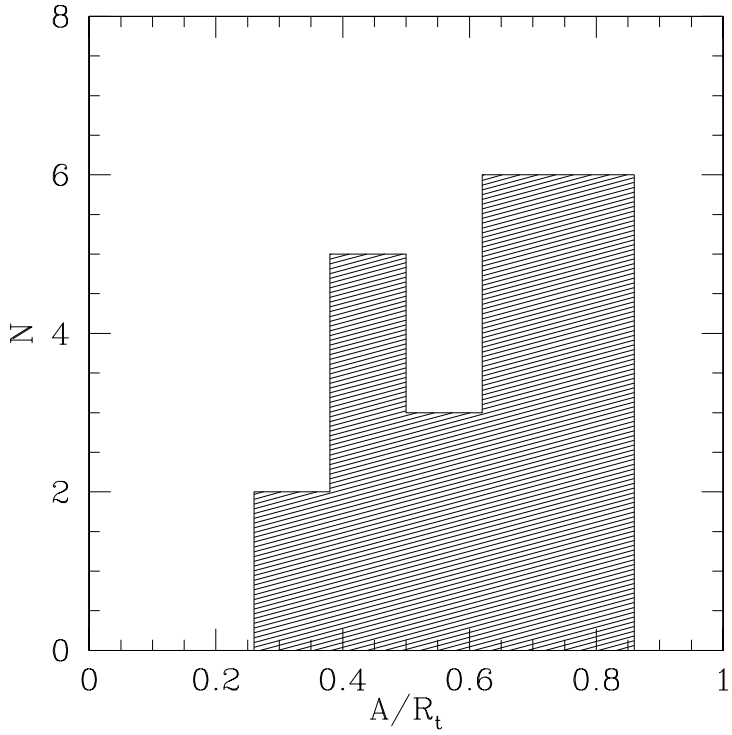

Figura 4.5: Histograma A/R_t para todas las galaxias alabeadas en el filtro I, donde A es el radio al que comienza el alabeo y R_t es el radio de truncamiento que Kregel, van der Kruit y de Grijs (2002) obtuvieron en el estudio que hicieron sobre truncamientos con la misma muestra de galaxias que nosotros.

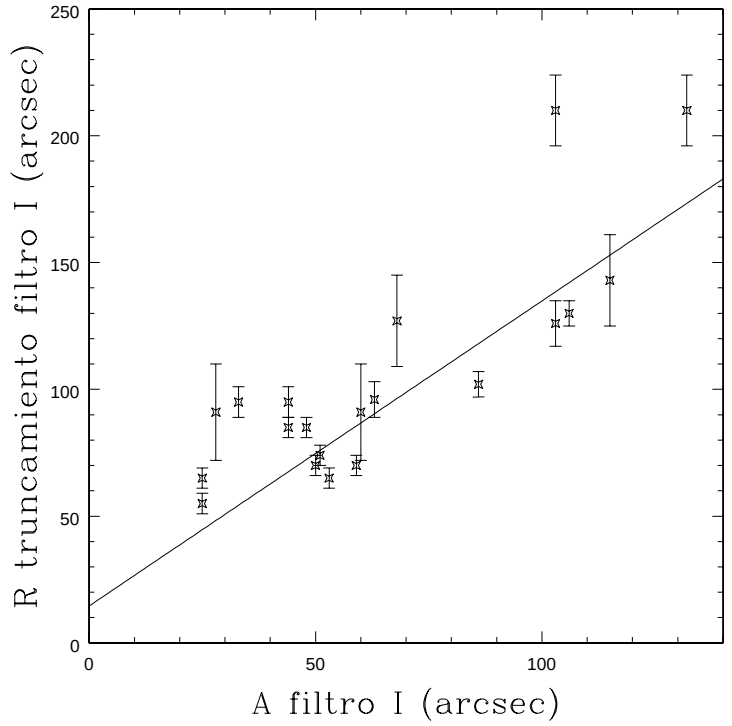

Figura 4.6: Radio de truncamiento, R_t, obtenido de Kregel, van Der Kruit y de Grijs (2002), comparado con el radio de alabeo, A, para el filtro I y galaxias alabeadas.

4.5. Conclusiones

Además de confirmar que el alabeo de los discos estelares es un fenómeno universal que no solo afecta al gas, hemos llegado a estas dos importante conclusiones que condicionan las hipótesis propuestas para explicarlo:

-Las galaxias S0 no presentan alabeos en sus discos.

-El disco de población estelar más vieja parece estar menos alabeado que el disco de gas y el de las estrellas recientemente formadas.

Es de destacar que tanto la curva y el grado de alabeo como el radio al cual empieza, son parámetros que no dependen del tipo de galaxia de disco; no hemos encontrado ninguna relación entre el grado de alabeo y el tipo morfológico. Por este motivo es aún más llamativo que tan sólo las galaxias disco S0 no muestren signos de alabeo.

La diferencia en el alabeo a diferentes longitudes de onda que hemos encontrado en algunas galaxias, confirma lo encontrado en nuestra propia Galaxia por Reylé et al. (2009), y que se podría interpretar como que las distintas componentes del disco (gas, polvo y estrellas) reaccionan de manera diferente a las fuerzas que originan el alabeo. No podemos olvidar, no obstante, que las diferentes morfologías que presentan los alabeos se pueden deber a la acción de varios mecanismos y no de un único responsable.

Las teorías que se proponen para explicar la formación y el mantenimiento del alabeo deben tener esto en cuenta y explicar por qué las galaxias con disco que carecen de gas no presentan alabeo. Los modelos que están basados en la gravedad no distinguen entre el tipo de material afectado, así que tendrían serios problemas para explicar este comportamiento. Si le sumamos la posible diferenciación en la forma y la magnitud de los alabeos a diferentes longitudes de onda, queda claro que debe existir un mecanismo que actúe sobre el gas y no sobre las estrellas para formar los alabeos. Hemos encontrado además alabeo en el infrarrojo cercano, con una frecuencia parecida al visible, lo que sugiere que el alabeo es una estructura que una vez formada, perdura en el tiempo a pesar de que la propia rotación de las galaxias podría disiparlo en una escala de tiempo de unos 2 Giga-años (Binney 1992). El mecanismo responsable de formarlos debería actuar permanentemente para mantenerlos.

El catálogo de galaxias del Hemisferio Sur es especialmente idóneo para realizar estudios estadísticos por el número de galaxias analizadas y los criterios de selección elegidos. De hecho ya ha sido utilizado para otros estudios: Saha y Jog (2006), Christlein y Zaritsky (2008), López-Corredoira et al. (2008), Revaz et al. (2009) y otros autores. También es muy útil como base de futuros trabajos sobre el alabeo para elegir galaxias interesantes de ser observadas con más detalle.

El cambio brusco que hay entre la zona del disco interna no alabeada y la externa alabeada ha sugerido a van der Kruit (2007) que esas dos regiones difieren en su formación y evolución.

4.6. Artículos

4.6.1. A catalog of warps in spiral and lenticular galaxies in the Southern hemisphere

Sánchez-Saavedra, M.L., Battaner, E., Guijarro, A., López-Corredoira, M., Castro-Rodríguez, N. 2003, A&A, 399, 457

4.6.2. Near-infrared and optical observations of galactic warps: a common, unexplained feature of most discs

Guijarro, A., Peletier, R.F., Battaner, E., Jiménez-Vicente, J., de Grijs, R., Florido, E. 2010, A&A, 519, 53

Capítulo 5

El Modelo Magnético en Truncamientos y Alabeos

En este último capítulo presentamos el campo magnético como el agente que induciría el truncamiento y el alabeo. Es la teoría desarrollada por nuestro grupo y la que indirectamente nos ha llevado al estudio observacional de estas estructuras en los bordes de los discos estelares aunque el análisis de las observaciones se ha hecho sin prejuicios teóricos. Es un trabajo presentado en 3 artículos internacionales.

5.1. Introducción

En el interior de las galaxias la gravedad es tan importante que la aportación de la fuerza magnética es insignificante, pero el campo magnético de las galaxias decrece lentamente con el radio de tal manera que no se puede ignorar, llegando a competir a grandes radios con la fuerza gravitatoria en las galaxias espirales y en las irregulares a todos los radios. Como ejemplo tenemos nuestra Galaxia (ver el primer artículo: Battaner, Florido y Guijarro 2001), donde el campo total es de 10 μG en el interior, 6 μG a 10 kpc y 4 μG a unos 17 kpc (Beck 2004). En algunas otras galaxias se ha medido una intensidad de campo magnético entre unos 10 μG y 50 μG (ver por ejemplo, Beck 2005). Así que si consideramos que en el medio intergaláctico tenemos campos del orden de unos pocos de μG (Kronberg 1994), es fácil considerar que en los bordes de las galaxias normales existan campos magnéticos conectados con el campo intergaláctico del orden de 1 a 5 μG. Con este valor, los campos magnéticos no deben ser ignorados pues tienen magnitudes que pueden competir con la fuerza gravitatoria debida sólo a la materia visible:

$$G\frac{M\rho}{R^2} \approx \frac{1}{8\pi}\frac{1}{R^2}\frac{d(R^2B_\varphi^2)}{dR} \tag{5.1}$$

donde M es la masa de la materia visible de la galaxia, ρ es la densidad y B_φ es la componente azimutal del campo magnético que podemos considerar independiente del radio galactocéntrico R. Si $\rho = \rho_0 e^{-R/R_0}$, tenemos que cuando R sea tal que

$$\frac{1}{4\pi}Re^{R/R_0} \approx \frac{GM\rho_0}{B_\varphi^2} \equiv 4\cdot 10^4\frac{M\rho_0}{B_\varphi^2} \tag{5.2}$$

la fuerza magnética es del orden de la gravitatoria. En la última igualdad M está en unidades de $10^{11}M_\odot$, ρ_0 en $10^{-23}gcm^{-3}$, B en μG y R en kpc, así si B_φ es en torno a 5, ρ_0 y M en torno a 1 y R_0 en torno a 3, tenemos que a un R de unos 14 kpc la influencia del campo magnético es comparable a la del campo gravitatorio.

El modelo magnético adoptado se basa en la teoría magnetohidrodinámica que Nelson (1988) y Battaner et al. (1992) desarrollaron para explicar la curva de rotación en galaxias sin la necesidad de incluir materia oscura. La fuerza magnética influye en el movimiento y distribución del gas

(hidrógeno atómico) interestelar que está lo suficientemente ionizado como para congelar las líneas de campo. Es una fuerza que hay que considerar en las regiones más externas, donde la gravedad ya no es tan importante y la curva de rotación se mantiene alta y plana. La estructura a gran escala del campo magnético puede ser circular (campo puro azimutal) o con líneas de campo abiertas al espacio. En cualquier caso la componente azimutal es grande y se puede considerar que $\mathbf{B} \equiv \vec{B} = (0, B_\varphi, 0)$. Usamos coordenas cilíndricas por la simetría propia de las galaxias.

5.2. El campo magnético y el truncamiento

Como hemos presentado en el capítulo 3, el truncamiento es una estructura que presentan la mayoría de los discos estelares de las galaxias, aunque aún no se ha llegado a conclusiones definitivas sobre la forma en la que la galaxia se termina o trunca. Tampoco se ha determinado qué teoría explica este fenómeno.

El modelo magnético, propuesto por Battaner, Florido y Jiménez-Vicente (2002) es una propuesta que además de explicar el truncamiento propiamente dicho, también explicaría la existencia de antitruncamientos.

En este modelo, la fuerza magnética que actúa sobre el gas ionizado y ayuda a contrarrestar, junto a la gravedad, el efecto de la fuerza centrífuga, desaparecería al formarse las estrellas. Estas estrellas recién formadas, al no estar afectadas por el magnetismo, se moverían a órbitas más externas produciendo el perfil antitruncado, o incluso podrían escapar de la galaxia en la dirección radial produciendo el perfil truncado. Para el caso de truncamientos Battaner, Florido y Jiménez-Vicente (2002) deducen que con un modelo simple magnético:

$$\mathrm{R_t} = \frac{2\mathrm{GM}}{\theta_0^2} \tag{5.3}$$

donde R_t es el radio de truncamiento, M es la masa visible de la galaxia y θ_0 es la velocidad de rotación asintótica, constante a radios grandes ($\theta_0 = \theta(\mathrm{R} \to \infty)$). Teniedo en cuenta la relación de Tully-Fisher $L \propto \theta_0^{3.5}$ y que $M \propto L$, donde L es la luminosidad de la galaxia, obtenemos de la ecuación anterior que:

$$R_t \propto \frac{2G\theta_0^{3.5}}{\theta_0^2} \propto 2G\theta_0^{1.5} \tag{5.4}$$

que es una de las relaciones que se obtuvieron a partir de las observaciones en el capítulo 3: $\mathrm{R}_t \propto \theta_0^n$ con n en torno a 1.5.

En ese capítulo se obtenía que las galaxias grandes, con h_R mayor, tenían un R_t mayor, y esto también se confirma en el modelo simple magnético: $\mathrm{R}_t \propto \mathrm{M}$. Además que el truncamiento aparezca principalmente en galaxias espirales de tipo tardío es compatible con que estas galaxias requieren campos magnéticos mayores y por tanto el truncamiento sea más frecuente. Para nuestra Vía Láctea donde la velocidad de rotación asintótica llega a unos 200 km/s, el radio de truncamiento estaría por tanto en torno a 17 kpc, que es compatible con el valor hallado por Porcel, Battaner y Jiménez-Vicente (1997) y Ruphy et al. (1996) de unos 15 kpc en la longitud de onda del infrarrojo. Hay que destacar que esta relación entre R_t y la velocidad asintótica de rotación, no ha sido explicada por ningún otro modelo.

Otro hecho observacional que explica este modelo es el aumento de R_t cuando disminuye la longitud de onda del filtro usado para la observación, que ha sido otra de las conclusiones obtenidas en el capítulo 3.

La posibilidad de que en el visible los perfiles radiales estén mejor descritos por una doble exponencial podría ser compatible con que en el infrarrojo exista un truncamiento completo y suave como hemos encontrado. Y es que las estrellas recién formadas, en el escenario magnético podrían estar escapandose. Si la velocidad de escape es aproximadamente igual a la velocidad de rotación, del orden de 100 km s^{-1}, y si el espacio que recorren es del orden de 10 kpc, el tiempo de escape podría ser del orden de 10^8 años, un tiempo que diferenciaría claramente las estrellas viejas de las recién formadas.

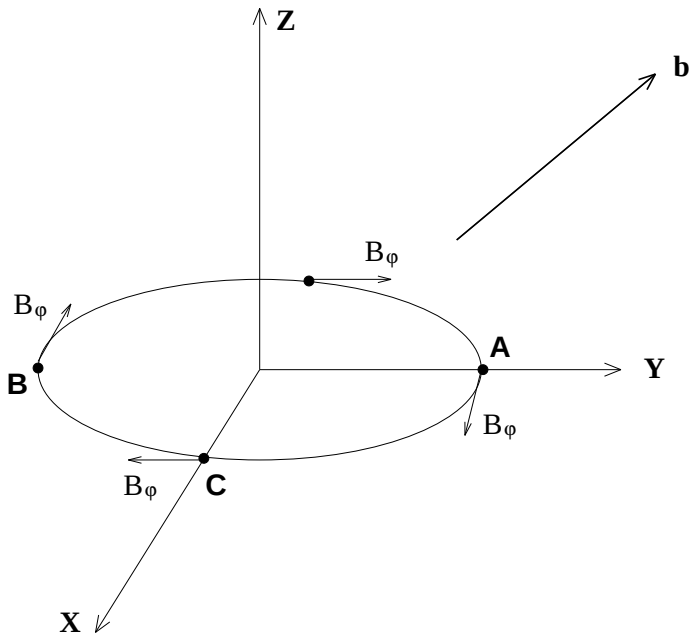

Figura 5.1: Campo magnético intergaláctico que produciría el alabeo.

5.3. El campo magnético y el alabeo

Battaner, Florido y Sánchez-Saavedra (1990) propusieron por primera vez al campo magnético intergaláctico para explicar el alabeo de las galaxias. Para ello el campo magnético debe tener una dirección, para tener máxima eficiencia, de unos 45^o con respecto al plano de la galaxia y una fuerza de entre unos 10^{-8} a 10^{-6} Gauss. Esto último es plenamente asumible, pues el campo intergaláctico es del orden de 1 a 3 μG al menos (ver por ejemplo, Kronberg 1994). Una dirección diferente de 45^o reduciría la fuerza considerablemente.

En las partes más externas del disco de las galaxias, las fuerzas debido a gravedad y magnetismo galáctico, son relativamente pequeñas, por lo que el campo magnético intergaláctico puede influir de una manera decisiva en la dinámica del gas.

Las líneas del campo magnético están congeladas con el gas del disco galáctico (es decir, el flujo magnético que atraviesa una determinada superficie es constante). La ecuación de movimiento del gas se puede escribir (Spitzer 1978, Battaner 1996):

$$\rho\frac{\partial \mathbf{v}}{\partial t} + \rho\mathbf{v}\cdot\nabla\mathbf{v} + \nabla p + \nabla\frac{B^2}{8\pi} - \nabla\cdot(\eta\varphi) = -\rho\nabla\mathcal{F} + \frac{1}{4\pi}\mathbf{B}\cdot\nabla\mathbf{B} \tag{5.5}$$

donde ρ es la densidad, $\mathbf{v}$ es la velocidad, t el tiempo, p la presión, $\mathbf{B}$ la intensidad de campo magnético, η el coeficiente de viscosidad, φ el tensor de cizalladura y $\mathcal{F}$ el potencial gravitatorio. La presión es debida al transporte de momento por nubes gaseosas y sus movimientos caóticos, más que al movimiento de átomos o moléculas. La fuerza magnética es:

$$\mathbf{F} = -\nabla[\frac{B^2}{8\pi}] + \frac{1}{4\pi}\mathbf{B}\cdot\nabla\mathbf{B} \tag{5.6}$$

Si $\mathbf{b}$ es el campo magnético intergaláctico, $\mathbf{B}$ el galáctico, el cual se supone azimutal $\mathbf{B} = (0, B_\varphi, 0)$ (Battaner y Sánchez-Saavedra 1986, Battaner, Florido y Sánchez-Saavedra 1988), un punto A contenido en el plano yz del campo externo, tendria $b_x = 0$, ver Figura 5.1. El gradiente de la presión magnética, $\frac{B^2}{8\pi}$, actuaría de igual manera en cualquier punto a lo largo de los bordes de la galaxia, por lo que no podría producir alabeos. Pero no es el caso del segundo término de la ecuación: $\frac{1}{4\pi}\mathbf{B}\cdot\nabla\mathbf{B}$

Lo vemos esquemáticamente con el punto A, si L es la longitud característica en la cual las regiones galácticas dominadas por $\mathbf{B}$ llegan a estar dominadas por $\mathbf{b}$, en el punto (r_A-$L/2$) el campo seía (B_ϕ, 0, 0) y a (r_A+$L/2$) seía (0, b_y, b_z). Un campo externo homogéneo o cercano a la

homogeneidad no podría existir dentro del disco galáctico, ya que estaría girado por la rotación galáctica, amplificado y destruido por las inestabilidades. En el punto A, por tanto, tendríamos un valor intermedio de ($B_\phi/2$, $b_y/2$, $b_z/2$). Así la fuerza en A sería del orden de:

$$\mathbf{F}_A = \frac{1}{8\pi}(B_\phi, b_y, b_z) \begin{pmatrix} 0 & 0 & 0 \\ -B_\phi/L & b_y/L & b_z/L \\ 0 & 0 & 0 \end{pmatrix} = \frac{1}{8\pi L} \begin{pmatrix} -b_y B_\phi \\ b_y^2 \\ b_y b_z \end{pmatrix} \tag{5.7}$$

En un punto azimutalmente opuesto, B, el campo magnético intergaláctico será igual, pero **B** sería igual a (-B_ϕ, 0, 0), y por tanto la fuerza será:

$$\mathbf{F}_B = \frac{1}{8\pi}(-B_\phi, b_y, b_z) \begin{pmatrix} 0 & 0 & 0 \\ -B_\phi/L & -b_y/L & -b_z/L \\ 0 & 0 & 0 \end{pmatrix} = \frac{1}{8\pi L} \begin{pmatrix} -b_y B_\phi \\ -b_y^2 \\ -b_y b_z \end{pmatrix} \tag{5.8}$$

Y en el punto C, $\mathbf{b} = (0, b_y, b_z)$ y **B** sería igual a (0, B_ϕ, 0), y por tanto la fuerza magnética será:

$$\mathbf{F}_C = \frac{1}{4\pi}(0, \frac{b_y - B_\phi}{2}, \frac{b_z}{2}) \begin{pmatrix} 0 & \frac{b_y + B_\phi}{L} & \frac{b_z}{L} \\ 0 & 0 & 0 \\ 0 & 0 & 0 \end{pmatrix} = 0 \tag{5.9}$$

Así vemos que en el punto A la fuerza tiene una componente vertical de valor ($b_y b_z/8\pi$L), en el punto B tiene el mismo valor pero sentido contrario, y en el punto C (y en un punto azimutalmente opuesto), es nula. Por lo tanto tenemos lo necesario para encontrarnos con un alabeo. Dicho alabeo será máximo cuando $b_y = b_z$, es decir, cuando el campo magnético intergaláctico forme un ángulo de 45^o grados con el plano de la galaxia. La intensidad del campo magnético necesario para producir una desviación a un radio R, sería aquella que compensara la componente vertical de la gravedad, es decir:

$$G\frac{M\rho}{R^2}\frac{h}{R} \cong \frac{b^2}{16\pi L} \tag{5.10}$$

donde h es la elevación del disco sobre el plano producida por la fuerza magnética.

Haciendo una estimación de los valores, podemos obtener que $b \approx 10^{-8}$ G. (R = 50 kpc, h = 1 kpc, L = 1 kpc, $\rho = 10^{-27}$ g cm^{-3}). Ver el artículo de Battaner y Jiménez-Vicente (1998).

Con este modelo se explicarían los hechos observacionales que hemos visto en el capítulo 4:

- La mayoría (si no todas) las galaxias espirales están alabeadas.
- Las galaxias S0 no muestran alabeo, porque carecen o tienen poco gas y por lo tanto no estarían afectadas por el campo magnético intergaláctico.
- El disco de población estelar más vieja parece estar menos alabeado que el disco del gas y el de las estrellas recientemente formadas. Esta teoría, provocaría un alabeo diferente según la población observada: el polvo y el gas estarían más alabeados que la materia neutra como las estrellas. Las estrellas nuevas (mostradas en los filtros del visible) seguirían en un principio la distribución del polvo y gas del que han nacido, por lo que mostrarían un alabeo más pronunciado que las estrellas más viejas (más luminosas en el infrarrojo). Este hecho fue encontrado por Florido et al. (1991) y más recientemente por Reylé et al. (2009) y está, en parte, confirmado con las observaciones presentadas en la tesis.

Además es un mecanismo que actúa permanentemente y justificaría que el alabeo sea una estructura galáctica duradera.

El campo magnético intergaláctico no varía mucho en dirección dentro de un grupo de galaxias, por lo que se esperaría una orientación similar en las galaxias que pertenecen a un mismo grupo. Este efecto fue investigado por Zurita y Battaner (1997) en el Grupo Local encontrando un alineamiento bastante significativo, entre la Vía Láctea, M31 y M33. También fue observado por Battaner, Florido y Sánchez-Saavedra en 1990 y Garrido et al. (1993) en otros grupos de galaxias.

5.4. Artículos

5.4.1. Magnetic Fields are not Ignorable in the Dynamics of Disks

Battaner, E., Florido, E., Guijarro, A. 2001, *Galaxy Disks and Disk Galaxies*, eds. Funes, J.G., Corsini, E.M., ASP Conference Series

5.4.2. Magnetic fields and the dynamics of the outer disk of spiral galaxies

Battaner, E., Florido, E., Guijarro, A., Castillo-Morales, A. 2005, AIP Conf. Proc., 784, 784

5.4.3. MAGNETIC FIELDS IN GALAXIES

Battaner, E., Florido, E., Guijarro, A., Rubiño-Martín, J.A., Ruíz-Granados, B., Zurita, A. 2008, LNEA, 3, 83

Capítulo 6

Conclusiones

En esta tesis hemos estudiado la estructura del disco estelar de las galaxias en su parte más externa. Intentamos responder a la pregunta: ¿qué ocurre o cómo terminan los discos estelares de las galaxias? En estas regiones a grandes radios galactocéntricos (R), la gravedad deja de ser la fuerza dominante ($\sim$ G $\frac{M\rho}{R^2}$) y podemos considerar otros aspectos, tales como las perturbaciones del medio intergaláctico, la influencia de posibles compañeras, la interacción de la galaxia y el cúmulo al que pertenece, el campo magnético y las distorsiones del halo de materia oscura. Con esta motivación elegimos estudiar el truncamiento y el alabeo, pues son dos de las estructuras que pueden ocurrir en los bordes de los discos estelares.

Aunque las observaciones de estas estructuras pueden proporcionar datos clave que permitan discernir entre unas teorías y otras, se plantearon de forma imparcial, más estudiando unos fenómenos sobre los cuales existe información escasa que como medio de reforzar algún modelo teórico, diferenciando completamente el proceso de observación y descripción y el de interpretación.

Hemos elegido galaxias con disco vistas de perfil y hemos realizado observaciones muy profundas en visible (B, V, I) y en infrarrojo cercano (J, H, K_S) alcanzando un brillo superficial de 28.5 $mag/arcsec^2$ en V y de 24.5 $mag/arcsec^2$ en J.

Los resultados y conclusiones del trabajo sobre los truncamientos del disco estelar son:

1. El disco estelar de las galaxias se extiende hasta un radio galactocéntrico menor que el disco gaseoso. Esto no es debido a límites en la sensibilidad de los telescopios. Al observar galaxias de perfil alcanzamos radios galactocéntricos que en galaxias con otras inclinaciones serían inobservables. Con el método de inversión utilizado para desproyectar los perfiles confirmamos que el truncamiento no es debido a la proyección del disco al verlo de perfil.

2. De las 14 galaxias espirales observadas en infrarrojo cercano, 10 están truncadas y 4 muestran un perfil exponencial sin truncamiento hasta el nivel de brillo que detectamos.

3. En media, el coeficiente R_t/h_R (R_t radio de truncamiento y h_R escala de longitud radial) que encontramos es de 3.6$\pm$0.8, un poco más bajo pero acorde con el encontrado (4.2$\pm$0.5) en trabajos anteriores de otros autores (van der Kruit y Searle 1982, Barteldrees y Dettmar 1994, de Grijs et al. 2000 y Pohlen et al. 2000). En nuestro trabajo, tenemos datos de galaxias de perfil en infrarrojo cercano donde la extinción y los efectos de la inclinación afectan menos que en el rango del visible, donde se puede estar infraestimando este valor.

4. Detectamos algunas diferencias entre el R_t que obtenemos para los distintos filtros, así que podemos decir que encontramos dependencia de color en él para algunas galaxias, siendo el radio más pequeño conforme aumentamos la longitud de onda. Esto podría interpretarse como que el disco de población más vieja se trunca antes que el de las estrellas más jóvenes. Hemos visto que la longitud de escala radial h_R depende de la longitud de onda (de Jong 1996) por lo que el estudio de la dependencia del color del radio de truncamiento se debe hacer con R_t y no con R_t/h_R.

5. Esta tendencia en la dependencia del truncamiento con el color se pone de manifiesto especialmente en el caso del estudio individual de la galaxia NGC 6504 puesto que combinamos observaciones de datos muy profundos, tanto en infrarrojo cercano como en visible. Podemos concluir que en las cuatro bandas observadas, V, J, H y K_S, todos muestran truncamiento real, ninguno de los perfiles obtenidos se ajusta a un perfil de doble exponencial. En particular en el perfil radial en la banda V el truncamiento se muestra a partir de 28.5 $mag/arcsec^2$ que, extrapolando, ocurre a un $R_t(V) = 85$ *arcsec*. En las bandas del infrarrojo cercano los perfiles radiales muestran tambien truncamiento, que ocurre a $R_t(K_S) = 74$ *arcsec*, es decir una diferencia de 3.3 kpc (asumimos una distancia de 63.18 Mpc).

6. Es la primera vez que se define la curva de truncamiento T(R), obteniendo como mejor resultado $T(R) \propto (R_t - R)^{-n}$ con n =0.8±0.3, un valor próximo a 1, es decir, que será completo a $R_t = R$. Las curvas de truncamiento que obtenemos de la misma galaxia vista de perfil y desproyectada, de cara, son diferentes, pero el radio de truncamiento es el mismo.

7. Aunque nuestra estadística es pobre, podemos sugerir que el truncamiento afecta principalmente a galaxias espirales de tipo tardío y que el radio de truncamiento aumenta con la velocidad de rotación máxima del modo: $R_t \propto V_m^c$, con c del orden de 1.5. Teniendo en cuenta la relación de Tully-Fisher, esto nos lleva a que R_t es mayor para galaxias mas brillantes. Este es el resultado que obtenemos cuando relacionamos el radio de truncamiento con la magnitud absoluta en la banda B.

El modelo magnético de Battaner, Florido y Jiménez-Vicente (2002) además de explicar la velocidad de rotación de las galaxias, podría explicar el truncamiento y el antitruncamiento. La fuerza magnética que actúa sobre el gas ionizado y ayuda a contrarrestar, junto a la gravedad, el efecto de la fuerza centrífuga, desaparecería al formarse las estrellas. Estas estrellas recién formadas, al no estar afectadas por el magnetismo, se moverían a órbitas más externas produciendo el perfil antitruncado, o incluso podrían escapar de la galaxia en la dirección radial produciendo el perfil truncado. Las otras propiedades estadísticas que hemos encontrado quedan también explicadas con el modelo magnético, pues simplificando, Battaner, Florido y Jiménez-Vicente (2002), que obtienen:

$$R_t = \frac{2GM}{\theta_0^2} \tag{6.1}$$

donde M es la masa visible de la galaxia y θ_0 es la velocidad de rotación asintótica, constante a radios grandes. Junto a la relación de Tully-Fisher $L \propto \theta_0^{3.5}$ y $M \propto L$, donde L es la luminosidad de la galaxia, obtenemos de la ecuación anterior que:

$$R_t \propto \frac{2G\theta_0^{3.5}}{\theta_0^2} \propto 2G\theta_0^{1.5} \tag{6.2}$$

esto justificaría la relación proporcional encontrada entre el radio de truncamiento y la velocidad de rotación máxima, además de que dicho radio sea mayor para galaxias más brillantes y que las galaxias más extendidas tengan radios de truncamiento mayores. Que el truncamiento afecte principalmente a galaxias espirales de tipo tardío es compatible con que estas galaxias requieren campos magnéticos mayores y por tanto estén más afectadas de truncamiento. El hecho de que el radio de truncamiento sea menor para las longitudes de onda mayores se podría explicar en el escenario magnético como que las estrellas recién formadas se estarían escapando. Si la velocidad de escape es aproximadamente igual a la velocidad de rotación, del orden de 100 km s^{-1}, y si el espacio que recorren es del orden de 10 kpc, el tiempo característico de escape podría ser del orden de 10^8 años, un tiempo que diferenciaría claramente las estrellas viejas de las recién formadas.

La presencia del alabeo del disco de gas neutro y el disco visible en galaxias, ya ha sido estudiada en varias ocasiones obteniendo como conclusión que prácticamente todas las galaxias están alabeadas.

En esta tesis se ha realizado un cartografiado del cielo del Hemisferio Sur, complementando al realizado en el Norte por Sánchez-Saavedra, Battaner y Florido (1990), en el que:

1. Se confirma la gran frecuencia de galaxias alabeadas en el visible, el 60 %. Los resultados son consistentes con los obtenidos en el cartografiado del Norte, en el que se encontraron que 42 de las 86 galaxias (49 %) examinadas mostraban un alabeo en el visible. Si se tiene en cuenta que el alabeo sólo será detectado si la línea de nodos es paralela o forma un ángulo adecuado (ver Sánchez-Saavedra, Battaner y Florido 1990) con la línea de visión, el número total de discos estelares alabeados podría ser próximo al 100 %. Todos los discos estelares de las galaxias espirales están alabeados.

2. No se han encontrado pruebas de esta desviación en las galaxias S0. Dichas galaxias, parecen carecer prácticamente de gas, por lo que constituiría una importante restricción a los modelos teóricos.

Además aportamos el estudio de los alabeos galácticos con datos muy profundos en cuatro filtros, tres en la banda visible y uno en el infrarrojo cercano (alcanzando un brillo superficial de 23 $mag/arcsec^2$ en K_S). Es la primera vez que se han usado los datos en el infrarrojo cercano para estudiar alabeos, sin embargo son esenciales para trazar la distribución de masa de las estrellas. Estas longitudes de ondas suministran una información esencial y complementaria para el estudio de los alabeos estelares:

1. Los alabeos en el rango del infrarrojo existen con una frecuencia parecida a los alabeos en el rango del visible. Es decir, la mayoría de las galaxias espirales están alabeadas (o todas). Esto sugiere que los alabeos son estructuras con una vida larga y que fueron formados en las etapas más tempranas de la evolución de la mayoría de las galaxias. El mecanismo responsable de la formación de los alabeos, por tanto, debería estar actuando permanentemente.

2. En 8 de las 20 galaxias observadas el alabeo es más pequeño en la longitud de onda del infrarrojo que en el visible. Incluso en 6 de estas 20 galaxias el alabeo infrarrojo es inexistente,

3. Confirmamos los resultados encontrados por otros autores de que la mayoría, si no todas, las galaxias S0 no presentan alabeo. Esto, combinado con lo anterior, sugiere una relación directamente proporcional entre la cantidad de gas de las galaxias y la capacidad de desarrollar el alabeo.

4. Exceptuando el caso de las galaxias S0, el alabeo no depende del tipo morfológico, ya que está presente en todos los tipos de galaxias de disco. El grado de alabeo también es independiente del tipo morfológico.

5. El alabeo a longitudes de onda visibles parece que empieza siempre antes que el alabeo del disco gaseoso medido en HI, aunque hay que tener en cuenta la baja resolución de los datos en HI. El alabeo del gas es siempre más pronunciado que el alabeo estelar.

Florido et al. (1991) ya encontraron en tres galaxias de perfil y en nuestra Galaxia, una clara dependencia con la longitud de onda dentro de la banda del visible, detectando que a colores más azules (que representan las poblaciones estelares más jovenes) la desviación del plano de las galaxias era mayor. Este efecto no está causado por el polvo que contiene la galaxia. El efecto de la extinción es siempre una separación entre el alabeo estelar y el gaseoso, y este efecto es mayor a longitudes de onda más cortas. Pero si hay alguna diferencia entre el alabeo a longitudes de onda azules y rojas, la extinción tiene el efecto opuesto, reducir la separación real entre alabeos.

En el panorama clásico, si el alabeo estuviera provocado por gravitación, las estrellas más nuevas, las viejas, el gas y el polvo podrían tener el mismo alabeo, ya que la gravedad actuaría sobre todos ellos de igual manera. Pero encontramos cierta diferencia entre los alabeos detectados en el visible y en el infrarrojo cercano. A esas longitudes de onda detectamos distintas poblaciones del disco. Parece que el disco de población vieja está menos alabeado que el disco de gas y el de las estrellas nuevas, que seguirían en un principio la distribución del polvo y gas del que han nacido. Con el campo magnético o la presión del gas intergaláctico como causantes del alabeo la capa de gas podría reaccionar más fuertemente que la componente estelar. El módelo magnético (Battaner, Florido y Sánchez-Saavedra 1990) explicaría que las galaxias S0 no muestren alabeo, porque al carecer o tener poco gas no estarían afectadas por el campo magnético intergaláctico. Además es

un mecanismo que actúa permanentemente y justificaría que el alabeo sea una estructura galáctica duradera.

Los alabeos en HI son mucho más grandes y extendidos, y empiezan, en general, en torno al truncamiento del disco estelar y están acompañados por una significativa disminución de la velocidad de rotación y de la distribución de la densidad superficial de HI (van de Kruit, 2000).

El truncamiento y el alabeo son por tanto, dos fenómenos universales y muy frecuentes, muy importantes para la dinámica de la periferia de las galaxias. Sería muy interesante proseguir con el trabajo añadiendo más galaxias a la muestra, y estudiar la posible relación entre las dos estructuras dinámicas estudiadas, el truncamiento y el alabeo.

Capítulo 7

Bibliografía

1. ARTÍCULOS

- Ann, H.B., Park, J-C 2006, New. Astr., 11, 293
- Battaner, E., Sánchez-Saavedra, M. L. 1986, ApJ, 302, 450
- Battaner, E., Florido, E., Sánchez-Saavedra, M. L. 1988, ApJ, 331, 116
- Battaner, E., Florido, E., Sánchez-Saavedra, M. L. 1990, A&A, 236, 1
- Battaner, E., Garrido, J.L., Membrado, M., Florido, E. 1992, Nature, 360, 652
- Battaner, E., Florido, E., Jiménez-Vicente, J., Porcel, C., Sánchez-Saavedra, M. L. 1997, The Impact of Large Scale Near-IR Sky Surveys, eds. F. Garzón et al. Dordrecht Kluwer Academic Publishers, Series Astrophysics and Space Science, 210, 49
- Battaner, E., Jiménez-Vicente, J. 1998, A&A, 332, 809
- Battaner, E., Florido, E., Jiménez-Vicente, J. 2002, A&A, 388, 213
- Barteldrees, A., Dettmar, R.J. 1994, A&AS 103, 475
- Beck, R. 2004, Ap&SSci, 289, 293
- Beck, R. 2005, Lecture Notes in Physics, 664, 41
- Binney, J. 1992, ARA&A, 30, 51
- Bosma, A. 1978, PhD Thesis, University of Groningen, The Netherlands
- Bosma, A. 1981, AJ, 86, 1791
- Brigg, F.H. 1990, ApJ, 352, 15
- Brinks, E., Burton, W.B. 1984, A&A, 141, 195
- Broeils, A.H., Rhee, M.H. 1997, A&A, 324, 877
- Burke, B.F. 1957, AJ, 62, 90
- Burstein, D., 1979, ApJ, 234, 829
- Camm, G.L. 1950, MNRAS, 110, 305
- Casali, M.M., Hawarden, T.G. 1992, JCMT-UKIRT Newslett., 3, 33
- Carter, B.S., Meadows, V.S. 1995, MNRAS, 276, 734
- Christlein, D., Zaritsky, D. 2008, ApJ, 680, 1053
- Corbelli, E., Schneider, S.E., Salpeter, E.E. 1989, AJ, 97, 390
- de Grijs, R. 1997, PhD Thesis, University of Groningen, The Netherlands
- de Grijs, R., Peletier, R.F., van der Kruit, P.C. 1997, A&A, 327, 966
- de Grijs, R. 1998, MNRAS, 299, 595
- de Grijs, R., Kregel, M., Wesson, K.H. 2001, MNRAS, 324, 1074

- de Jong, R.S. 1996, A&A, 313, 45
- de Vaucouleurs, G. 1958, ApJ, 128, 465
- Dekel, A., Shlosman, I. 1983, *Internal Kinematic & Dynamics of Galaxies*, ed. E. Athanassoula. Dordrecht: Reidel, 187, IAU Symp. 100
- Djorgovski, S., Sosin, C. 1989, ApJ, 341, 13
- Eggen, O.J., Lynden-Bell, D., Sandage, A.R. 1962, ApJ, 136, 478
- Erwin, P., Beckman, J.E., Pohlen, M. 2005, ApJ, 626, 81
- Erwin, P., Pohlen, M., Beckman, J.E. 2008, AJ, 135, 20
- Erwin, P., Pohlen, M., Beckman, J.E., Gutiérrez, L., Aladro, R. 2008, ASP Conference Serie, 390, 251
- Fall, S.M., Efstathiou, G. 1980, MNRAS, 193, 189
- Florido, E., Prieto, M., Battaner, E., Mediavilla, E., Sánchez-Saavedra, M.L. 1991, A&A, 242, 301
- Freeman, K.F. 1970, ApJ, 160, 811
- García-Ruiz, I. 2001, PhD Thesis, University of Groningen, The Netherlands
- García-Ruiz, I., Kuijken, K., Dubinski, J. 2002a, MNRAS, 337, 459
- García-Ruiz, I., Sancisi, R., Kuijken, K. 2002b, A&A, 394, 769
- Garrido, J.L., Battaner, E., Sánchez-Saavedra, M.L., Florido, E. 1993, A&A, 271, 84
- Habing, H.J. 1988, A&A, 200, 40
- Herschel, W. 1785, Phil. Trans., LXXV, 213
- Hunter, C., Toomre, A. 1969, ApJ, 155, 747
- Jiménez-Vicente, J., Porcel, C., Sánchez-Saavedra, M.L., Battaner, E. 1997, Ap&SS, 253, 225
- Kahn, F.D., Woltjer, L. 1959, ApJ, 130, 705
- Kapteyn, J.C. 1922, ApJ, 55, 302
- Kennicutt, R.C. 1989, ApJ, 344, 685
- Kent, S.M., Dame, T.M., Fazio, G. 1991, ApJ, 378, 131
- Kerr, F.J. 1957, AJ, 62, 93
- Kobayashi, N., Tokunaga, A.T. 2000, ApJ, 532, 423
- Kormendy, J. 2007, IAU Symp., 245, 107
- Kregel, M., van Der Kruit, P.C., de Grijs, R. 2002, MNRAS, 334, 646
- Kregel, M. 2003, PhD Thesis, University of Groningen, The Netherlands
- Kronberg, P.P. 1994, Rep. Progress in Physics, 57:4, 325
- Larson, R.B. 1976, MNRAS, 176, 31
- Lauberts A., Valentijn, E.A. 1989, *The Surface Photometry Catalogue of the ESO-Uppsala Galaxies*, ESO (ESO-LV)
- Lequeux, J., Guélin, M. 1996, *Cold Dust and Galaxy Morphology*, eds. Block, D.L., Greenberg, J.M., Kluwer Academic Publishers, Dordrecht, 209, 422
- López-Corredoira, M., Betancort-Rijo, J., Beckman, J.E. 2002, A&A, 386, 169
- López-Corredoira, M., Florido, E., Betancort-Rijo, J., Trujillo, I., Carretero, C., Guijarro, A., Battaner, E., Patiri, S. 2008, A&A, 488, 511
- Masset, F., Tagger, M. 1997, A&A, 318, 747
- Nelson, A.H. 1988, MNRAS, 233, 115
- Ostriker, E.C., Binney, J.J. 1989, MNRAS, 237, 785
- Patterson, F.S. 1940, Harvard Bull., 919, 9

- Peletier, R.F., Balcells, M. 1996, AJ, 111, 2238
- Peletier, R.F. 2008, ASP Conference Series, 390, 232
- Pérez, I. 2004, A&A, 427, 17
- Pohlen, M. 2001, PhD Thesis, Ruhr-University Bochum, Germany
- Pohlen M., Dettmar R.-J., Lütticke R., Aronica G. 2002, A&A, 392, 807
- Pohlen, M., Beckman, J.E., Huettemeister, S., Knapen, J.H., Erwin, P., Dettmar, R.-J. 2004, *Penetrating Bars through Masks of Cosmic Dust*, eds. Block, D.L., Freeman, K.C., Puerari, I., Groess, R, Kluwer Academic Publishers, London, 713
- Pohlen, M., Trujillo, I. 2006, A&A, 454, 759
- Pohlen, M., Zaroubi, S., Peletier, R.F., Dettmar R-J. 2007, MNRAS, 378, 594
- Porcel, C., Battaner, E., Jiménez-Vicente, J. 1997, A&A, 322, 103
- Porcel, C., Garzón, F., Jiménez-Vicente, J., Battaner, E. 1998, A&A, 330, 136
- Reshetnikov V., Combes F. 1998, A&A 337, 9
- Reshetnikov V., Battaner, E., Combes, F., Jiménez-Vicente, J. 2002, A&A, 382, 513
- Revaz, Y., Pfenniger, D., Combes, F., Bournaud, F. 2009, A&A, 501, 171
- Reylé, C., Marshall, D.J., Robin, A.C., Schultheis, M. 2009, A&A, 495, 819
- Robin, A.C., Creze, M., Mohan, V. 1992, ApJ, 400, 25
- Rogstad, D.H., Lockhart, I.A., Wright, M.C.H. 1974, ApJ 193, 309
- Ruphy, S., Robin, A.C., Epchtein, N., Copet, E., Bertin, E., Fouque, P., Guglielmo, F. 1996, A&A, 313, 21
- Saha, K., Jog, C.J. 2006, A&A, 446, 897
- Saha, K., de Jong, R., Holwerda, B. 2009, MNRAS, 396, 409
- Sánchez-Saavedra, M.L., Battaner, E., Florido, E. 1990, MNRAS, 246, 458
- Sánchez-Salcedo, F.J., Reyes-Iturbide, J., Hernandez, X. 2006, MNRAS, 370, 1829
- Sancisi, R. 1976, A&A, 53, 159
- Schwarzkopf, U., Dettmar, R.J. 2000, A&A, 361, 451
- Sparke, L.S. 1984, ApJ, 280, 117
- Sparke, L.S., Casertano, S. 1988, MNRAS 234, 873
- Tinsley, B.M., Larson, R.B. 1977 *Evolution of galaxies and stellar populations*, New Haven: Yale University Observatory
- Thim, F., Hoessel, J.G., Saha, A., Claver, J., Dolphin, A., Tammann, G.A. 2004, AJ, 127, 2322
- Thuan, T.X., Gunn, J.E. 1976, PASP, 88, 543
- Tubbs, A.D., Sanders, R.H. 1979, ApJ, 230, 736
- van der Kruit, P.C. 1979, Astron. Astrophys. Suppl. Ser., 38, 15
- van der Kruit, P.C., Searle, L. 1981a, A&A, 95, 105
- van der Kruit, P.C., Searle, L. 1981b, A&A, 95, 116
- van der Kruit, P.C., Searle, L. 1982a, A&A, 110, 61
- van der Kruit, P.C., Searle, L. 1982b, A&A, 110, 79
- van der Kruit, P.C. 1988, A&A, 192, 117
- van der Kruit, P.C. 2001, *Galaxy Disks and Disk Galaxies*, eds. Funes, J.G., Corsini, E.M., ASP Conference Series, 230, 119
- van der Kruit, P.C. 2007, A&A, 466, 883
- van der Kruit, P.C., Freeman, K.C. 2011, ARA&A, 49, 301

- Wainscoat, R.J., Freeman, K.C., Hyland, A.R., 1989, ApJ, 337, 163
- Wainscoat, R.J., Cowie, L.L. 1992, AJ, 103, 33
- Weinberg, M. D. 1998, MNRAS, 299, 499
- Weinberg, M. D., & Blitz, L. 2006, ApJ, 641, L33
- White, S., Rees, M. 1978, MNRAS, 183, 341
- Zurita, A., Battaner, E. 1997, A&A, 322, 86

2. LIBROS

- Battaner, E. 1986 *Fluidos Cósmicos*. Lábor. Barcelona.
- Battaner, E. 1996 *Astrophysical Fluid Dynamics*. Cambridge University Press. Cambridge.
- Binney, J. 1991 *Dynamics of Disk Galaxies*. B. Sundelius. Göteborg. Sweden.
- Binney, J., Tremaine, S. 1987 *Galactic Dynamics*. Princeton University Press.
- Binney, J., Merrifield, M. 1998 *Galactic Astronomy*. Princeton University Press.
- Clayton, D. D. 1983 *Principles of Stellar Evolution and Nucleosynthesis*. University of Chicago Press. Chicago.
- Gilmore, G.F., King, I.R., van der Kruit, P.C. 1989 *The Milky Way as a Galaxy*. University Science Books. California.
- Mihalas, D., Binney, J. 1981 *Galactic Astronomy*. Freeman and Company. 2nd Edition. New York.
- Hubble, E.P. 1936 *Realm of the Nebulae*. New Haven. Yale University Press
- Ruzmaikin, A.A., Shukurov, A.M., Sokoloff, D.D. 1988 *Magnetic Fields of Galaxies*. Kluwer Academic Publishers. London.
- Sofue, Y. 1987, *Intergalactic Magnetic Fields*, eds. Beck, R., Grave, R., Springer, Berlin Heildelberg New York
- Spitzer, L. 1978, *Physical processes in the interstellar medium*. Wiley-VCH, Hoboken, NJ. New York.
- Walker, G. 1987 *Astronomical Observations*. Cambridge University Press. Cambridge.

3. ARTÍCULOS DE ESTA TESIS

- Battaner, E., Florido, E., Guijarro, A. 2001, *Galaxy Disks and Disk Galaxies*, eds. Funes, J.G., Corsini, E.M., ASP Conference Series
- Battaner, E., Florido, E., Guijarro, A., Castillo-Morales, A. 2005, AIP Conf. Proc., 784, 784
- Battaner, E., Florido, E., Guijarro, A., Rubiño-Martín, J.A., Ruíz-Granados, B., Zurita, A. 2008, LNEA, 3, 83
- Florido, E., Battaner, E., Guijarro, A., Garzón, F., Jiménez-Vicente, J. 2001, A&A, 378, 82
- Florido, E., Battaner, E., Guijarro, A., Garzón, F., Castillo-Morales, A. 2006a, A&A, 455, 467
- Florido, E., Battaner, E., Guijarro, A., Garzón, F., Castillo-Morales, A. 2006b, A&A, 455, 475
- Florido, E., Battaner, E., Zurita, A., Guijarro, A. 2007, A&A, 472, L39
- Guijarro, A., Peletier, R.F., Battaner, E., Jiménez-Vicente, J., de Grijs, R., Florido, E. 2010, A&A, 519, 53
- Sánchez-Saavedra, M.L., Battaner, E., Guijarro, A., López-Corredoira, M., Castro-Rodríguez, N. 2003, A&A, 399, 457

A&A 378, 82–96 (2001)
DOI: 10.1051/0004-6361:20011190

Astronomy & Astrophysics

Near infrared observations of the truncation of stellar disks

E. Florido[1], E. Battaner[1], A. Guijarro[1], F. Garzón[2], and J. Jiménez-Vicente[3]

[1] Dpto. Física Teórica y del Cosmos, Universidad de Granada, Spain
[2] Instituto de Astrofísica de Canarias, Vía Láctea, s/n, La Laguna, Tenerife
[3] Groningen Kapteyn Laboratorium, Groningen, The Netherlands

Received 20 April 2001 / Accepted 22 August 2001

Abstract. We present a first study of truncation of the stellar disks of spiral galaxies in the near infrared. Observations of NGC 4013, NGC 4217, NGC 6504 and NGC 5981 were made with the CAIN NIR camera on the CST in Tenerife. This wavelength range provides the best description of the phenomenon, not only because extinction effects are minimized, but also because the distribution of the old stellar population is directly obtained. The four galaxies are edge-on and an inversion method was developed to obtain the deprojected profiles. We did not assume any model of the different galactic components. The "truncation curve", i.e. $T(R) = \mu(R) - \mu_{\rm D}(R)$, where μ is the actual surface brightness in mag/arcsec^2 and $\mu_{\rm D}$ the exponential disk surface brightness, has been obtained with unprecedented precision. It is suggested that $T(R)$ is proportional to $(R_{\rm t} - R)^{-1}$, where $R_{\rm t}$ is the truncation radius, i.e. the radius beyond which no star is observed.

Key words. galaxies: structure, photometry

1. Introduction

At large radii the stellar density of disks decreases faster than an exponential until reaching a cut-off or truncation radius $R_{\rm t}$, where it vanishes. This morphological feature was discovered by van der Kruit (1979) and later studied in more detail by van der Kruit & Searle (1981a,b, 1982). Recently, this phenomenon has been reconsidered by means of samples larger than the seven edge-on galaxies observed by van der Kruit and Searle and by improved observational techniques. Barteldrees & Dettmar (1994), Pohlen et al. (2000), Pohlen et al. (2000) and de Grijs et al. (2001) have provided the basic information about truncations in the optical range for external galaxies. Our Galaxy also presents a truncation, although it is more difficult to observe (Habing 1988; Robin et al. 1992; Ruphy et al. 1996; Freudenreich 1998). Porcel et al. (1997) found that the Milky Way cut-off radius cannot be placed at distances larger than 15 kpc. Truncations of stellar disks have been reviewed by van der Kruit (2000). Much remains to be done both from theory and observations to understand this phenomenon.

A) Lack of theoretical explanation

The above studies have established the universality of the phenomenon. Most galaxies, if not all, seem to have truncated stellar disks, sensitivity limits alone are unable to explain this feature. This fact emphasizes the theoretical importance of the topic. However, truncations constitute one of the most important challenges in galactic dynamics. Though several hypotheses have been considered, this phenomenon remains completely unexplained.

It was suggested by van der Kruit (2000) that stellar truncation is accompanied by a significant drop in rotation velocity, with NGC 4013, NGC 891 and NGC 5907 being clear examples of this. If this fact is confirmed, and actually takes place in most truncated disks, it would mean that there is a true decrease in the radial distribution of the total density, i.e. the sum of both, the gas and the stellar densities. Theories suggesting that stellar truncation is due to a cut-off of the star formation rate beyond a certain radius should be reconsidered, as in this case the total gas plus star density would not present any discontinuity. The confirmation of a drop in rotation velocity close to the stellar truncation would pose serious difficulties for the most promising hypothesis, maintained by Kennicutt (1989) and others, in which star formation does not proceed when the gas density is lower than a certain threshold value and would reject all theories in which stars do not exist beyond the truncation radius, because they are not formed.

Another argument against the absence of star formation as the cause of stellar truncation is that we do see star formation beyond the truncation radius of the

Send offprint requests to: E. Florido, e-mail: estrella@ugr.es

Milky Way. Molecular clouds are often associated with HII regions, IRAS sources, H_2O masers and other objects characterizing the presence of the formation of high mass stars (Mead et al. 1987; Mead et al. 1990; Brand & Wouterloot 1994; Rudolph et al. 1996; Williams & McKee 1997; May et al. 1997; Kobayashi & Tokunaga 2000, and others). A high star formation rate is also observed in other galaxies (Lequeux & Guelin 1996). Wouterloot et al. (1988) and Ferguson et al. (1998) found the important result that the amount of star formation per unit mass of H_2 at $R = 15$ kpc is equal to that in the solar neighbourhood. The ratio $N(\mathrm{HII})/\sigma(H_2)$ at $R = 15$ kpc was found to be higher (by a factor 10/7) than in the solar neighbourhood. Though some differences are found between the outer galaxy molecular clouds and the inner ones at $\sim R_\odot$, they have much in common, such as a similar star formation efficiency (Santos et al. 2000) and kinetic temperature (Brand & Wouterloot 1996). The similarities are more noticeable if we compare molecular clouds at $R > R_\mathrm{t}$ (where R_t is the truncation radius) and $R < R_\mathrm{t}$ but close to R_t. This was done by Brand & Wouterloot (1991, 1994) and Wouterloot et al. (1993) with their sample for 16 kpc $< R <$ 20 kpc and the sample by Mead & Kutner (1988) for $R \sim 13$ kpc. More information about molecular clouds beyond the solar radius has been provided by Brand & Wouterloot (1995), Wouterloot & Brand (1996) and Wouterloot et al. (1995, 1997). The range of masses and sizes are very similar, and hence the densities should be similar. Cloud formation could be much more inefficient than at smaller R (Brand & Wouterloot 1991). There is indeed, a sharp decrease in H_2, but not that pronounced in HI gas, which might suggest that the formation of molecular clouds out of HI gas is not as efficient beyond some radius. Small unobservable clouds could have no star forming capacity. However, the sudden step of the rotation curve mentioned by van der Kruit (2000) remains unexplained.

A simplified but reasonable picture would then be: the amount of molecular hydrogen and the number of clouds decrease; but the density within a cloud remains more or less constant; therefore, if there is a minimum H_2 density for star formation it cannot explain the truncation of the stellar disk.

Then the puzzling question is: if there is star formation beyond R_t, where are the stars? There are two possible answers: a) star formation at these large radii is a recent or transient process, so that stars have not been continuously filling this region. Suppose, for instance, that the outer disk has been formed recently, because the disk forms slowly and its radius increases over time. This hypothesis is considered as a possibility by de Grijs et al. (2000) and van der Kruit (2000) and has some theoretical support from early works by Larson (1976) and Gunn (1982). Given our present uncertainties about disk formation, though, this hypothesis is rather speculative. b) stars, once born, then migrate away. This could be the case if stars and gas have different dynamical behaviours, being subject to different forces. Newly formed stars could be subject to other forces and migrate from their birth place.

B) Observational problems

There are two basic features in the surveys and analysis carried out until now which are improved in this work. First, previous observational studies have been made at optical wavelengths, and therefore extinction introduces a severe limitation on the interpretation of the results. Second, the analysis is usually based upon a specific galaxy model with various components of which the space distribution is specified by means of a number of free parameters, which are determined by fitting the observations. However, with this procedure, what is obtained is, in part, what is assumed. Mathematical expressions are still insufficient for many galaxy components.

This fact is specially problematic in the truncation region. It is known that the truncation is not completely sharp, but rather starts as a smooth deviation of the "exponential" disk (i.e. linear when using μ). A truncation curve $T(R)$ would quantify this smooth deviation and can be defined precisely as $T(R) = \mu(R) - \mu_\mathrm{D}(R)$ where $\mu(R)$ is the observed surface brightness in mag/arcsec^2 and $\mu_\mathrm{D}(R)$ is the exponential surface brightness extrapolated from the inner disk. We know $T(R_\mathrm{t}) = \infty$ in units of mag/arcsec^2, where R_t is the truncation radius. Previous analysis have mainly considered R_t. Truncations are an interesting object of study, as they could reveal the historical and dynamical properties of a galaxy. However the whole truncation curve, $T(R)$ also contains valuable information. It is therefore worrying that the mathematical expression of $T(R)$ was assumed rather than obtained as a chief objective.

To avoid the extinction deformation of the radial profiles, we have observed in the near infrared, so we are mostly dealing with the old stellar population. We present observations in J and Ks. Extinction in J is more severe than it is in Ks. Therefore, conclusions obtained from our measurements in Ks are more reliable.

Complementary studies in other colours has been addressed by the above cited texts. NIR CCD-like arrays already exist some years, but the recent improvement of two-dimension detectors and, in particular, that of CAIN, has made it possible to reach the truncation region.

To avoid model-dependent results, we have used a numerical inversion method. Binney & Tremaine (1987) describe another analytic method to carry out this deprojection, based on the Abell integral. In our procedure, however, only two assumptions are necessary: axisymmetry and negligible extinction. These two conditions are by no means guaranteed in a disk galaxy but it should be taken into account that axisymmetry is implicitly assumed in other procedures. Moreover, we have two sides in an edge-on galaxy, which are all very similar in our sample. Even if a non-axisymmetric disk could exhibit two similar sides when a galaxy is seen edge-on, this is rather improbable. Extinction is a problem when using methods based on previous modeling, as dust often has a ring structure rather than following an exponential law and the dust

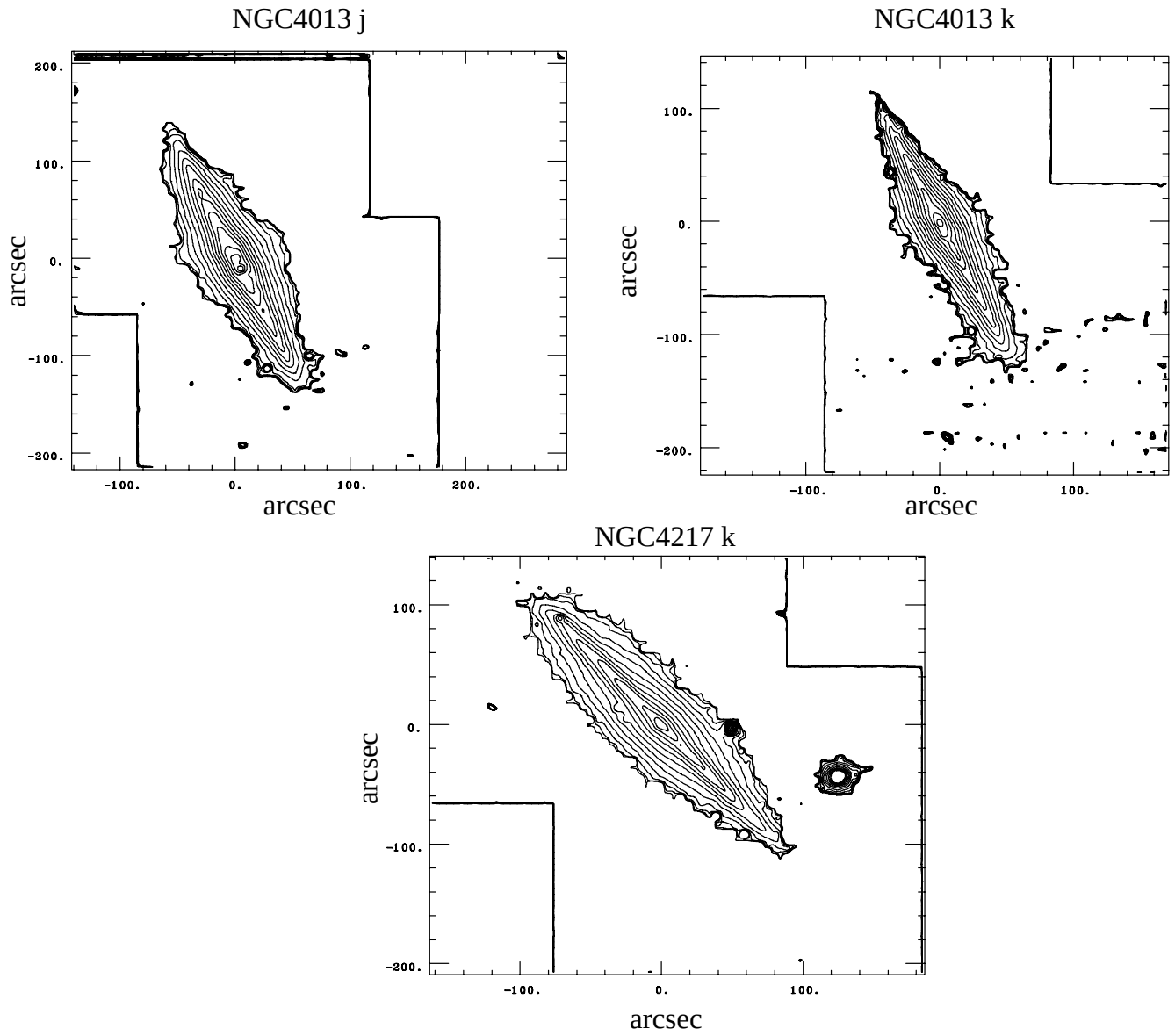

Fig. 1. Contour maps for the observed galaxies: The interval between isophotes is 0.5 magnitudes/arcsec^2 in all maps. The lower value is 15 magnitudes/arcsec^2 for NGC 5981, NGC 4013 in Ks, NGC 6504 in Ks and NGC 6504 in H; 15.5 mag/arcsec^2 for NGC 6504 in J and NGC 4217 in Ks and 16 for NGC 4013 in J. East is at bottom and North on right.

Table 1. Observational parameters for the galaxies.

Galaxy	Day	Passband	Exp. time object+sky(m)	Seeing	3σ level mag/arcsec^2
NGC 4013	17, 19	Ks	96	1.94	20.6
	13, 17	J	80	1.80	22.0
NGC 4217	16	Ks	96	1.27	20.4
	18	J	80	1.39	21.8
NGC 5981	20	Ks	64	1.45	19.9
NGC 6504	16	Ks	88	1.27	20.4
	15	J	64	2.96	21.5
	18	H	64	1.57	20.5

Table 2. Physical parameters for the observed galaxies obtained from LEDA database (`http://leda.univ-lyon1.fr`): RA and DEC are the right ascension and declination in 2000, PA is the position angle, d the distance and mabs the absolute B-magnitude.

Galaxy	RA (h m s)	Dec (o ′ ″)	Type	PA o	d (Mpc)	$m_{\rm abs}$
NGC 4013	11 58 31.5	43 56 51	Sb	66	11.16	−19.47
NGC 4217	12 15 50.8	47 05 30.8	Sb	50	13.64	−19.96
NGC 5981	15 37 53.5	59 23 28.7	Sbc	140	30.18	−20.34
NGC 6504	17 56 5.7	33 12 31.7	Sbc	94	63.18	−22.28

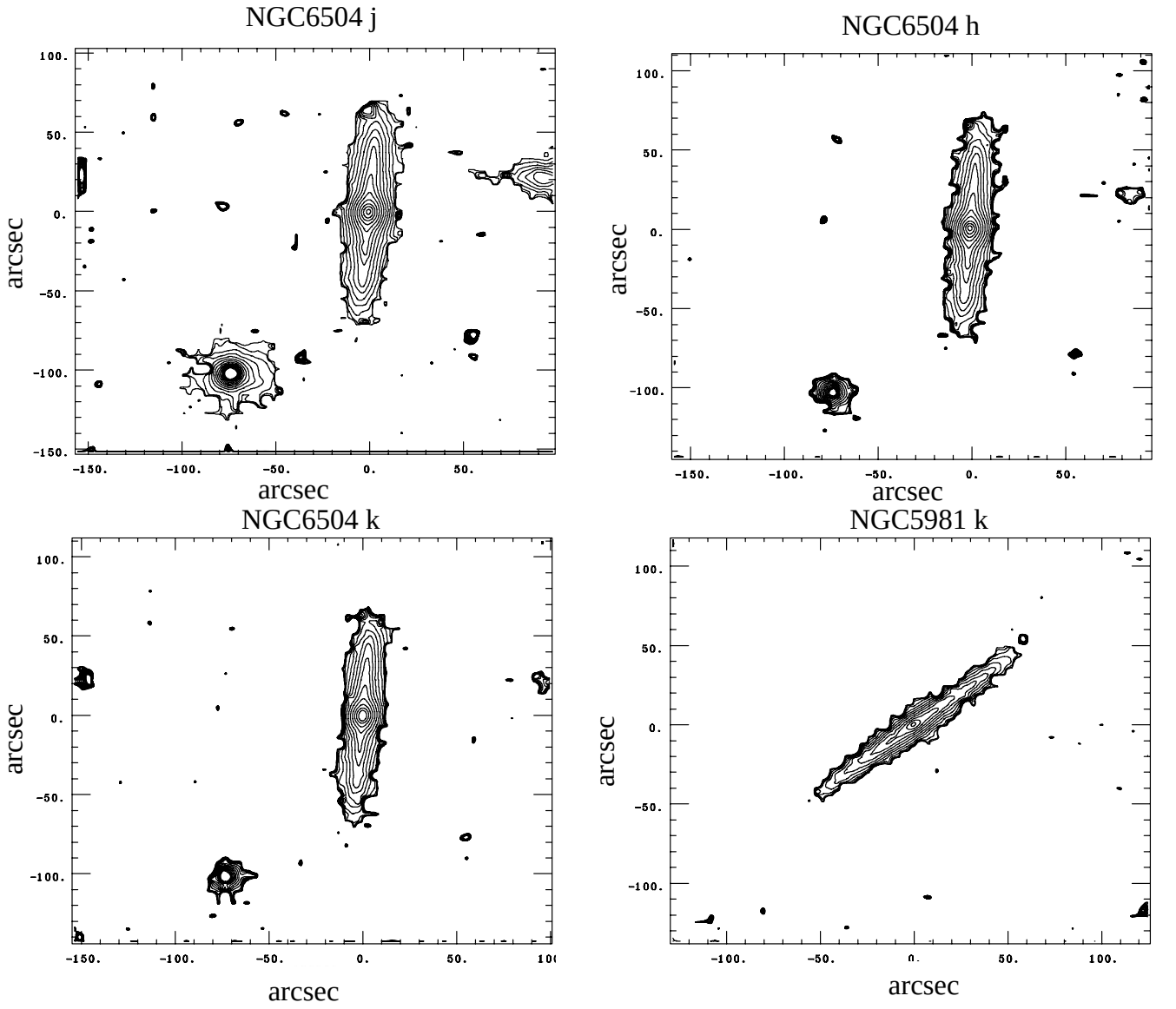

Fig. 1. continued.

distribution must be risky prescribed. Dealing with NIR observations and observing that our $\mu(z)$-profiles do not show a secondary minimum produced by a dust lane, inspires confidence in our method. Also, extinction is probably no longer important in the peripheral truncation region.

With this small number of assumptions required, we obtain a non-model-dependent deprojection.

2. Observations and reduction

The observations were carried out at the 1.5 m CST in the Teide Observatory, Tenerife, with the NIR camera CAIN. This is a common user 2D NIR image camera equipped with a 256^2 NICMOS detector array. Two different plate scales (0.4 and 1.0 arcsec/pixel) are selectable to obtain a narrow or wide field image. We used the wide field optics, which has an effective field of view of 4.3×4.3 arcmin. The objects were selected according to their projected size (D_{25}) to fit within that FOV. The detector control and read–out system was, at the time of the observations, based on dedicated transputer design electronics. In June 1999, the electronics was upgraded to a new design based on San Diego State University controller, adapted in house to the NIR, which provides better noise figures and stability. The transputer controller exhibits several noise correlated patterns which have to be removed during the reduction process by the use of specifically designed software routines.

The observed galaxies were the edge-on galaxies NGC 4013, NGC 4217, NGC 6504 and NGC 5981. They were observed in the period 13–19 April 1999, as shown in Table 1. The basic physical parameters of these galaxies are shown in Table 2.

In order to correct for the bright and rapidly varying NIR sky background, the telescope was alternatively pointed to six fields in the sky in the order

$O_1S_1S_2O_2O_1S_3S_4O_2$, where the S's are background and the O's contain the galaxy. The O_2 field was offset with respect to O_1, 15″ N and 15″ E. S_1 was 600″ W from O_1; S_2, 900″ W; S_3, 600″ E from O_2; S_4, 900″ W. Each exposure lasted about 2 min.

It was very important to perform good flat fielding, sky subtracting and mosaicing. We used the data reduction package developed by R. Peletier, REDUCE, within IRAF, which is specially suitable for data with a large sky background. We took object images, bias frames at the beginning and/or at the end of the night, dark frames for the two exposure times used (10 and 30 s) and flatfields to calibrate the sensitivity of the array. We took bright and dark flatfields for each filter with the same integration time; these were then combined and subtracted to remove the effects of dark current, telescope and dome.

The calibration was done by using the UKIRT Faint Standard Stars (Casali & Hawarden 1992) fs18, fs23, fs24, fs27 and fs28. We took 4 blocks of 15 images each, for every filter and for every star, at least three times per night, for different air masses. After calibration the isophote contour maps for the four observed galaxies (see Fig. 1) were obtained by means of IRAF Newcont.

3. The deprojection method

We divide the disk into rings with constant ΔR and assume a constant emissivity within a ring, i.e. a constant emission per unit volume in the direction of the observer l_i (see Fig. 2). From the edge-on surface brightness, I, we must deduce l_i, taking into account that many rings contribute to the integral I, being the contribution of each ring weighted by a different area. Once l_i is obtained we must integrate in the vertical direction to determine what would be seen if the galaxy were face-on. First, in the equation

$$I_k = 2\Sigma_i A_{ki} l_i \tag{1}$$

we must obtain l_i through an inverse method. The index k denotes the different pixels under observation for $z = 0$. The index i denotes the different rings in which the galactic plane is divided. A_{ki} are the areas shown in Fig. 2.

If $k > 0$

$$A_{ki} = \int_{(k-1/2)\Delta}^{(k+1/2)\Delta} \left((i+1/2)^2\Delta^2 - x^2\right)^{1/2} \mathrm{d}x - \underline{\int_{(k-1/2)\Delta}^{(k+1/2)\Delta} \left((i-1/2)^2\Delta^2 - x^2\right)^{1/2} \mathrm{d}x} \tag{2}$$

where x is an integration variable, Δ is the pixel size.

The second integral must not be calculated for $i = k$; this is the meaning of the symbol $\underline{\quad}$ placed below the integral. In all cases, we must have $i \geq k$.

If $k = 0$

$$A_{0i} = 2\int_0^{\Delta/2} \left((i+1/2)^2\Delta^2 - x^2\right)^{1/2} \mathrm{d}x - \underline{2\int_0^{\Delta/2} \left((i-1/2)^2\Delta^2 - x^2\right)^{1/2} \mathrm{d}x}. \tag{3}$$

The second integral must not be calculated for $i = 0$.

As an example,

$$\begin{aligned} A_{00} &= 2\int_0^{\Delta/2} \left(\tfrac{\Delta^2}{4} - x^2\right)^{1/2} \mathrm{d}x \\ &= \left[x\left(\tfrac{\Delta^2}{4} - x^2\right)^{1/2} + \tfrac{\Delta^2}{4}\sin^{-1}\tfrac{x}{\Delta/2}\right]_0^{\Delta/2} \\ &= \tfrac{\Delta^2}{4}\sin^{-1}\tfrac{\Delta/2}{\Delta/2} = \tfrac{\Delta^2}{4}\sin^{-1}1 = \tfrac{\Delta^2}{4}\tfrac{\pi}{2}. \end{aligned} \tag{4}$$

In fact, this is a semicircle of radius $\Delta/2$, with area $\frac{1}{2\pi}(\Delta/2)^2$.

In general, to calculate the above integrals we take into account that:

$$\int \left(a^2 - x^2\right)^{1/2} \mathrm{d}x = \frac{1}{2}\left[x\left(a^2 - x^2\right)^{1/2} + a^2\sin^{-1}\frac{x}{|\,a\,|}\right]. \tag{5}$$

We thus obtain

$$\begin{aligned} 2A_{ki} = \Delta^2 \Bigg(&\left(k+\tfrac{1}{2}\right)\left(\left(i+\tfrac{1}{2}\right)^2 - \left(k+\tfrac{1}{2}\right)^2\right)^{1/2} \\ &- \left(k-\tfrac{1}{2}\right)\left(\left(i+\tfrac{1}{2}\right)^2 - \left(k-\tfrac{1}{2}\right)^2\right)^{1/2} \\ &\underline{-\left(k+\tfrac{1}{2}\right)\left(\left(i-\tfrac{1}{2}\right)^2 - \left(k+\tfrac{1}{2}\right)^2\right)^{1/2}} \\ &\underline{+\left(k-\tfrac{1}{2}\right)\left(\left(i-\tfrac{1}{2}\right)^2 - \left(k-\tfrac{1}{2}\right)^2\right)^{1/2}} \\ &+ \left(i+\tfrac{1}{2}\right)^2\sin^{-1}\tfrac{k+1/2}{i+1/2} - \left(i+\tfrac{1}{2}\right)^2\sin^{-1}\tfrac{k-1/2}{i+1/2} \\ &\underline{-\left(i-\tfrac{1}{2}\right)^2\sin^{-1}\tfrac{k+1/2}{i-1/2} + \left(i-\tfrac{1}{2}\right)^2\sin^{-1}\tfrac{k-1/2}{i-1/2}}\Bigg). \end{aligned} \tag{6}$$

Once the areas A_{ki} are calculated we need only obtain the inverse matrix. But there is a much simpler procedure, beginning with the maximum k pixel ($k = N$) and going backwards until $k = 0$.

For $k = N$

$$I_N = 2A_{NN}l_N \tag{7}$$

$$l_N = I_N/2A_{NN}. \tag{8}$$

In general

$$l_k = \frac{I_k - 2\Sigma_{i=k+1}^{N} A_{ki}l_i}{2A_{kk}} \tag{9}$$

because to calculate l_k we already know all l_m for $m > k$.

If we repeat this procedure for each z we obtain a matrix l_{iz}. The deprojection simply implies the integration of l_{iz} over z, and hence the surface brightness if the galaxy were observed face-on, i.e. for the deprojected galaxy, I_i would simply be

$$I_i = \Sigma_z l_{iz}. \tag{10}$$

The determination of N, the last measurable point at which the galaxy signal and the sky background merge, is important. Several initial trials indicated that the deprojection was not affected by the choice of N, with the exception of the truncation region. Even in this case, the effect was only significant when the value of N was too large. We have adopted the 3σ-criterion.

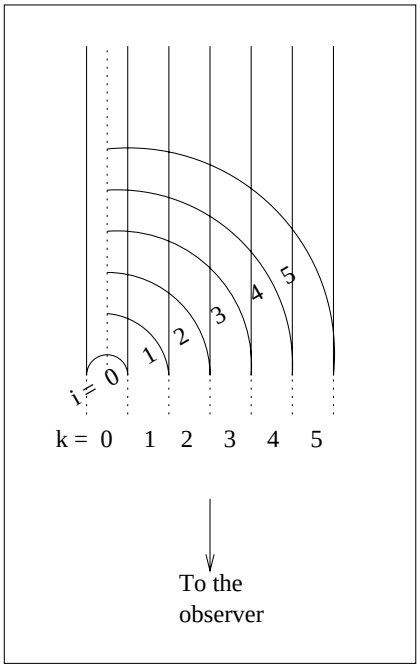

Fig. 2. Scheme for the inversion method. Subindex i denotes the disk rings. Subindex k denotes radial distances on the edge-on observed galaxies.

3.1. The errors introduced by the inversion method

Two sources of errors arise from the method itself, one of which is due to the choice of the last point considered as the transition between galaxy and background sky. As the value of the deprojected surface brightness of the more external points partly decides the values at a given position, the choice of the starting point is important. After some trials it was found that the standard 3σ-criterion was satisfactory and only unrealistic (much higher or lower) starting points produced a significantly different truncation curve.

Another source of errors arises from the formula involved, which implies a propagation of errors. The deprojected profile is slightly noisier than the observed one. Doubts could arise as to whether an error at a point, due for instance to a foreground star or just due to an error inherent in the instruments, could have a large influence at points far from the star. To evaluate the typical errors introduced by this effect, let us consider Eq. (9).

Suppose the individual errors in surface brightness, due to observation and instrumental errors, are $\Delta I_k \equiv \Delta I$, all approximately equal (around 2σ). With A being a typical value of A_{ik} we would have, approximately

$$\begin{aligned}\Delta^2 l_k &= \tfrac{1}{(2A)^2}\Delta^2 I_k + \left(\tfrac{2A}{2A}\right)^2 \textstyle\sum_{i=k+1}^{N} \Delta^2 l_i \\ &= \tfrac{1}{(2A)^2}\Delta^2 I_k + \left(\tfrac{1}{(2A)^2}\Delta^2 I_{k+1} + \ldots\right) \\ &= \tfrac{1}{(2A)^2}(N-k)\Delta^2 I.\end{aligned} \tag{11}$$

Therefore

$$\Delta l_k \sim \frac{\sqrt{N-k}}{2A}\Delta I. \tag{12}$$

Integrating in z, to obtain $I_{\mathrm{d},k}$ would therefore introduce an error of

$$\Delta I_{\mathrm{d},k} = \sqrt{\mathcal{N}_k}\frac{\sqrt{N-k}}{2A}\Delta I \tag{13}$$

where $\mathcal{N}_k$ is the number of layers in z, to be considered in this sum. Hence

$$\Delta\mu = (2.5\log e)\frac{\sqrt{\mathcal{N}_k}\sqrt{N-k}}{2A}\frac{\Delta I}{I} \approx \frac{\sqrt{\mathcal{N}_k}\sqrt{N-k}}{2A}\frac{\Delta I}{I}. \tag{14}$$

For a point in the inner part of the galaxy, let us take as typical values $\mathcal{N}_k \sim 20$; $N-k \sim 20$, $A \sim 1$, $I \sim 300\sigma$, $\Delta I \sim \sigma$. Then, $\Delta\mu$ is obtained to be of the order of 0.03 magnitudes.

For a point in the truncation region, $\mathcal{N}_k \sim 4$; $N-k \sim 4$, $A \sim 5$, $I \sim 10\sigma$, $\Delta I \sim \sigma$. Then, $\Delta\mu \sim 0.04$ mag.

For the last adopted point, $\mathcal{N}_k \sim 1$; $N-k \sim 1$, $A \sim 10$, $I \sim 3\sigma$, $\Delta I \sim \sigma$, we again obtain 0.03 mag.

We conclude that errors due to the method are of the order of 0.03 mag and that this error is constant throughout the disk. At the rim, the large relative errors in brightness are compensated by a larger typical area, A, as well as by the small numbers of z-layers available. Errors in the method itself are therefore less than 0.1 mag.

4. Results

In order to apply this inversion method, we first rotated all galaxies. The observed (projected) radial profiles were obtained for the interval $z = 0 \pm \Delta z$, where Δz was small ($\approx$10–30 arcsec), and different for each galaxy. We used data only up to the radius where the surface brightness was equal to 3σ. Particular care was taken when relatively bright stars were at the rim of the galaxy.

We then applied the model for each colour, each side and each galaxy. The quantity l_{iz} was obtained, and then the intensity I_i. Results are shown in Fig. 3.

The bulge, the quasi-exponential disk and in some cases the ring, are clearly visible. What is remarkable is the truncation, which is readily observed. The truncation of all galaxies is defined in such detail that the truncation region can be studied with unprecedented precision.

Note that a large portion of the curves in Fig. 3 corresponds to points below or far below the 3σ-level given in Table 1. The 3σ criterion was applied to the "observed" points, but the profiles in Fig. 3 show "calculated" points. Due to the deprojection method we are deducing values of the deprojected surface brightness that would be unobservable if the galaxy were face-on, and which are therefore below the observational 3σ-level. This fact implies that the truncation phenomenon is undetectable in face-on galaxies, at least with the noise level of our observations. Also note that the 3σ level is within the R-range used to fit the exponential disks. But again we must take into

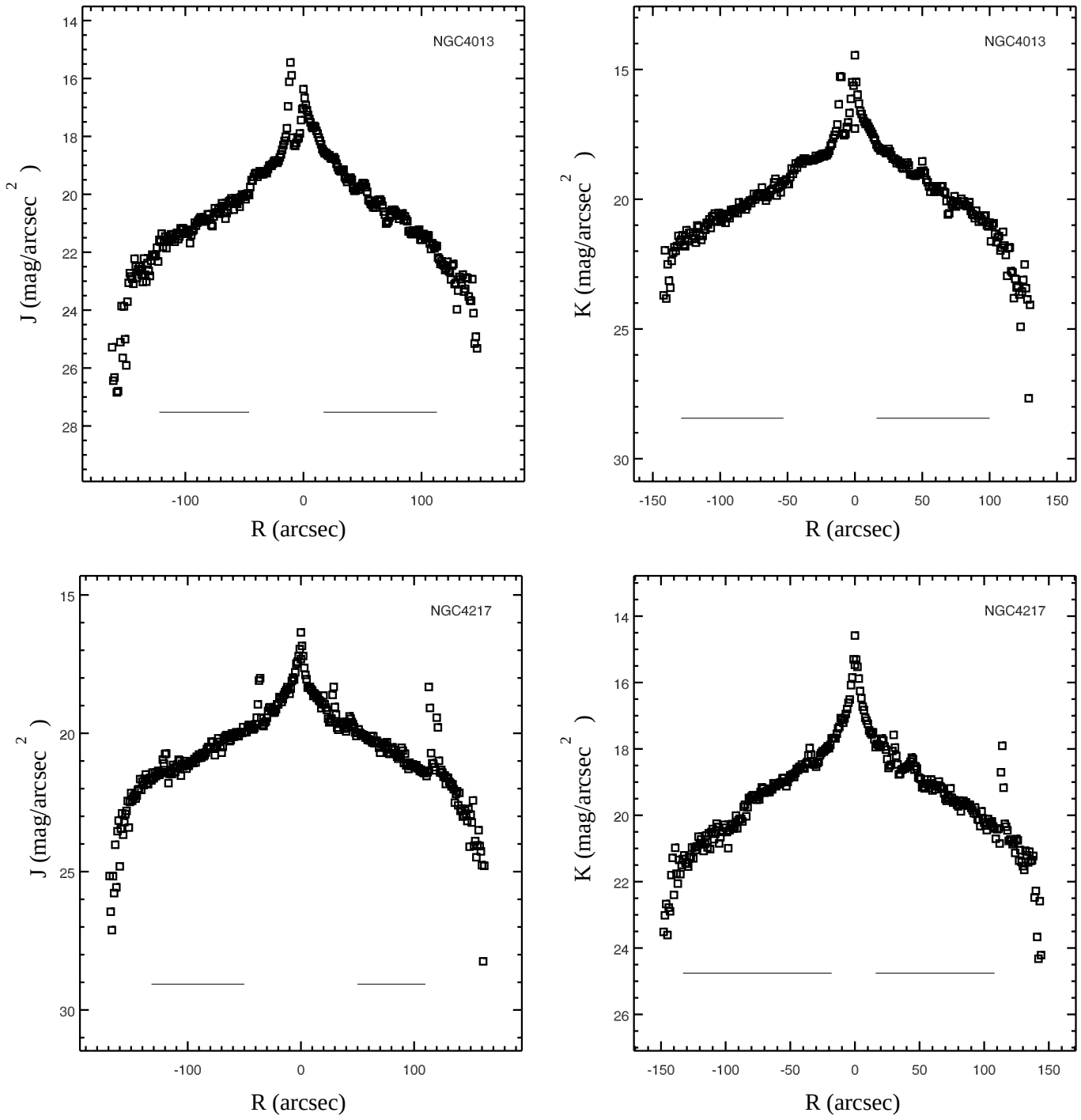

Fig. 3. Profiles obtained with the inversion method. Negative values in R axis denote eastern side of the galaxies. Horizontal bars indicate the region in which the radial scale length was calculated.

account the difference between observed and deprojected points. Observed surface brightness should be obtained as an integration of deprojected surface brightness, and are therefore much higher.

4.1. The truncation curve

First, we obtained the radial scale length by excluding points belonging either to the bulge or to the truncation region, or even some parts of the galaxy where the radial variation was not a clear exponential function (see the horizontal lines in Fig. 3). Assuming a law of the type $I = I_0 \mathrm{e}^{-R/R_\mathrm{d}}$ we obtained

$$\mu = \mu_0 + \frac{1.086}{R_\mathrm{d}} R \tag{15}$$

where μ and μ_0 are magnitudes per squared arc-second, $\mu_0 = \mu(R = 0)$, R is the galactocentric radius and R_d the

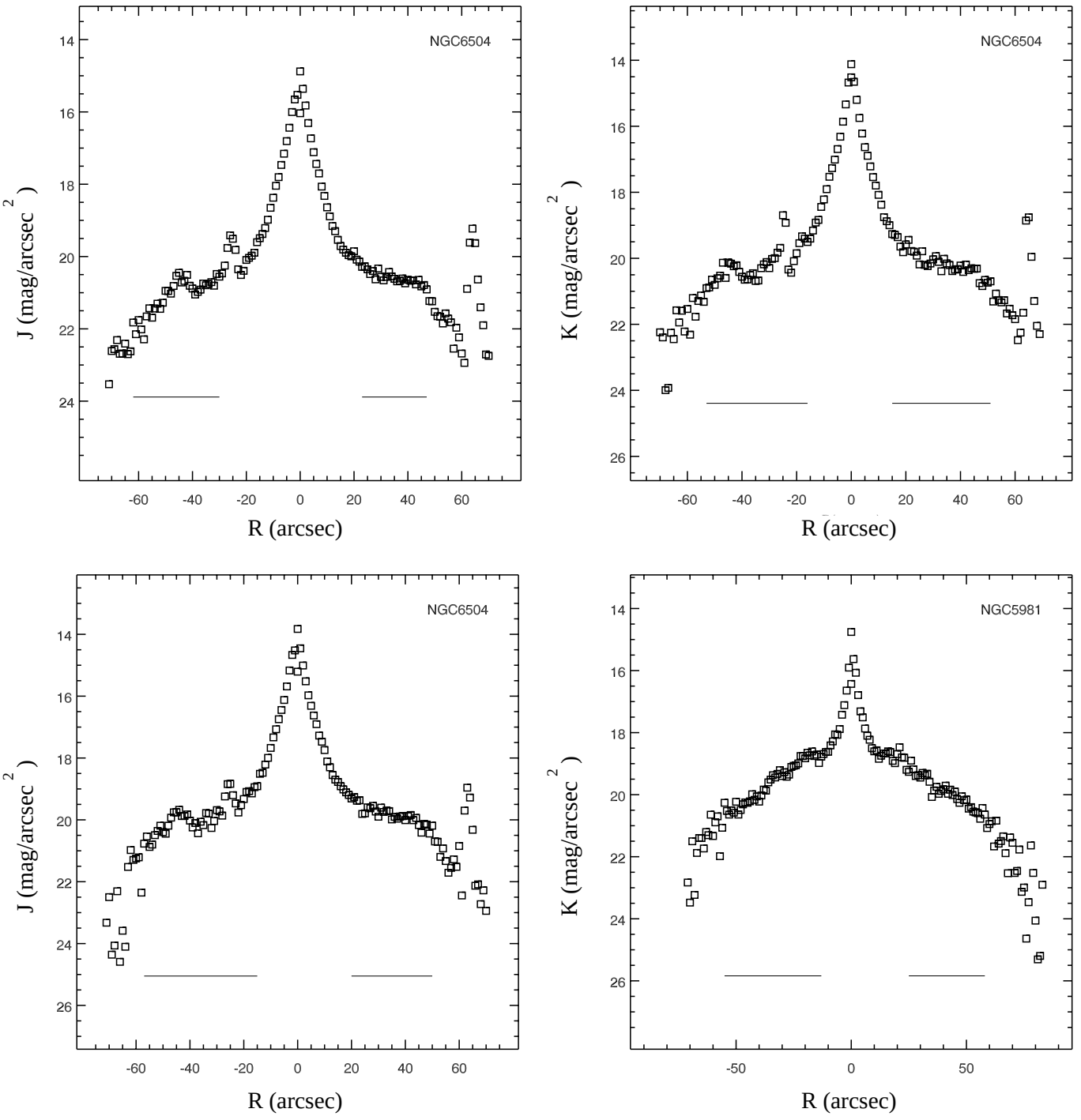

Fig. 3. continued.

radial scale length. Results are summarized in Table 3. Our results can be compared with those obtained by van der Kruit & Searle (1982) for those galaxies present in both their and our sample. They found $R_{\rm d} = 49.45''$ versus our value of $48.38''$ in J and $37.83''$ in Ks for NGC 4217. In the case of NGC 4013 they obtained $40.34''$ whereas our data give $40.06''$ in J and $33.52''$ in Ks. A change in scalelength between the visual and NIR means that the colour of the galaxy changes with R, either because of a true variation of the stellar population or to a variation due to extinction.

In the definition of the truncation curve

$$T(R) = \mu(R) - \mu_{\rm D}(R) \tag{16}$$

$\mu_{\rm D}(R)$ is equal to $\mu_0 + (1.086/R_{\rm d})R$, i.e. the function $\mu(R)$ if it were a pure exponential. Plots of $T(R)$, the truncation curve, are the main objectives of this research, and are given in Fig. 4. Clearly, points of $T(R)$ in the bulge region are meaningless.

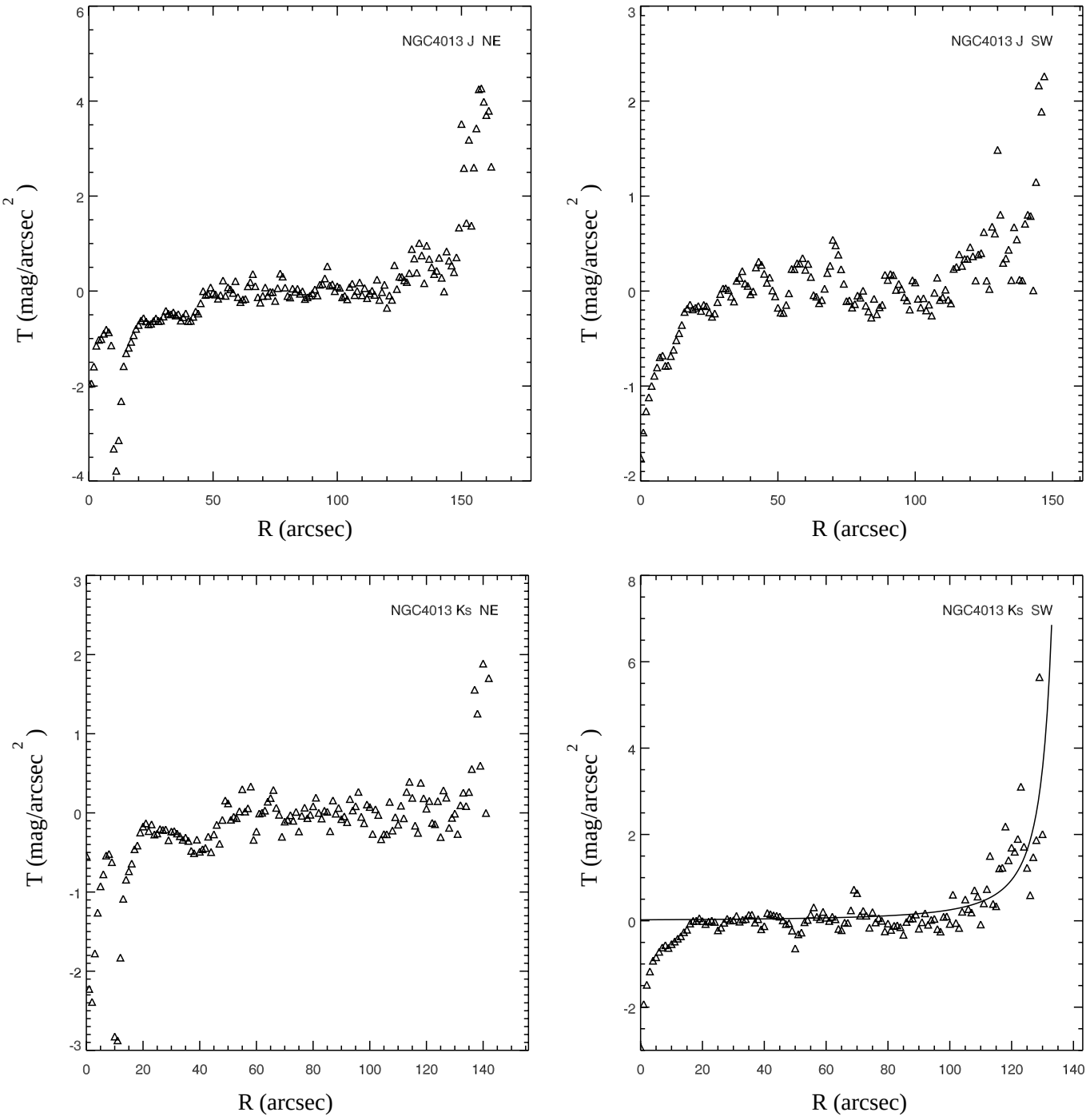

Fig. 4. Truncation curves. In the case NGC 4013, SW side, Ks filter, the fitted profile has been included, as an example.

In order to fit these curves, we have considered the three-parameter function

$$T = \frac{a}{(R_{\rm t} - R)^n} \tag{17}$$

where a and n are fitting parameters, as well as $R_{\rm t}$, the truncation radius, because for $R = R_{\rm t}$ we obtain $T = \infty$, so there is a complete truncation for $R = R_{\rm t}$. This function has been selected because T can be very small for the large inner range where $R \ll R_{\rm t}$, but becomes larger for R close to $R_{\rm t}$. Clearly this function cannot be applied for $R > R_{\rm t}$.

The fit is outlined in Table 4. In the particular case of the NW side of NGC 6504, a bright field star is located in the truncation region. We have made different calculations with and without the star, starting before or beyond it, but the results did not differ significantly. Nevertheless, our plot for the NW side of NGC 6504 should be interpreted with extreme caution.

Values of a have a large scatter. This parameter is related to the brightness close to the cutoff radius, compared with the 3σ level. More attention should be paid to the value of the parameter n, as it is an exponent, therefore

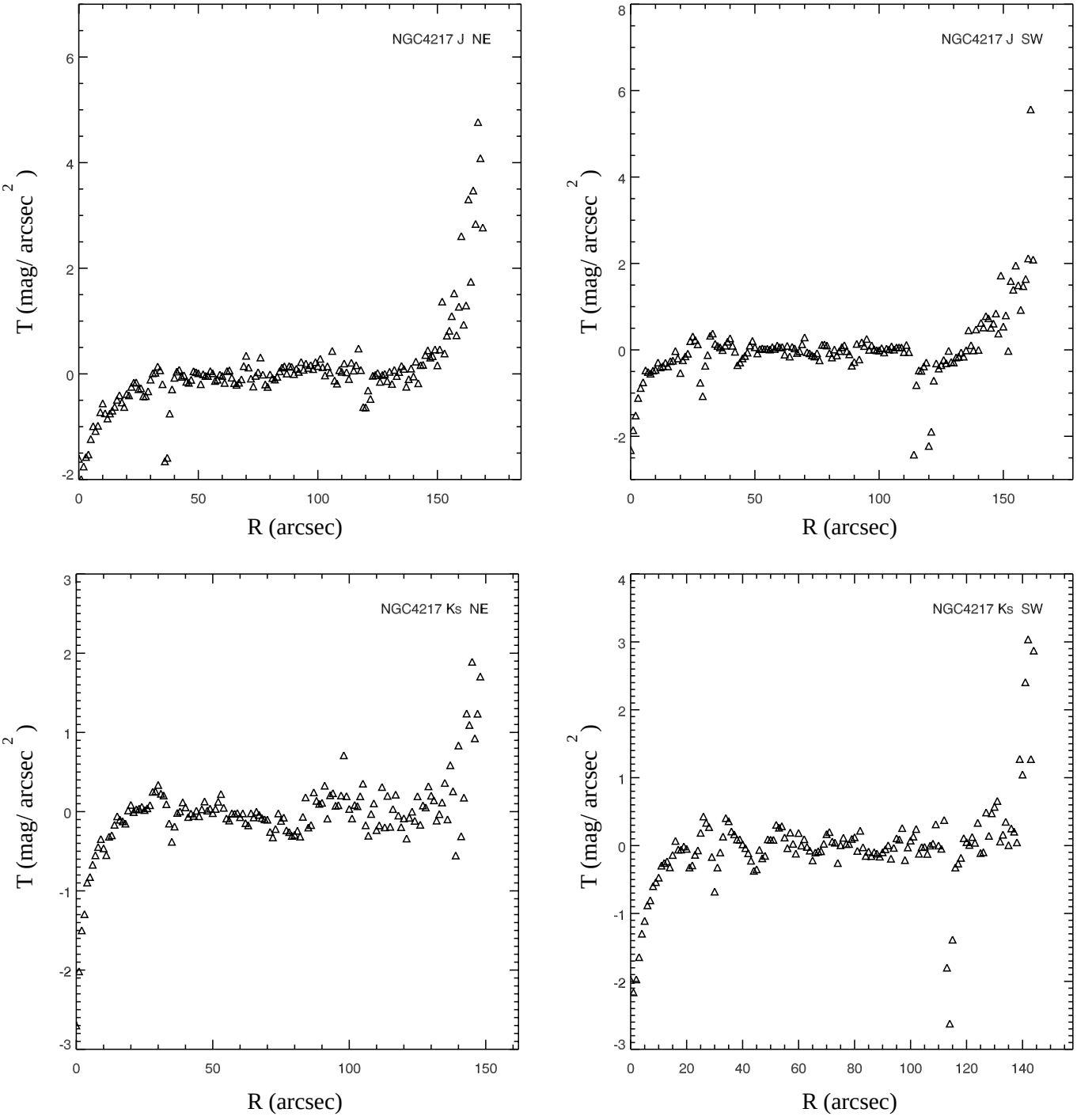

Fig. 4. continued.

characterizing the function by which the stellar population abruptly ceases. We obtain a mean value of 1.24 $\sim$ 5/4, including all filters, sides and galaxies. The mean value for the Ks filter is probably more representative as it is more free from extinction distortions and more accurately accounts for the stellar population. But in this case the result is remarkably similar: 1.25 with a rms of about 0.4. The closer integer (unity) fully lies in the range of acceptable values.

The average truncation radii show a large dispersion for the different galaxies. For the average Ks values we obtain: NGC 4013, $R_{\rm t}$ = 7.76 kpc; NGC 4217, $R_{\rm t}$ = 10.02 kpc; NGC 6504, $R_{\rm t}$ = 22.97 kpc; NGC 5981, $R_{\rm t}$ = 12.42 kpc. Probably the truncation would be sharper when observed with a better seeing. However no relation was found between derived truncation parameters and seeing, and therefore this effect does not significantly modify our results.

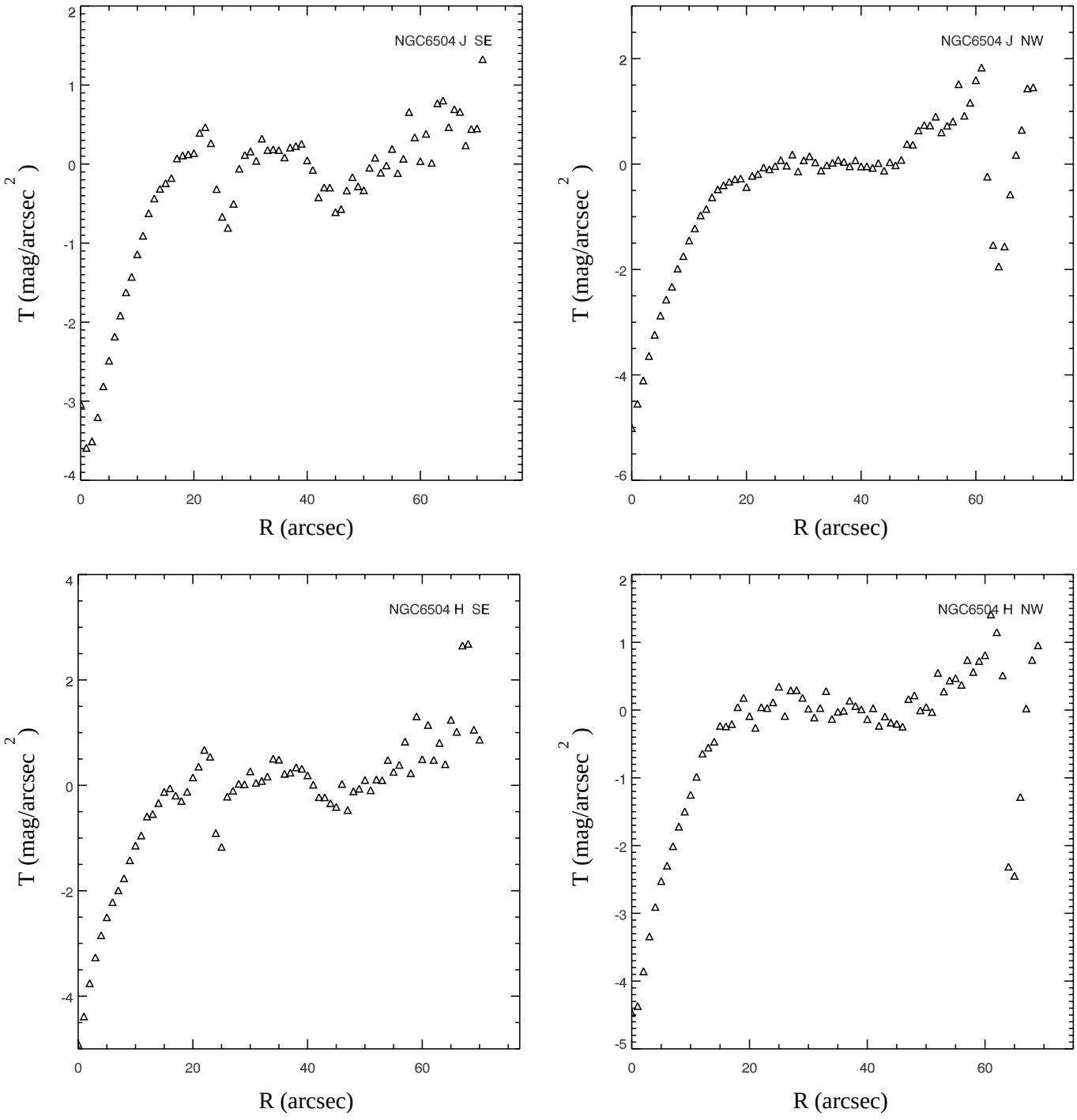

Fig. 4. continued.

5. Discussion

A great deal of attention has been paid previously to the coefficient R_t/R_d. In the early work by van der Kruit & Searle (1982) it was estimated to be about 4.2 ± 0.5. De Grijs et al. (2000) also give values (4.3 ± 0.3, 3.8 ± 0.5, 4.5 ± 0.4 and 2.4 ± 0.3) for the four galaxies in their sample. Pohlen et al. (2000a,b) found much lower values, around 2.9 ± 0.7 and Barteldrees & Dettmar (1994) give a mean value of 3.7 ± 1.0. In this work, where extinction and inclination effects have almost been eliminated, we also deduce lower values than van der Kruit & Searle (1982), with 3.2 being the mean value for all the profiles considered. If we limit ourselves to the values for the longest wavelength, i.e. Ks, we obtain for the four galaxies: NGC 4013, 4.31; NGC 4217, 4.03; NGC 6504, 2.27; NGC 5981, 3.62 (mean value of the two sides of the galaxy). The mean value for Ks is 3.6 ± 0.8. Given the high σ, our value is compatible with all previous results. Clearly, a 4-galaxy sample is too small, and more information including more types

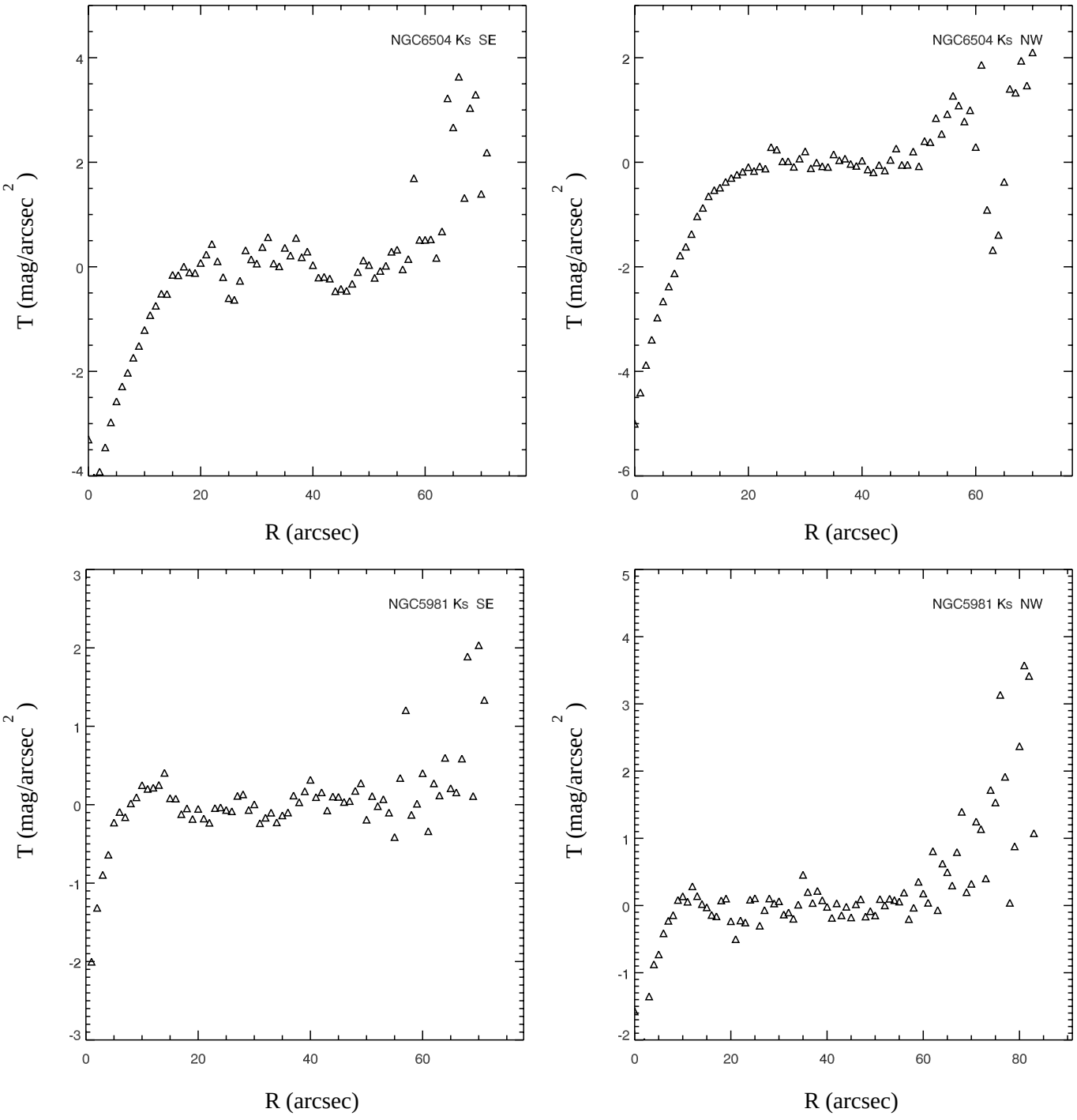

Fig. 4. continued.

of galaxies is necessary. But the data for our galaxies fit very well in Fig. 2 in Pohlen et al. (2000). So, we agree with their statement that *large disks with regard to their scalelengths* $R_{\rm d}$ *are short in terms of their cut-off radii.*

Because the extinction was assumed to be negligible in our NIR data, we cannot draw any conclusions about it. But, we consider that the Ks data give the most reliable results.

In general, extinction would produce an apparent higher value of the radial scale length, while $R_{\rm t}$ would be less affected as truncation takes place in regions where extinction is less important. Therefore it is believed that the optical values for $R_{\rm t}/R_{\rm d}$ are underestimated.

The difference would not be excessive, as we obtain lower but comparable values for the two galaxies we have in common with van der Kruit and Searle. The slope of the points in Fig. 5 gives the $R_{\rm t}/R_{\rm d}$ ratio. In Fig. 6 we observe a sharp correlation between $R_{\rm t}$ and the absolute magnitude of the galaxies. The brighter the galaxy, the larger the disk is found to be. This is not unexpected, but

Table 3. Adjusted parameters for the disk.

Galaxy	Passband	Side	R_d (arcsec)	R_d (kpc)	μ_o (mag/arcsec^2)
NGC 4013	J	NE	48	2.58	18.98
		SW	32	1.75	18.12
	Ks	NE	37	1.99	17.82
		SW	30	1.63	17.38
NGC 4217	J	NE	53	3.51	18.93
		SW	44	2.89	18.67
	Ks	NE	35	2.35	17.28
		SW	40	2.65	17.44
NGC 5981	Ks	SE	21	3.10	17.86
		NW	24	3.45	18.01
NGC 6504	J	SE	25	7.54	19.07
		NW	54	16.39	19.89
	Ks	SE	29	8.99	18.51
		NW	38	11.57	18.83
	H	SE	32	9.91	19.02
		NW	32	9.75	18.99

Table 4. Fit parameters for the truncation curve.

Galaxy	Passband	Side	R_t (arcsec)	R_t (kpc)	a	n	R_t/R_d
NGC 4013	J	NE	160	8.65	2.43	1.10	3.34
		SW	155	8.38	3.56	0.77	4.79
	Ks	NE	147	7.95	5.64	1.04	3.98
		SW	140	7.57	281.46	1.90	4.64
NGC 4217	J	NE	170	11.24	11.59	1.15	3.20
		SW	165	10.91	12.30	1.12	3.78
	Ks	NE	155	10.25	7.10	1.00	4.36
		SW	148	9.79	1.07	0.59	3.69
NGC 5981	Ks	SE	73	10.68	1.27	0.68	3.44
		NW	90	13.17	55.70	1.62	3.81
NGC 6504	J	SE	75	22.97	1.15	0.55	3.05
		NW	70	21.44	665	2.57	1.29
	Ks	SE	75	22.97	28.79	1.48	2.56
		NW	75	22.97	68.72	1.73	1.98
	H	SE	75	22.97	10.48	1.14	2.32
		NW	70	21.44	16.94	1.43	2.20

the correlation seems to be tight. Figure 7 shows that n is not clearly dependent on a typical parameter of a spiral, such as R_d.

We find some colour dependence in the truncation radii. This is quite clear for NGC 4217 (151″ in Ks, 167″ in J; this tendency is confirmed by its value in the optical given by van der Kruit & Searle (1982) of 202″). It is also clear for NGC 4013 (143″ in Ks, 157″ in J; this tendency is confirmed by its value in the optical of 165″ given by van der Kruit & Searle). However, NGC 6504 does not show this colour dependence, R_t being nearly independent of wavelength. We have only one filter for NGC 5981. We suggest that R_t could be lower for the older population, but this conclusion is not at all firm. This fact could indicate that the stellar disk has grown, but the observational evidence is scarce to ascertain any interpretation of this colour dependence.

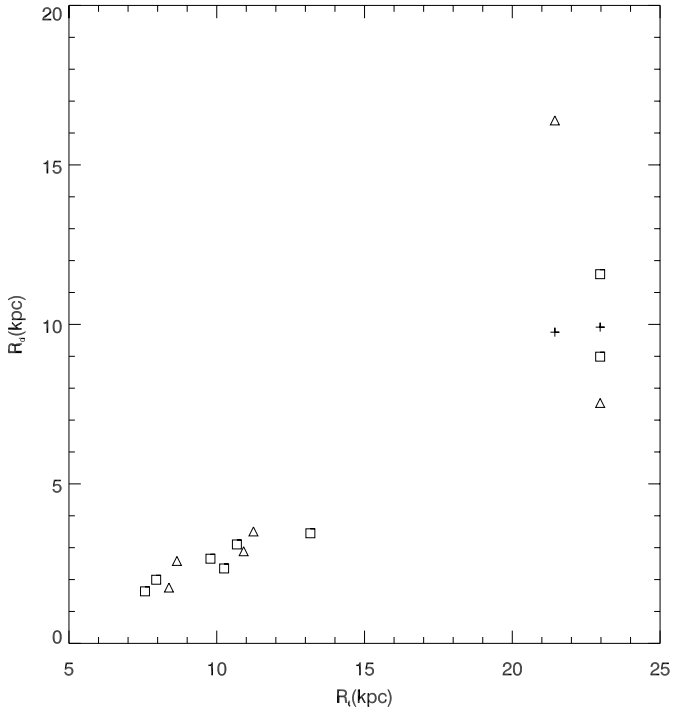

Fig. 5. R_d versus R_t. Squares, Ks filter; triangles, J-filter and crosses, H-filter.

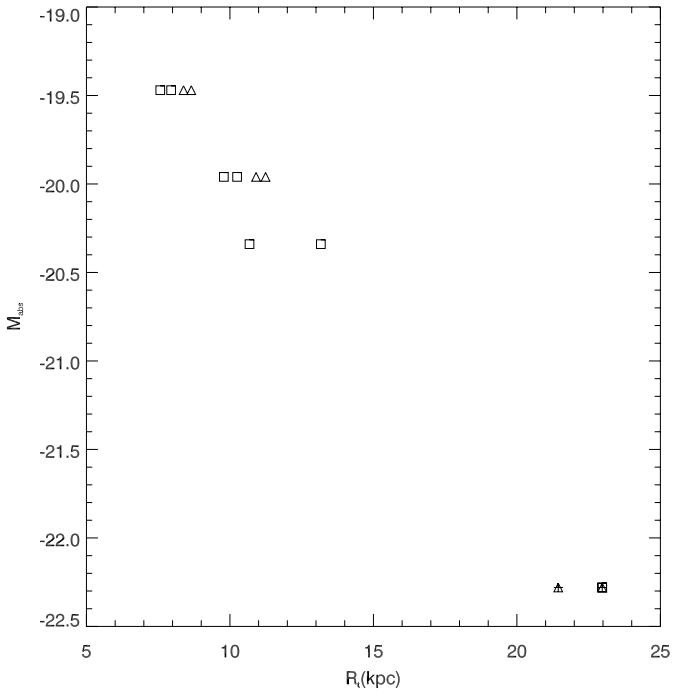

Fig. 6. Absolute M-magnitude versus R_t. Symbols as in Fig. 5.

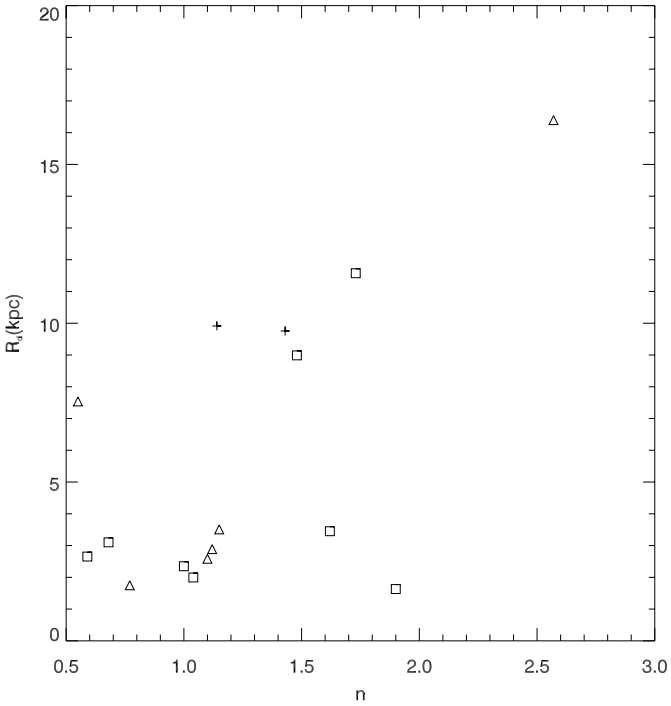

Fig. 7. $R_{\rm d}$ versus n. Symbols as in Fig. 5.

The coefficient n has no clear relation with other basic parameters of the galaxies. In particular no relation with colour was found. We have obtained 1.25, with the simplest possible value (unity) compatible within the error range. The simplest truncation curve compatible with our data would therefore be

$$T \propto \frac{1}{R_{\rm t} - R}. \tag{18}$$

This is an important result. As the truncation is not sharp (e.g. de Grijs et al. 2000) the shape of the truncation curve should be investigated by theoretical methods, and compared with Eq. (18). The theoretical prediction of this truncation curve would be more restrictive than that of any other observable parameters.

Asymmetries have been observed but these are not large. The parameter

$$2\frac{|(R_{\rm t}({\rm E}) - R_{\rm t}({\rm W}))|}{R_{\rm t}({\rm E}) + R_{\rm t}({\rm W})} \tag{19}$$

(where E and W denote the two sides of the galaxies) characterizing the relative degree of asymmetry was only 0.05, 0.05, 0.00 and 0.21, for NGC 4013, NGC 4217, NGC 6504 and NGC 5981 respectively, if we only take into account the more confident values of Ks.

A potentially very restrictive fact suggested by van der Kruit (2000), that the rotation curve has a decreasing step just after the truncation, can neither be rejected nor confirmed as the rotation curve of NGC 4013 (Verheijen 1997) shows this step 4 kpc after $R_{\rm t}$, but it is apparently not present for NGC 4217 (see also Verheijen 1997).

6. Conclusions

The stellar disk is less extended than the gaseous disk and this is not the result of sensitivity limits of optical telescopes: there is a physical mechanism that produces a relatively sharp truncation. To investigate this mechanism, the advantages of observing in the near infrared are obvious as we are looking for a phenomenon concerning the stars, and because the results are not as affected by extinction problems, whose radial distribution is not "a priori" known. The advantages of an inversion method not prescribing ad-hoc mathematical models for the different galactic components have been shown. In particular, the use of a model with several free parameters for the truncation region prevents us from obtaining the function we seek, i.e. the detailed way in which the stellar component leaves the exponential distribution and becomes completely truncated at $R_{\rm t}$.

To investigate the mechanism responsible for the truncation of the stellar disk, more observational effort is needed, especially in the near infrared. Also, more theoretical work is needed as many of the hypotheses advanced up to now fail to explain firm constraints that have been established by observations.

The possible relation between $R_{\rm t}$ and warps, which was considered by van der Kruit (2000) is not clear: for NGC 4013 and NGC 6504, we can see in Florido et al. (1991) that the warps begin at a radius that is much smaller than $R_{\rm t}$.

Two important conclusions can be extracted from this work:

- The coefficient $R_{\rm t}/R_{\rm d}$ has been found to be lower than in some previous works, being for Ks 3.6 ± 0.8, at least for the four galaxies observed;
- We suggest that a colour dependence of the truncation radius exists: truncation seems to take place at lower radii for larger wavelengths, but this was only for 2/3 of the small sample. More observations are needed.

We present plots of the truncation curve $T(R)$, which is one of the main objectives of this work. These plots are more informative than the truncation radius itself. Nevertheless, we have tried to fit these $T(R)$ curves. A reasonable candidate formula is of the type $T(R) \propto (R_{\rm t} - R)^{-n}$, where the exponent n has been found to be 1.25 ± 0.4. This suggest $n = 5/4$, with unity being a value within the errors. A simple suggestion is therefore

$$T(R) \propto 1/(R_{\rm t} - R). \tag{20}$$

Acknowledgements. We are thankful to Dr. Peletier for providing his very efficient reduction software REDUCE and for many helpful discussions during the period of this work.

The CST is operated on the island of Tenerife by the Instituto de Astrofísica de Canarias in the Spanish Observatorio del Teide of the Instituto de Astrofísica de Canarias.

This paper has been supported by the "Plan Andaluz de Investigacion" (FQM-108) and by the "Secretaría de Estado de Política Científica y Tecnológica" (AYA2000-1574).

References

Barteldrees, A., & Dettmar, R. J. 1994, A&AS, 103, 475

Binney, J., & Tremaine, S. 1987, Galactic Dynamics (Princeton University Press)

Brand, J., & Wouterloot, J. G. A. 1991, in The interstellar disk-halo connection in Galaxies, ed. H. Bloemen, 121

Brand, J., & Wouterloot, J. G. A. 1994, A&AS, 103, 503

Brand, J., & Wouterloot, J. G. A. 1995, A&A, 303, 851

Brand, J., & Wouterloot, J. G. A. 1996, in Unsolved problems of the Milky Way, ed. L. Blitz & P. Teuben, 561

Casali, M. M., & Hawarden, T. G. 1992, JCMT-UKIRT Newslett., 3, 33

Ferguson, A. M., Gallagher, J. S., & Wyse, R. F. G. 1998, AJ, 116, 673

Florido, E., Prieto, M., Battaner, E., Mediavilla, E., & Sanchez-Saavedra, M. L. 1991, A&A, 242, 301

Freudenreich, H. T. 1998, ApJ, 492, 495

de Grijs, R., Kregel, M., & Wesson, K. H. 2001 [astro-ph/0002523]

Gunn, J. E. 1982, in Astrophysical Cosmology, Vatican City State, 233

Habing, H. J. 1988, A&A, 200, 40

Kennicutt, R. C. 1989, ApJ, 344, 685

Kobayashi, N., & Tokunaga, A. T. 2000, ApJ, 532, 423

van der Kruit, P. C. 1979, A&AS, 38, 15

van der Kruit, P. C. 2001, in Galaxy Disks and Disk Galaxies, ed. J. G. Funes, & E. M. Corsini, ASP Conf. Ser.

van der Kruit, P. C., & Searle, L. 1981a, A&A, 95, 105

van der Kruit, P. C., & Searle, L. 1981b, A&A, 95, 116

van der Kruit, P. C., & Searle, L. 1982, A&A, 110, 61

Larson, R. B. 1976, MNRAS, 176, 31

Lequeux, J., & Guélin, M. 1996, in New Extragalactic Perspectives, The New South Africa, ed. D. Block

May, J., Alvarez, H., & Bronfman, L. 1997, A&A, 327, 325

Mead, K. N., & Kutner, M. L. 1988, ApJ, 330, 399

Mead, K. N., Kutner, M. L., & Evans, N. J. 1990, ApJ, 354, 492

Mead, K. N., Kutner, M. L., Evans, N. J., Harvey, P. M., & Wilking, B. A. 1987, ApJ, 312, 321

Pohlen, M., Dettmar, R. J., & Lütticke, R. 2000, A&A, 357, L1

Pohlen, M., Dettmar, R. J., Lütticke, R., & Schwarzkopf, U. 2000, A&AS, 144, 405

Porcel, C., Battaner, E., & Jiménez-Vicente, J. 1997, A&A, 322, 103

Robin, A. C., Crézé, M., & Mohan, V. 1992, ApJ, 400, L25

Rudolph, A. L., Brand, J., de Geus, E. J., & Wouterloot, J. G. A. 1996, ApJ, 458, 653

Ruphy, S., Robin, A. C., Epchtein, N., et al. 1996, A&A, 313, L21

Santos, C. A., Yun, J. L., Clemens, D. P., & Agostinho, R. J. 2000, ApJ, 540, L87

Verheijen, M. A. W. 1997, Ph.D. Thesis, Kapteyn Institute

Williams, J. P., & McKee, C. F. 1997, ApJ, 476, 166

Wouterloot, J. G. A., & Brand, J. 1996, A&AS, 119, 439

Wouterloot, J. G. A., Brand, J., & Henkel, C. 1988, A&A, 191, 323

Wouterloot, J. G. A., Fiegle, K., Brand, J., & Winnewisser, G. 1995, A&A, 301, 236

Wouterloot, J. G. A., Fiegle, K., Brand, J., & Winnewisser, G. 1997, A&A, 319, 360

A&A 455, 467–473 (2006)
DOI: 10.1051/0004-6361:20053310

Astronomy & Astrophysics

Truncated stellar disks in the near infrared

I. Observations⋆

E. Florido[1], E. Battaner[1], A. Guijarro[1,2], F. Garzón[3,4], and A. Castillo-Morales[1]

[1] Departamento de Física Teórica y del Cosmos, Universidad de Granada, Spain
e-mail: estrella@ugr.es
[2] Centro Astronómico Hispano Alemán, Almería, Spain
[3] Instituto de Astrofísica de Canarias, 38200 La Laguna, Spain
[4] Departamento de Astrofísica, Universidad de La Laguna, Tenerife, Spain

Received 26 April 2005 / Accepted 10 May 2006

ABSTRACT

We present NIR surface photometry of 11 edge-on galaxies obtained in the course of a long term project aimed at analysing the occurrence and type of the truncation of the outer disks. Observations were carried out at the 1.5 m CST (Carlos Sánchez Telescope) in Tenerife (Spain) using the CAIN infrared camera. 7 galaxies exhibit clear truncation on their disk profiles and 4 galaxies were observed to be clearly untruncated within observational limits. We describe the truncations as real, smooth and complete (as suggested by extrapolation and in the sense that the measured truncation curve goes into the noise at a truncation radius $R_{\rm tr}$), following a decline proportional to $(R_{\rm tr} - R)^{-n}$ (where R is the radius). Despite its deep photometric reach, the data presented do not permit a detailed exploration of the region where optical data show a second slope. Special care was taken concerning the surface brightness deprojection of edge-on galaxies, which was carried out by two methods, one comprising the inversion of Abel's integral equation and the other following a numerical method. These methods gave nearly identical results. NIR observations of truncations could differ from observations in the optical, since the two domains trace different stellar populations.

Key words. galaxies: structure – galaxies: spiral

1. Introduction

It is widely accepted that the galactic disk brightness profiles, at least in the inner regions where the contribution of the bulge to the observed emission is still low, can be reproduced with an exponential function. At large radii, it is found that the stellar distribution often departs from this simple description and decreases much faster. One of the goals of this paper is to contribute to determining the functional form of such a rapid decline.

This decline of the stellar density was discovered by van der Kruit (1979), who denoted it as truncation. In this and subsequent papers (van der Kruit & Searle 1981a,b) the basic properties of truncations were described as well as the first theoretical ideas to explain them. Some recent studies have found that there is no complete truncation, but rather a sharp change in the exponential constant, called a "break" (Pohlen et al. 2002a; Pohlen et al. 2004, and references therein).

Let us define the truncation curve as

$$\tau(R) = \mu(R) - \mu_{\rm D}(R) \quad (1)$$

as in Florido et al. (2001) (hereafter F01). Here, R is the radius, μ the actual surface brightness (in mag arcsec^{-2}), and $\mu_{\rm D}$ the same quantity obtained by the extrapolation of $\mu(R)$ in the inner disk, where the exponential decline can be followed unambiguously.

What is $\tau(R)$? Does it depend on the observed wavelength? These questions, of fundamental importance to understanding this phenomenon, motivated the present paper and are only partially answered. Nevertheless, the observations reported here will contribute to achieving a final description, which is difficult to assess because truncations (or "breaks") take place at a very low brightness in regions with a very low S/N ratio. The different theoretical models currently proposed are still far from obtain the functional form of $\tau(R)$, but they should be able to do so eventually. Excellent reviews of the question have already been made, such as those by van der Kruit (2001) and Pohlen et al. (2004).

We opted to observe at NIR wavelengths, for the following reasons: firstly, the old stellar population, which makes up the great majority in the galactic disk of spiral galaxies, can be better traced, as it emits the bulk of its flux at NIR. There is also a contribution to the observed flux from the young population and from AGB stars, but this tends to be restricted spatially to specific areas within the disk (e.g. spiral arms and bulges) and does not change the basic trend in the stellar distribution throughout the disk. Another important argument is that the extinction effects are minimised and so the observed brightness distribution more closely resembles the true stellar distribution, while the stellar flux still largely dominates the measured flux. This is not the case at longer wavelengths, at which the extinction is even lower. Also, the instrumental set-up allows us to reach outer regions on the galactic disks, where truncations are normally found, due to a combination of an excellent dry site, a telescope designed and maintained for NIR observations and cryogenic instrumentation with background contamination controlled via a cold stop.

Most previous studies (for example, Barteldrees & Dettmar 1994; de Grijs et al. 2001; Kregel et al. 2002; Pohlen et al. 2002a) have been carried out at optical wavelengths. To be

⋆ Figures 4–8 and Appendices A and B are only available in electronic form at http://www.edpsciences.org

complete, we mention the paper by Schwarzkopf & Dettmar (2000) as it contains a sample of 110 highly inclined galaxies, containing also K_s data for 41 of the galaxies, but most of these are probably not deep enough.

As a complement to this large amount of statistical data, detailed studies of the truncation curve are required. The observations reported in the present paper and in F01 are considerably deeper than those of any previous study dealing with NIR photometry on the outskirts of spirals, here reaching values of 20–23 mag arcsec^{-2} in J and 18.5–21 mag arcsec^{-2} in K_s, which correspond to a face-on surface brightness in the range of 25–26 mag arcsec^{-2} in J and 24–25 mag arcsec^{-2} in K_s. The increase of limiting magnitudes from edge-on to face-on views depends on the galaxy, mainly due to its inclination and thickness. These sensitivity limits enable us to extend the structural analysis to the outer areas of the disks, at galactocentric radii of comparable size to those achieved in optical studies.

F01 presented NIR observation dealing with truncations, and the present paper can be considered as a continuation of the former. The telescope and the infrared camera proved to be very efficient for investigating the low surface brightness at the outskirts of disks.

More NIR observations are necessary, especially taking into account that optical and NIR observations may differ substantially and that this difference can be crucial. Recent star formation beyond the truncation (or break) radius would have a larger influence in the blue but very little influence in the NIR range.

Different studies of truncations have used different techniques and so the results presented are not easily comparable. Some groups observe edge-on galaxies, while others consider face-on galaxies. Comparison is especially difficult when the data used are obtained at different wavelengths. For correct identification of the differences between optical and NIR observations a parallel study of the same galaxies would be preferable, using the same analysis. This would be the best way to determine, definitively, whether there is a clear difference between the results obtained using the different types of wavelengths. We present here the results of our NIR survey which are noticeably deep and interesting in themselves. Observations at these wavelengths can provide vital clues to our understanding of the truncation phenomenon.

2. The truncation curve in the literature

Different descriptions for the truncation curve are classified in the schematic plot shown in Fig. 1. The face-on $\mu(R)$ and the truncation curve $\tau(R)$ are plotted for four basic truncation types. This classification concerns the models considered to interpret the observed profiles. We have adopted this scheme of using the face-on $\mu(r)$ in the truncation curve to homogenise data coming from observations of both, face-on and edge-on galaxies. To render the last ones comparable with the former ones, we must deproject them. Deprojected profiles are intended to represent the true structure of the galaxy.

Type 1. A sharp cut-off is introduced in the model. This idealisation is justified by the fact that the truncation curve interval is relatively narrow.

The early observations by van der Kruit (1979) and van der Kruit & Searle (1981a,b) suggested profiles belonging to type 1 and were interpreted as a sharp cut-off in face-on galaxies that provided a relatively smooth truncation when the galaxy was seen edge-on. A sharp cut-off profile can appear as a smooth decreasing by the line of sight integration which is inherent to the observation of edge-on galaxies. Later on,

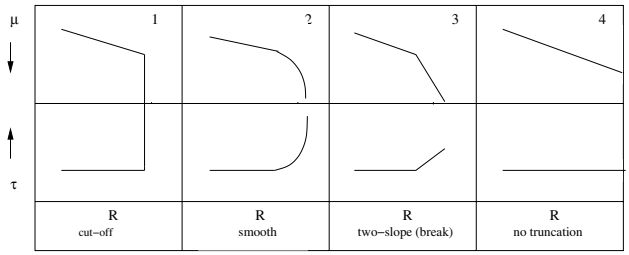

Fig. 1. Different ways to describe the truncation phenomenon.

Wainscoat et al. (1992) and many other works adopted this profile, after the work by van der Kruit and Searle.

Type 2. A "smooth" profile, in which truncation is gradual, i.e. the first derivative is a continuous function and the truncation becomes complete at R_{tr}, i.e. $\mu = \infty$ for $R > R_{tr}$ (within observational errors). There is a transition region of a few kiloparsecs. The edges are rounded in these profiles.

Note that when we state that truncations are complete, this is an ideal description that is obtained by extrapolation. The zero intensity level is, of course, unreachable. However, in some galaxies the truncation curve is so well defined that "naked eye" extrapolation suggests that the truncation is complete.

F01 presented NIR $\mu(R)$ and $\tau(R)$ in agreement with this "smooth" description. The plots in their Fig. 3 for NGC 4013 and NGC 5981 clearly suggest that the first derivative $d\mu/dR$ is a continuous function (in contrast, for example, to type 3). The real curve gradually moves away from the inner exponential to reach very large values. F01 proposed a function of the type

$$\tau(R) = \frac{\text{constant}}{(R_{tr} - R)^n} \tag{2}$$

and after fitting the data, n was found to be close to unity. This function is a very simple one, a power law, for a continuous curve with a continuous derivative function.

The type 2 profile is a smooth version of the classical sharp cut-off type 1 profile, avoiding a discontinuous derivative which is seldom found in nature. Profiles 1 and 2 are essentially the same, with the addition of a taring function, $\tau(R)$, to connect the exponential disk and the sharp cut-off with slope ∞ in the type 1 profile. The introduction of a taring function has been considered by Casertano (1983) and by de Grijs et al. (2001), who thus obtained a "soft cut-off" profile. However, they adopted other functions that differ from our Eq. (2).

Type 3. The radial profiles show a two-slope shape separated by a rather sharp "break" radius. At the break radius, the inner exponential is followed by another exponential decline with a different slope. In this case, there is no real truncation, i.e. the truncation is not complete as in the type 2 profiles. This conclusion has also been reached by Pohlen et al. (2002a, 2004) and others.

This profile is very well defined in NGC 5923 (Pohlen et al. 2004). It is noticeable that this galaxy is face-on (in early observations, truncations have been studied in edge-on galaxies) which avoids deprojection effects. The two-slope profile description has also been reported by Erwin et al. (2005) and others.

Type 4. The galaxy has no break and no truncation. This description corresponds to the early paper by Freeman (1970) where the disk was considered to be purely exponential.

The profiles reported in this paper fit the type 2 "smooth" truncation profile, following Eq. (2). Our NIR data are not deep enough to permit a confident exploration, e.g. with sufficient

Table 1. Basic properties of the galaxies.

Galaxy	RA	Dec	PA	D	Type	$m_{\rm abs}$	$\log D_{25}$	$\log v_m$
	hh mm ss	dd mm ss	d	Mpc				
(1)	(2)	(3)	(4)	(5)	(6)	(7)	(8)	(9)
NGC 522	01 24 45.91	09 59 40.5	33.3	39.0	Sbc	–20.53	1.44	2.252
NGC 684	01 50 14.03	27 38 44.2	88.8	50.4	Sb	–21.53	1.53	2.368
MCG-01-05-047	01 52 49.01	–03 26 51.2	161.4	71.5	Sc	–21.77	1.47	2.410
NGC 781	02 00 09.02	12 39 21.5	13.0	49.8	Sab	–20.87	1.18	
NGC 2654	08 49 11.91	60 13 13.9	65.0	19.2	SBab	–20.09	1.62	2.295
UGC 4906	09 17 39.94	52 59 34.3	49.0	32.6	Sa	–20.26	1.30	2.228
NGC 2862	09 24 55.10	26 46 29.0	114.0	58.5	SBbc	–21.44	1.41	2.464
NGC 3279	10 34 42.61	11 11 50.7	152.0	19.9	Scd	–19.27	1.44	2.208
NGC 3501	11 02 47.35	17 59 22.6	28.0	16.2	Sc	–19.05	1.54	2.147
NGC 5981	15 37 53.55	59 23 30.9	139.5	36.1	Sc	–20.61	1.43	2.424
NGC 6835	19 54 33.09	–12 34 02.5	72.0	23.0	SBa	–19.55	1.38	1.803

Columns: (1) galaxy name; (2) and (3) coordinates (2000); (4) position angle; (5) distance, considering $H_0 = 70\,{\rm km\,s^{-1}\,Mpc^{-1}}$; (6) morphological type; (7) absolute B-magnitude; (8) log of apparent diameter (D_{25} in 0.1′) and (9) log of maximum velocity rotation (in $\rm km\,s^{-1}$) from radio observations. All the parameters are obtained from the LEDA database (`http://leda.univ-lyon1.fr`) except the position angles.

S/N, of the region in which recent optical observations find the second slope after a break.

In this paper, we present the data observed without theoretical preconceptions. It will be followed by a second one showing that the magnetic model matches the statistical properties derived from the data reported in this paper.

3. Data

As in F01, the observations were carried out at the 1.5 m CST at the Teide Observatory, Tenerife, with the NIR camera CAIN equipped with a 256^2 NICMOS 3 detector array. The plate scale, with the wide field optics used, was 1.0″/pixel and the effective field of view was $4.3' \times 4.3'$. For the CAIN camera, the controller of the detector is based on a San Diego State University architecture, which provides low noise and high stability while permitting fast reading of the whole array, in about 50 ms. In all cases, the read-out mode was the FOWLER mode, in which an equal number of non-destructive readings are taken, without time delays in between, immediately after the initial reset and before the final one, after the selected integration time has elapsed. Thus, the pedestal and final flux levels are better determined, by averaging each group of readings independently. The final signal is then the difference between the last and first averages. The observational characteristics are the same as in F01 (also explained in Castro-Rodríguez & Garzón 2003). The observations were carried out in 4 campaigns. The weather was generally good, being most of the nights photometric, on which we took the data from the standard stars and galaxies. A consistency check was performed for several bright objects against 2MASS point source catalogue, confirming that our measurements and those of 2MASS are consistent.

The observed galaxies and their main physical parameters are depicted in Table 1. Most of these were obtained from the LEDA database. The position angle (PA) is measured on the image with an automatic routine which delivers high precision values; for most of the galaxies the value obtained coincides with that of the LEDA database, the differences being $\leq 2°$. The orientation of the detector chip with respect to the sky was kept constant throughout the observation runs, so there was no systematic effect due to changes in the instrument configuration. The PA was measured from the North celestial pole, increasing towards the East. Distances were obtained with $H_0 = 70\,{\rm km\,s^{-1}\,Mpc^{-1}}$ taking into account the mean heliocentric radial velocity ($\rm km\,s^{-1}$). All galaxies are edge-on, with an inclination $i = 90°$ in LEDA. They were also selected to be, as far as possible, free of Milky Way stars in the outer edge and in such a way that their projected size (D_{25}) fitted within the FOV. No other physical parameters (other than angular size and galactic latitude) were adopted for the selection; thus, although selection bias cannot be discarded, it is believed improbable.

At these wavelengths, the night airglow emission is bright and rapidly varying; therefore, we used the classical observational ON-OFF method with a nodding frequency compatible with that of the background variation in the sky and with an equal integration time on each pointing. The integration time interval was split into several frames to avoid exceeding the linear well depth of the detector due to the high sky flux, in particular in the $K_{\rm s}$ band. Alternating exposures were taken of the galaxy and the adjacent sky, separated by two minutes at most, for effective sky subtraction. Special care was taken with the flat-fielding and sky subtraction. For the reduction steps, we used several IRAF tasks and the IRAF package REDUCE, developed by R. Peletier.

The observations were carried out in 4 campaigns. Table 2 shows the references for each galaxy: Campaign 1 took place in October 2001, Campaign 2 in March 2002, Campaign 3 between October and November 2002 and Campaign 4 in March 2003. Table 2 also describes the following observational parameters of the galaxies observed: the filter, the individual exposure time per frame (5 or 6 s for $K_{\rm s}$ and H and 30 s for J), the number of frames at each position (4 for J and 20 or 24 for $K_{\rm s}$ and H), the number of images per galaxy (usually 20 for J and 24 for $K_{\rm s}$ and H); thus, the total exposure time was 40 (J) or 48 ($K_{\rm s}$ and H) minutes for the object. The last column shows the detection limit calculated as 3 times the STDDEV over the mean value of the background level, measured directly on the images in areas free from emission of the galaxy object. The typical seeing value was, on average, a little in excess of 1″. In Fig. 4 we plot contour maps for these galaxies.

4. Deprojection

It is clear that the deprojection technique is critical in the reduction process. In some cases, an initial inspection of the original profiles may suggest a truncation which disappears after

Table 2. Observational parameters of the galaxies.

Galaxy	C	B	$T_{\rm exp}/F$ (s)	F/P	Pointing	T ob.(m)	3σ mag/arcsec^2
(1)	(2)	(3)	(4)	(5)	(6)	(7)	(8)
NGC 522	3	J	30	4	20	40	20.6
	3	$K_{\rm s}$	5	24	24	48	21.1
NGC 684	1	J	30	4	20	40	20.5
	1	$K_{\rm s}$	5	24	24	48	18.6
MCG-01-05-047	3	J	30	4	20	40	22.7
	3	$K_{\rm s}$	5	24	24	48	20.7
NGC 781	3	J	30	4	20	40	22.9
	3	$K_{\rm s}$	5	24	24	48	20.7
NGC 2654	3	J	30	4	20	40	22.6
	3	$K_{\rm s}$	5	24	24	48	21.0
UGC 4906	4	J	30	4	20	40	22.0
	4	$K_{\rm s}$	5	24	24	48	20.9
NGC 2862	3	J	30	4	20	40	22.7
	3	$K_{\rm s}$	5	24	24	48	20.7
	3	H	5	24	24	48	21.5
NGC 3279	2	J	30	4	20	40	22.0
	2	$K_{\rm s}$	6	20	24	48	20.4
NGC 3501	4	J	30	4	20	40	22.3
	2	$K_{\rm s}$	6	20	24	48	20.4
NGC 5981	2	J	30	4	20	40	21.9
	2	$K_{\rm s}$	6	20	24	48	20.2
NGC 6835	1	J	30	4	20	40	20.1
	1	$K_{\rm s}$	5	24	24	48	18.7

Columns: (1) galaxy name; (2) campaign (1, Oct. 2001; 2, March 2002; 3, Oct.–Nov. 2002; 4, March 2003); (3) band; (4) individual exposure time per frame; (5) number of frames at each position; (6) images per galaxy; (7) exposure time for the galaxy and (8) the 3σ level of the background variation over its mean value.

deprojection. To assure that the deprojection method works satisfactorily, we carried out two tests:

a) Deprojection was performed by two different, independent methods. The first of these is described in detail in F01, while the second is based on Abel's integral equation (Binney & Tremaine 1987). Despite the fact that the numerical calculations involved in these methods are intrinsically different, the results obtained by the F01 method and by using Abel's integration are almost indistinguishable. The F01 method was subsequently adopted, because of the few assumptions needed, and to use the same reduction process for the sake of coherence when merging the present data with those obtained in F01. Thus, a larger and more homogeneous statistical sample is ensured. Moreover, the F01 method can be generalised to more realistic conditions, including extinction.

b) We have tested that the projection of the deprojected profile (x points) perfectly matched the original profile (△ points) in a zero order test (Fig. 2). A deprojected profile corresponded to only one original profile and an original profile corresponded to only one deprojected profile. For example, our smooth deprojected profiles were not produced by a face-on profile with a sharp cut-off.

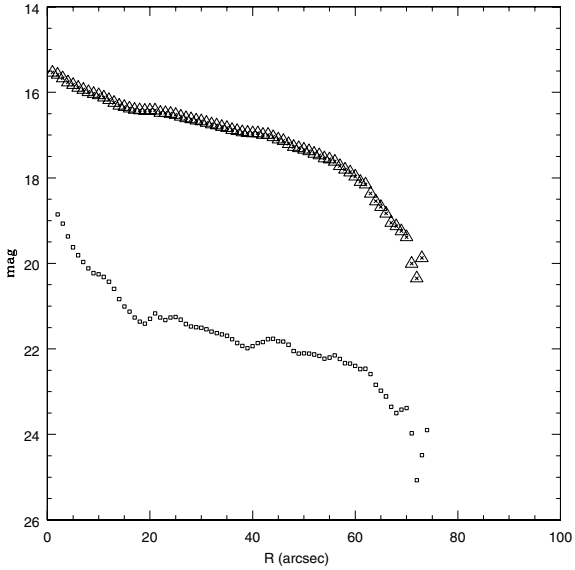

Fig. 2. Test for the deprojection method. Symbols are: △, input curve; □, deprojected curve; x, projection of the deprojected curve.

We took the z-integrated profiles as the original input profile for the deprojection method, i.e. those profiles obtained by summing all the input radial profiles for each z. These z-integrated profiles were obtained as follows: first the galaxies were rotated to make the major axis perpendicular to the ordinate axis. From $I(r,z)$, where I is surface brightness, r is the abscissa and z the ordinate, the z-integrated profile is then obtained as $I(r) = \Sigma_{z=a}^{b} I(r,z)$, where a and b are the limits of a box which contains the 3σ isophote of galaxies. We have not masked any foreground stars. We thus create an artificial profile. If we wished to obtain the truncation curve as a function of z, this z-integration would prevent it. This could be interesting, for instance, to see if the truncation were different for the thin and the thick disks, which is especially important in early type spirals. Moreover, in early type galaxies the extended bulge could smear out a possible truncation in a z-integrated profile. This cannot be undertaken when using face-on observations.

Certainly, by z-integrating we cannot obtain the emission per unit volume in the galaxy. However, this procedure has two important advantages: firstly, we can work with a profile which has a much better signal/noise ratio, and secondly, the effect of the

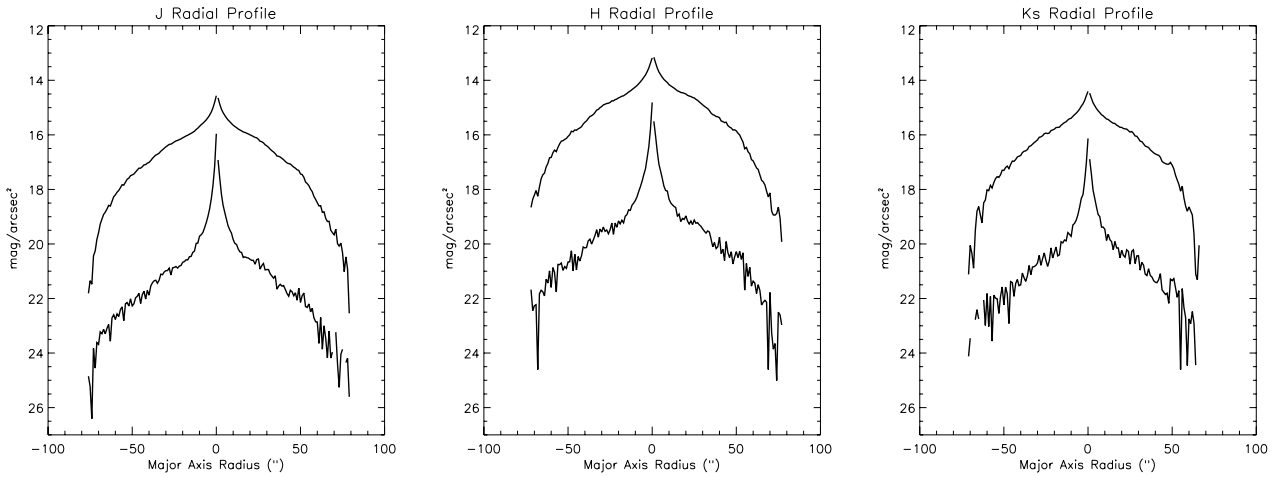

Fig. 3. NGC 2862: z-integrated profile (upper) and deprojected profile (lower) for each filter.

large extinction dependence on z is greatly reduced. Suppose, for instance, a dust lane for $z = 0$ or around $z = 0$. The row $z = 0$ would give meaningless results because of severe extinction. By summing all the z rows, the effects of localized dust lanes are reduced.

The z-integration apparently leads to a loss of information. However, this effect is irrelevant if the final product of the deprojection method is the face-on view. In Fig. 3 we plot both the z-integrated and the deprojected profiles for a selected galaxy, NGC 2862, for the three filters to illustrate the difference.

It might be thought that in order to obtain the face-on view the sequence "deprojection, then z-integration" is not equivalent to the sequence "z-integrating, then deprojection". From the description of the deprojection method in F01 it can be demonstrated that the two sequences are equivalent. This is shown in Appendix A.

Therefore, the method itself does not introduce important errors (as concluded in F01). However, important errors could be introduced if the required assumptions are not accomplished. These assumptions are axisymmetry, the absence of extinction, and an inclination equal to 90°. In other words, the deprojected profile need not necessarily coincide with the real face-on profile. They only coincide when the required assumptions are met.

With respect to axisymmetry, it is clear that when the galaxy lacks this property then deprojection cannot reproduce the real face-on view. This source of potential errors is inevitable in this and in any other deprojection method. The problem has infinite solutions, as from a 2D distribution it is not possible to obtain a 3D one without certain assumptions. Fortunately, in the galaxies observed, the noticeable east-west symmetry suggests that they are reasonably axisymmetric.

An estimation of this error is not easy. NIR data of face-on galaxies have not been reported in the literature up to these large radii, so we cannot use additional real data for this estimate. The only galaxy for which we have at our disposal NIR data at large radii is the Milky Way. Wainscoat et al. (1992) have modelled the Milky Way in order to reproduce IRAS data, including NIR arms which are the mean sources of non-axisymmetries. The over-density due to one NIR arm is very small. From these data about the relative importance of arm with respect the unperturbed disc and taking into account the contribution to the flux of each spectral type, from Porcel (1997) we obtain that the contribution is mainly due to stars of spectral types B8 V to F5 V and is only 1%. When the propagation of errors in the deprojection method is considered, this figure becomes representative of the error introduced by one-arm asymmetries by the deprojection method. Galaxies reported here could be less symmetric than the Milky Way, but we estimate that this kind of error can be ignored.

Extinction is another inevitable source of errors, particularly if there is a non-axisymmetric distribution of dust. However, the problems introduced by extinction are reduced in the present approach because we work in the NIR and because prior z-integration avoids the effects of inhomogeneities on the distribution of dust, e.g. dust lanes in the plane.

We used only galaxies with $i = 90°$, following LEDA. However, the LEDA galaxies may deviate typically 2° from edge-on, which could be a source of errors. Our galaxies have a minor-axis of $70'' \sin 2° = 2.4''$, which is higher than our resolution about $1''$. In Appendix B we show that inclinations $i > 88°$ do not introduce noticeable errors.

Another important step in the analysis was to calculate the slope of the exponential function of the form $I(R) = I_0 \exp(-R/h)$ in the inner part. This parameter h is present in the definition of $\tau(R)$ and it is necessary to be able to estimate $R_{\rm tr}/h$, another parameter that is derived in all the studies made of truncations/breaks. The region for calculating h was decided upon by visual estimation. h is calculated in the deprojected profiles. Noise and intrinsic variations in surface brightness do not permit the determination of h with an error of less than about 10%.

The use of a visual decision regarding the interval for calculating h does not introduce large uncertainties, because of the broad region in which the exponential behaviour provides a good fit. If the photometric profiles are divided into bulge, exponential and truncation shapes (with no sharp transitions) the choice of an excessively large interval would provide an underestimation of h, while the choice of one that was excessively small would give large errors. But excluding these two extreme cases, the value of h is nearly independent of the choice of the interval. Therefore, this subjective choice does not introduce additional errors.

The main results are presented in Table 3, for each side of the galaxies. After the deprojection process, by fitting the exponential profile, we obtain μ_0, the central surface brightness of the disk, and h, the radial scale length. Then we estimate $R_{\rm tr}$, the truncation radius, and n, the exponent in Eq. (2). We also calculate $R_{\rm tr}/h$.

Table 3. Photometrical and structural parameters of the target list.

Galaxy	Passband	Side	μ_0 (mag/arcsec^2)	h (kpc)	h (arcsec)	R_{tr} (kpc)	R_{tr} (arcsec)	n	R_{tr}/h
(1)	(2)	(3)	(4)	(5)	(6)	(7)	(8)	(9)	(10)
NGC 522	J	SW/NE	20.6/20.6	7.2/6.1	38/32	14/14	73/72	1.0/1.0	1.9/2.2
	K_s	SW/NE	21.1/20.9	8.0/6.3	42/33	11/11	59/60	0.5/0.7	1.4/1.8
NGC 684	J	NW/SE	18.8/18.6	5.3/4.6	22/19				
	K_s	NW/SE	16.8/17.3	3.7/4.1	15/17				
MCG-01-05-047	J	NW/SE	20.9/20.9	10.4/11.3	30/33	30/29	85/84	0.6/0.7	2.8/2.6
	K_s	NW/SE	19.5/19.6	8.4/9.4	24/27	28/27	82/79	1.0/1.0	3.4/2.9
NGC 781	J	SW/NE	19.4/19.8	2.6/3.1	11/13	11/11	46/45	0.9/0.8	4.2/3.5
	K_s	SW/NE	18.3/18.0	2.6/2.3	11/9	10/10	41/40	0.5/0.3	3.5/4.3
NGC 2654	J	NE	18.9	1.5	17				
	K_s	NE	17.3	1.4	15				
UGC 4906	J	SW/NE	18.3/18.3	1.9/1.7	12/11				
	K_s	SW/NE	17.3/17.3	1.7/1.7	11/10				
NGC 2862	J	NW/SE	19.5/19.6	5.9/6.0	21/21	22/22	77/76	1.1/0.9	3.7/3.6
	K_s	NW/SE	18.5/18.5	5.9/5.6	21/20	19/18	66/65	0.8/0.7	3.2/3.3
	H	NW/SE	18.7/18.7	6.4/5.8	23/20	21/20	74/69	1.1/0.3	3.3/3.4
NGC 3279	J	NW/SE	19.9/19.6	4.7/3.1	48/32	8/8	79/82	1.5/1.0	1.6/2.6
	K_s	NW/SE	18.5/18.3	3.8/2.9	39/30	7/7	69/74	1.2/1.2	1.8/2.4
NGC 3501	J	SW/NE	20.2/19.9	2.1/1.7	27/22	8/9	100/110		3.7/5.1
	K_s	SW/NE	18.1/18.0	1.6/1.6	21/20	6/	82/	0.5/	3.9/
NGC 5981	J	NW/SE	19.4/19.3	4.3/4.2	25/24	15/14	88/79	0.9/0.9	3.6/3.3
	K_s	NW/SE	18.1/18.0	4.0/3.7	23/21	13/12	74/70	0.9/0.0	3.2/3.3
NGC 6835	J	NW/SE	18.1/18.1	1.8/1.8	16/16				
	K_s	NW/SE	17.4/17.4	1.8/1.8	16/16				

Columns: (1) galaxy name; (2) filter; (3) side of the galaxy; (4) central surface brightness; (5) & (6) radial scale-length in kpc and in arcsec; (7) and (8) truncation radius in kpc and arcsec; (9) parameter n obtaining from Eq. (2); (10) ratio between truncation radius and scale-length. All values are deprojected (face-on).

5. Results

The galaxies observed can be grouped taking into account the existence of truncation, as follows:

a) Truncated galaxies: NGC 522, MCG-01-05-047, NGC 781, NGC 2862, NGC 3279, NGC 3501 and NGC 5981. Our study is mainly focused on this group.

b) Untruncated galaxies: NGC 684, UGC 4906, NGC 2654 and NGC 6835. Of course we cannot assure that these are not truncated, but only state that no truncation was observed for face-on values of $J < 23$ mag/arcsec^2 in NGC 684, for $J < 24$ mag/arcsec^2 in UGC 4906, for $J < 25$ mag/arcsec^2 in NGC 2654 or for $J < 22$ mag/arcsec^2 in NGC 6835. We refer to the J filter limits since in these galaxies the J band data covers a more extended region in the object, as can be seen in Fig. 4. In consequence we did not detect truncations out to 3.5 radial scale-lengths for NGC 684, 5.0 for UGC 4906, 5.9 for NGC 2654 or 3.3 for NGC 6835.

We deduce that approximately 2/3 of the considered galaxies are truncated, a sufficiently large value to highlight, once more, the importance of this effect. Although this figure must be approached with some caution, the overall conclusion must be that truncations/breaks are a fairly common feature of normal spirals. It is also evident that we cannot speak of untruncated galaxies, but merely of galaxies for which truncation is not observed within the limits of our observational capabilities.

In Fig. 5, we plot the deprojected profiles for these galaxies. Figure 5 also show $\tau(R)$ obtained from Eq. (1) for these galaxies and for two galaxies (MCG-01-05-047 and NGC 5981), included as examples, we show the fitted truncation curve.

Table 3 shows that the truncation radii obtained with the J filter is always larger than the value obtained with the K_s filter, the ratio being $R_{tr}(J)/R_{tr}(K_s) = 1.15$. The dispersion of the data is 0.04, but our error in determining this quantity is larger, at about 0.5.

The identification performed is not free of definition problems. Let us assume a galaxy with an extended (not sharp) "break" region and with the second outer exponential lying beyond observation capabilities. This could have been classified as "smooth" despite being a "break" galaxy. The data for some of our galaxies strongly suggest that the "smooth" description is physically different from the two-slope type, but this identification is not easy. Subjective inspection is probably essential to determine whether the change in the slope is gradual or sharp or, equivalently, whether the first derivative is a continuous or a discontinuous function. Given the mounting body of evidence provided by Pohlen et al. (2002a, 2004), Pérez (2004), Erwin et al. (2005), Trujillo & Pohlen (2005) and others in obtaining clear two-slope profiles, we could have fit the data to this model. But considering that our data do not permit the exploration of the second-slope region and considering that the NIR and the optical profiles do not necessarily coincide, we follow an independent approach.

In the previous paper by F01, the deprojected profiles of NGC 4013 (both J and K_s, both sides), NGC 4217 (K_s, left side) and NGC 5981 (K_s, right side) are clear examples of a gradual decline and a continuous first derivative. Notice that NGC 5981 is present in both papers (in the first one only in K_s). The K_s-images are very similar as expected, but in the first campaign better observing conditions allowed us to reach slightly more distant radii. The difficulties inherent in subjective discrimination cannot be easily surmounted by statistical methods, as the break point should be determined manually. Thus, we prefer the "smooth" truncation, type-2 profiles with gradual decline and gradual variation of the first derivative.

We then fitted the observation points to the function in Eq. (2). $R_{\rm tr}$ was obtained by extrapolation and the "constant" and the value of n by standard fitting methods. The n value is particularly interesting. The results are shown in Table 3.

This fitting features the compromise of a gradual transition from a pure exponential to a continuously bending profile. This is, however, provided automatically by the function given in Eq. (2). $\tau(R)$ becomes negligible for values of R not far from $R_{\rm tr}$. For example, assuming $n = 1$ as a typical value, it is found that τ is only 10% of the value for $R = 0.95R_{\rm tr}$, for a value of R one radial length less than $R_{\rm tr}$. Therefore, the result is practically independent of the starting point in the fitting (provided the bulge zone is excluded). The real curves in Fig. 5 show how fast τ decreases far from the truncation radius.

The mean value of n is 0.8 with $\sigma = 0.3$. This supports the conclusion by F01 who also found a coefficient close to unity. Therefore, we propose

$$\tau(R) \propto \frac{1}{(R_{\rm tr} - R)^{0.8}}. \quad (3)$$

Notice that the face-on and edge-on truncation curves differ but $R_{\rm tr}$ is the same (Fig. 3). Therefore, this value is unaffected by the use of a deprojection technique. The $R_{\rm tr}$ values obtained in other studies without deprojection are equally valid for statistical studies.

The $R_{\rm tr}$ and n parameters are obtained independently. The value of $R_{\rm tr}$ tells us "where" the truncation takes place and the values of n tell us "how sharp" the truncation is.

6. Conclusions

In order to obtain more information about the truncation of the stellar disk, it is necessary to incorporate observations in the NIR, which is the best tracer of the old population and relatively free of extinction problems, and to use larger telescopes. On the other hand, observations in the optical and in the NIR should be considered complementary, as both wavelength ranges may give information about different aspects of the feature. In fact, they may differ not only in the value of certain fitting parameters, but in the functional form of the truncation curve itself. For example, beyond the truncation (or break) radius, non negligible star formation could affect the young population distribution but not that of the old population. If stars did not move from their birthplace, a difference in the blue and the NIR profiles would not be expected, but stars can move.

If there is a (smooth and complete) truncation in the IR, as shown by F01 and this study, and a sharp break in the optical, as shown by Pohlen et al. (2004), this is not necessarily a contradiction; it could be the sign of differing behaviour patterns in the optical and in the near infrared, for dynamic reasons. We choose the traditional description introduced by van der Kruit (1987), introducing a taring function to smooth out the sharp cut-off, also called a soft cut-off, and propose a truncation curve proportional to $(R_{\rm tr} - R)^{-n}$, with $n = 0.8 \pm 0.3$, a value close to 1, i.e. it becomes complete at $R = R_{\rm tr}$. This is the profile of type 2, labelled "smooth" in Fig. 1.

The type 3 profile is clearly different from that of type 2, either due to the different information provided by the NIR and the optical, or due to insufficient coverage of the NIR observations. In the light of the former consideration, we have chosen the simplest fit suggested by our data, but they are not deep enough to conclude that an external region with a second slope does not exist.

Unfortunately, there are not many galaxies measured in both the optical and the NIR. One of them is NGC 522, which was measured in the optical by Pohlen et al. (2002b). This galaxy is a very good example of a two-slope with a narrow break region in between, when measured in the optical. However, as can be seen in Fig. 5, the J-profile on the right hand side seems to be smooth. The left side as well as the right Ks side could be described as a two-slope. The data does not allow us to clearly distinguish between these two types. Hence, no clear conclusions can be obtained from this comparison. This important point should be addressed in a future study.

As the radial scale height is a natural unit of length in a spiral galaxy, $R_{\rm tr}/h$ is a parameter characterising truncations. For these galaxies, we found the following values for $R_{\rm tr}/h$: 3.2 for J and 2.9 for $K_{\rm s}$, with $\sigma = 0.9$ and 0.8 respectively for each filter. The colour dependences of $R_{\rm tr}$ will be discussed in Paper II. These values are in reasonable agreement with previous estimations. For comparison, it should be taken into account that the difference between the radius at which the truncation curve leaves the inner exponential and the radius at which the truncation finishes is of the order of 20–30″, and that in the break description only the first value is meaningful.

It is not easy to establish how often galaxies are truncated, due to the difficulty in determining whether a given galaxy is non truncated or whether $R_{\rm tr}$ is too distant to be observed. If we consider 7 out of 11 galaxies truncated, this is equivalent to approximately 2/3. However, this figure should be considered with some caution as our sample is small. However, we confirm that the frequency of truncated galaxies is high, which makes this topic of crucial importance in our understanding of the evolution of disk galaxies.

Acknowledgements. This paper has been supported by the "Plan Andaluz de Investigación" (FQM-108) and by the "Secretaría de Estado de Política Científica y Tecnológica" (AYA2004-08251-C02-02, ESP2004-06870-C02-02). This research has made use of the Hyper Leda database.

References

Barteldrees, A., & Dettmar, R.-J. 1994, A&AS, 103, 475
Binney, J., & Tremaine, S. 1987, Galactic Dynamics, Princeton Ser. in Astrophys. (Princeton Univ. Press)
Casertano, S. 1983, MNRAS, 203, 735
Castro-Rodríguez, N., & Garzón, F. 2003, A&A, 411, 55
Erwin, P., Beckman, J. E., & Pohlen, M. 2005, ApJ, 626, L81
Florido, E., Battaner, E., Guijarro, A., Garzón, F., & Jiménez-Vicente, J. 2001, A&A, 378, 82 (F01)
Freeman, K. C. 1970, ApJ, 160, 811
de Grijs, R., Kregel, M., & Wesson, K. H. 2001, MNRAS, 324, 1074
Kregel, M., van der Kruit, P. C., & de Grijs, R. 2002, MNRAS, 334, 646
van der Kruit, P. C. 1979, A&AS, 38, 15
van der Kruit, P. C. 2001, in Galaxy Disks and Disk Galaxies, ed. J. G. Funes, & S. J. E. M. Corsini, ASP Conf. Ser., 230, 119
van der Kruit, P. C., & Searle, L. 1981a, A&A, 95, 105
van der Kruit, P. C., & Searle, L. 1981b, A&A, 95, 116
Pérez, I. 2004, A&A, 427, L17
Pohlen, M., Dettmar, R. J., Lütticke, R., & Aronica, G. 2002a, A&A, 392, 807
Pohlen, M., Dettmar, R. J., Lütticke, R., & Aronica, G. 2002b, ASP Conf. Proc., 275, 15
Pohlen, M., Beckman, J., Hüttemeister, S., et al. 2004, in Penetrating Bars through Masks of Cosmic Dust, ed. D. L. Block, et al. (Berlin: Springer), 713
Porcel, C. 1997, Ph.D. Thesis. University of Granada, 105
Schwarzkopf, U., & Dettmar, R.-J. 2000, A&A, 361, 451
Trujillo, I., & Pohlen, M. 2005, ApJ, 630, L17
Wainscoat, R., Cohen, M., Volk, K., Walker, H. J., & Schwartz, D. E. 1992, ApJS, 83, 111

Online Material

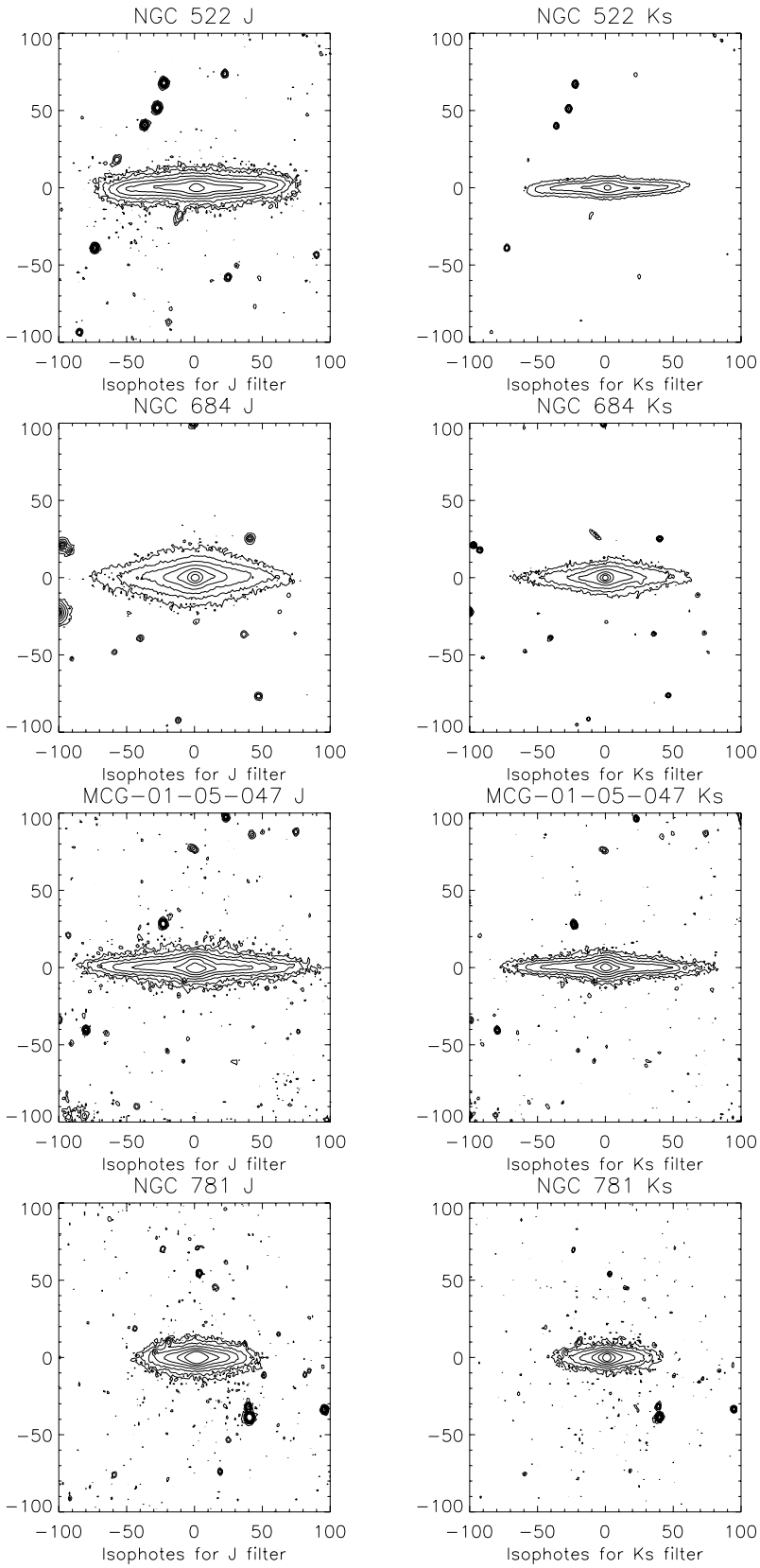

Fig. 4. Contour maps for the observed galaxies for J, H and Ks filters. The isophotes are equidistant (in units of $n * 3\sigma$ equiv. to a step of +0.75 mag/arcsec^2) starting at our noise level (see Table 2). Galaxies are rotated, but N is closer to the top and E to the left.

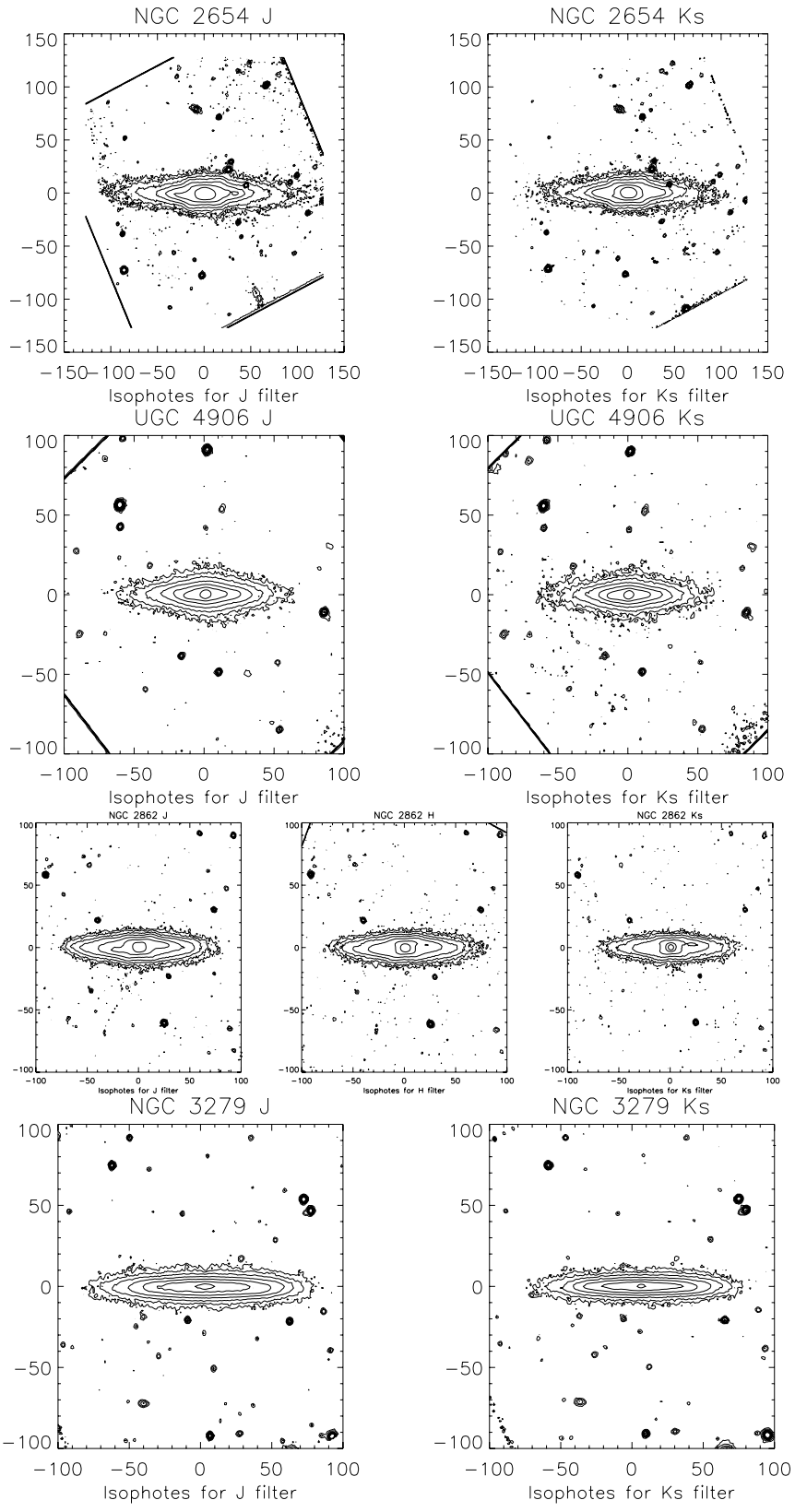

Fig. 4. continued.

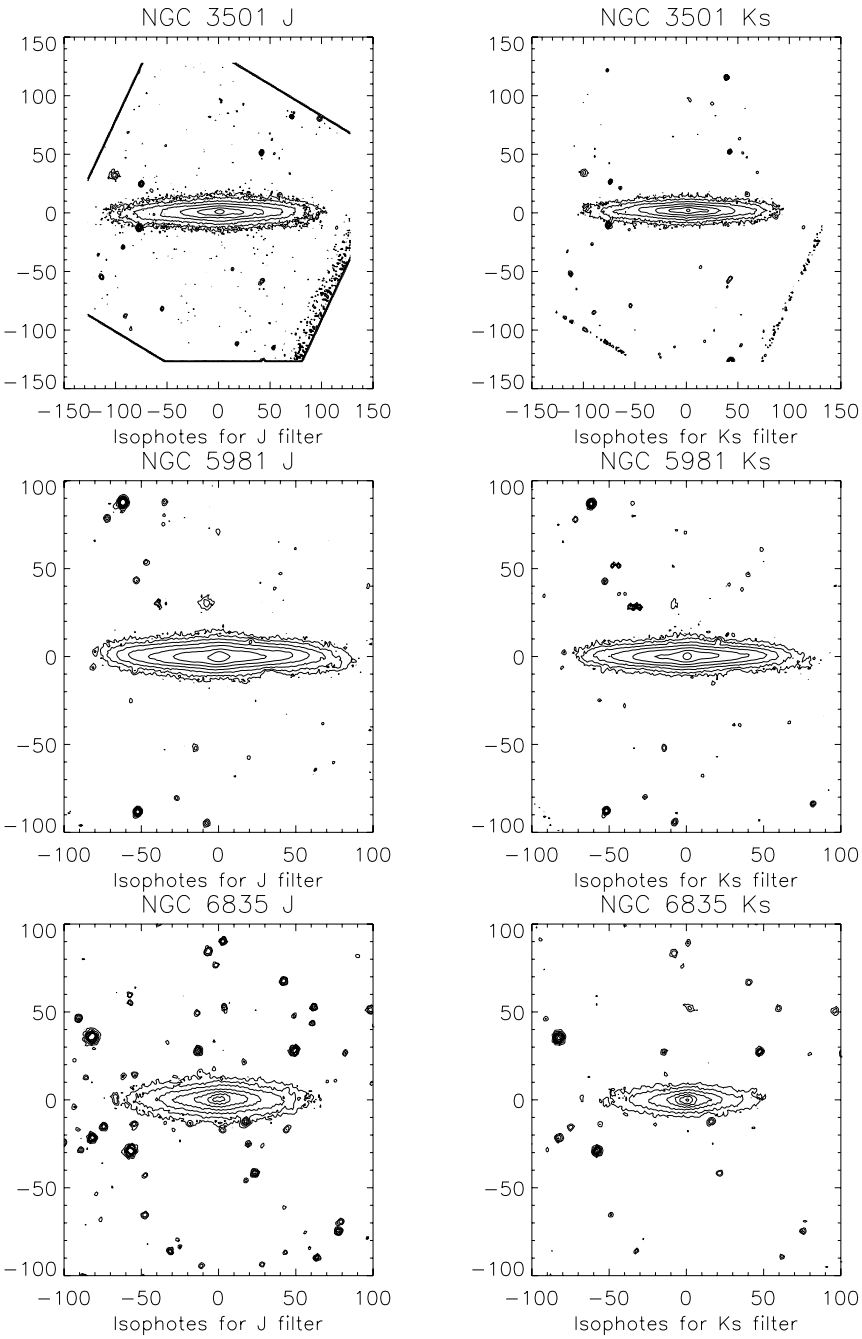

Fig. 4. continued.

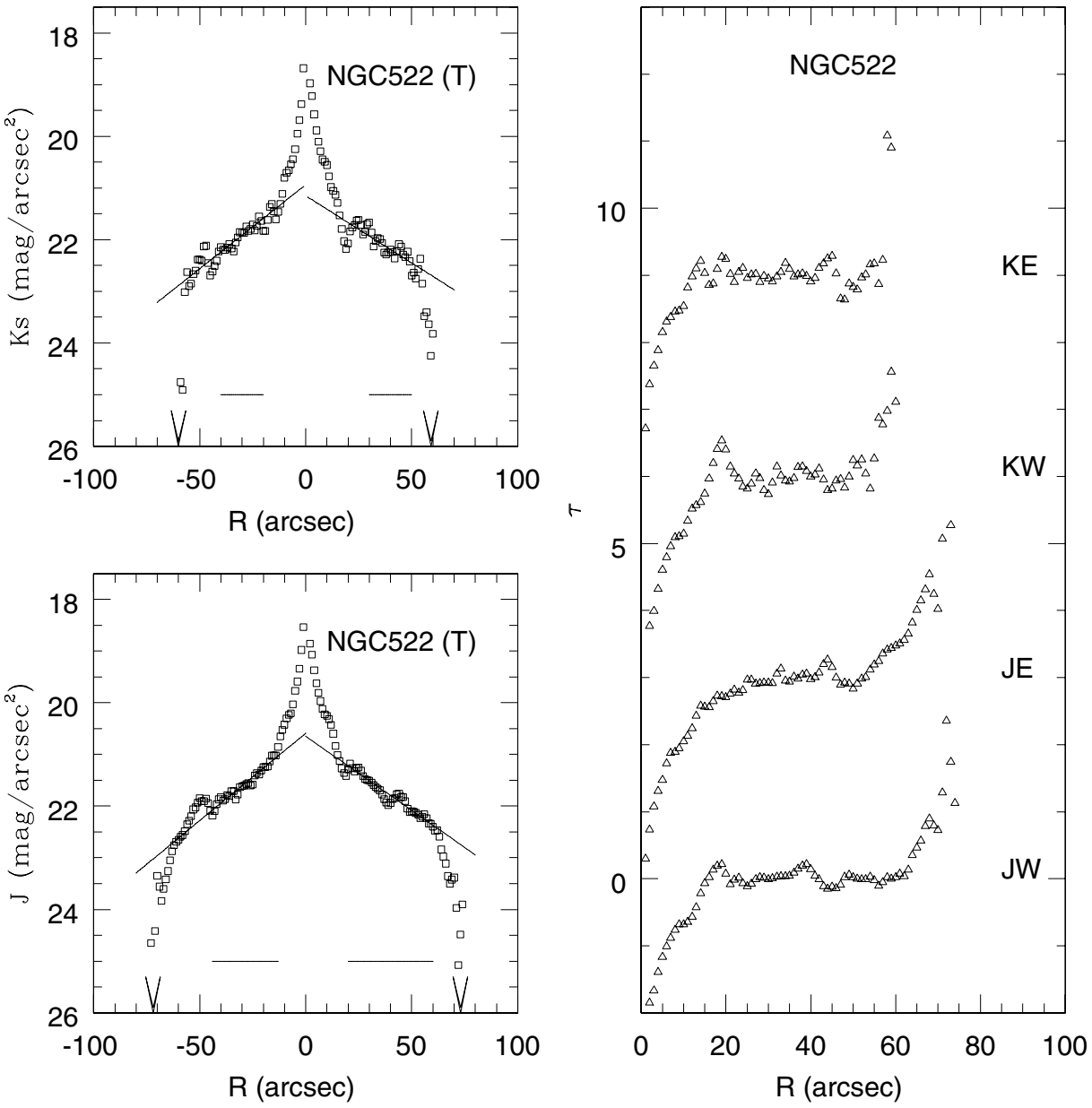

Fig. 5. Deprojected profiles for all galaxies. Left: The solid line is the exponential fit with the parameters in Table 3. Horizontal bars indicate the region in which the radial scale length was calculated and the arrow the truncation radius.(T) is for truncated galaxies and (U) for untruncated ones. Right: For each of these galaxies we have represented the truncation curve (τ) from the Eq. (1) and, as an example, we have plot the fitted function of Eq. (2) for two of them.

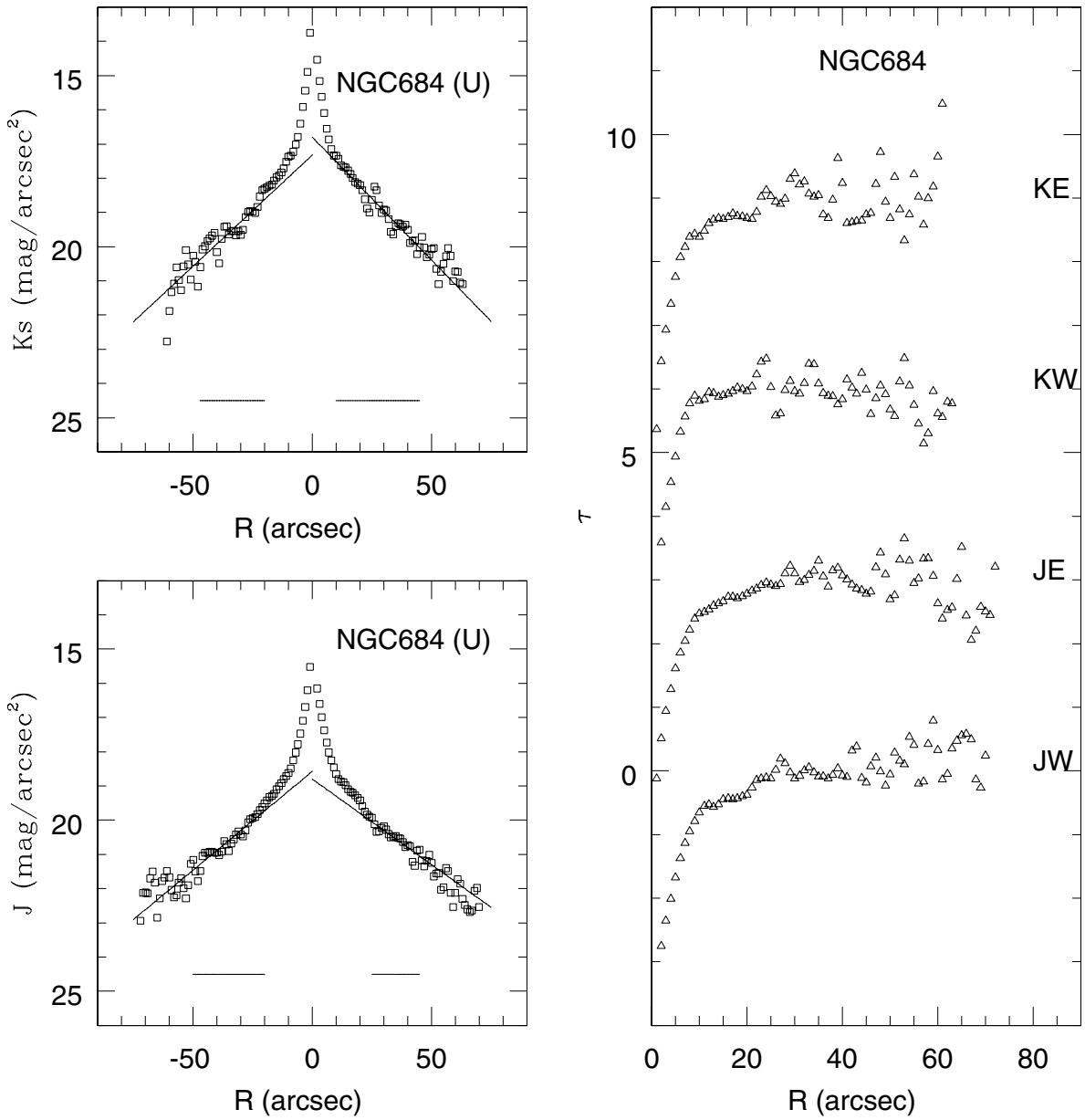

Fig. 5. continued.

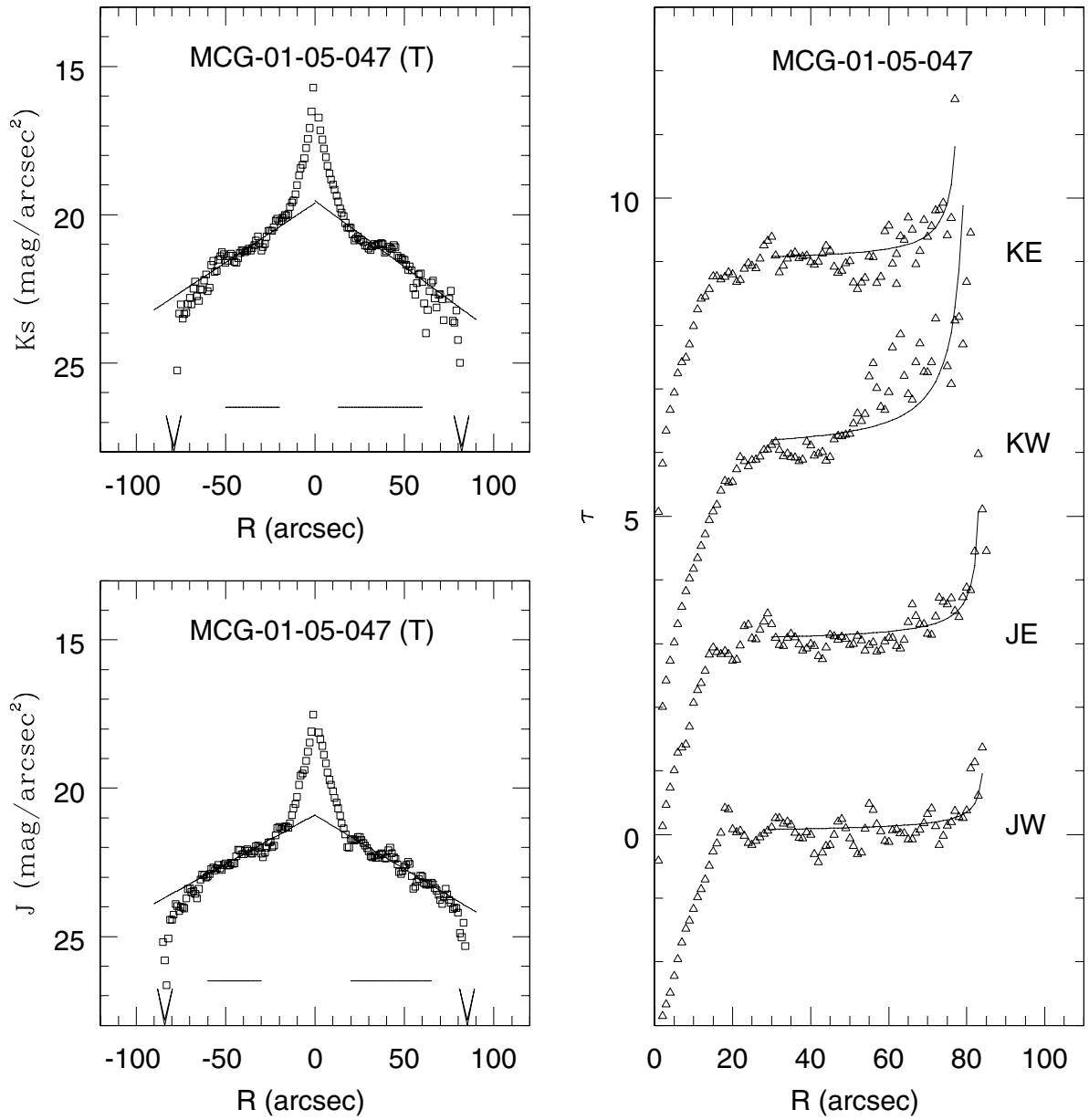

Fig. 5. continued.

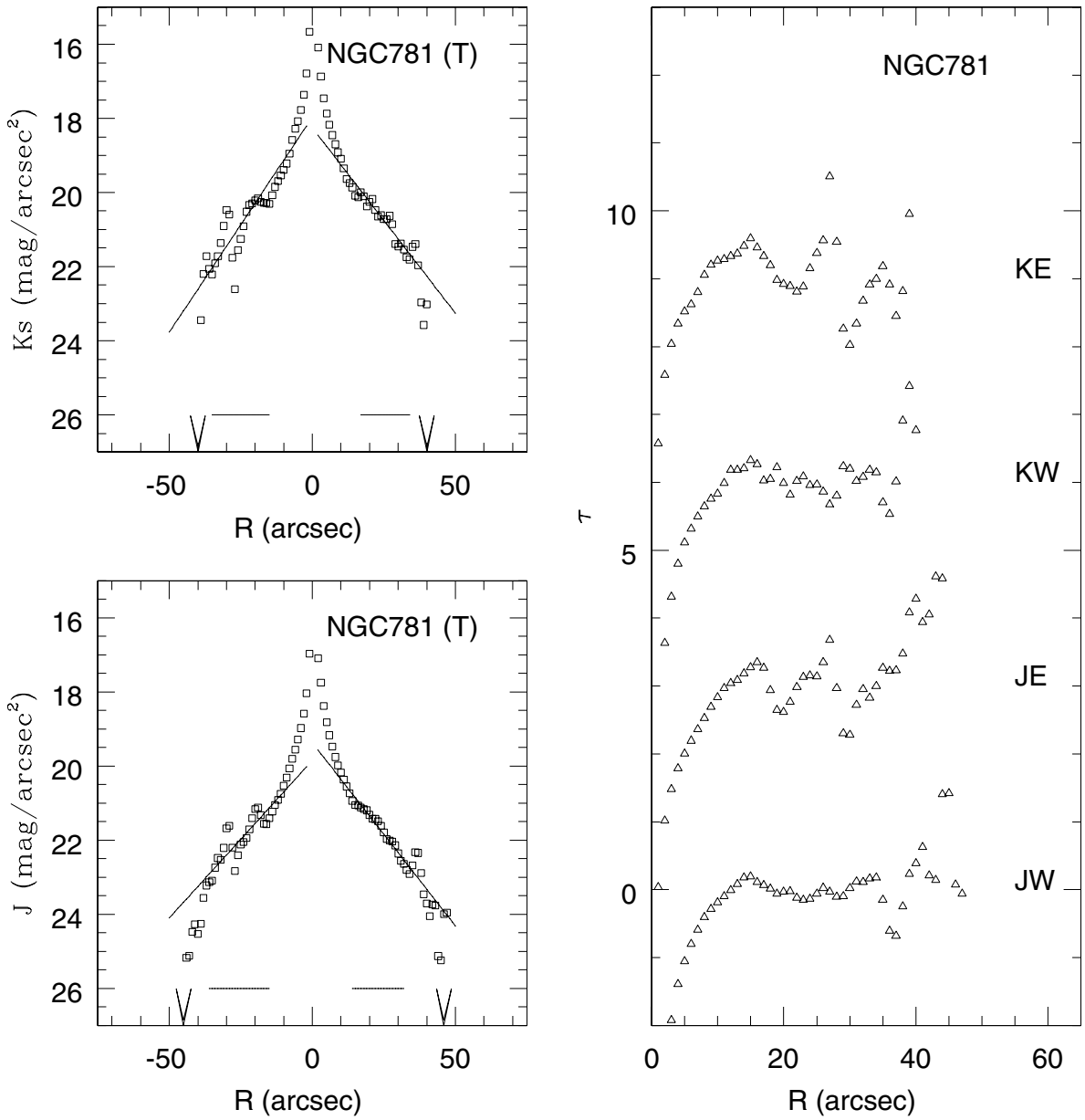

Fig. 5. continued.

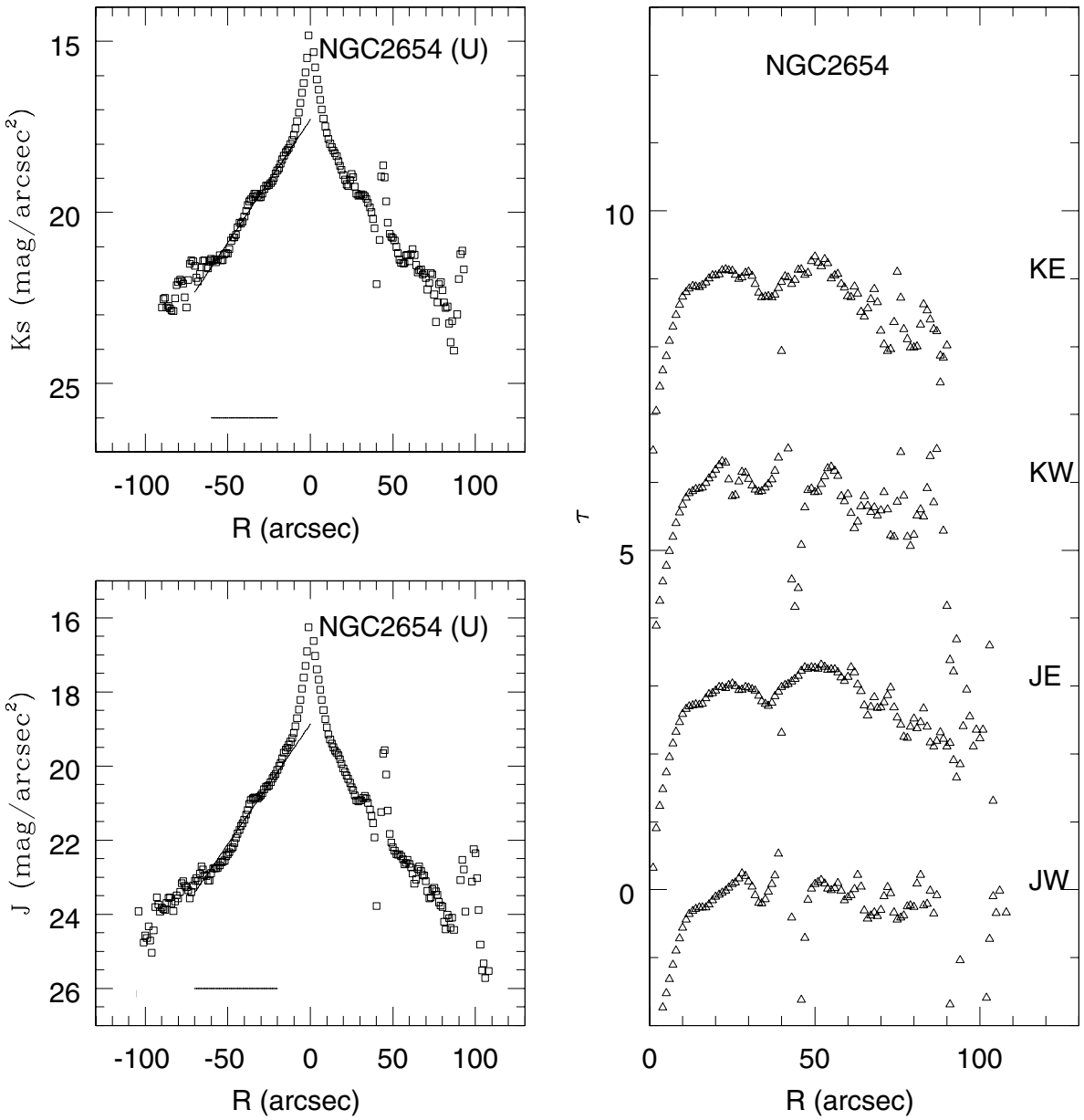

Fig. 5. continued.

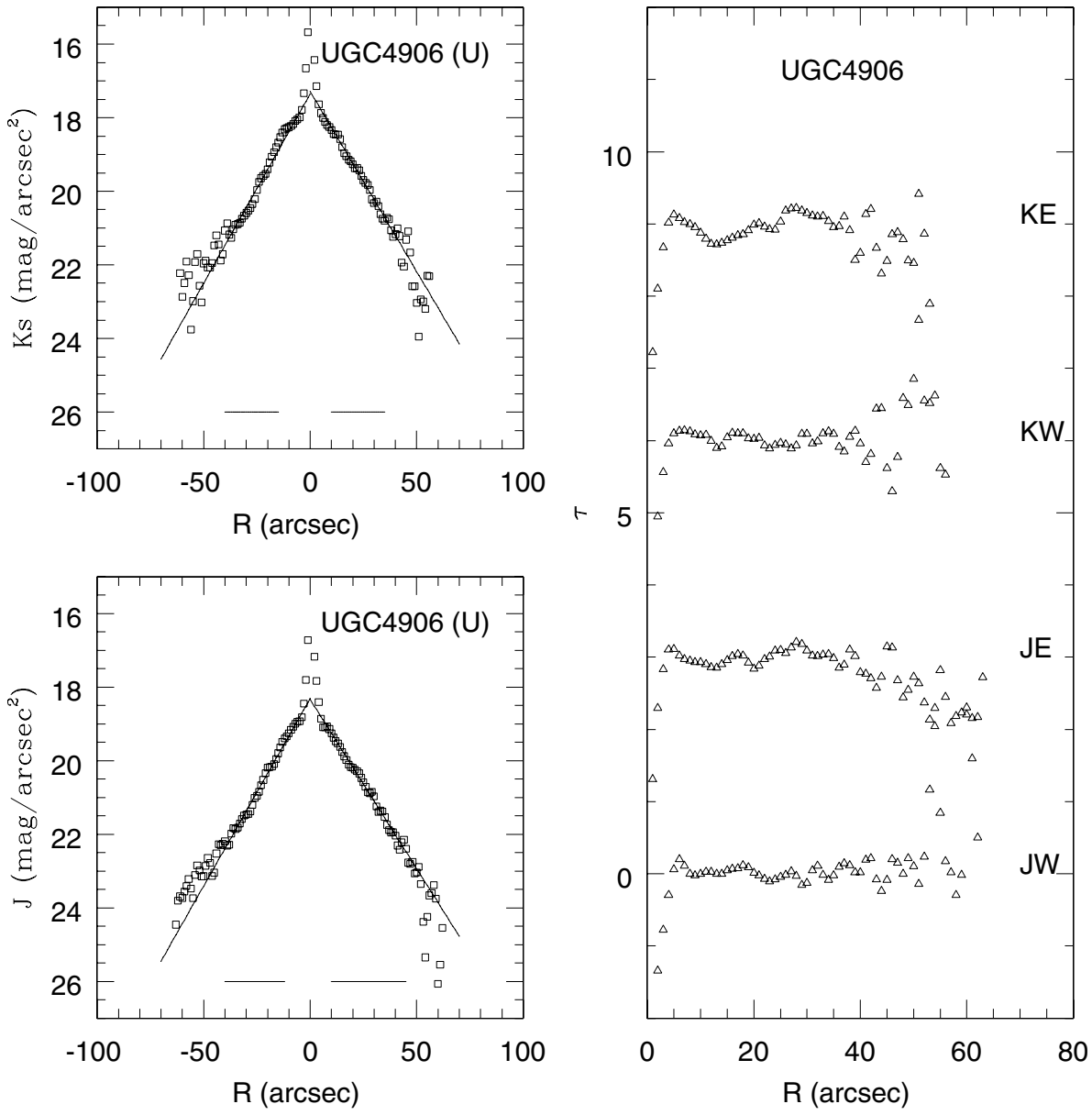

Fig. 5. continued.

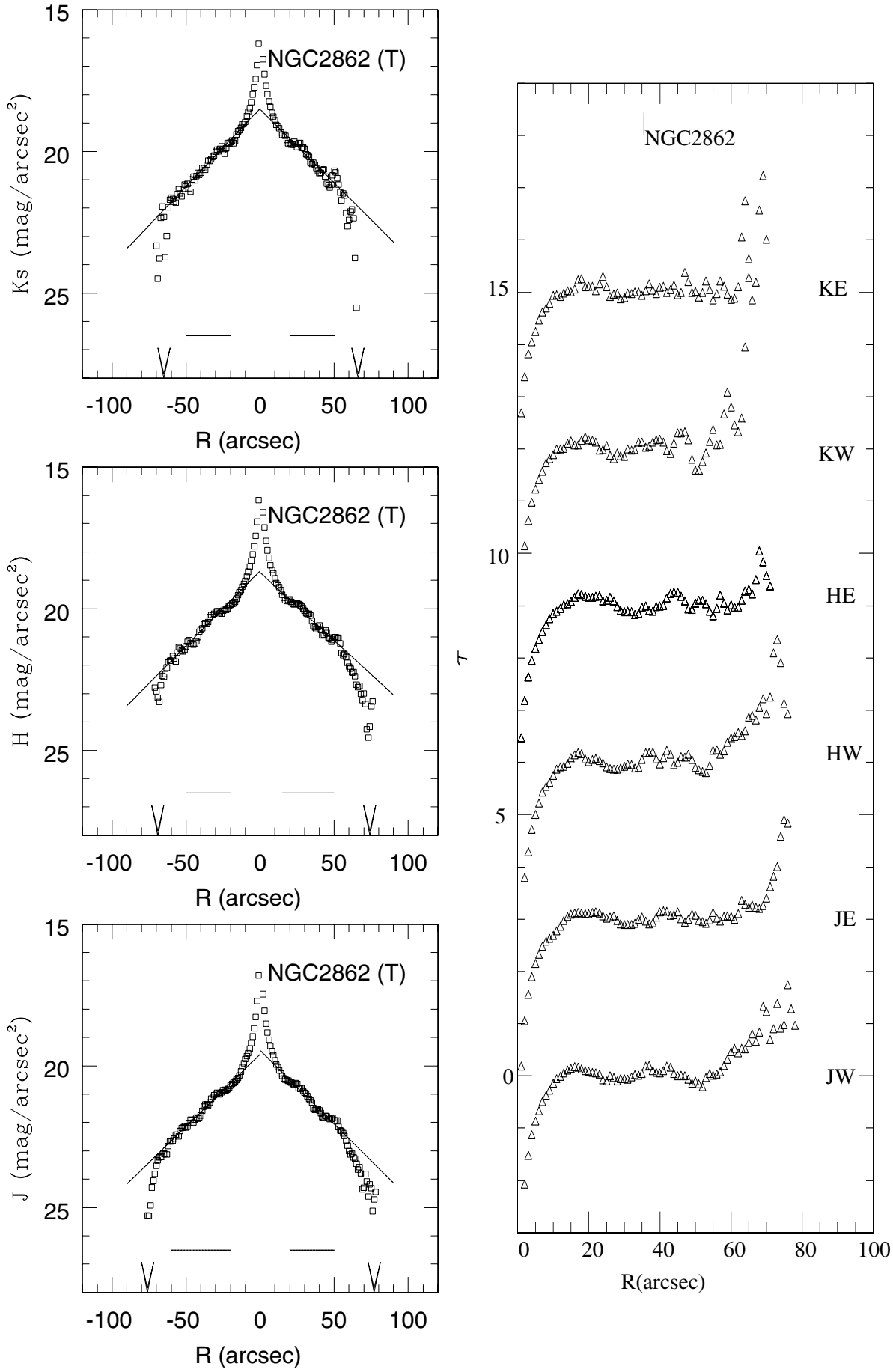

Fig. 5. continued.

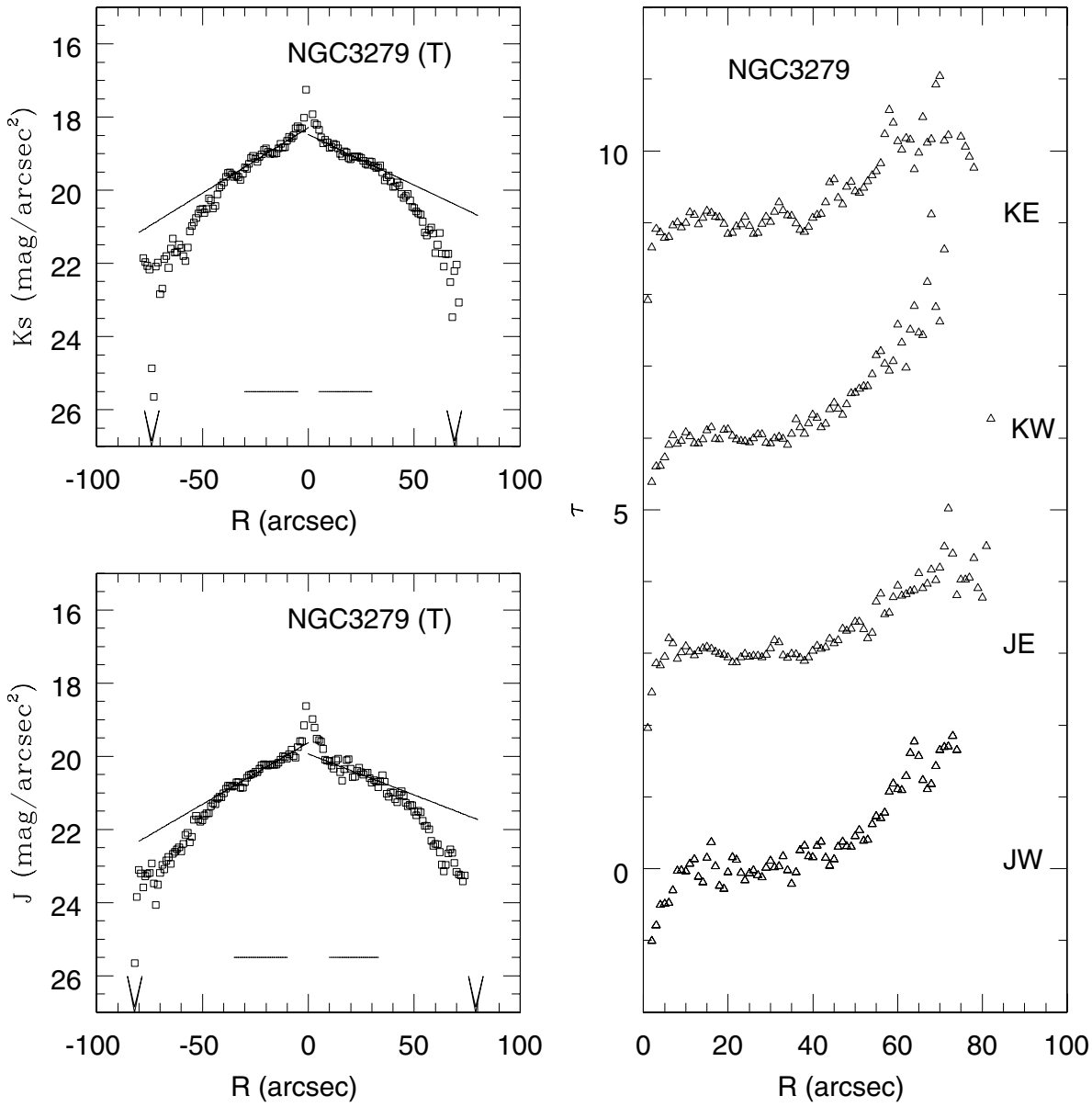

Fig. 5. continued.

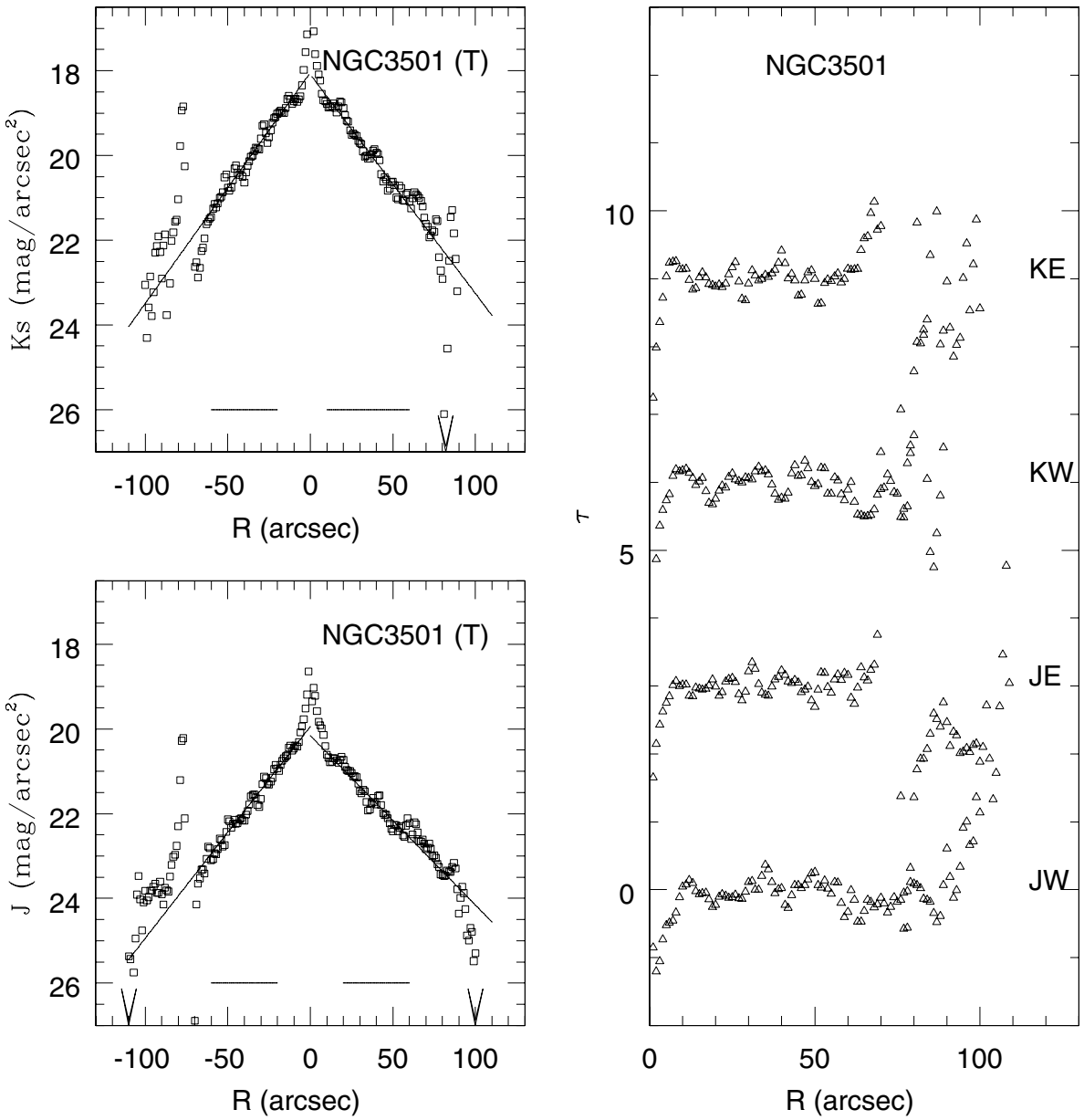

Fig. 5. continued.

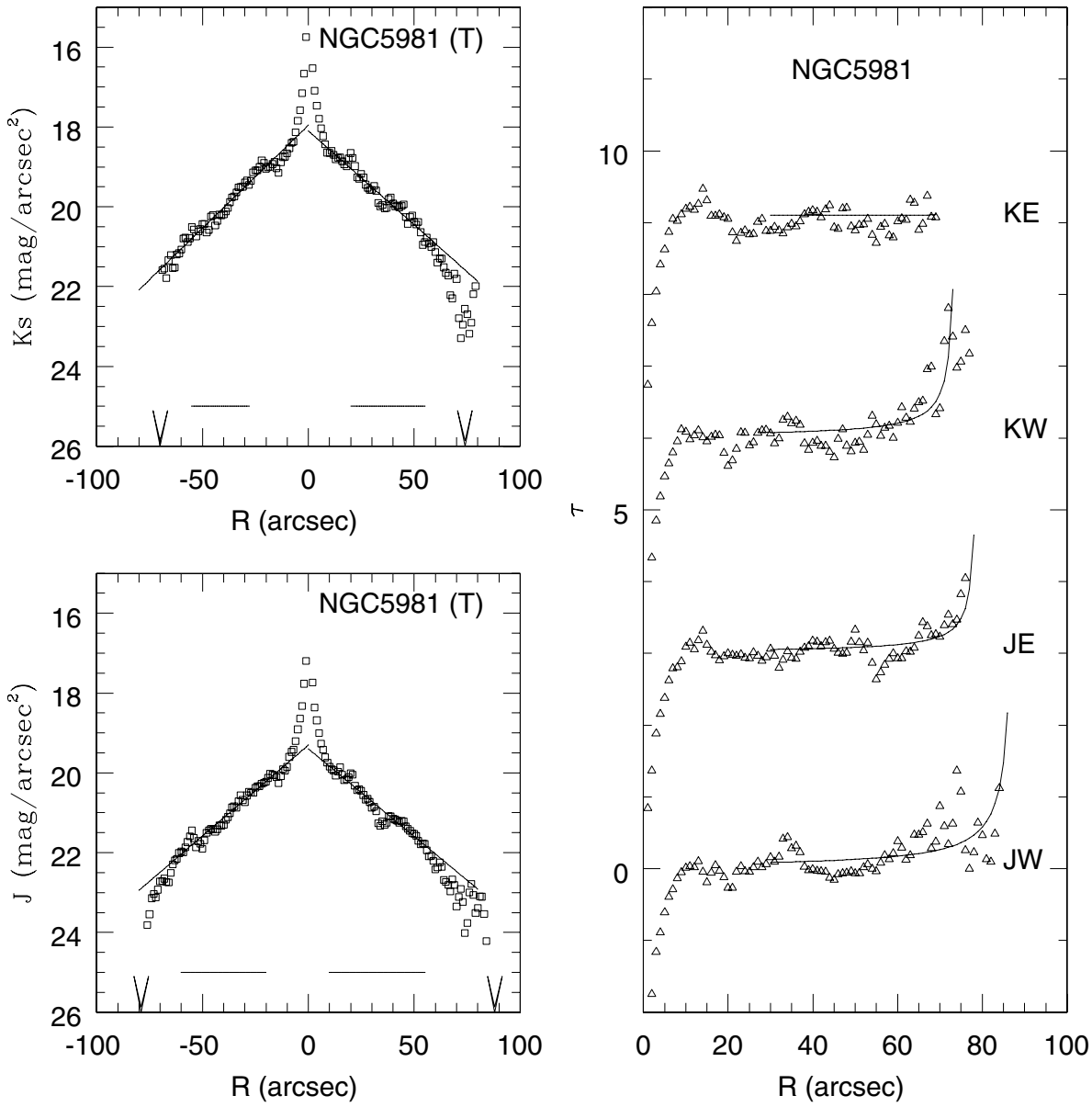

Fig. 5. continued.

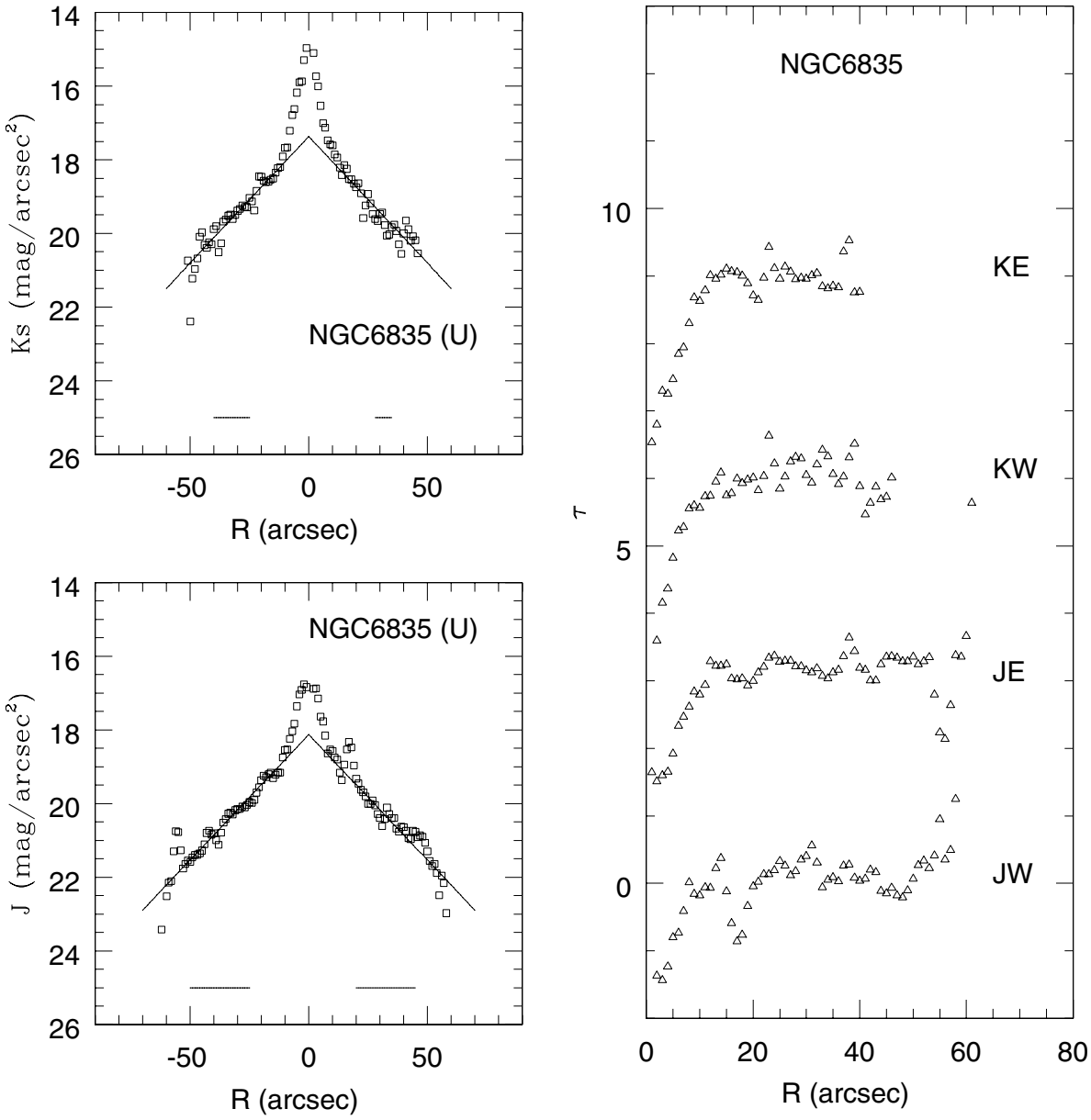

Fig. 5. continued.

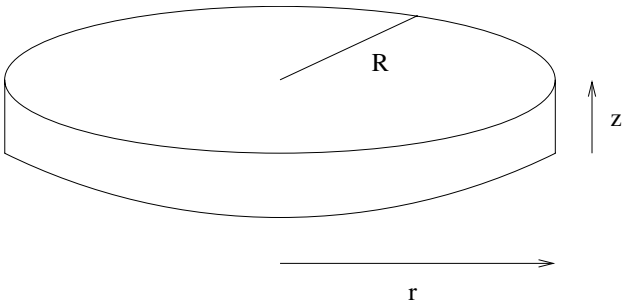

Fig. 6. Definition of the involved quantities in Appendix A.

Appendix A: *z*-integrating + deprojecting = deprojecting + *z*-integrating.

For our purpose the two reduction steps of z-integrated and deprojecting can be interchanged, as we are only interested in obtaining the face-on view of the galaxy.

We observe $I(r, z)$, the surface brightness of the edge-on galaxy. We want to obtain $I(R)$, the surface brightness as a function of the galactocentric radius, for a face-on galaxy.

We take the pixel size as unity.

We can follow two procedures:

a) first summing in z, then deprojecting;
b) first deprojecting, then summing in z.

In the first case, from $I(r, z)$ we obtain $I(r) = \Sigma_z I(r, z)$, then obtain $I(R) = \frac{I(r)}{A(R,r)}$ (quantities are those defined in F01). This last equation is schematic. Of course, $I(R)$ is obtained by a series of more complicated steps but they are essentially of this type and to follow the series step by step does not introduce any change.

In the second case from $I(r, z)$ we obtain $l(R, z)$ as $l(R, z) = \frac{I(r,z)}{A(R,r)}$ (observe that the areas A depend on R and r but not on z). Then we sum in z

$$I(R) = \Sigma_z l(R, z) = \Sigma_z \frac{I(r, z)}{A(R, r)} = \frac{1}{A(R, r)} \Sigma_z I(r, z) = \frac{1}{A(R, r)} I(r)$$

obtaining exactly the same result as in the first procedure.

Appendix B: An inclination 90° > i> 88° does not introduce important errors.

These errors depend not only on i but also on the angular resolution. Suppose a galaxy with $i = 88°$. Along the minor axis distances are reduced by a factor $\sin 2° = 0.035$. We want to know the size OO′ perpendicular to the major axis (Fig. 7). In an exponential disk, the galaxy has no end and $\overline{\mathrm{OO}'} = \infty$. However we want a characteristic value as at P the density is higher and decreases rapidly when we go from P to O′. We must find $I(x)$ for a given r.

We assume $I = I_o \exp(-R/h)$, hence $I(x) = I_o \exp -(r^2 + x^2)^{1/2}$, where r is a constant. First we work with unprojected distances. By a Taylor expansion

$$\left(r^2 + x^2\right)^{1/2} \approx r + \frac{1}{2}\frac{x^2}{r}$$

therefore

$$I(x) = I_o e^{-r/h} e^{-\frac{1}{2}\frac{x^2}{rh}} = I(P) e^{-\frac{1}{2}\frac{x^2}{rh}}$$

where $I(P) = I(R = r)$ is a constant.

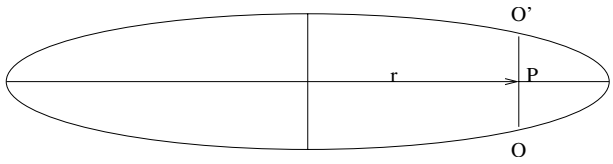

Fig. 7. High inclination view of the galaxy.

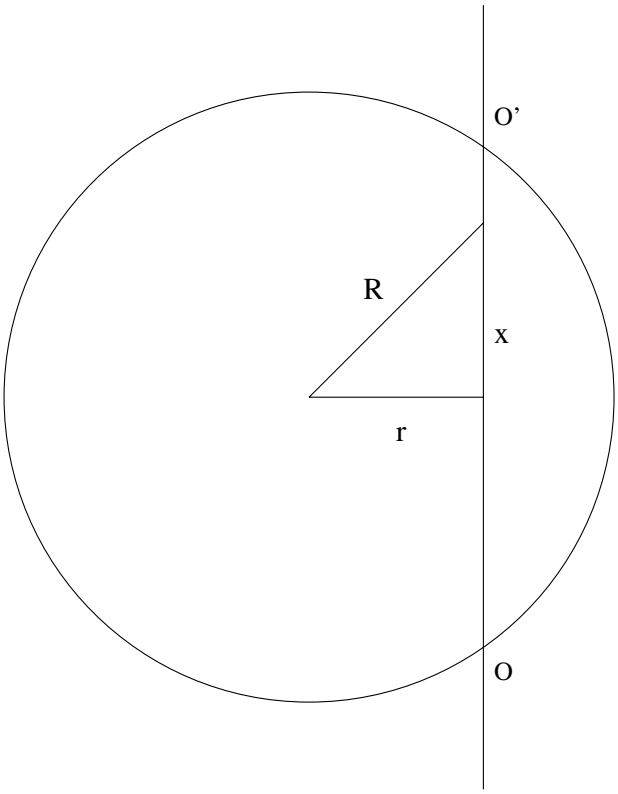

Fig. 8. Definition of the involved quantities in Appendix B.

We now find a characteristic OO′ distance, considering that it corresponds to a value of x at which $I(x)$ is $I(P)/e$

$$e^{-\frac{1}{2}\frac{x^2}{rh}} = \frac{1}{e}$$
$$\frac{1}{2}\frac{x^2}{rh} = 1$$
$$x = \sqrt{2rh}.$$

For typical values in our galaxies, $r = 40''$, $h = 10''$, we have $x = 30''$. And now we project $30'' \sin 2° = 1''$. This is of the order of the pixel size. Therefore our pixel size is too large to appreciate the $i \neq 90°$ inclination. Therefore, variations in z are mainly attributable to real variations in the vertical direction for $i \geq 88°$.

A&A 455, 475–479 (2006)
DOI: 10.1051/0004-6361:20053311

Astronomy & Astrophysics

Truncated stellar discs in the near infrared

II. Statistical properties and interpretation

E. Florido[1], E. Battaner[1], A. Guijarro[1,2], F. Garzón[3,4], and A. Castillo-Morales[1]

[1] Departamento de Física Teórica y del Cosmos, Universidad de Granada, Spain
e-mail: estrella@ugr.es
[2] Centro Astronómico Hispano Alemán, Almería, Spain
[3] Instituto de Astrofísica de Canarias, 38200 La Laguna, Spain
[4] Departamento de Astrofísica, Universidad de La Laguna, Tenerife, Spain

Received 26 April 2005 / Accepted 20 December 2005

ABSTRACT

The results obtained in Paper I are used to study possible relationships between the truncation radius of stellar discs in the NIR and structural parameters of the galaxies. The NIR truncation radius is larger for brighter galaxies, being proportional to V_m^c with $c \approx 3/2$, and with V_m being the asymptotic rotation velocity at large radii (when the rotation curve becomes flat), and is lower for higher wavelengths. When it is normalized to the scalelength, the truncation is an increasing function of the central surface brightness and is lower for late type galaxies, although these correlations are weaker. These relations are in agreement with the scenario of magnetically driven truncations.

Key words. galaxies: structure – galaxies: magnetic fields

1. Introduction

Paper I (Florido et al. 2006) presented the result of the observation of 18 edge-on spiral galaxies in the NIR in order to study the truncation of the stellar disc, the main objective being to describe the truncation curve. This curve is defined as the progressive decrease of the photometric profile taking place at large radii with respect to the mean exponential profile obtained at moderate radii. In this paper we study the relationship of truncation to other parameters of the galaxy. We investigate some key properties that could restrict some of the theoretical scenarios that have been proposed: what types of galaxy show truncation and what relation exists between the truncation, radius, mass, luminosity, rotation velocity at large radii, type, central surface brightness and age of stellar population. The results obtained from this study will be merged with those from a previous one (Florido et al. 2001) in order to obtain a larger sample. No merger with other observations in the optical has been attempted, as the assumption of the same behaviour for optical and NIR truncations is not theoretically justified.

In early works by van der Kruit (1979) truncations were found to have sharp cut-offs. In Paper I and in Florido et al. (2001) truncations were found to be smooth. In these latter two papers it was shown that the smooth behaviour of truncations was not due to projection effects, but was real, existing even in deprojected profiles. In some recent papers (e.g. Pohlen et al. 2002; Pérez 2004) this description is replaced by a two-exponential profile with a sharp elbow. There is increasing evidence favouring the two-slope description, at least in the optical. We are not interested here in the shape of the profile (see Paper I); it may even be that the differences between authors are due to a true difference between the NIR and the optical. For the present, it is not our goal to determine whether this discrepancy is real or is a result of the low signal/noise at these very large radii, especially important in the NIR, and we refer to a "truncation (break)" or simply "truncation".

In Paper I it was proposed that most galaxies in the NIR seem to have a truncation curve that is proportional to $(R-R_{\rm tr})^{-n}$ where $n \approx 1$, R is the radius and $R_{\rm tr}$ is the truncation radius at which the truncation seems to be complete, as obtained by extrapolation of the data.

2. Theoretical models

There are at present at least four alternatives to explain truncations (or breaks): a) the collapse model; b) the threshold model; c) the magnetic model; and d) the interaction model.

According to the collapse model, which was introduced by van der Kruit (1987), truncations were formed in the collapse of the protogalaxy, and would correspond to the maximum angular momentum of the protogalaxy. The gas beyond the truncation was accreted in later phases of galactic evolution. Ferguson & Clark (2001) presented a model in which the truncation/break is also a result of the initial conditions in the gas.

The threshold model was introduced by Kennicutt (1989). Here, when the gas density falls below a certain threshold, star formation should cease. A recent model by Schaye (2004) improved the dynamic mechanism by which the star formation threshold is established. Van den Bosch (2001) presented a hybrid model combining the collapse and threshold models. Elmegreen & Hunter (2006) reproduce two-slope profiles in a threshold model which includes several local effects of SF.

Kregel & van der Kruit (2004) have shown that the threshold model is better supported by the observations than is the collapse model. The model by Schaye (2004) predicts an increase of $R_{\rm tr}/h$ for small radial scale lengths and an increase of $R_{\rm tr}/h$ for higher central intensities and for low surface brightness discs.

For an extensive discussion of the different models, see the review by Pohlen et al. (2004). See also the discussion in Battaner et al. (2002).

In the magnetic model of truncations (Battaner et al. 2002), a centripetal magnetic force acting on the gas makes an important contribution to the redistribution of stars once they are born. If the gas rotates under the equilibrium of gravity plus magnetic forces versus the centrifugal force, and if the magnetic force is suddenly suppressed in the star formation process, the newborn stars would migrate and eventually escape. Some important modification of the mass distribution of the stellar density is therefore unavoidably expected at the region where the magnetic force becomes non negligible in the dynamics of the gas.

The interaction model is only rarely defended (Noguchi & Ishibashi 1986). Schwarzkopf & Dettmar (2000) found similar properties of truncations for isolated galaxies and for interacting galaxies. However, close inspection of the large amount of data provided by these authors reveals some differences. Interacting galaxies have a ratio $R_{\rm tr}(R)/R_{\rm tr}(K)$ that is always larger than one (R is red, K in the NIR), i.e. the truncation radius is larger at shorter wavelengths (with a mean ratio of about 1.6); however, in non-interacting galaxies, this ratio is closer to unity. Thus interaction effects should not be ruled out.

3. Results

Paper I presented new observations of edge-on galaxies observed in the NIR. In all, 18 galaxies were observed, but 5 of them were too noisy, 4 untruncated (within observational limits) and 2 uncertain. Therefore, only 7 galaxies were available to study truncations. Five of them, namely NGC 522 (Sbc), MGC-01-05-047 (Sc), NGC 2862 (SBbc), NGC 3279 (Scd) and NGC 5981 (Sc), were very clearly examples of this phenomenon. There are also two galaxies in which the truncation is not evident but that can be included in our study. These are NGC 781 (Sab) and NGC 3501 (Sc). We also use three truncated galaxies from Florido et al. (2001): NGC 4013 (Sb), NGC 4217 (Sb) and NGC 6504 (Sbc). Therefore the subsample of truncated galaxies adopted in this study is formed by 10 galaxies, 7 from Paper I and 3 from Florido et al. (2001). As we have data for both sides of the galaxies, and measure at least in two filters (J and $K_{\rm s}$), we have $2 \times 2 \times 10 = 40$ points for our statistical subsample.

However, these 40 data points are not independent. Because of the azimuthal symmetry of the galaxies, the results obtained at both sides should be similar (as, in fact, they are) and therefore correlated. Moreover, the closeness of the filter wavelengths, for J and $K_{\rm s}$ (for a few galaxies, also H), does not permit us to consider the J and $K_{\rm s}$ points as really independent, except when considering a differential colour behaviour. The fact that we measure in two filters and on both sides permits us to work with smaller errors, but strictly speaking we have only 10 points for our sample, i.e. the number of galaxies selected. Despite the smallness of the sample, we present the more complete data for truncations in the NIR.

A) Truncation versus Hubble type

At first glance, even for such a small number of galaxies, it seems that truncations are found more often in late type galaxies.

This is a suggestion and is not based on statistics, as the number of galaxies is too low and many more observations would be required. However, we take note of this potential discrimination, as it could be coherent with other findings shown later. This suggestion should be considered with caution, also, because the selection of our samples was not based on physical criteria, but rather considering appropriate angular size, large galactic latitude and date of observations. Therefore the possibility that a bias may be responsible cannot be ruled out.

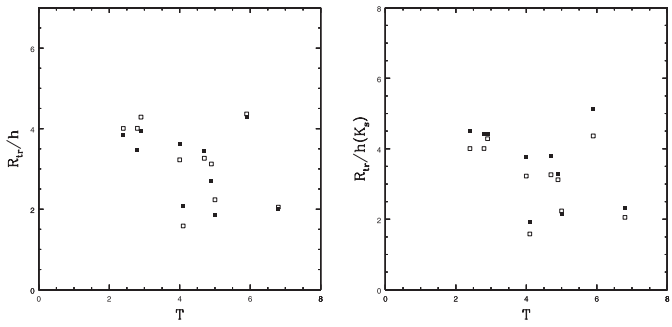

Fig. 1. Ratio of truncation radius to scalelength ($R_{\rm tr}/h$) versus morphological type T (from the LEDA database, `http://leda.univ-lyon1.fr`). Symbols are: open square for $K_{\rm s}$ and filled square for J. In the first panel we plot $R_{\rm tr}/h$ when $R_{\rm tr}$ and h are obtained by the same filter. In the second one we plot $R_{\rm tr}/h(K_{\rm s})$ using $h(K_{\rm s})$ for this ratio with each filter.

We looked for a relation of $R_{\rm tr}(J)/h(J)$ versus T, where $R_{\rm tr}$ is the truncation radius, h is the radial scale length and T is the galaxy type. J and $K_{\rm s}$ are the filters used (Fig. 1). The following tendency was observed: the larger the value of parameter T, the smaller that of $R_{\rm tr}(J)/h(J)$ is. This fact is consistent with the above suggestion that truncation is a phenomenon mainly affecting late-type spirals.

For some relationships, if we want to adopt h as a length representative of the size of the galaxy, then $h(K_{\rm s})$ better represents the "true" radial scale length, as it is less affected by extinction and better represents the old stellar population. Therefore, we have plotted $R_{\rm tr}(J)/h(K_{\rm s})$ and $R_{\rm tr}(K_{\rm s})/h(K_{\rm s})$. In this case, the relationship seems to be reinforced.

Therefore, truncation could be a phenomenon that mainly affects late type spirals. This relation is also found when the large sample of Schwarzkopf & Dettmar (2000) is used. This suggestion, although attractive, remains to be confirmed.

B) Colour dependency of truncations

Table 1 reveals an evident property: $R_{\rm tr}(J) > R_{\rm tr}(K_{\rm s})$. This is so even if the differences are small, because in all galaxies, on all sides, we find $R_{\rm tr}(J) > R_{\rm tr}(K_{\rm s})$, with the exception of NGC 6504. Therefore, there is a dependence of $R_{\rm tr}$ with colour. This number of values is not small but we have applied three tests in order to discard an effect of chance: the T test, the Wilcoxon test and the sign test. In all three tests, the null hypothesis of null difference between $R_{\rm tr}(J)$ and $R_{\rm tr}(K_{\rm s})$ was rejected. Taking, as usual, a contrast size of $\alpha = 0.05$, in every case the significance level (P-value) was much less than 0.05, being 0.004 for the T test. Therefore, $R_{\rm tr}(J)$ is unambiguously higher than $R_{\rm tr}(K_{\rm s})$. This significant difference informs us about a relation with the age of the population.

With respect to relative values, taking the radial scale-length as the unit, we obtain $\langle (R_{\rm tr}/h)\rangle_J = 3.12$ with $\sigma = 0.85$ and $\langle (R_{\rm tr}/h)\rangle_{K_{\rm s}} = 3.21$ with $\sigma = 0.93$. As mentioned above, $h(K_{\rm s})$ better represents the size of the galaxy. Then, we obtain $\langle R_{\rm tr}(J)/h(K_{\rm s})\rangle = 3.57$ with $\sigma = 1.06$. Of course $\langle R_{\rm tr}(J)/h(K_{\rm s})\rangle$ is significantly higher than $\langle R_{\rm tr}(K_{\rm s})/h(K_{\rm s})\rangle$.

These values are in reasonable agreement with other values found in the literature (Pohlen et al. 2002; Barteldrees & Dettmar 1994). For comparison, it should be taken into account that some authors give $R_{\rm br}$ or the point where the break takes place and oth-

Table 1. Basic properties of the galaxies.

Galaxy	$R_{tr}(J)$ (Kpc)	R_{tr} (K_s) (Kpc)	M_B	$\log V_m$	T	μ_o (J) (mag/arcsec^2)	$\mu_o(K_s)$ (mag/arcsec^2)	h (J) (Kpc)	$h(K_s)$ (Kpc)
(1)	(2)	(3)	(4)	(5)	(6)	(7)	(8)	(9)	(10)
NGC 522	13.7	11.2	–20.53	2.252	4.1	20.6	21.0	6.6	7.1
MGC-01-05-047	29.3	27.9	–21.77	2.410	4.9	20.9	19.6	10.8	8.9
NGC 781	11.0	9.8	–20.87		2.4	19.6	18.1	2.9	2.4
NGC 2862	21.7	18.6	–21.44	2.464	4.0	19.5	18.5	6.0	5.8
NGC 3279	7.8	6.9	–19.27	2.208	6.8	19.8	18.4	3.9	3.4
NGC 3501	8.2	7.0	–19.05	2.147	5.9	20.0	18.1	1.9	1.6
NGC 4013	8.5	7.8	–19.50	2.276	2.9	18.6	17.6	2.2	1.8
NGC 4217	11.1	10.0	–19.97	2.298	2.8	18.8	17.4	3.2	2.5
NGC 5981	14.6	12.6	–20.61	2.424	4.7	19.3	18.0	4.2	3.9
NGC 6504	22.2	23.0	–22.53		5.0	19.5	18.7	11.9	10.3

Columns: (1) Galaxy name; (2) truncation radius in J; (3) truncation radius in K_s; (4) absolute B-magnitude; (5) Log of maximum velocity rotation (in km s^{-1}) from radio observations; (6) morphological type code; (7) central surface brightness in J; (8) central surface brightness in K_s; (9) and (10) radial scale-lengths in J and K_s. Columns 4–6 are obtained from the LEDA database (`http://leda.univ-lyon1.fr`). The values of $R_{tr}(J)$, $R_{tr}(K_s)$, $h(J)$ and $h(K_s)$ were independently obtained for both sides of each galaxy. The figure given in this table is the mean value.

ers where it ends. Furthermore, our data in the NIR do not have to coincide with optical data, the differences being important.

C) Truncation and rotation and luminosity

Figure 2 clearly shows a relation between R_{tr} and V_m, the asymptotic rotation velocity (taken from LEDA). R_{tr} (measured in kpc) is an increasing function of V_m, which is emphasized in the log-log plot, showing a relation of the type $R_{tr} \propto V_m^c$. A relationship between R_{tr} and V_m was first obtained observationally by Pohlen et al. (2004). This is clearly supported by our present findings, in another wavelength range, with less scattering and with the mathematical function being determined quantitatively. This fact can be used to restrict the number of theoretical models, as we will see in the discussion.

As different truncation values were detected for J and for K_s, we have analyzed this relation ($\log R_{tr}$, $\log V_m$) for the two filters independently (Fig. 2). Standard Pearson correlations are used because the relation appears to be fairly linear in log space with classical significance tests. For [$\log R_{tr}(J)$, $\log V_m$] the correlation coefficient is 0.83, the slope is 1.54 with error 0.28 and the $\log R_{tr}$ at the origin is −2.45. The P-value is 0.001, much less than 0.05, and therefore the null hypothesis of the absence of a linear relation between both quantities is clearly rejected. For [$\log R_{tr}(K_s)$, $\log V_m$] the correlation coefficient is again 0.83, the slope is 1.58 with a typical error of 0.29 and the value of R_{tr} at the origin is −2.61. The P-value is 0.002, again much lower than 0.05. For both filters, the slope of the regression line (1.54 ± 0.28 and 1.58 ± 0.29) can be approximated to the value 1.5, which is more useful when looking for simple low-power relations.

A relationship physically connected to this one (R_{tr}, V_m) is the relation (R_{tr}, L) with L the luminosity of the galaxy. This is shown in Fig. 3, where we plot $\log R_{tr}$ versus the absolute B-magnitude, showing a clear relation, with R_{tr} being larger for brighter galaxies. A statistical analysis is unnecessary as this relation is a consequence of the previous one, taking into account the Tully-Fisher relation.

D) Other relationships

Figure 4 plots R_{tr} versus h and shows a clear correlation between the two parameters. Thus, more extended galaxies have larger truncation radii, in agreement with Kregel (2003). Larger galaxies have lower truncation radii when measured with the radial scale length as the unit. This relation seems to be non-linear.

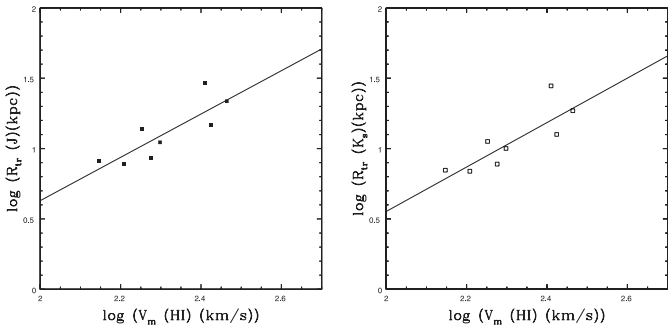

Fig. 2. Log of truncation radius versus log of maximum velocity rotation. Symbols as in Fig. 1.

Figure 5 shows R_{tr}/h versus μ_o (deprojected central surface brightness). This relation has been studied by Kregel & van der Kruit (2004), as mentioned above. Although the scatter of the points is much higher, we see that R_{tr}/h seems to be a decreasing function of μ_o. The correlation coefficient for [$R_{tr}(J)$, μ_o] is only 0.39 and is the same for [$R_{tr}(K_s)$, μ_o]. Therefore, the non existence of this relation cannot be statistically rejected, as the P-value is (in both cases) 0.091, larger than the usual value of 0.05. The correlation coefficient for [$R_{tr}/h(K_s)$, μ_o] is again very poor for J (−0.41) and the P-value very large, 0.071 (>0.05). However, for K_s the P-value is less than 0.04 and the correlation coefficient −0.73. Therefore, for the K_s filter there is a more significant relation: the larger the μ_o value, the lower the truncation radius when measured with $h(K_s)$ as the unit.

4. Discussion

Despite the relatively small size of our sample (10 galaxies), some clear relationships between the truncation radius and structural parameters of galaxies have been found. These relations are obtained in the near infrared and therefore some caution must be taken when comparing with optical data, as they could differ. For example, star formation can take place beyond the truncation; optical measurements would be sensitive to newborn stars but not NIR measurements. The difference could be very large when comparing data in the U-filter and our NIR data and less so when using the R-band and the I-band. It should also be taken into account that young stars are visible in the NIR, especially red

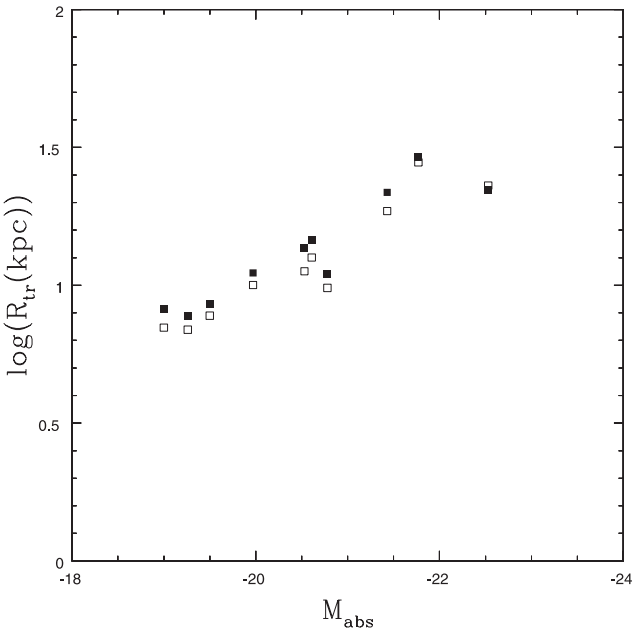

Fig. 3. Truncation radius versus absolute *B*-magnitude. Symbols as in Fig. 1.

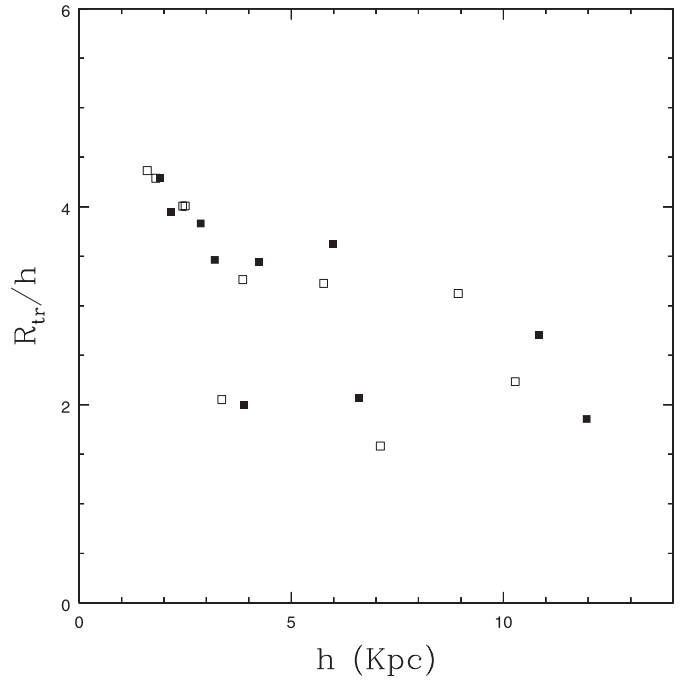

Fig. 4. Ratio of truncated radius to scalelength. Symbols as in Fig. 1.

supergiants. Nevertheless, optical and NIR data provide different information. This difference would be larger if stars moved from their birthplace. The results obtained are summarized here:

- Late-type galaxies seem to be more affected by the mechanism of truncations.
- Bright galaxies have larger $R_{\rm tr}$.
- $R_{\rm tr} = \text{const.} \times V_m^c$ ($c \cong 1.5$).
- Larger galaxies (higher h) have larger $R_{\rm tr}$.
- $\langle R_{\rm tr}(J)/h(K_{\rm s})\rangle = \alpha(J) \approx 3.57$; $\langle R_{\rm tr}(K_{\rm s})/h(K_{\rm s})\rangle = \alpha(K_{\rm s}) \approx 3.21$; hence, we find lower values for $K_{\rm s}$. The difference is small but $R_{\rm tr}(J) > R_{\rm tr}(K_{\rm s})$ for all galaxies with only one exception. Statistical tests show that this difference is significant.
- $R_{\rm tr}/h$ is an increasing function of the central surface brightness, $I_{\rm o}$, even if the correlation seems to be very weak.

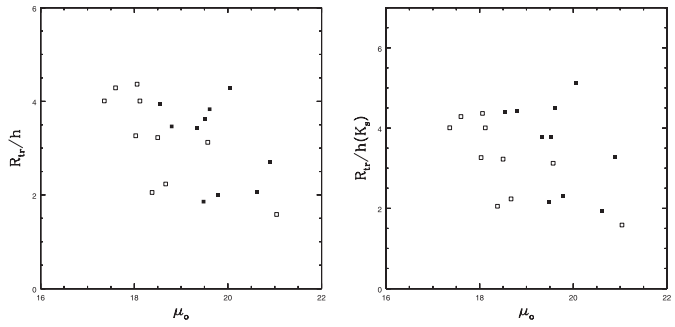

Fig. 5. *Left panel*: ratio of truncated radius to scalelength versus deprojected central surface brightness. *Right panel*: always considering the scalelength in $K_{\rm s}$. Symbols as in Fig. 1.

All these properties can be used to put restrictions on the different theoretical models. Other groups should confirm these results with larger samples of galaxies, with independent NIR observations. Clearly, taking into account the fact that some galaxies lie behind many Milky Way stars and/or that the observations were noisy, the number of galaxies in our sample is low and should be enlarged.

The above results agree very well with the magnetic model of Battaner et al. (2002). In this model an inward magnetic force is added to gravity to explain the high rotation velocity and flat rotation curve of the gas.

From the observational point of view, it is now evident that large magnetic centripetal forces exist, as can be directly deduced from observational magnetic field strengths and energy densities in the Milky Way, NGC 6946 and M 31 (Beck 2004; Battaner & Florido 2005). These measurements show large values of the magnetic field strength and, what is more important, such low gradients of the field, i.e. such a low decline of the field for increasing radii, that an important centripetal magnetic force does exist; this is now empirically demonstrated. These magnetic forces act on the gas and are in equilibrium with gravitational and centrifugal forces. When stars are formed this equilibrium is destroyed and stars escape, thus producing the truncation.

In the simplest version of the magnetic model, Battaner et al. (2002) obtained a formula for the truncation radius

$$R_{\rm tr} \approx \frac{2GM}{V_m^2} \tag{1}$$

where M is the visible galactic mass and θ_0 is the constant value of the rotation velocity at large radii.

As $M \propto L$ and the Tully-Fisher relation establishes that $L \propto V_m^c$ (where c lies between 3 and 4), it is concluded that

$$R_{\rm tr} \propto V_m^{(c-2)} \tag{2}$$

with the exponent $(c - 2)$ being between 1 and 2. This fact matches Fig. 2 very well, showing $R_{\rm tr} \propto V_m^x$, where $x = 1.54 \pm 0.28$ (approximately 1.5 within the estimated error) and the constant of proportionality is 0.004 kpc km$^{-1/2}$ s$^{1/2}$ for J. If we fit the data in $K_{\rm s}$ the values obtained are: $x = 1.58 \pm 0.29$ and the constant of proportionality is 0.002 kpc km$^{-1/2}$ s$^{1/2}$. On the other hand, this would imply that more massive (or more luminous) galaxies would have larger $R_{\rm tr}$, so that the truncation might become undetectable if $R_{\rm tr}$ is larger than the last observable point.

Using the Tully-Fisher relation again, we find $R_{\rm tr} \propto L^{1-\frac{2}{c}}$, the exponent $(1-\frac{2}{c})$ being between 1/3 and 1/2, which also explains Fig. 3.

The magnetic model can also explain the relation between $R_{\rm tr}/h$ and μ_0, the surface brightness at the centre. From Eq. (2) and $M \propto L \propto I_0 h^2$ (where L is the luminosity and I_0 the intensity, in physical units, at the centre) and the Tully-Fisher relation, taking now for simplicity $L \propto V_m^4$

$$\frac{R_{\rm tr}}{h} \propto \frac{L}{V_m^2 h} \propto \frac{L^{1/2}}{h} \propto \frac{I^{1/2}h}{h} = I_0^{1/2}. \quad (3)$$

As $\mu \propto -\log I$, the magnetic model predicts a relation between $R_{\rm tr}$ (when measured in radial scale units) and μ_0, the central surface brightness. Any other characteristic galactic magnitude (such as h itself) cancels out.

The magnetic model also predicts $R_{\rm tr}/h \propto M^{1/2}/h$, and hence it explains an observational fact mentioned above: extended galaxies, with large values of h, have smaller truncation radii (measured with the radial scale length, h, as the unit). In this case, the presence of $M^{1/2}$ in the formula would make the relation $[R_{\rm tr}/h, h]$ be affected by a high degree of scatter, and the relation is certainly more complex than that.

The fact that the magnetic model satisfactorily explains the relations found here does not necessarily imply that all other models should be excluded. For instance, on qualitative grounds, the threshold model (e.g. Schaye 2004) could predict a relationship between absolute magnitude and truncation if the threshold gas surface density were located further out in a bright galaxy. Some development of this model to explain the findings of this paper is necessary. The magnetic model remains an interesting alternative, as it predicts not only a qualitative relation, but also the mathematical function.

5. Conclusions

The magnetic model satisfactorily explains all the statistical properties reported in this paper. We thus propose this scenario as responsible for producing truncations. The agreement is particularly noticeable concerning the relation between truncation radius and the power 3/2 of the asymptotic rotation velocity.

Magnetic forces are important in the rotation dynamics of the gas, as deduced from observed magnetic field strengths. These forces no longer act when gas is converted into stars, which must have a large influence on the stability of the orbits of young stars, even leading to massive escape.

Large galaxies of type Sa and Sb have less need for dark matter, hence, in the magnetic interpretation, they require lower magnetic fields, i.e. the truncation would be a less important effect in large (massive and luminous) galaxies, especially those with a prominent bulge. The fact that late-type galaxies, which are bulge-poor, could be more affected by truncations is in agreement with the magnetic scenario.

Pohlen et al. (2004) found several examples of truncations in edge-on SO galaxies. Even if these galaxies are at present gas-poor, they had both gas and star formation in the past. Thus, the mechanisms suggested by the magnetic hypothesis would have been operating in the past, and they would have inherited truncations.

The fact that the truncation in the optical could be better described by a two-exponential profile could be compatible with a smooth, complete truncation in the near infrared. The newly formed stars would be, under the magnetic interpretation, in the process of escaping. If the escape speed is roughly equal to V_m, i.e. of the order of 100 km s^{-1}, and if the length of the escape path is of the order of ~10 kpc, the escape time would be of the order of 10^8 years, a time that differentiates clearly between new-born and old stars. The fact that $R_{\rm tr}(K_{\rm s}) < R_{\rm tr}(J)$ also fits this interpretation.

In the magnetic interpretation, the truncation corresponds to a true decrease in the total mass (stars + gas) and a connection with a decrease in the rotation velocity should be expected. This decrease has been observed (Casertano 1983; van der Kruit 2001; Bottema 1995) although this fact requires more observational support and may be explained by other means.

Acknowledgements. This paper has been supported by the "Plan Andaluz de Investigación" (FQM-108) and by the "Secretaría de Estado de Política Científica y Tecnológica" (AYA2004-08251-C02-02, ESP2004-06870-C02-02). We are indebted to Andrés González-Carmona who helped us with the statistical analysis. We also acknowledge the LEDA data base organisation, which was highly useful for this research. Thanks to the anonymous referee for valuable comments and suggestions that have contributted to improve the final version of the paper.

References

Barteldrees, A., & Dettmar, R.-J. 1994, A&AS, 103, 475
Battaner, E., & Florido, E. 2005, A&A, accepted
Battaner, E., Florido, E., & Jiménez-Vicente, J. 2002, A&A, 388, 213
Beck, R. 2004, Ap&SS, 289, 293
van den Bosch, F. C. 2001, MNRAS, 327, 1334
Bottema, R. 1995, A&A, 295, 605
Casertano, S. 1983, MNRAS, 203, 735
Elmegreen, B. G., & Hunter, D. A. 2006, ApJ, 636, 712
Ferguson, A. M. N., & Clark, C. J. 2001, MNRAS, 325, 781
Florido, E., Battaner, E., Guijarro, A., Garzón, F., & Jiménez-Vicente, J. 2001, A&A, 378, 82
Florido, E., Battaner, E., Guijarro, A., Garzón, F., & Castillo-Morales, A. 2006, A&A, 455, 467 (Paper I)
Kennicutt, R. C. 1989, ApJ, 344, 685
Kregel, M. 2003, Ph.D. Thesis, Univ. of Groningen
Kregel, M., & van der Kruit, P. C. 2004, MNRAS, 355, 143
van der Kruit, P. C. 1979, A&AS, 38, 15
van der Kruit, P. C. 1987, A&A, 173, 59
van der Kruit, P. C. 2001, in Galaxy Disks and Disk Galaxies, ed. J. G. Funes, & E. M. Corsini, ASP Conf. Ser., 230, 119
Noguchi, M., & Ishibashi, S. 1986, MNRAS, 219, 305
Pérez, I. 2004, A&A, 427, L17
Pohlen, M., Dettmar, R. J., Lütticke, R., & Aronica, G. 2002, A&A, 392, 807
Pohlen, M., Beckman, J. E., Hüttemeister, S., et al. 2004, in Penetrating Bars through Masks of Cosmic Dust, ed. D. L. Block, K. C. Freeman, & I. Puerari, Astrophys. Spac. Sci. Library, 713
Schaye, J. 2004, ApJ, 609, 667
Schwarzkopf, U., & Dettmar, R.-J. 2000, A&A, 361, 451

A&A 472, L39–L42 (2007)
DOI: 10.1051/0004-6361:20078214

Astronomy & Astrophysics

Letter to the Editor

The truncation of the stellar disc of NGC 6504

E. Florido[1,3], E. Battaner[1,3], A. Zurita[1,3], and A. Guijarro[1,2,3]

[1] Departamento de Física Teórica y del Cosmos, Universidad de Granada, Spain
e-mail: estrella@ugr.es
[2] Centro Astronómico Hispano Alemán, Almería, Spain
[3] Instituto Carlos I. Física Teórica y Computacional, Universidad de Granada, Spain

Received 4 July 2007 / Accepted 19 July 2007

ABSTRACT

Context. This is the first work reporting observations of the truncation of a stellar disc, in both the optical and the NIR spectral ranges. No galaxy has been observed at both wavelengths with the required depth. The optical radial profiles of spiral galaxy discs seem to suggest a double exponential behaviour, whilst NIR profiles seem to show a real truncation.
Aims. We study one galaxy with the best available resolution and detail, in both optical and NIR bands, with the same deprojection method and similar reduction procedures, to see if the different descriptions are real.
Methods. Optical observations (V band) were made with the William Herschel Telescope. NIR observations (J, H, K_s) were made with the CAIN infrared camera on the Carlos Sánchez Telescope in Tenerife (Spain). The deprojection method was that described in Florido et al. (2001, A&A, 378, 82; 2006a, A&A, 455, 467).
Results. NGC 6504 has a real truncation in both the optical and the NIR radial profiles. A double exponential does not fit the observed optical profile. The truncation radius is larger in the V band than in the NIR by ∼10 arcsec, about 3 kpc (equivalent to about 10%). We examine the constraints of this observation in theoretical scenarios.

Key words. galaxies: fundamental parameters – galaxies: photometry – galaxies: structure

1. Introduction

The truncation of stellar discs was discovered by van der Kruit (1979). In this and subsequent papers (van der Kruit & Searle 1981a,b, 1982a,b) the truncation was described as a relatively sharp outer edge in the surface brightness distribution. Since then, there have been many interesting works (Barteldrees & Dettmar 1994; de Grijs et al. 2001, and others) on disc truncations. In the pioneer papers by van der Kruit & Searle, there was a truncation radius, $R_{\max}$, beyond which the surface brightness drops to undetectable values. The interpretation of these and later works was that the truncation was complete, i.e. that there was no emission beyond $R_{\max}$ (see, for instance, Wainscoat et al. 1992), and this is the actual meaning of the word "truncation". The truncation radius must therefore be estimated by extrapolation. The difference between the observed light profile and the extrapolated exponential of the inner disc was called the truncation curve by Florido et al. (2001, hereinafter F1), who suggested a $(R_{\max} - R)^{-\alpha}$ profile with α close to unity. The conclusions obtained by F1 and Florido et al. (2006a, hereinafter F6A) were based on NIR imaging of edge-on galaxies.

Recent optical observations have shown that there is no real truncation (as defined by van der Kruit), but a break separating the inner and the outer exponential surface brightness radial profiles, with an outer radial scale length which is usually, but not always, shorter than the inner one. This description has been proposed by Pohlen et al. (2002a, 2004), Pohlen & Trujillo (2006), Erwin et al. (2005) and others. Pérez (2004) and Trujillo & Pohlen (2005) have shown that young galaxies at $z \sim 1$ can also be described with a double exponential. The break is noticeably sharp.

The question arises: are these real truncations or breaks? Are some stellar discs truncated and others simply "broken"? Are galaxy disc light profiles truncated in the NIR and "broken" in the optical? Are we dealing with the same phenomenon? The aim of this work is to answer these questions. To date, no galaxy has been measured in both the NIR and the optical, at least with the depth required for measuring the faint outer parts of galaxy discs. Another problem when comparing results is that some authors observe face-on galaxies and others edge-on ones, therefore using very different techniques, with the deprojecting method being particularly important. It would therefore be very interesting for one team to perform detailed observations of one single galaxy, with the highest quality of images in both the optical and the NIR, and with the same deprojection technique, thereby avoiding differences in reduction methods.

The selected galaxy was NGC 6504, an edge-on Sab galaxy with a total B magnitude of 13.05. The reason for this selection is that in F1 it was not clear if this galaxy was truncated or "broken"; no other selection criterion was taken into account. The deprojection technique was that presented in F1 and used in F1 and F6A. In both papers the error estimation introduced by this method was discussed in detail. It is worth mentioning here that the truncation curve is modified after deprojection, but the truncation radius is not (F1).

2. Observations

The V band imaging of NGC 6504 was obtained in service mode at the 4.2 m William Herschel Telescope (WHT) at the Observatorio del Roque de Los Muchachos in La Palma, using the prime focus imaging platform (PFIP) instrument and the

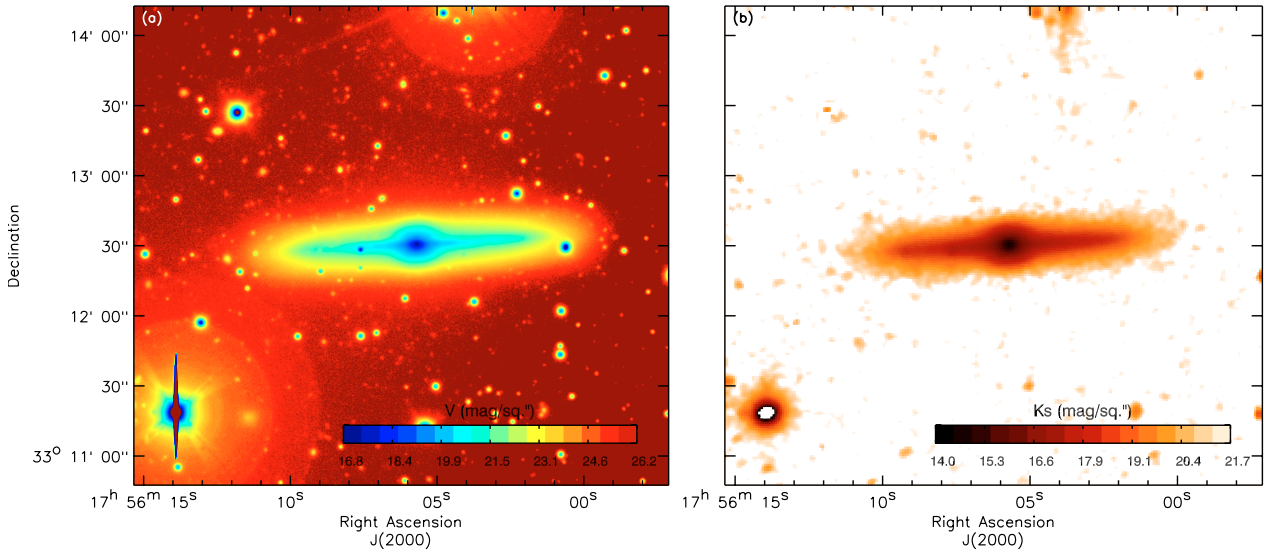

Fig. 1. a) V-band image of NGC 6504. **b)** K_s-band image of NGC 6504 where the foreground stars have been removed for obtaining the surface brightness profiles (see Sect. 3 or F1 for further details). Both images show the same field of view.

Harris V filter. The observations were taken on July 10, 2003 under photometric sky and ∼1″ seeing. The PFIP detector is a mosaic of two thinned 2048 × 4096 EEV-42-80 CCDs providing a field of view of ∼16.1′ × 16.1′ and a pixel scale of 0.236″/pix. Given the relatively small angular size of the galaxy (∼2.6′ diameter at 25 mag/arcsec^2), it was centred on CCD2. NGC 6504 was observed for a total integration time of 6800 s (split into 42 images of 150 s, one image of 200 s and one of 300 s), during which the airmass varied between 1.06 and 1.95.

Three different Landolt (Landolt 1992) standard star fields were observed during the night (on CCD2) at airmasses ranging from 1.08 to 2.6.

The data were processed using standard techniques with IRAF[1]. These comprise overscan subtraction and bias, and flat field corrects. The individual images were then sky substracted, aligned and combined. The spatial resolution of the final combined images is 1.1″.

The IRAF package DAOPHOT was used to perform aperture photometry of the 11 stars of the Landolt standard star fields. The photometric calibration (which does not take into account colour terms) yielded a photometric zero point for ADU s^{-1} of 26.20+/−0.01, and an extinction coefficient of −0.109+/−0.005. The limiting magnitude for signal-to-noise ratio per pixel equal to 3 in the final reduced image is 26.3 mag arcsec^{-2}.

The image was astrometrically calibrated using the task ASTROM in GIPSY (van der Hulst et al. 1992), and identifying our foreground stars in the Palomar plates. The accuracy of the astrometric calibration was ∼0.3″. The final reduced image is shown in Fig. 1a.

The NIR observations and data reduction techniques on which the results presented in this paper are based were described in detail in F1. These observations were carried out at the 1.5 m CST in the Teide Observatory, Tenerife, with the infrared camera CAIN.

The IRAF package was also used for the NIR bands. Flatfielding and sky substraction were performed very carefully as we were dealing with extremely low brightness at the rim of the galaxy. To this end, the telescope was pointed alternately to six sky fields, also alternating object-sky, in order to correct properly for the fast atmospheric variations.

Star substraction was carried out following methods described in F1, following verification that this substraction was sufficient to obtain the truncation curve. Figure 1b shows the star substracted K_s image. However, a bright star seen in the SE part of the galaxy in the V band could have distorted the V-profile and was eliminated from the analysis. Calibration was performed using the 2MASS catalogue. After these processes, the galaxy was rotated to render the x-axis and the major axis coincident. Then we obtained profiles at several z (distance from the galactic plane). By using the IMPLOT task the position of the 3σ-level was determined. We deprojected the z-profiles with the numerical method described in F1, and finally all the z-profiles were summed to obtain the final radial profile.

3. Results

In Figs. 2–4 we plot the NW side V-band profile compared with those in J, H and K_s at both sides. All these curves are deprojected, and only points above 3σ (before deprojection) are plotted. The V curve has higher spatial resolution and reaches larger radii. We think there is no need of a statistical analysis to conclude directly from these figures that:

1. None of the profiles correspond to a double exponential description. In particular, the V band profile shows a monotonic decrease, without a break. The slope becomes monotonically larger until reaching V = 28.5 mag/arcsec^2 where the slope is extremely high. These profiles are interpreted as a non-sharp but complete truncation.
2. There is a clear difference between the truncation radius in the optical and the NIR bands. An extrapolation provides an estimated value of $R_{max}(V)$ = 85 arcsec and $R_{max}(K_s)$ = 74 arcsec. This difference corresponds to ≈3.3 kpc, assuming a distance of 63.18 Mpc for this galaxy. The difference between the NIR bands is not as high. A colour dependence of the truncation radius was already found by Florido et al. (2006b; thereafter F6B) where

[1] IRAF is distributed by the National Optical Astronomy Observatories, which is operated by the Association of Universities for Research in Astronomy, Inc. (AURA) under cooperative agreement with the National Science Foundation.

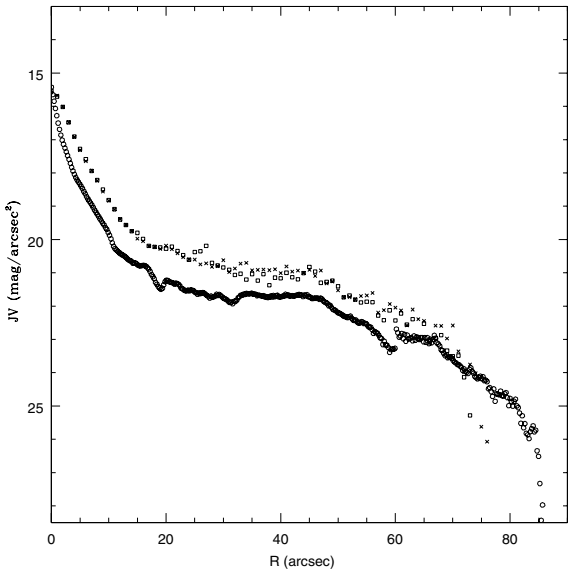

Fig. 2. *V* band profile of NGC 6504 (circles) compared with the eastern side (squares) and the western side (crosses) profiles in *J* band.

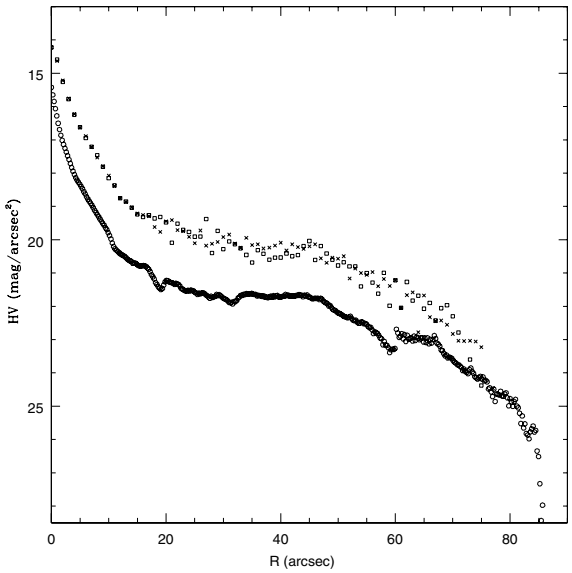

Fig. 3. *V* band profile of NGC 6504 (circles) compared with the eastern side (squares) and the western side (crosses) profiles in *H* band.

$R_{\max}(J) > R_{\max}(K_s)$ for all galaxies in the sample, with only one exception, NGC 6504.

3. Even if this conclusion cannot be reached with only one galaxy, this result strongly suggests that NIR truncations are associated with optical truncations. However, the location of the truncation radius depends on the colour. Nevertheless, the galaxy NGC 6504, and probably many others, does have a real truncation.

4. Discussion

We should now consider the kind of restraints the results of this paper introduce to the different proposed scenarios for explaining disc truncations. This discussion should take into account the arguments given by van der Kruit (2007) in a recent paper. We could classify these scenarios into small and large scale dynamics. In small scale dynamic models, the truncation or break

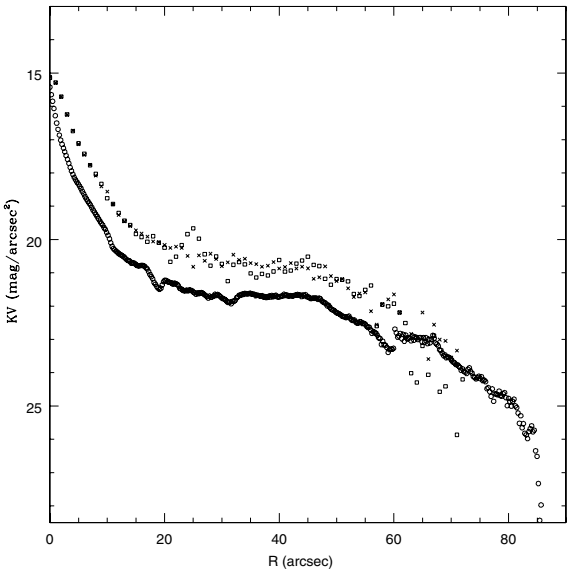

Fig. 4. *V* band profile of NGC 6504 (circles) compared with the eastern side (squares) and the western side (crosses) profiles in K_s band.

is due to some inability of the gas to form stars, for instance, due to a threshold in the density (van der Kruit & Searle 1981a; Kennicutt 1989; Schaye 2004), or due to an excessive local angular momentum in the collapsing clouds induced by differential rotation (Fall & Efstathiou 1980).

Van der Kruit (2007) has provided abundant bibliographic and direct findings about a sudden drop in the rotation curve at the truncation radius. This drop indicates a sudden decrease of the total density (gas + stars) which, if confirmed, should be an important constraint to small scale dynamic models. Battaglia et al. (2006) also found a drop of 25 km s^{-1} in NGC 5055.

Van der Kruit (2007) proposes that the disc of the galaxy was formed in two steps. In the first step the inner disc was formed with a maximum size given by the truncation radius, and this boundary was set by the maximum specific angular momentum in the material forming the disc. The extragalactic gas falling in later, in the second step, produces the outer warped gaseous region.

This model implies in-falling motions, and is therefore considered as a large scale dynamic process. This scenario should take into account that optical warps exist in a region formed before the infalling, i.e. for $R < R_{\max}$. There are several catalogues of optical warps (Sánchez-Saavedra et al. 1990, 2003; Reshetnikov & Combes 1999), and for $z \sim 1$ spirals (Reshetnikov et al. 2002). In addition, differential precession could destroy warps. We understand, however, that in the van der Kruit scenario, what is essential is that there was a first step in which $R_{\max}$ was established; the warps in the outer disc could be produced by other, or additional, means.

The magnetic model (Battaner et al. 2002) also involves large scale dynamical processes. Here, there is an inward magnetic force acting on the gas. When stars are formed this force no longer acts; therefore stars can move outwards and even escape. The truncation occurs at a point beyond which stars escape from the galaxy. It is noteworthy that, at least on quantitative grounds, this model is able to explain both truncations and "antitruncations". The word "antitruncation" was introduced by Erwin et al. (2005) for galaxies with the radial scale-length of the outer exponential larger than that of the inner one. In the NIR, antitruncations are found as well, NGC 2654 being a good example (F6B).

In the magnetic model, the antitruncation should correspond to that region in which recently formed stars would have moved outwards but not escaped. Beyond this antitruncation region the truncation cut-off would exist. It should be noted here that the magnetic model is able to explain the correlation between $R_{\rm max}$ (or $R_{\rm break}$) and the rotation velocity for larger R found by Pohlen et al. (2004) and F6B.

The conclusion of this work is based only on one galaxy but it could be representative of a frequently observed type of galaxy. Real truncations in the NIR have been observed: NGC 4013, NGC 4217, NGC 5981 (F1), NGC 522, NGC 2862, NGC 3279 and MCG-01-05-047 (F6A) are good examples. The colour dependence was anticipated in F6B.

The model by van der Kruit (2007) and the magnetic model do explain the existence of a real truncation, but the colour dependence is somewhat puzzling. We have shown that the IR truncation (which traces older stars) takes place at smaller galactocentric radii than the optical. In the former model, the outer disc could have been growing with time and therefore the truncation radii could have been displaced to larger radii differentially in the optical. In the latter model, new born stars beyond $R_{\rm max}$ would be in the process of escaping, which could increase the optical truncation radius, as the escaping time can be of the order of 10^8 years.

Acknowledgements. This paper has been supported by the "Consejería de Educación y Ciencia de la Junta de Andalucía" and by the "Secretaría de Estado de Política Científica y Tecnológica" (AYA2004-08251-C02-02,ESP2004-06870-C02-02). The WHT is operated on the island of La Palma by the Isaac Newton Group in the Spanish Observatorio del Roque de los Muchachos of the Instituto de Astrofísica de Canarias. We are very grateful to the ING staff for taking the service *V* band observations. The CST is operated on the island of Tenerife by the Instituto de Astrofísica de Canarias.

References

Barteldrees, A., & Dettmar, R. J. 1994, A&AS, 103, 475
Battaglia, G., Fraternali, F., Oosterloo, T., & Sanicisi, R. 2006, A&A, 447, 49
Battaner, E., Florido, E., & Jiménez-Vicente, J. 2002, A&A, 388, 213
Erwin, P., Beckman, J. E., & Pohlen, M. 2005, ApJ, 626, L81
Fall, S. M., & Efstathiou, G. 1980, MNRAS, 193, 189
Florido, E., Battaner, E., Guijarro, A., Garzón, F., & Jiménez-Vicente, J. 2001, A&A, 378, 82 (F1)
Florido, E., Battaner, E., Guijarro, A., Garzón, F., & Castillo-Morales, A. 2006a, A&A, 455, 467 (F6A)
Florido, E., Battaner, E., Guijarro, A., Garzón, F., & Castillo-Morales, A. 2006b, A&A, 455, 475 (F6B)
de Grijs, R., Kregel, M., & Wesson, K. H. 2001, MNRAS, 324, 1074
van der Hulst, J. M., Terlouw, J. P., Begeman, K., Zwitser, W., & Roelfsema, P. R. 1992, in Astronomical Data Analysis Software and Systems I, ed. D. M. Worall, C. Biemesderfer, & J. Barnes, ASP Conf. Ser., 25, 131
Kennicutt, R. C. 1989, ApJ, 344, 685
van der Kruit, P. C. 1979, A&AS, 38, 15
van der Kruit, P. C. 2007 [arXiv:astro-ph/0702486]
van der Kruit, P. C., & Searle, L. 1981a, A&A, 95, 105
van der Kruit, P. C., & Searle, L. 1981b, A&A, 95, 116
van der Kruit, P. C., & Searle, L. 1982a, A&A, 110, 61
van der Kruit, P. C., & Searle, L. 1982b, A&A, 110, 79
Landolt, A. U. 1992, AJ, 104, 340
Pérez, I. 2004, A&A, 427, L17
Pohlen, M., & Trujillo, I. 2006, A&A, 454, 759
Reshetnikov, V., & Combes, F. 1999, A&A, 138, 131
Reshetnikov, V., Battaner, E., Combes, F., & Jiménez-Vicente, J. 2002, A&A, 382, 513
Sánchez-Saavedra, M. L., Battaner, E., & Florido, E. 1990, MNRAS, 246, 458
Sánchez-Saavedra, M. L., Battaner, E., Guijarro, A., López-Corredoira, M., & Castro-Rodríguez, N. 2003, A&A, 399, 457
Schaye, J. 2004, ApJ, 609, 667
Trujillo, I., & Pohlen, M. 2005, ApJ, 630, L17
Wainscoat, R., Cohen, M., Völk, Walker, H. J., & Schwartz, D. E. 1992, ApJS, 83, 111

A&A 399, 457–467 (2003)
DOI: 10.1051/0004-6361:20021751

Astronomy & Astrophysics

A catalog of warps in spiral and lenticular galaxies in the Southern hemisphere

M. L. Sánchez-Saavedra[1], E. Battaner[1], A. Guijarro[2], M. López-Corredoira[3], and N. Castro-Rodríguez[3,4]

[1] Dpto. Física Teórica y del Cosmos, Universidad de Granada, Avd. Fuentenueva, 18002 Granada, Spain
[2] Centro Astronómico Hispano Alemán, 04080 Almería, Spain
[3] Astronomisches Institut der Universitat Basel, Venusstrasse 7, Binningen, Switzerland
[4] Instituto de Astrofísica de Canarias, 38205 La Laguna, Tenerife, Spain

Received 26 April 2002 / Accepted 22 November 2002

Abstract. A catalog of optical warps of galaxies is presented. This can be considered complementary to that reported by Sánchez-Saavedra et al. (1990), with 42 galaxies in the northern hemisphere, and to that by Reshetnikov & Combes (1999), with 60 optical warps. The limits of the present catalog are: logr25 > 0.60, B_t < 14.5, $\delta(2000) < 0°$, $-2.5 < t < 7$. Therefore, lenticular galaxies have also been considered. This catalog lists 150 warped galaxies out of a sample of 276 edge-on galaxies and covers the whole southern hemisphere, except the Avoidance Zone. It is therefore very suitable for statistical studies of warps. It also provides a source guide for detailed particular observations. We confirm the large frequency of warped spirals: nearly all galaxies are warped. The frequency and warp angle do not present important differences for the different types of spirals. However, no lenticular warped galaxy has been found within the specified limits. This finding constitutes an important restriction for theoretical models.

Key words. catalogs – galaxies: structure – galaxies: spiral – galaxies: elliptical and lenticular, cD

1. Introduction

As peripheral features, disc warps are better observed in 21 cm. This has been the preferred observational technique since their discovery by Sancisi (1976) and the study by Bosma (1981) until more recent samples such as those analyzed by García-Ruíz (2001) and García-Ruíz et al. (2000). Optical observations provide an important complementary tool. Even if the relation between optical and radio warps remains unclear (García-Ruíz 2001), the great advantage of optical observations lies in the much larger samples available. Catalogs of warped galaxies have been useful to establish observational restrictions to explain warps. Sánchez-Saavedra et al. (1990) first produced a catalog of 42 optical warps in the northern hemisphere out of a sample of 86 galaxies analyzed. The most noticeable result was that, taking into account the probability of non-detection of warps when the line of nodes lies in the plane of the sky, nearly all galaxies are warped, confirming the suggestion made by Bosma (1981) for HI warps. Warps are therefore a universal feature, common for nearly all spiral galaxies. Even this large frequency is a severe restriction for theoretical models. As Reshetnikov and Combes said: "Differential precession wraps any warp", in contrast with the large frequency of real warped galaxies.

Send offprint requests to: M. L. Sánchez-Saavedra,
e-mail: malusa@ugr.es

Reshetnikov & Combes (1999) studied 540 edge-on galaxies, from which a sub-sample of 60 warped galaxies was presented. One of the most noticeable new results reported in their work was that warps were more frequent in denser environments. They also found that the warping mechanism is equally efficient in all types of spirals.

Detailed studies of particular warped galaxies in the optical, such as those by Florido et al. (1991) and by de Grijs (1997), the latter including 44 galaxies, are also of great interest, evidently, but the production of catalogs has greater statistical power.

Here, we have examined all the galaxies contained in LEDA, with logr25 (log 10 of axis ratio (major/minor axis)) > 0.60, B_t (total B-magnitude) < 14.5, $\delta(2000) < 0°$, $-2.5 < t$ (morphological type code) < 7. The number of galaxies fulfilling these requirements is 276, which is our basis for this work, in which the galaxies were analyzed by means of the DSS. Only discs with a warp angle *wa* (measured from the galactic center to the last observable point with respect to the galactic plane) larger than 4° are considered to be warped.

To determine the warp angle, *wa*, and other geometrical parameters of a warp, or even the very existence of a warp, subjective criteria were used in previous catalogs and are in turn used in the present one. Objective procedures (Jiménez-Vicente 1998; Jiménez-Vicente et al. 1998) present some problems when applied to a very large number of galaxies and were

disregarded. More specifically, in some galaxies it was necessary to apply the automatic star removing procedure to an excessively large number of stars, rendering the map highly distorted. Also the separation of real warps and spiral arms was difficult to define, even for galaxies where this separation is clear to the human eye.

Our work presents 150 warps extracted from 276 edge-on galaxies. The recent study by Reshetnikov & Combes (1998, 1999) extracted 60 warps from 540 edge-on galaxies. It is evident that these authors used stricter criteria to define when a galaxy is definitely warped. Our sample and scope are complementary. The Reshetnikov & Combes sample is limited by coordinates $0^{\rm h} \leq \alpha\ (1950) \leq 14^{\rm h}$, $\delta\ (1950) \leq -17.5^{\circ}$; ours by $\delta(2000) \leq 0^{\circ}$ only. That implies that the study by Reshetnikov & Combes covers 17% of the whole sky, whereas ours covers 50%. This, however, is not strictly true because a large part of the Southern Sky is covered by the Zone of Avoidance due to the large extinction near the galactic plane. Taking into account this Avoidance Zone ($-15^{\circ} \leq b \leq 15^{\circ}$) our sample would cover about 40% of the whole sky. Even if based on a smaller number of edge-on galaxies, this large coverage renders the present study more useful for certain statistical tasks, such as the distribution of the orientation of warps.

Another important difference between the work by Reshetnikov & Combes and the present study is that the former only pays attention to the discs of spiral galaxies while ours includes lenticular galaxies. This inclusion is very important from the theoretical point of view because, roughly speaking, lenticulars have a disc but not gas; in other words, the distribution of stars in lenticulars is very similar to that in spiral galaxies. This is an overgeneralisation, because even if the amount of gas in lenticulars is less than in even late-type spirals, lenticulars do process some gas in the outer parts. Another important difference between lenticulars and spirals is that the former have a dominant bulge. This fact makes analysis less simple, as huge bulges could in principle affect the formation of warps. In any case observations of warps in lenticulars have yet to be made and may introduce decisive restrictions on the mechanisms behind warps.

A large number of theories can be found in the literature: non-spherical dark halos misaligned with the disc (Sparke & Casertano 1988; Dubinski & Kuijken 1995), gas infall into the dark matter halo (Ostriker & Binney 1989; Binney 1992) or directly into the disc (López-Corredoira et al. 2002), interactions with companions or small satellites (Weinberg 1998), intergalactic magnetic fields (Battaner et al. 1990), etc. Kuijken & García-Ruíz (2001) recently presented a concise review summarizing several mechanisms proposed to explain warps.

The large fraction of warped galaxies seems to exclude one of the most obvious models, based on interactions, but this hypothesis has been reconsidered by Weinberg (1998), assuming a strong tidal amplification by the gravitational wake of a satellite, although this fact was not confirmed by García-Ruíz (2001) who also argued that the warp of the Milky Way induced by the Magellanic Clouds should have been predicted to have a very different orientation from that observed. Warps are common in merging systems (Schwarzkopf & Dettmar 2001) but it remains unclear whether mergers or interactions can explain all, or at least most, warps.

Warps are more frequent in denser environments (Reshetnikov & Combes 1999). Early $z \approx 1$ warps were considered by Reshetnikov et al. (2002). Early warps were larger, which favors the interaction model. Other models cannot be completely excluded from the observation of early $z \approx 1$ warps. Magnetic fields were also much stronger and the rate of infall of matter onto a galaxy was higher.

García-Ruíz (2001) observed that, even if galaxies with extended discs may be warped, extended discs are less frequent in denser environments.

The observational study of warps in lenticular galaxies is crucial. If warps are absent or are less common in lenticular galaxies which are gas-poor, those models based on gravitation alone would have difficulty in explaining this fact. Models in which a permanent torque acts on the gas of the galaxy would have the preference. For instance, models like that by Kahn & Woltjer (1959) or its more recent version by López-Corredoira et al. (2002) would be favored. Note that neither model requires the assumption that galaxies have a large dark matter halo. The magnetic model, in which intergalactic magnetic fields maintain the warp structure, would acquire additional support from this fact.

It therefore seems that the compilation of large samples of warped galaxies, even if they contain just a few parameters about their position, the parent galaxy and the magnitude and shape of the warping, contributes as much as the detailed examination of the HI maps of a few galaxies.

2. The new catalog

The catalog presented here is shown in Table 1. Column 1 gives the pgc number, Col. 2 the galaxy-name or the alternate name, Cols. 3 and 4 the source position for the epoch J2000, the right ascension (al2000, hours decimal value) and declination (de2000, degrees decimal value), Col. 5 the log 10 of apparent diameter (d25 in 0.1′), Col. 6 the log 10 of the axis ratio (major axis/minor axis) and Col. 7 the morphological type code (t), (directly adopted from LEDA). Columns 8–11 are the result of our analysis, with the following meaning:

Column 8, labelled *N/S*, specifies the apparent warp rotation, *S* clockwise, *N* counterclockwise. The *N* and *S* shapes are really two sides of the same galaxy. This difference is therefore completely unimportant from the physical point of view. However, we have kept the information because it is needed when studying the distribution of warps in space, for instance, when considering the orientation of warps in a cluster of galaxies (see for instance, Battaner et al. 1991) *L* means that only one of the two sides of the galaxy is warped. *U* means that the two warps are not antisymmetric, i.e. that the apparent warp rotation on the two sides of the edge-on galaxies has opposite directions. In this column, "-" means unwarped and "?" unclear.

Column 9, labelled *(wa)E–W*, gives the warp angle, defined as the angle between the outermost detected point and the mean position of the plane of symmetry, as defined by the internal unwarped region. *E* indicates the side of the galaxy closer to the

Table 1. Sample of spiral galaxies. In the 8th column "-" means unwarped and "?" unclear; in the 9th column "b" means arms, "c" means corrugated and "0" means unwarped.

pgc	galaxy-name	al2000	de2000	logd25	logr25	t	*N/S*	(*wa*)E–W (°)	β (°)	α_s
43	ESO 293-27	0.00817	−40.48400	1.32	0.60	3.9	*LS*	?	-	-
474	MCG-7-1-9	0.10585	−41.48350	1.53	0.62	6.0	*N*	7–7	30–31	0
627	NGC 7	0.13899	−29.91700	1.39	0.67	4.9	*U*	7–7	31–31	0
725	ESO 241-21	0.17223	−46.41940	1.34	0.62	3.1	*N*	11–10	39–24	0.05
1335	ESO 78-22	0.34918	−63.85740	1.34	0.79	4.3	*S*	6–9	17–31	0.2
1851	NGC 134	0.50616	−33.24550	1.92	0.64	4.0	*N*	11–8	22–31	0.16
1942	ESO 473-25	0.53050	−26.72010	1.41	0.84	4.9	*N*	5–7	-	0.17
1952	ESO 79-3	0.53390	−64.25240	1.45	0.72	3.1	*N*	9–7	27–21	0.13
2228	NGC 172	0.62067	−22.58500	1.31	0.72	4.0	*S*	7–7	-	0
2482	NGC 217	0.69267	−10.02120	1.45	0.65	0.5	*N*	9–10	-	0.05
2789	NGC 253	0.79252	−25.28840	2.43	0.66	5.1	*N*	7–9	22–27	0.13
2800	MCG-2-3-15	0.79624	−9.83460	1.24	0.64	3.1	*U*	7–7	-	0
2805	MCG-2-3-16	0.79641	−9.89970	1.48	0.82	6.7	*S*	14–10	-	0.17
2820	NGC 259	0.80091	−2.77630	1.46	0.65	4.0	*S*	7–9	45–45	0.13
3743	NGC 360	1.04763	−65.60990	1.57	0.89	4.3	*N*	8–7	22–17	0.07
4440	IC 1657	1.23536	−32.65060	1.41	0.65	3.8	*S*	7–11	21–39	0.22
4912	ESO 476-5	1.35492	−22.80050	1.29	0.61	3.9	*N*	10–14	27–34	0.17
5128	NGC 527	1.39947	−35.11520	1.23	0.62	0.1	*N*	7–7	22–22	0
5688	NGC 585	1.52839	−0.93300	1.34	0.66	1.0	*N*	5–3	-	0.25
6044	ESO 297-16	1.63329	−40.06770	1.20	0.61	5.9	*N*	9–7	17–16	0.13
6161	ESO 413-16	1.66594	−28.69710	1.29	0.67	3.9	*S*	8–7	17–16	0.07
6242	ESO 3-4	1.69266	−83.21210	1.28	0.70	4.1	*S*	7–7	22–27	0
6966	MCG-1-5-47	1.88028	−3.44720	1.48	0.87	4.8	*S*	2–7	-	0.56
7298	ESO 245-10	1.94570	−43.97350	1.34	0.61	3.2	?	?	-	-
7306	IC 176	1.94814	−2.01910	1.29	0.68	5.1	*N*	7–7	22–22	0
7427	ESO 297-37	1.97033	−39.54460	1.27	0.67	4.1	*N*	3–7	-	0.4
8326	ESO 30-9	2.17801	−75.03880	1.40	0.61	4.8	*S*	4–5	-	0.11
8581	MCG-1-6-77	2.24055	−7.36840	1.36	0.78	2.7	?	?	-	-
8673	IC 217	2.26957	−11.92660	1.34	0.67	5.8	*U*	5–6	-	0.09
9582	NGC 964	2.51835	−36.03420	1.33	0.60	1.9	*S*	3–6	-	0.33
10645	ESO 546-25	2.81346	−19.97110	1.16	0.73	3.6	-	0–0	-	-
10965	NGC 1145	2.90931	−18.63550	1.47	0.74	5.1	*N*	?–4	-	-
11198	MCG-2-8-33	2.96379	−10.16720	1.45	0.63	0.2	*N*	14–11	22–16	0.12
11595	ESO 248-2	3.08523	−45.96350	1.47	0.69	6.9	*S*	10–10	18–18	0
11659	NGC 1244	3.10866	−66.77640	1.26	0.63	2.1	*S*	6–6	9–9	0
11851	IC 1898	3.17224	−22.40440	1.53	0.77	5.8	*N*	5–3	23–11	0.25
11931	NGC 1247	3.20399	−10.48070	1.54	0.82	3.8	*N*	4–5	-	0.11
12521	NGC 1301	3.34317	−18.71590	1.34	0.66	4.2	*N*	9–6	17–11	0.2
13171	IC 1952	3.55728	−23.71280	1.40	0.66	4.1	*N*	8–6	18–13	0.14
13458	NGC 1406	3.65626	−31.32200	1.59	0.70	4.4	*S*	3–5	20–11	0.25
13569	NGC 1422	3.69191	−21.68240	1.36	0.63	2.4	-	0–0	-	-
13620	NGC 1421	3.70818	−13.48830	1.54	0.60	4.1	?	?	-	-
13646	MCG-2-10-9	3.71559	−12.91570	1.50	0.90	5.0	*N*	7–5	27–18	0.17
13727	NGC 1448	3.74221	−44.64400	1.88	0.65	5.9	S	9–8	45–25	0.06
13809	ESO 358-63	3.77189	−34.94240	1.69	0.64	4.7	*LS*	3–0	-	1
13912	IC 2000	3.81879	−48.85810	1.63	0.74	6.1	*N*	5–5	-	0
13926	ESO 482-46	3.82835	−26.99350	1.55	0.82	5.1	?	c	-	-
14071	NGC 1484	3.90487	−36.97110	1.40	0.69	3.5	*S*	5–5	-	0

Table 1. continued.

pgc	galaxy-name	al2000	de2000	logd25	logr25	*t*	*N/S*	*(wa)*E–W (°)	β (°)	α_s
14190	NGC 1495	3.97255	−44.46650	1.46	0.73	5.1	*S*	4–9	-	0.38
14255	NGC 1511A	4.00542	−67.80730	1.28	0.63	1.3	*S*	7–7	-	0
14259	ESO 483-6	4.00724	−25.18150	1.43	0.79	3.2	*S*	5–7	-	0.17
14337	ESO 117-19	4.04233	−62.31570	1.31	0.76	3.9	-	0–0	-	-
14397	NGC 1515	4.06748	−54.10270	1.72	0.62	4.0	*N*	5–8	10–10	0.23
14824	IC 2058	4.29847	−55.93440	1.49	0.94	6.6	*S*	4–6	-	0.2
15455	ESO 202-35	4.53769	−49.67520	1.44	0.81	3.3	*N*	5–5	16–11	0
15635	NGC 1622	4.61015	−3.18920	1.52	0.73	2.0	*S*	5–10	13–21	0.33
15654	NGC 1625	4.61841	−3.30340	1.37	0.64	3.1	*S*	6–6	11–?	0
15674	NGC 1628	4.62671	−4.71480	1.27	0.64	3.1	*N*	8–9	11–17	0.06
15749	ESO 157-49	4.66038	−53.01200	1.28	0.66	4.1	*S*	11–11	21–21	0
15758	IC 2103	4.66323	−76.83680	1.28	0.76	4.9	?	b	-	-
16144	IC 2098	4.84561	−5.41870	1.35	0.87	5.9	-	0–0	-	-
16168	MCG-1-13-22	4.85739	−3.12210	1.22	0.60	3.0	*S*	4–4	-	0
16187	IC 2101	4.86165	−6.22970	1.23	0.66	5.0	?	?	-	-
16199	ESO 361-15	4.86601	−33.17860	1.44	0.68	6.1	*S*	7–7	9–17	0
16239	NGC 1686	4.88184	−15.34620	1.25	0.71	4.0	*N*	4–7	–16	0.27
16636	MCG-1-13-50	5.05475	−2.93560	1.39	0.82	3.0	-	0–0	-	-
16849	NGC 1827	5.16768	−36.95890	1.48	0.76	5.9	?	-	-	-
16893	MCG-1-14-3	5.19493	−3.09160	1.16	0.67	3.1	N	7-5	-	0.17
17027	ESO 362-11	5.27748	−37.10210	1.68	0.75	4.1	*N*	6–4	11–6	0.2
17056	IC 407	5.29517	−15.52370	1.24	0.70	4.9	*S*	6–6	-	0
17174	NGC 1886	5.36352	−23.81260	1.51	0.77	3.9	-	0–0	-	-
17248	MCG-2-14-16	5.41515	−12.68870	1.28	0.77	2.0	-	0-0	-	-
17433	NGC 1963	5.55355	−36.39980	1.46	0.78	5.8	?	?	-	-
17969	ESO 555-2	5.84077	−19.72620	1.34	0.74	3.9	*S*	6–6	-	0
17993	ESO 160-2	5.85418	−53.57480	1.26	0.63	3.0	?	?	-	-
18394	ESO 5-4	6.09456	−86.63220	1.58	0.68	2.9	-	0–0	-	-
18437	ESO 121-6	6.12505	−61.80710	1.60	0.75	5.1	*S*	3-3	-	0
18765	ESO 489-29	6.28479	−27.38620	1.52	0.72	3.9	-	0–0	-	-
18833	NGC 2221	6.33750	−57.57740	1.33	0.66	1.1	*U*	7–6	18–11	0.08
19996	ESO 491-15	7.01183	−27.36820	1.35	0.68	5.0	*N*	3–3	-	0
20903	ESO 428-28	7.39406	−30.05070	1.39	0.84	5.3	*U*	-	-	-
21338	ESO 257-19	7.58538	−46.92470	1.40	0.74	6.2	?	b	-	-
21815	ESO 311-12	7.79281	−41.45170	1.57	0.74	0.1	*S*	3–3	6–8	0
21822	ESO 560-13	7.79774	−18.74840	1.48	0.77	4.0	*N*	10–4	18–8	0.4
22174	ESO 35-18	7.91809	−76.41310	1.53	0.65	4.9	-	0–0	-	-
22272	ESO 494-7	7.94852	−24.90810	1.45	0.63	4.3	-	0–0	-	-
22338	ESO 209-9	7.97080	−49.85160	1.80	0.83	6.0	*N*	5–5	9–17	0
22910	ESO 89-12	8.16682	−64.93620	1.41	0.86	4.1	*N*	7–7	15–17	0
23558	ESO 495-12	8.39769	−25.83820	1.27	0.67	3.0	*S*	11–11	14–17	0
23672	IC 2375	8.43881	−13.30300	1.28	0.70	3.0	*S*	17–14	40–27	0.1
23992	ESO 562-14	8.55493	−17.95650	1.15	0.64	3.0	*N*	9–10	34–45	0.05
23997	NGC 2613	8.55626	−22.97330	1.85	0.62	3.2	?	c	-	-
24225	ESO 563-3	8.62196	−20.93980	1.21	0.65	0.4	-	0–0	-	-
24479	ESO 563-14	8.71596	−20.05070	1.38	0.66	6.5	?	c	-	-
24685	ESO 563-21	8.78801	−20.03590	1.48	0.81	4.1	*S*	3–5	-	0.25
25400	ESO 60-24	9.04451	−68.22650	1.46	0.78	2.9	*S*	2–5	-	0.43

Table 1. continued.

pgc	galaxy-name	al2000	de2000	logd25	logr25	*t*	*N/S*	*(wa)*E–W (°)	β (°)	α_s
25886	MCG-1-24-1	9.18087	−8.88820	1.63	0.63	3.3	S	5-5	-	0
25926	ESO 564-27	9.19844	−20.11760	1.65	0.94	6.1	*S*	2–2	-	0
26561	IC 2469	9.38368	−32.45070	1.75	0.68	1.9	*N*	6–6	11–15	0
26632	ESO 433-19	9.40089	−28.17720	1.15	0.76	0.8	-	0–0	-	-
27135	ESO 373-8	9.55577	−33.03250	1.76	0.81	6.0	-	0–0	-	-
27468	ESO 373-13	9.63908	−33.86110	1.13	0.81	0.2	*U*	4–4	8–8	0
27735	MCG-1-25-22	9.70339	−4.71400	1.28	0.66	4.0	*N*	7–7	16–16	0
27982	NGC 2992	9.76169	−14.32750	1.56	0.62	1.0	?	?	-	-
28117	ESO 499-5	9.78709	−24.84040	1.41	0.64	5.0	*S*	10–15	31–17	0.2
28246	IC 2511	9.82372	−32.84200	1.50	0.65	1.5	*N*	8–10	18–22	0.1
28283	IC 2513	9.83403	−32.88580	1.49	0.60	2.2	-	0–0	-	-
28308	MCG-2-25-20	9.83718	−12.05720	1.25	0.78	6.8	*LS*	7–0	18–	1
28778	ESO 435-14	9.96341	−28.50670	1.40	0.86	4.9	*N*	5–5	11–14	0
28840	ESO 435-19	9.98502	−30.24980	1.53	0.86	4.7	*U*	4–5	8–8	0.11
28909	IC 2531	9.99880	−29.61540	1.83	0.96	5.0	-	0–0	-	-
29096	ESO 316-18	10.04541	−42.09030	1.40	0.85	4.9	*S*	5–6	-	0.09
29691	NGC 3157	10.19515	−31.64220	1.35	0.62	5.0	-	0–0	-	-
29716	ESO 263-15	10.20551	−47.29430	1.49	0.91	5.8	-	0–0	-	-
29743	ESO 436-1	10.21327	−27.83950	1.50	0.80	4.3	*N*	5–5	-	0
29841	ESO 567-26	10.23436	−21.97680	1.32	0.72	4.1	-	0–0	-	-
30716	ESO 375-26	10.45064	−36.22700	1.30	0.74	4.1	-	0–0	-	-
30887	NGC 3263	10.48691	−44.12300	1.78	0.64	5.9	?	?	-	-
31154	ESO 436-34	10.54559	−28.61290	1.35	0.65	3.0	-	0–0	-	-
31426	IC 624	10.60427	−8.33410	1.41	0.61	1.2	*S*	6–3	11–11	0.33
31626	ESO 437-22	10.63830	−28.88600	1.22	0.63	4.0	?	c	-	-
31677	ESO 437-30	10.65422	−30.29910	1.50	0.73	4.0	*LN*	6–0	9–	1
31723	NGC 3333	10.66387	−36.03610	1.32	0.63	4.3	*LN*	6–0	14–	1
31919	ESO 501-80	10.71052	−23.93550	1.36	0.67	5.0	-	0–0	-	-
31995	ESO 318-4	10.73068	−38.26280	1.45	0.63	5.1	*N*	5–5	18–18	0
32271	NGC 3390	10.80110	−31.53260	1.54	0.73	2.7	*N*	3–4	-	0.14
32328	ESO 264-43	10.81209	−45.42020	1.30	0.64	3.1	-	0–0	-	-
32550	ESO 569-14	10.85682	−19.88890	1.54	0.72	6.3	*LN*	8–0	14–	1
35539	NGC 3717	11.52557	−30.30770	1.78	0.64	3.1	?	?	-	-
35861	NGC 3749	11.59794	−37.99470	1.53	0.60	1.0	*U*	14–14	27–27	0
36315	ESO 571-16	11.70260	−18.16960	1.21	0.66	3.9	*N*	6–3	11–8	0.33
37178	NGC 3936	11.87235	−26.90650	1.60	0.73	4.4	-	0–0	-	-
37243	ESO 379-6	11.88444	−36.63820	1.42	0.90	4.9	*N*	3–2	-	0.2
37271	ESO 440-27	11.88987	−28.55320	1.64	0.83	6.7	*S*	4–3	11–11	0.14
37304	IC 2974	11.89692	−5.16780	1.36	0.69	4.7	*S*	5–5	9–9	0
37334	ESO 320-31	11.90167	−39.86450	1.42	0.88	5.1	-	0–0	-	-
38426	MCG-2-31-17	12.11402	−11.09900	1.31	0.77	6.0	S	7–6	16–10	0.08
38464	IC 3005	12.12049	−30.02330	1.38	0.76	5.6	*N*	3–5	6–9	0.25
38841	ESO 321-10	12.19502	−38.54850	1.31	0.83	0.8	-	0–0	-	-
40023	ESO 380-19	12.36725	−35.79230	1.50	0.76	5.8	-	0–0	-	-
40284	NGC 4348	12.39832	−3.44330	1.49	0.70	4.1	*N*	10–11	18–21	0.05
42684	ESO 268-33	12.70824	−47.55780	1.32	0.71	4.9	-	0–0	-	-
42747	UGC 7883	12.71593	−1.22940	1.42	0.61	6.0	*N*	7–11	13–27	0.22
43021	ESO 507-7	12.76168	−26.24320	1.41	0.82	4.0	-	0–0	-	-

Table 1. continued.

pgc	galaxy-name	al2000	de2000	logd25	logr25	t	*N/S*	*(wa)*E–W (°)	β (°)	α_s
43224	ESO 507-13	12.80150	−27.57800	1.25	0.62	4.1	*N*	6–6	11–11	0
43313	IC 3799	12.81658	−14.39910	1.40	0.88	6.7	-	0–0	-	-
43330	NGC 4700	12.81883	−11.41060	1.47	0.75	4.9	*N*	8–9	11–18	0.06
43342	NGC 4703	12.82187	−9.10850	1.39	0.69	3.1	-	0–0	-	-
43679	MCG-1-33-32	12.87411	−9.75390	1.39	0.92	6.7	-	0–0	-	-
44254	UGC 8067	12.95337	−1.70690	1.28	0.66	3.5	-	0–0	-	-
44271	NGC 4835A	12.95364	−46.37780	1.43	0.62	5.8	-	0–0	-	-
44358	MCG-1-33-60	12.96300	−9.63360	1.51	0.94	6.7	-	0–0	-	-
44409	NGC 4835	12.96883	−46.26320	1.67	0.69	4.0	?	b	-	-
44931	MCG-1-33-71	13.03043	−8.33620	1.45	0.85	4.9	*N*	8–7	8–9	0.07
44966	ESO 381-51	13.03531	−33.11870	1.19	0.70	2.8	-	0–0	-	-
45006	MCG-3-33-28	13.04054	−17.67920	1.42	0.92	4.9	*N*	5–7	11–21	0.17
45098	ESO 443-42	13.05827	−29.82900	1.46	0.83	3.1	*N*	7–5	17–14	0.17
45127	MCG-1-33-76	13.06291	−5.13370	1.27	0.61	4.9	*N*	6–6	11–11	0
45279	NGC 4945	13.09060	−49.47090	2.31	0.67	6.1	*N*	8–8	18–18	0
45487	ESO 508-11	13.12910	−22.85680	1.48	0.79	6.7	-	0–0	-	-
45911	ESO 576-11	13.21811	−19.97810	1.47	0.79	5.7	-	0–0	-	-
45952	NGC 5022	13.22530	−19.54800	1.38	0.69	3.4	-	0–0	-	-
46441	NGC 5073	13.32241	−14.84440	1.54	0.79	5.0	*S*	6–6	17–15	0
46650	ESO 40-7	13.36095	−77.53510	1.46	0.80	5.1	*N*	2–9	4–14	0.63
46768	IC 4231	13.38707	−26.30050	1.25	0.65	4.3	-	0–0	-	-
46928	ESO 382-58	13.42014	−33.65550	1.41	0.73	3.9	?	c	-	-
47345	ESO 383-5	13.48987	−34.27190	1.52	0.72	3.8	*N*	4–8	11–27	0.33
47394	NGC 5170	13.49692	−17.96620	1.91	0.84	4.9	-	0–0	-	-
47948	ESO 509-74	13.59484	−24.07400	1.40	0.72	4.7	*N*	5–5	11–11	0
48359	ESO 220-28	13.67018	−51.14220	1.31	0.75	4.2	-	0–0	-	-
49106	IRAS 13471-4839	13.83850	−48.90490	1.25	0.72	3.6	*S*	25–25	?	0
49129	ESO 383-91	13.84225	−37.28920	1.41	0.81	6.7	*N*	5–9	11–17	0.29
49190	ESO 384-3	13.85615	−37.62870	1.23	0.67	3.0	*S*	10–9	22–14	0.05
49586	NGC 5365A	13.94436	−44.00730	1.45	0.68	3.0	*N*	5–5	11–8	0
49676	IC 4351	13.96504	−29.31490	1.76	0.69	3.2	*N*	6–7	11–14	0.08
49750	NGC 5365B	13.97766	−43.96420	1.21	0.65	2.0	-	0–0	-	-
49788	ESO 325-42	13.98897	−40.06910	1.21	0.63	3.2	*S*	5–5	-	0
49836	ESO 221-22	14.00347	−48.26770	1.37	0.69	6.8	*S*	2–6	4–8	0.5
50676	NGC 5496	14.19388	−1.15890	1.64	0.69	6.5	S	8–9	39–45	0.06
50798	ESO 271-22	14.22487	−45.41360	1.41	0.73	5.9	-	0–0	-	-
51288	IC 4402	14.35379	−46.29830	1.68	0.69	3.2	?	c	17–11	-
51613	ESO 1-6	14.45741	−87.77160	1.48	0.64	5.9	-	0–0	-	-
52410	IC 4472	14.66980	−44.31610	1.35	0.66	5.0	-	0–0	-	-
52411	ESO 512-12	14.66983	−25.77610	1.45	0.82	3.2	*N*	5–5	16–16	0
52824	ESO 580-29	14.79267	−19.76510	1.34	0.80	4.9	*N*	6–6	11–11	0
52991	ESO 580-41	14.84346	−18.15090	1.30	0.70	4.3	-	0–0	-	-
53361	ESO 327-31	14.92637	−38.27700	1.36	0.74	5.0	-	0–0	-	-
53471	MCG-7-31-3	14.96256	−43.13190	1.18	0.70	4.4	?	?	-	-
54348	ESO 581-25	15.22503	−20.67680	1.54	0.70	6.9	?	c	-	-
54392	ESO 274-1	15.23711	−46.81250	2.05	0.76	6.6	-	0–0	-	-
54637	ESO 328-41	15.30663	−38.50690	1.40	0.69	3.1	*S*	5–7	9–11	0.17
56077	IC 4555	15.80448	−78.17830	1.30	0.64	5.9	-	0–0	-	-

Table 1. continued.

pgc	galaxy-name	al2000	de2000	logd25	logr25	*t*	*N/S*	*(wa)*E–W (°)	β (°)	α_s
57582	UGC 10288	16.24027	−0.20780	1.68	0.94	5.3	-	0–0	-	-
57876	IC 4595	16.34586	−70.14160	1.49	0.75	5.0	-	0–0	-	-
58742	ESO 137-38	16.68135	−60.39340	1.48	0.60	4.4	?	?	-	-
59635	ESO 138-14	17.11666	−62.08300	1.57	0.80	6.7	-	0–0	-	-
60216	ESO 138-24	17.40184	−59.38210	1.30	0.65	4.9	*S*	9–9	17–17	0
60595	IC 4656	17.62894	−63.72950	1.39	0.61	5.0	-	0–0	-	-
60772	ESO 139-21	17.73619	−60.97850	1.32	0.60	3.0	-	0–0	-	-
62024	IC 4717	18.55492	−57.97400	1.22	0.61	3.0	-	0–0	-	-
62529	ESO 281-33	18.88273	−42.53750	1.24	0.61	3.0	?	?	-	-
62706	IC 4810	19.04974	−56.15860	1.57	0.91	6.6	-	0–0	-	-
62722	NGC 6722	19.06100	−64.89480	1.46	0.67	2.9	*S*	5–5	8–8	0
62782	IC 4819	19.11826	−59.46550	1.47	0.73	6.0	*S*	5–2	8–	0.4
62816	ESO 231-23	19.14551	−51.04600	1.25	0.67	3.0	*U*	6–6	11–14	0
62922	IC 4827	19.22261	−60.86010	1.47	0.68	2.0	*LN*	4–0	8–0	1
62938	IC 4832	19.23426	−56.60900	1.37	0.64	1.3	*N*	9–9	17–17	0
62964	IC 4837A	19.25435	−54.13250	1.62	0.73	3.1	*N*	7–7	15–15	0
63161	ESO 184-63	19.39455	−55.06580	1.36	0.72	2.9	*N*	7–6	21–22	0.08
63297	ESO 184-74	19.50854	−57.28420	1.25	0.70	2.9	?	b	-	-
63395	IC 4872	19.59511	−57.51840	1.51	0.76	6.7	*S*	2–3	–11	0.2
63509	ESO 142-30	19.67763	−60.04800	1.26	0.67	4.9	?	b	-	-
63577	IC 4885	19.73113	−60.65150	1.29	0.64	4.9	*S*	7–7	11–11	0
64180	ESO 105-26	20.15782	−66.21610	1.18	0.64	4.2	?	?	-	-
64240	NGC 6875A	20.19888	−46.14380	1.47	0.70	4.2	?	b	-	-
64597	IC 4992	20.39088	−71.56520	1.34	0.88	5.1	*S*	3–3	8–8	0
65665	IC 5054	20.89587	−71.02410	1.32	0.62	1.1	?	?	-	-
65794	ESO 286-18	20.96403	−43.37390	1.42	0.79	3.8	*U*	6–2	9–3	0.5
65915	IC 5071	21.02221	−72.64490	1.53	0.67	4.8	*N*	6–6	39–23	0
66064	ESO 235-53	21.08624	−47.78900	1.39	0.67	3.0	*N*	9–9	22–22	0
66101	ESO 235-57	21.10602	−48.16920	1.37	0.69	3.9	-	0–0	-	-
66530	IC 5096	21.30611	−63.76130	1.50	0.71	4.0	*N*	8–4	18–11	0.33
66545	ESO 145-4	21.31419	−57.64030	1.34	0.61	5.0	?	b	-	-
66617	ESO 287-9	21.35448	−46.15240	1.25	0.73	4.3	-	0–0	-	-
66836	NGC 7064	21.48398	−52.76610	1.52	0.76	5.3	-	0–0	-	-
67045	NGC 7090	21.60794	−54.55740	1.89	0.77	5.1	-	0–0	-	-
67078	ESO 287-43	21.63656	−43.93260	1.30	0.77	6.1	-	0–0	-	-
67158	ESO 531-22	21.67475	−26.52590	1.44	1.02	4.4	*S*	?–4	–11	-
67782	ESO 288-25	21.98822	−43.86700	1.40	0.90	4.1	-	0-0	-	-
67904	NGC 7184	22.04401	−20.81320	1.78	0.65	4.5	*N*	3–3	9–9	0
68223	IC 5171	22.18238	−46.08210	1.38	0.61	3.8	*N*	6–6	11–11	0
68329	NGC 7232A	22.22810	−45.89360	1.33	0.70	2.0	*N*	6–6	14–14	0
68389	IC 5176	22.24848	−66.84810	1.64	0.82	4.3	*N*	3–3	6–6	0
69011	IC 5224	22.50824	−45.99330	1.19	0.61	2.2	-	0–0	-	-
69161	NGC 7307	22.56463	−40.93330	1.55	0.61	5.9	*N*	11–10	31–22	0.05
69539	NGC 7361	22.70498	−30.05800	1.60	0.65	4.6	*S*	5–5	14–14	0
69620	IC 5244	22.73710	−64.04230	1.46	0.73	3.0	*N*	3–2	8–4	0.2
69661	NGC 7368	22.75876	−39.34150	1.48	0.75	3.1	*N*	9–6	18–14	0.2
69707	IC 5249	22.78511	−64.83150	1.59	1.07	6.8	-	0–0	-	-
69967	NGC 7400	22.90582	−45.34670	1.41	0.63	4.0	-	0–0	-	-

Table 1. continued.

pgc	galaxy-name	al2000	de2000	logd25	logr25	t	*N/S*	*(wa)*E–W (°)	β (°)	α_s
70025	NGC 7416	22.92829	−5.49650	1.50	0.68	3.0	*S*	4–4	9–9	0
70070	IC 5269B	22.94356	−36.24970	1.58	0.72	5.6	-	0–0	-	-
70081	IC 5264	22.94796	−36.55430	1.39	0.72	2.4	*N*	5–5	16–16	0
70084	MCG-2-58-11	22.94754	−8.96760	1.31	0.67	4.7	*S*	7–4	16–8	0.27
70142	IC 5266	22.97244	−65.12970	1.24	0.61	3.1	-	0–0	-	-
70324	NGC 7462	23.04623	−40.83400	1.62	0.71	4.1	-	0–0	-	-
71309	ESO 291-24	23.39472	−42.40210	1.22	0.61	5.0	?	?	-	-
71800	IC 5333	23.58140	−65.39590	1.24	0.71	3.4	*LN*	7–0	22–	1
71948	ESO 240-11	23.63039	−47.72630	1.74	0.92	4.8	-	0–0	-	-
72178	ESO 292-14	23.70990	−44.90460	1.43	0.88	6.5	*N*	2–5	6–11	0.43

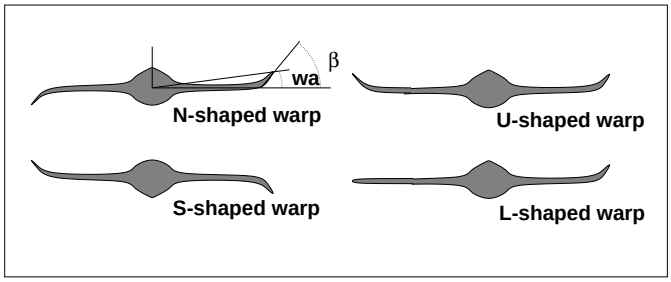

Fig. 1. Definitions of angles and types of warps.

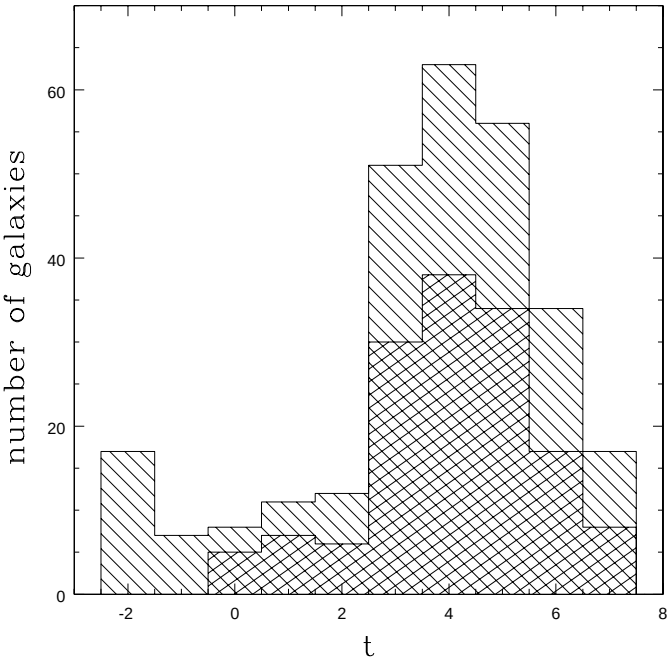

Fig. 2. Distribution of types of warped spiral and lenticular galaxies. Lined shadow area represents all galaxies (warped and unwarped). Squared shadow area represents warped galaxies.

east. *W*, the side of the galaxy closer to the west. In this column, c indicates the presence of noticeable corrugations, and b means that the observed apparent warps could actually be arms. These are not included as true warps.

The angle β in Col. 10 is the angle between the outermost detected point and the point where the warp starts (see Fig. 1).

Finally, Col. 11 gives α_s, the degree of asymmetry, defined as

$$\alpha_s = \frac{|wa(\mathrm{E}) - wa(\mathrm{W})|}{wa(\mathrm{E}) + wa(\mathrm{W})}. \quad (1)$$

The catalog for lenticular galaxies is presented independently in Table 2. In this case, we have considered 26 galaxies with the same limits as those used for spiral galaxies. In addition, galaxies with logr25 > 0.57 were considered. This enlarged the sample by another 12 lenticulars. This sample is complete with the above-mentioned limits.

3. Basic results

Figure 2 gives the distribution of types of warped spiral galaxies, together with the distribution of types for the complete (warped + unwarped) sample. Neither differs significantly from the general distribution of all spirals. The two distributions are so similar, differing only in the size of the sample, that it can be clearly concluded that for spiral galaxies the frequency of warps is completely independent of the type.

The degree of warping is independent of the type, both as defined by the warp angle *(wa)* (see Fig. 3) and the angle β (see Fig. 4). This important property was pointed out by Reshetnikov & Combes (1999).

In the case of lenticular galaxies, the result is noticeably different, however. None of the 38 lenticular galaxies in our sample is warped. Warping distorts discs with a similar frequency and amount for $t > 0$, but the transition at $t = 0$ is very sharp for this feature. This fact could be interpreted in two ways.

Firstly, the lenticular dominant bulges could hamper the formation of warps. There is no obvious theoretical argument favoring this interpretation. On the other hand, the fact that all types of spirals have the same warp frequency and as the size of the bulge is a decreasing function of type, the bulge mass seems to have a small influence on the magnitude of the warp. Therefore, it might be suggested that for a galaxy to be warped it must have large amounts of gas.

Figure 5 shows the relation between *wa* and β, which gives some geometrical characteristics of the warp. For moderate warps, there is a clear correlation between *wa* and β, as

Table 2. Sample of lenticular galaxies.

pgc	galaxy-name	al2000	de2000	logd25	logr25	*t*	*N/S*
5210	NGC 530	1.41159	−1.58770	1.24	0.58	−0.3	-
5430	NGC 560	1.45706	−1.91310	1.30	0.57	−2.4	-
6117	NGC 643	1.65349	−75.01100	1.22	0.60	−0.2	-
12662	ESO 301-9	3.38191	−42.18790	1.30	0.69	−1.7	-
13169	NGC 1355	3.55654	−4.99880	1.20	0.61	−2.1	-
13241	ESO 548-47	3.57875	−19.02900	1.40	0.60	−0.8	-
13277	IC 335	3.59187	−34.44660	1.37	0.58	−1.6	-
14495	NGC 1529	4.12195	−62.89900	1.10	0.58	−2.2	-
15388	IC 2085	4.52344	−54.41690	1.35	0.64	−1.2	-
19811	NGC 2310	6.89821	−40.86220	1.62	0.74	−1.9	-
24195	ESO 562-23	8.60971	−20.47010	1.36	0.61	−0.9	-
24966	ESO 371-26	8.90906	−32.93740	1.49	0.68	−1.5	-
25202	ESO 90−12	8.97290	−66.72830	1.34	0.62	−1.8	-
25943	ESO 433-8	9.20360	−30.91120	1.32	0.66	−1.9	-
30177	NGC 3203	10.32623	−26.69820	1.45	0.65	−1.3	-
30792	NGC 3250D	10.46610	−39.81490	1.24	0.71	−1.9	-
30938	IC 2584	10.49771	−34.91160	1.16	0.57	−2.0	-
31369	MCG-2-27-9	10.59093	−14.12990	1.32	0.58	−1.0	-
31504	ESO 437-15	10.61611	−28.17810	1.33	0.58	−2.0	-
36417	NGC 3831	11.72187	−12.87700	1.38	0.60	−0.8	-
37326	NGC 3957	11.90028	−19.56820	1.49	0.64	−1.0	-
42486	NGC 4603C	12.67865	−40.76350	1.24	0.59	−2.0	-
43929	NGC 4784	12.91030	−10.61300	1.19	0.60	−1.8	-
45650	MCG-3-34-4	13.16221	−16.60210	1.35	0.59	−1.0	-
46081	NGC 5038	13.25063	−15.95170	1.19	0.62	−1.9	-
46150	NGC 5047	13.26347	−16.51940	1.43	0.71	−2.0	-
46166	NGC 5049	13.26648	−16.39550	1.28	0.64	−2.0	-
46525	NGC 5084	13.33799	−21.82700	2.03	0.60	−1.8	-
49006	ESO 445-42	13.81359	−31.15510	1.14	0.74	−0.4	-
49300	ESO 445-65	13.87963	−29.92950	1.18	0.62	−2.2	-
49840	ESO 384-26	14.00407	−34.03760	1.19	0.57	−1.9	-
50242	IC 4333	14.08889	−84.27290	1.20	0.62	−1.8	-
62692	NGC 6725	19.03230	−53.86470	1.36	0.65	−2.0	-
63039	ESO 184-53	19.30533	−53.47730	1.10	0.60	−1.8	-
63049	NGC 6771	19.31105	−60.54560	1.37	0.64	−1.0	-
65055	ESO 234-53	20.60682	−49.25780	1.28	0.59	−2.0	-
66908	ESO 47-34	21.52875	−76.48040	1.21	0.66	−2.0	-
69638	NGC 7359	22.74651	−23.68700	1.35	0.58	−1.8	-

expected. However, for very large values of β, *wa* remains constant. Actually, a threshold value for *wa* seems to exist at around 14°. The farther away the warp starts, the steeper it rises. Theoretical work should pay attention to this fact.

Asymmetry seems to be unrelated to the morphological type. Figure 6 shows that no large asymmetric warps are found in early types, but as the frequency of these early types is much lower, this result cannot be considered significant.

The frequency of warps is summarized in the following table:

Total frequency of warped spiral galaxies			
Total frequency of warps 60%			
Within warped galaxies, the frequencies are:			
N	*S*	*L*	*U*
50%	38%	5%	7%

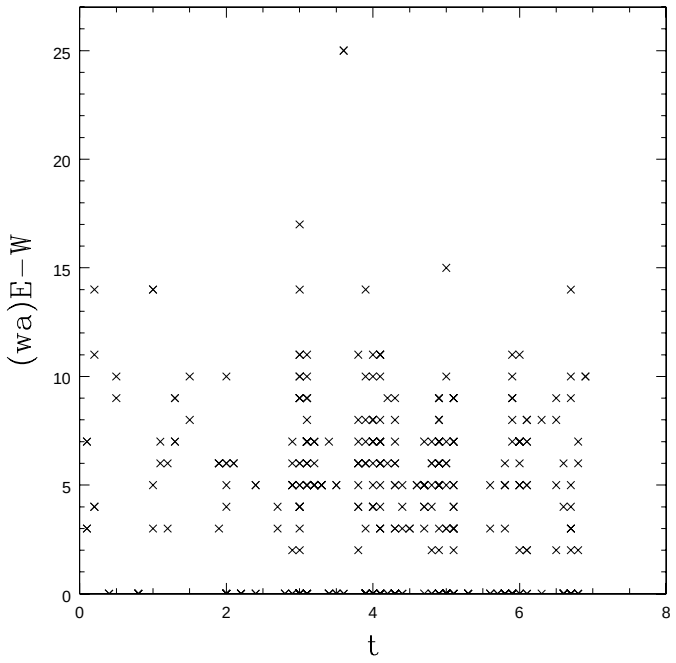

Fig. 3. Warp angle versus type.

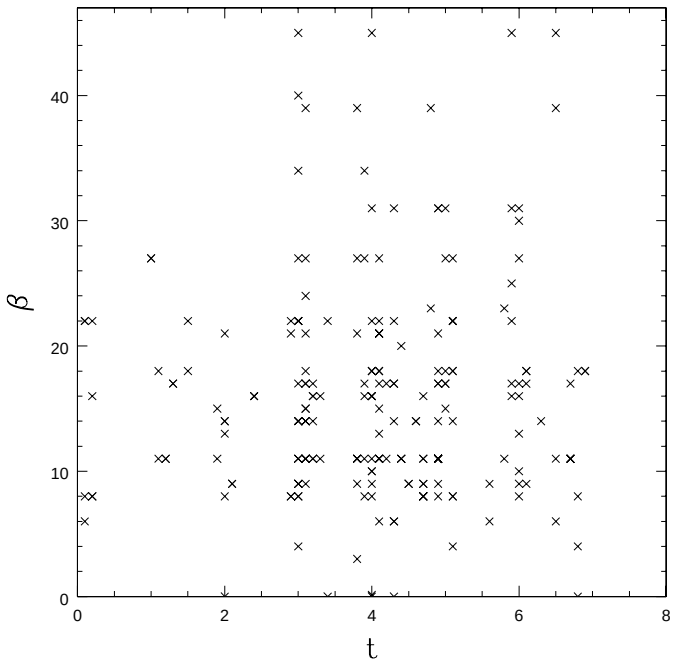

Fig. 4. Angle β versus type.

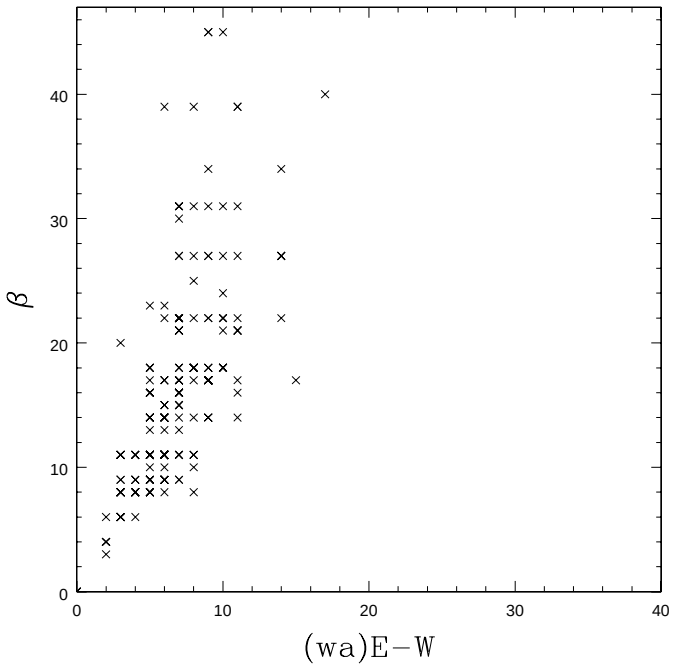

Fig. 5. Relation between *wa* and β.

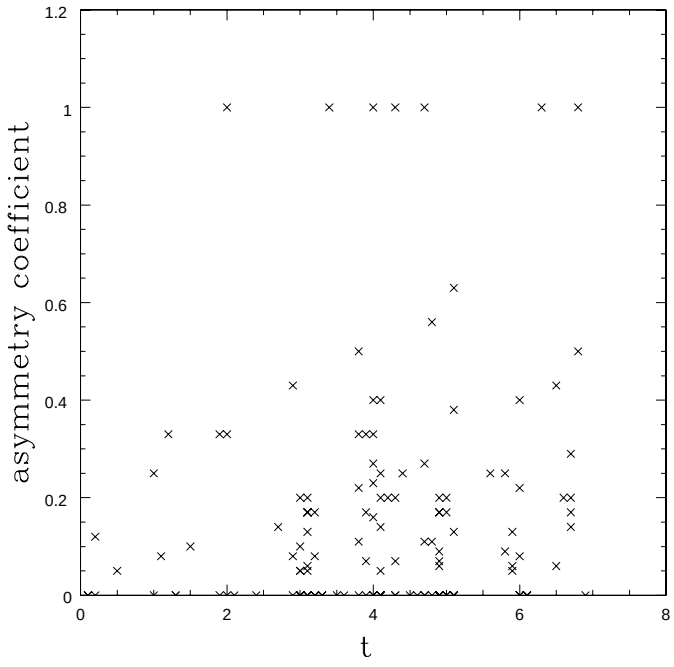

Fig. 6. Asymmetry coefficient versus type.

The N and S frequencies are similar, as expected, as these characteristics depend on the observer rather than on the galaxy. The difference, 50% and 38%, is not significant (it is within the statistical errors). The frequency of U warps is a parameter of theoretical importance, however, the different scenarios predicting different values. As stated by Castro-Rodríguez et al. (2002) an L warp, or even any asymmetric warp can be interpreted as a (N+U) or as a (S+U) warp.

4. Conclusions

1. This catalog contains a large sample of warped galaxies (150), covering the complete southern hemisphere. We present the whole sample of 250 spirals and 26 lenticulars, with limits logr25 > 0.60, $B_t < 14.5$, $\delta < 0°$, $-2.5 < t < 7$. It is especially suitable for statistical analysis and, indeed, has already been used to study the relation between intrinsic parameters and warps by Castro-Rodríguez et al. (2002). The catalog may obviously be used to choose which galaxies are to be observed in detail.

2. There is the unavoidable problem of the existence of other contaminant effects that could present the appearance of warps. Reshetnikov & Combes (1998) estimated that about 20% of the features assumed to be warps could actually be spiral arms. This value could be applied here. This effect introduces small errors into our calculated frequencies, which should be taken into account in statistical studies.
3. We confirm that warps appear to be a universal feature in spiral galaxies. The frequency of warps is very high (60%), and because of the difficulty (or impossibility) of detecting warps with the line of nodes in the plane of sky, it is concluded that most (if not all) galaxies are warped. Bosma (1981), Sánchez-Saavedra et al. (1990) and Reshetnikov & Combes (1999) previously reached this conclusion.
4. We also confirm, by means of a larger amount of data, the finding by Reshetnikov & Combes (1999) that warps are equally present in all types of spirals. The distribution of warps for the different types of spirals coincides with the distribution of galaxies with type. The maximum observed warp angle either from the center (*wa*) or from the starting radius of the warps (β) has no relation with the type of spiral. We have observed that very large values of β do not correspond to large warp angles of *wa*. Shorter warps are steeper.
5. We found no warped lenticular galaxies at all among the 26 galaxies within our limits, with logr25 > 0.60. We enlarged the sample to reach logr25 > 0.57 and again, none of the 38 lenticulars was warped. There is a sudden transition at $t = 0$. All spirals are warped; no lenticular is warped. The main difference between spirals and lenticulars is probably that the former are gas rich and the latter gas poor. Gas seems to be a necessary ingredient in the warp mechanism. Models based on gravitation alone would have serious difficulties in explaining this.

Acknowledgements. We acknowledge the use of the LEDA database (`http://leda.univ-lyon1.fr`) and the Digitized Sky Survey (DSS) of NASA's SkyView facility (`http://skyview.gsfc.nasa.gov`) located at NASA Goddard Space Flight Center.

References

Battaner, E., Florido, E., & Sánchez-Saavedra, M. L. 1990, A&A, 236, 1
Battaner, E., Garrido, J. L., Sánchez-Saavedra, M. L., & Florido, E. 1991, A&A, 251, 402
Binney, J. J. 1992, ARA&A, 30, 51
Bosma, A. 1981, AJ, 86, 1791
Castro-Rodríguez, N., López-Corredoira, M., Sánchez-Saavedra, M. L., & Battaner, E. 2002, A&A, 391, 519
Dubinski, J., & Kuijken, K. 1995, ApJ, 442, 492
Florido, E., Prieto, M., Battaner, E., Mediavilla, E., & Sánchez-Saavedra, M. L. 1991, A&A, 242, 301
García-Ruíz, I. 2001, Ph.D. Thesis, Groningen University
García-Ruíz, I., Kuijken, K., & Dubinski, J. 2000, MNRAS, submitted, preprint [astro-ph/0002057]
de Grijs, R. 1997, Ph.D. Thesis, Groningen University
Jiménez-Vicente, J. 1998, Ph.D. Thesis, Granada University
Jiménez-Vicente, J., Porcel, C., Sánchez-Saavedra, M. L., & Battaner, E. 1998, Ap&SS, 253, 225
Kahn, F. D., & Woltjer, L. 1959, AJ, 130, 705
Kuijken, K., & García-Ruíz, I. 2001, Galaxy Disks and Disk Galaxies, ed. J. G. Funes, S. J., & E. M. Corsini, ASP Conf. Ser., 230, 401
López-Corredoira, M., Betancort, J. A., & Beckman, J. 2002, A&A, to be published
Ostriker, E. C., & Binney, J. J. 1989, MNRAS, 237, 785
Reshetnikov, V., & Combes, F. 1998, A&A, 337, 9
Reshetnikov, V., & Combes, F. 1999, A&A, 138, 101R
Reshetnikov, V., Battaner, E., Combes, F., & Jiménez-Vicente, J. 2002, A&A, 382, 513
Sánchez-Saavedra, M. L., Battaner, E., & Florido, E. 1990, MNRAS, 246, 458
Sancisi, R. 1976, A&A, 53, 159
Schwarzkopf, U., & Dettmar, R. J. 2001, A&A, 373, 402
Sparke, L., & Casertano, S. 1988, MNRAS, 234, 873
Weinberg, M. D. 1998, MNRAS, 299, 499

A&A 519, A53 (2010)
DOI: 10.1051/0004-6361/201014506

Astronomy & Astrophysics

Near-infrared and optical observations of galactic warps: a common, unexplained feature of most discs

A. Guijarro[1,2], R. F. Peletier[3], E. Battaner[1], J. Jiménez-Vicente[1], R. de Grijs[4,5], and E. Florido[1]

[1] Dpto. Física Teórica y del Cosmos, Universidad de Granada, Granada, Spain
e-mail: aguijarr@ugr.es
[2] Centro Astronómico Hispano Alemán, Almería, Spain
[3] Kapteyn Astronomical Institute, Groningen, The Netherlands
[4] Kavli Institute for Astronomy and Astrophysics and Department of Astronomy, Peking University, Beijing, PR China
[5] Department of Physics & Astronomy, The University of Sheffield, UK

Received 26 March 2010 / Accepted 10 June 2010

ABSTRACT

Context. Warps occurring in galactic discs have been studied extensively in HI and in the optical, but rarely in the near-infrared (NIR) bands that trace the older stellar populations.
Aims. We provide NIR data of nearby edge-on galaxies, combined with optical observations, for direct comparison of the properties of galactic warps as a function of wavelength, and calculate warp curves for each galaxy and obtain the characteristic warp parameters. We discuss these properties as possible constraints to the different mechanisms that have been proposed for the development and persistence of galactic warps.
Methods. We observed 20 galaxies that were selected from a statistically complete diameter-limited subsample of edge-on disc galaxies. We used the Cerro Tololo Infrared Imager (CIRIM) at the CTIO 1.5 m Ritchey-Chretien telescope to acquire the NIR data. We used the 1.54 m Danish and 0.92 m Dutch telescopes at the European Southern Observatory's La Silla site for our optical observations.
Results. Our results show that 13 of our 20 sample galaxies are warped, with the warp more pronounced in the optical than at NIR wavelengths. In the remaining seven galaxies, no warp is apparent within the limitations of our automated detection method. The transition between the unperturbed inner disc and the outer, warped region is rather abrupt. S0 galaxies exhibit very small or no warps. The magnetic model remains one of a number of interesting formation scenarios.

Key words. galaxies: general – galaxies: photometry – galaxies: structure

1. Introduction

Most spiral galaxies, including our own, exhibit warped discs. This has long been known based on observations of both the extended neutral-gas (HI) component (Sancisi 1976; Bosma 1981; Briggs 1990; García-Ruiz et al. 2002b) and optical starlight (Sánchez-Saavedra et al. 1990; Florido et al. 1991; Reshetnikov & Combes 1998; Ann & Park 2006). The first detections of warped discs came from 21 cm line observations of our own Galaxy (Burke 1957; Kerr 1957; Burton 1988). Based on a sky survey covering the Northern Hemisphere, Sánchez-Saavedra et al. (1990) first reported the high frequency of optical warps in disc galaxies, which they later confirmed in Sánchez-Saavedra et al. (2003) based on an extended catalogue that also included the Southern Hemisphere. These studies took into account that warps can only be detected when their orientation (projection) is favourable (i.e., not in the line of sight). A noteworthy and important result, established in the later paper, is that they did not find any warped S0 galaxies. Here, we therefore pay special attention to S0 galaxies. Reshetnikov et al. (2002) find that warps were also common in the past, with even greater magnitudes at $z \approx 1$.

Edge-on galaxies are usually chosen to study warps, although dynamical warps in the HI distribution of galaxies of intermediate inclination have also been reported, e.g., in M 83 (Rogstad et al. 1974), NGC 5033, NGC 5055, NGC 2841, and NGC 7331 (Bosma 1978), M 31 (Brinks & Burton 1984), and M 33 (Corbelli et al. 1989). García-Ruiz et al. (2002b) analysed HI observations and find that all edge-on galaxies that have an extended HI disc (with respect to the optical component) are warped.

Ann & Park (2006) find that 73% of the 325 galaxies in their well-defined sample of almost perfectly edge-on galaxies ($a/b > 9.5$, where a/b is the major-to-minor axis ratio at $\mu_B = 25$ mag arcsec^{-2}) exhibit optical warps. Recently, Reylé et al. (2009) have found that a warp is present in the stellar, dust, and gas discs of the Milky Way, which are all asymmetric and characterised by a similar line of nodes. The Milky Way's HI gas warp is the strongest, followed by the dust warp, while the stellar warp is significantly smaller (by a factor of approximately two). They conclude that this comparison shows that the different components react differently to the forces responsible for the origin of the warp. The most important additional information that we provide here (not yet been discussed by other authors) is a multiwavelength study of galactic warps in one NIR and three optical filters.

Considerable effort has gone into establishing the physical origin and stability of warps. Numerous mechanisms have been proposed and explored, but they have thus far not provided a definitive and satisfactory physical explanation (see, e.g., the

reviews by Binney 1992; Battaner et al. 1997; van der Kruit 2007). Kerr (1957), Hunter & Toomre (1969), Weinberg (1998), Weinberg & Blitz (2006), and others have suggested that warps can result from tidal interactions with a satellite or neighbouring galaxy. This hypothesis can explain warps neither in isolated galaxies (Sancisi 1976; Tubbs & Sanders 1979; Sparke 1984) nor in the Milky Way, if the latter was produced by an interaction with the Large Magellanic Cloud (see García-Ruiz et al. 2002a). Hunter & Toomre (1969) and Dekel & Shlosman (1983) proposed that the Galactic warp is a result of oscillations in the disc, either triggered by an interaction with another galaxy in the past or caused by the disc being embedded in a nonspherical halo of dark matter. Sparke & Casertano (1988) showed that some discrete oscillation modes can survive. This theory is not without problems, however; for instance, Binney (1991) showed that the halo should then respond to its misalignment with the disc, thus destroying the warp in a few orbital periods. Alternatively, a nonlinear coupling between a spiral wave and two warp waves could create a warp (Masset & Tagger 1997). The efficiency of this mechanism is too low in the stellar disc except at its outer edge (near a Lindblad resonance), where the spiral wave slows down and is coupled efficiently to the warp waves. At those radii, the energy of the spiral arm can almost be completely converted into transmitted and reflected warp waves, which can be observed as corrugations in the disc.

Warping could thus be a natural response of the outer disc to a series of stimulations, and it seems that the responsible mechanism does not necessarily have to be the same in each galaxy. In any case, observations of large edge-on galaxies could contribute to the definitive determination of the dominant scenario. The intergalactic medium could also play an important role by accretion of matter as galaxies move along their paths (Kahn & Woltjer 1959; López-Corredoira et al. 2002; Sánchez-Salcedo 2006). Battaner et al. (1990) explained warps by intergalactic magnetic fields, which would produce a direct distortion in the distribution of the gas. The stellar system would also indirectly reach a warped distribution because stars are formed from gas, but this would result in a difference between young and old stars. Colour gradients in warps can thus provide an important clue. Based on this model, gas-poor S0 galaxies should not exhibit warps.

In this paper, we present new, deep NIR and optical observations of 20 edge-on galaxies. NIR wavelengths have rarely been used to date to study warps. They are, however, essential for better tracing the stellar mass distribution, because at infrared (IR) wavelengths ($1 < \lambda < 5$ μm) dust extinction is minimised (the absorption, in magnitudes, in the K filter is 10% of that in the V band, $A_K/A_V \sim 0.1$). NIR emission is also a better tracer of old stellar populations, one of our major objectives in this study. Therefore, these wavelengths provide essential complementary information for studying stellar warps.

2. Sample

Our sample was selected by de Grijs (1997, 1998) from the Surface Photometry Catalogue of the ESO-Uppsala Galaxies (ESO-LV; Lauberts & Valentijn 1989). This catalogue contains large numbers of galaxies that have been selected and parameterised uniformly. The galaxies were originally selected on ESO-Schmidt survey plates covering declinations $\delta \leq -17.5°$, excluding the area within 15° of the Galactic Equator, at Galactic latitudes $|b| < 15°$. We selected 20 candidate galaxies from a statistically complete diameter-limited subsample of edge-on disc galaxies (de Grijs 1997, 1998), with the following characteristics (see Table 1):

- $D_{25}(B) \geq 2.2'$, i.e., with optical diameters (at a surface brightness level of $\mu_B = 25$ mag arcsec^{-2}) larger than 2.2′;
- isolated galaxies, i.e., without significant neighbours within a distance greater than or equal to five times their optical diameters. They should be classified as noninteracting and undisturbed;
- inclination, $i > 87°$;
- morphological type range from S0 to Sd, i.e., revised Hubble types later than $T = -2$ (spiral and lenticular galaxies).

The inclinations were determined assuming an intrinsic flattening $(b/a)_0 = 0.11$ (de Grijs 1997, 1998), so that our sample contains highly inclined galaxies in which warps should be easy to detect. This could introduce a bias against early types or galaxies with prominent bulges that should be taken into account in the discussion of the warp phenomena. Using this approach, we try to avoid the common confusion between spiral arms, corrugations, and warps.

3. Observations and data reduction

The sample was observed at

- near-infrared wavelengths, with the *Cerro Tololo Infrared IMager* (CIRIM) at the 1.5 m Ritchey-Chretien Telescope of the Cerro Tololo Inter-American Observatory (CTIO) on October 22–27, 1998 (Prop0020). CIRIM is equipped with a 256 × 256-pixel HgCdTe NICMOS3 array (Rockwell Science) with a pixel scale of 1.16″. We observed our sample galaxies through the $K_{\rm short}$ filter ($\equiv K_{\rm s}$), characterised by an effective wavelength $\lambda_{\rm eff} = 2.15$ μm (Wainscoat & Cowie 1992). We opted for this filter instead of the longer-wavelength K filter ($\lambda_{\rm eff} = 2.20$ μm) because the sky brightness in $K_{\rm s}$ is lower than in the K band (for instance, at UKIRT, Hawaii, the sky brightness is 13.5 and 13.0 mag arcsec^{-2} in $K_{\rm s}$ and K, respectively[1]) and $K_{\rm short}$ is almost as little affected by dust as the K band, $A_{K_{\rm s}} \sim 0.11$ mag airmass^{-1}; and
- optical wavelengths. We obtained our observations using two telescopes of the European Southern Observatory (ESO) at La Silla, Chile, including the 1.54 m Danish telescope (equipped with a 1081 × 1040-pixel TEK CCD with 0.36″ pixel^{-1}) and the 0.92 m Dutch telescope (equipped with a 512 × 512-pixel TEK CCD with 0.44″ pixel^{-1}), both in the standard Johnson B and V and Thuan & Gunn (1976) i filters.

The observations and optical data-reduction techniques on which the results presented in this paper are based were described in detail in de Grijs (1998). Here, we focus on the reduction of the IR data.

To study stellar warps in disc galaxies, we need to obtain reliable data at the very low surface brightnesses in their outermost regions. Our observational data reached surface brightnesses fainter than 26 mag arcsec^{-2} in the B band. This is only 6% of the sky brightness ($\mu_{B,\rm sky} = 23$ mag arcsec^{-2}), so that we had to be particularly careful in measuring the sky brightness. The sky background in NIR passbands is much higher than in the optical ($\mu_{K,\rm sky} = 13$ mag arcsec^{-2}) and can change significantly

[1] http://www.jach.hawaii.edu/UKIRT/instruments/uist/imaging/imaging.html

Table 1. Global galaxy parameters from the ESO-LV Catalogue (Lauberts & Valentijn 1989).

Galaxy	RA(J2000.0) (hh:mm:ss.s)	Dec(J2000.0) (dd:mm:ss)	Hubble type	a/b (axis ratio)	$D_{25}(B)$ (arcsec)	B mag (total)	$B-R$ (tot) (mag)	Radial velocity (km s^{-1})	PA (deg) (N→E)
ESO026-G06	20:48:28.3	−78:04:09	6.7 ± 1	9.3	134.9	15.48 ± 0.30	+1.37	2323[1)]	76.0
ESO033-G22	05:31:41.8	−73:44:58	6.8 ± 1	12.5	131.8	15.56 ± 0.19	+0.86	3932[1)]	170.0
ESO142-G24	19:35:42.3	−57:31:10	6.6 ± 1	8.4	237.1	14.03 ± 0.24	+1.30	2027[1)]	6.0
ESO157-G18	04:17:54.4	−55:56:04	6.5 ± 1	6.6	186.2	13.90 ± 0.48	+0.96	1139	18.0
ESO201-G22	04:09:00.4	−48:43:36	4.8 ± 1	7.3	151.4	14.73 ± 0.32	···	4014	59.0
ESO202-G35	04:32:15.6	−49:40:31	3.4 ± 1	6.2	184.1	13.38 ± 0.31	+1.06	1856	133.0
ESO235-G53	21:05:10.4	−47:47:17	3.0 ± 0	6.0	153.1	14.53 ± 0.26	+1.85	5110	49.0
ESO240-G11	23:37:49.3	−47:43:34	4.7 ± 1	10.0	331.1	13.05 ± 0.21	+1.35	2817	129.0
ESO288-G25	21:59:17.6	−43:52:02	4.2 ± 1	6.5	153.1	13.97 ± 0.21	+1.30	2484	53.0
ESO311-G12	07:47:34.2	−41:27:07	0.1 ± 1	6.4	251.2	12.83 ± 0.28	+1.69	848[1)]	14.0
ESO340-G08	20:17:11.0	−40:55:22	6.0 ± 1	24.0	192.8	15.45 ± 0.20	+0.95	3004[1)]	34.0
ESO340-G09	20:17:20.2	−38:40:29	7.0 ± 1	9.0	160.3	14.52 ± 0.27	···	2546	98.0
ESO358-G26	03:35:30.8	−34:26:49	−1.6 ± 2	4.2	153.1	12.90 ± 0.40	+1.19	1660	84.0
ESO358-G29	03:36:31.4	−35:17:38	−2.0 ± 1	3.9	153.1	12.47 ± 0.18	+1.45	1740	139.2
ESO416-G25	02:48:41.3	−31:32:09	3.2 ± 1	6.0	141.3	14.68 ± 0.25	+1.38	4992	31.0
ESO460-G31	19:44:21.2	−27:24:22	4.8 ± 1	9.5	154.9	15.15 ± 0.21	···	5352[1)]	92.0
ESO487-G02	05:21:48.6	−23:48:45	3.9 ± 1	7.5	199.5	13.62 ± 0.26	+1.35	2088[1)]	60.0
ESO531-G22	21:40:29.5	−26:31:40	4.5 ± 1	8.7	154.2	13.94 ± 0.35	···	3639[1)]	8.0
ESO555-G36	06:07:41.5	−19:54:54	5.5 ± 1	11.5	139.6	15.60 ± 0.58	+1.62	···	146.0
ESO564-G27	09:11:54.3	−20:07:04	6.1 ± 1	14.0	278.6	14.39 ± 0.90	+1.36	2178	168.0

Notes. [1)] Heliocentric radial velocities from Mathewson et al. (1992).

on temporal and spatial scales the order of two minutes and two arcmin, respectively. It was therefore necessary to obtain as many sky frames as object frames to perform sky subtraction with sufficiently high accuracy. We took sky and object frames alternately, using the same exposure time for each individual frame (60 s) and employing interframe shifts of ∼2 arcmin. An additional reason we needed to obtain separate sky frames is that the IR arrays used were not large enough to properly sample the sky on the science frames. Incorrect background subtraction can cause the sky level to be either underestimated (so that sky flux will contribute to the surface brightness at large galactic radii) or overestimated (resulting in a fictitious radial cut-off). Figure 1 illustrates the importance of careful background subtraction in the K_s band, where the sky contribution is greater than in optical passbands. The figure shows the major- and the minor-axis (vertical, z) surface brightness profiles of four galaxies, binned radially. The effects of oversubtraction can be seen clearly in the minor-axis surface brightness profiles: they show artificial cut-offs, and the negative background values result in undefined surface brightnesses at these z heights.

We used a special software package for our NIR data reduction, customised to reduce and analyse very deep data of extended objects observed in the IR, as a set of IRAF[2] tasks. The program removes spurious stars in sky frames, subtracts cleaned, scaled sky frames from object frames taken immediately prior to or after the relevant object frame, and flatfields the differences. It uses a median sky frame to detect and remove stars in the sky frames.

We observed several standard stars from the SAAO/ESO/ISO Faint Standard Stars Catalogue (Carter & Meadows 1995) to calibrate our targets and used the Wainscoat & Cowie (1992) correction to convert K_s to K magnitudes. These stars were observed at least three times per night, at different airmasses, to calculate the prevailing atmospheric extinction with sufficient accuracy. We observed a total of 21 standard stars. These observations reached a surface brightness of approximately 23 mag arcsec^{-2} in K_s.

[2] IRAF is distributed by the National Optical Astronomy Observatories, which are operated by the Association of Universities for Research in Astronomy, Inc., under cooperative agreement with the US National Science Foundation.

4. Data analysis

First, we aligned the images in all of the B, V, I, and K_s filters. We took special care to subtract foreground stars. This is necessary and important because foreground stars projected close to a galaxy can contaminate the galaxy's luminosity distribution and lead to erroneous results. We used a master mask constructed by adding the individual masks for each of the passbands. In each mask, the stars were marked with circles of radius around twice the FWHM to avoid contributions from any residual starlight. In some galaxies observed near the Galactic plane, this meant that a large number of pixels had to be masked.

To determine the warp curve (tracing the position of the intensity maxima as a function of radius), we employed three different methods.

1. First, we calculated the intensity maxima using vertical cuts (perpendicular to the galactic plane). This resulted in very noisy profiles for the optical data and also sometimes for the NIR data, because the presence of a dust lane frequently resulted in a double-peaked luminosity distribution.
2. Second, we calculated the luminosity distribution's first moment, with which we obtained reliable results (although it also depended on the position of the dust lane). This method was applied mainly at blue wavelengths to compensate for background stars.
3. Third, we fitted Gaussian profiles. We fitted each vertical trace (parallel to the minor axis of the galaxy) in the selected zone to a Gaussian function. We considered this the best approach, because the contribution of the dust lane is less important in optical data than when using the other two methods. Gaussians can be matched to vertical profiles that contain a dip caused by a dust lane without problems in almost perfectly edge-on galaxies.

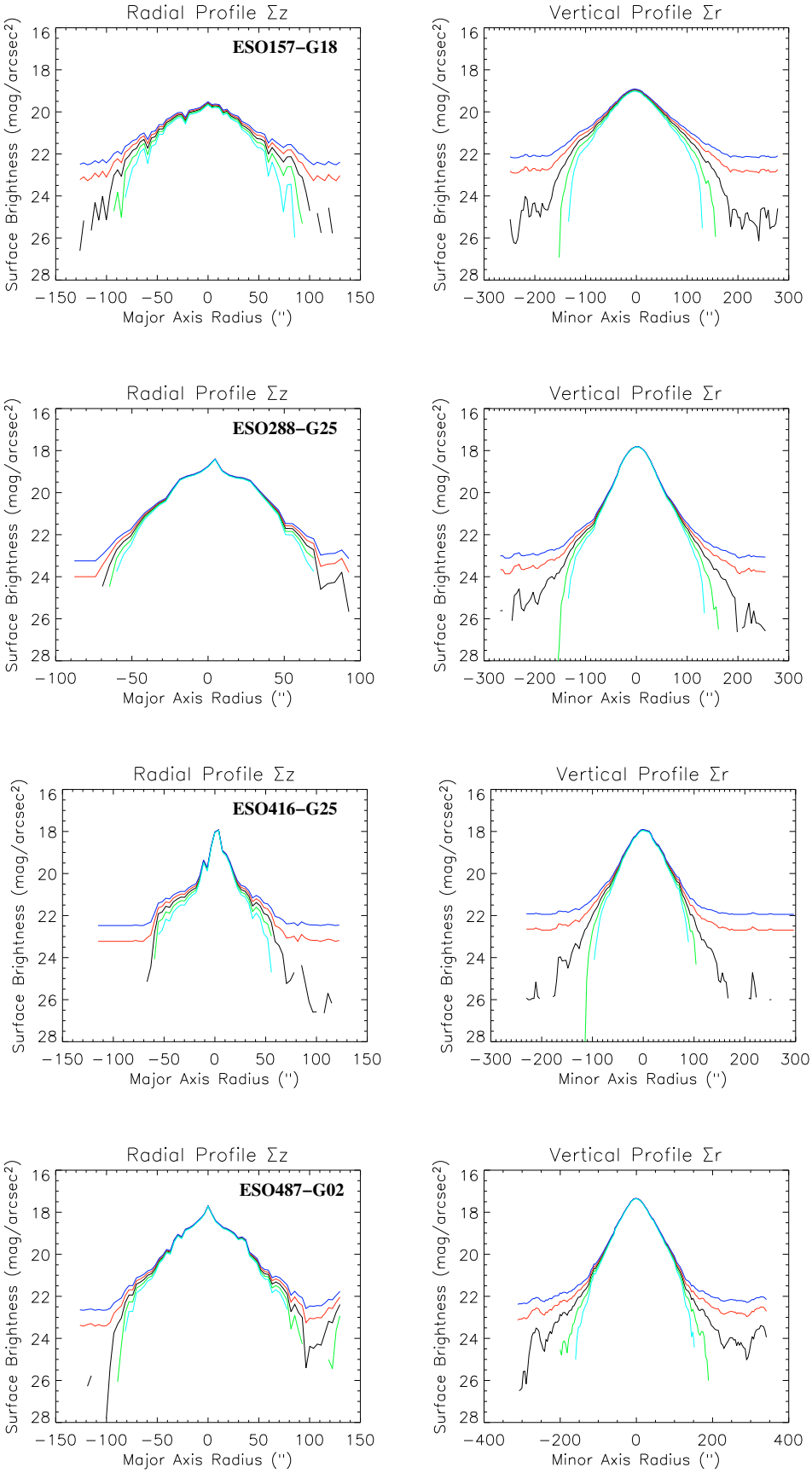

Fig. 1. K_s-band luminosity profiles of four galaxies. The lines in each panel represent, *from top to bottom*, -2σ (blue), -1σ (red), profile after subtraction of our best estimate of the sky background (black), $+1\sigma$ (green), and $+2\sigma$ (sky blue). (σ is the sky noise in the regions we used to determine the sky-background levels.)

4.1. Warp curves from the Gaussian fit

As a first step, we rotated our galaxies (to align their major axes with the horizontal axis) using an iterative method until the position angle (PA) had been determined to an accuracy of approximately 0.05 degrees. We used the PA from the ESO-LV Catalogue as a starting point; we then iteratively fitted a straight line to the central region of the galaxy. Our results are shown in Fig. 2 as isophote maps of our 20 galaxies.

To calculate the warp curves, we fitted Gaussians to the vertical profiles of the galaxies in each filter. We only considered data with a signal-to-noise ratio greater than 3 ($\sigma = \sqrt{\sigma_{\rm sys}^2 + \sigma_{\rm std}^2}$, where $\sigma_{\rm sys}$ is the systematic error associated with the random background noise and $\sigma_{\rm std}$ the standard deviation), and with the FWHM of the peak smaller than 100 pixels. The results of our analysis are presented in Fig. 3, where the warp curves are shown only for those values with error bars smaller than 0.5″. This estimated error bar can be computed by scaling the standard deviation (1σ error) by the measured χ^2 value.

4.2. Warp parameters

It is convenient to use a geometric definition of a warp, e.g., for statistical studies. For an edge-on galaxy, the suitable coordinates correspond to the two directions contained in the plane of the sky: the direction defined by the major axis of the galaxy, x, and the direction of the rotation axis of the galaxy, y. The centre of the galaxy is the origin of coordinates. A warp curve is defined as the locus of points (x_i, y_i) tracing the distribution of the highest intensities, where y_i is the position of the centre of the best-fitting Gaussian at a given x_i.

We derived the parameter ω (defined in Jiménez-Vicente et al. 1997),

$$\omega = \frac{1}{L^3}\int_{-L/2}^{+L/2} xy\mathrm{d}x, \tag{1}$$

where L is the full size of the edge-on galaxy (the diameter at 3σ above the sky background). The absolute value of ω is a measurement of the strength of a warp, while its sign distinguishes between N-like ($\omega > 0$) and S-like ($\omega < 0$) warps. These types are defined from the similarity of the warp shape and the type letters (see Fig. 4 for definition of types of warps). This definition is nondimensional and, therefore, independent of a galaxy's distance and size. It is also independent of the units used and does not strongly depend on the angular resolution of the observations (although a higher resolution would enable a more precise evaluation). For numerical purposes, we have

$$\omega = \frac{1}{L^3}\sum_{i=-L/2}^{L/2} x_i y_i. \tag{2}$$

We can also define this parameter for both sides of our galaxies: $\omega_{\rm R}$ for the right-hand side ($^1/_{L^3}\sum_{i=0}^{L/2} x_i y_i$) and $\omega_{\rm L}$ for the left-hand side ($^1/_{L^3}\sum_{i=-L/2}^{0} x_i y_i$). Because of the flattening of the radial profile in the inner regions of our sample galaxies, it is not critical to have a precise estimate of the position of the galaxy centre. Warps can appear in three flavours (cf. López-Corredoira et al. 2008). The N- or S-like warps have $\omega_{\rm R}$ and $\omega_{\rm L}$ of the same sign, the signs of $\omega_{\rm R}$ and $\omega_{\rm L}$ for U-like warps differ, and L-like warps apply to galaxies in which only one side is warped. The difference between N- and S-like warps is unimportant from a physical point of view. However, we have retained this information because it is needed, for instance, when considering the orientation of warps in a cluster of galaxies (see, e.g., Battaner et al. 1991).

With this parameter we can, for example, objectively compare the appearance of a galaxy at several wavelengths to determine whether a colour gradient exists within the warp. We can also detect warps that would otherwise not have been found. Warps are not always completely symmetric, in which case this parameter would hide the information of the clearly warped side of the galaxy. To avoid this problem, we calculated the warp parameters on either side of our galaxies independently, along with $\alpha_{\rm s}$, the degree of asymmetry (Sánchez-Saavedra et al. 2003),

$$\alpha_{\rm s} = \frac{|\omega_{\rm R} - \omega_{\rm L}|}{\omega_{\rm R} + \omega_{\rm L}}\,. \tag{3}$$

One of the most important errors in estimating ω arises from imperfectly determining the PA of the major axis, resulting in an error θ in the PA. Since $\theta \neq 0$, we introduce the error

$$\Delta\omega = \frac{1}{L^3}\int_{-\infty}^{\infty} x(x\tan\theta)\mathrm{d}x \approx \frac{1}{3L^3}L^3\theta \approx \frac{\theta}{3}\,. \tag{4}$$

As θ is, in general, approximately 0.05° (9×10^{-4} radians), we estimate $\Delta\omega$ to be of the order of 3×10^{-4} rad. A large warp can have a value of 10×10^{-4} and a barely perceptible warp 5×10^{-4} rad. In the remainder of this paper, we consider a galaxy as warped if its calculated ω is clearly greater than the associated error. (See Table 2 for our results.)

For those galaxies showing an appreciably warped disc, we fitted a number of additional parameters to the warp curves. We tried to use the function proposed by Jiménez-Vicente et al. (1997), but it had too many fitting parameters so the fits were resticted to the simple description:

$$y = \begin{cases} 0 & |x| < |A| \\ C(x - A) & |x| \geq |A|. \end{cases} \tag{5}$$

This function reproduces the warp's shape as a first approximation; i.e., it is flat up to a point and then deviates from the symmetry plane until it asymptotically reaches a new direction. The interpretation of the parameters A and C is as follows,

- A is the starting point of the warp. It has dimensions of length;
- C is the (nondimensional) value of the asymptotic slope.

Throughout the rest of the paper, we refer to parameters A and C as those obtained by fitting the experimental points to Eq. (5). These values are shown in Table 3 for the different bands. In addition, we use the angles α and β, which are most widely used to represent the warp amplitude (Sánchez-Saavedra et al. 2003) Here, α is the angle between the line connecting the galaxy's centre and the outermost detected point, and the disc's major axis, while β is the angle between the disc's major axis and the line from the outermost detected point to the point where the warp starts (A): see Fig. 4.

We obtained the same result for the warp parameter ω, whether it was calculated starting from the galaxy centre or from the starting point of the warp, A. This confirms that it is not critical to have a precise estimate of the position of the galaxy centre because of the radial flattening in the inner regions of our galaxies. In some galaxies, such as ESO142-G24 or ESO157-G18, the warp sets off in one direction, turns back to the mean plane, and ends in the opposite hemisphere. The Milky Way's warp

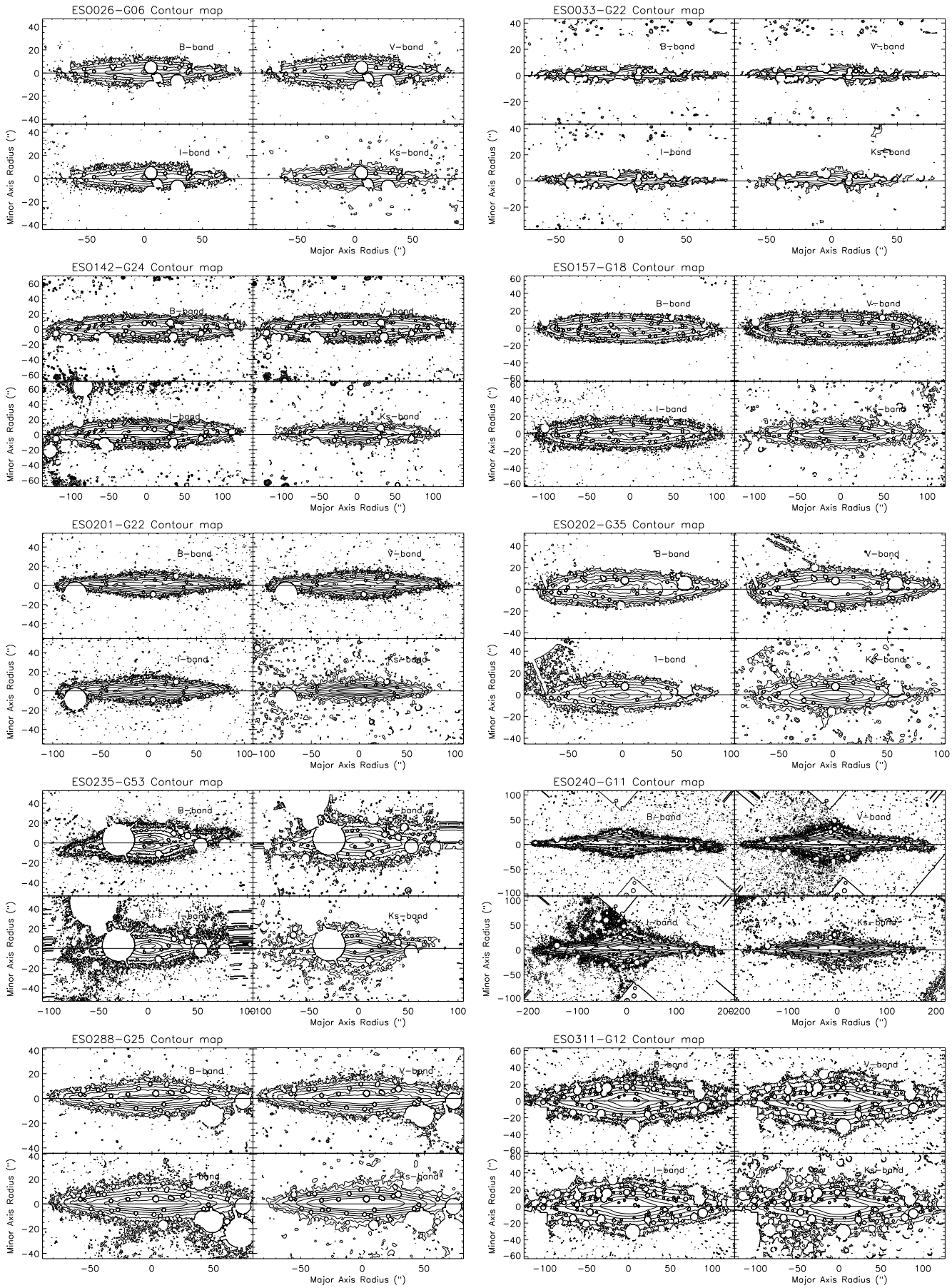

Fig. 2. Contour maps of our 20 galaxies in the four filters analysed. The isophotes are equidistant (in units of $n \times 3\sigma$ with $n = 1, 2, 3, \ldots$, equivalent to steps of 0.75 mag arcsec^{-2}), starting at $\sim 3\sigma$ above the sky background. The galaxies have been rotated, but N is close to the top, E to the left.

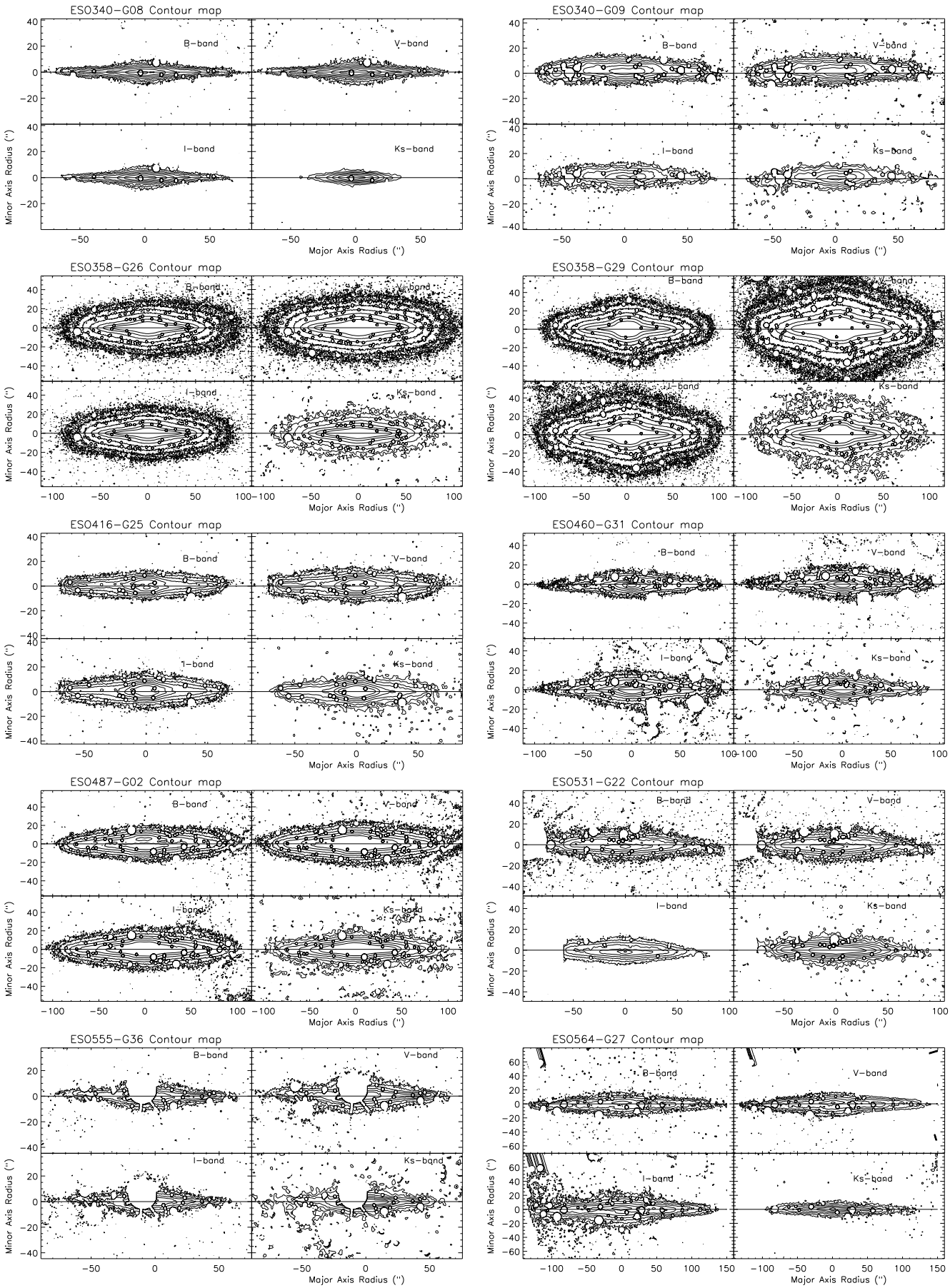

Fig. 2. continued.

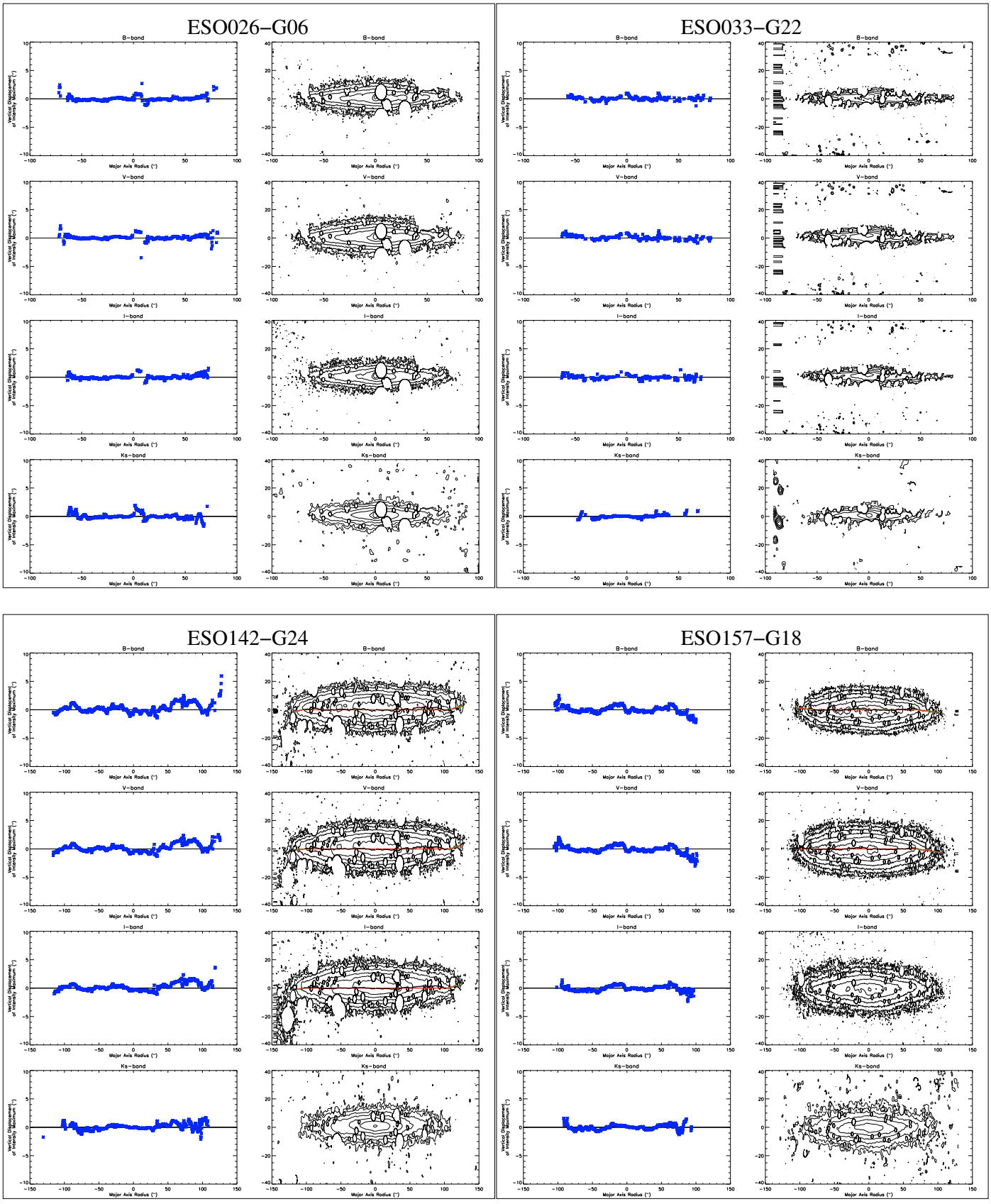

Fig. 3. *Left*: warp curves and right: contour maps, for the different filters of our 20 galaxies. The warp curve (green line) is put on top only for those values with an error bar less than 0.5″. The red line shows the fitted warp curve. The isophotes are equidistant (in units of $n * 3\sigma$ equiv. to a step of +0.75 mag/arcsec^2) starting at a level of about 3σ above the sky background. The galaxy is rotated, but N is closer to the top and E to the left. The scale on the y-axis is enlarged to show a better curve.

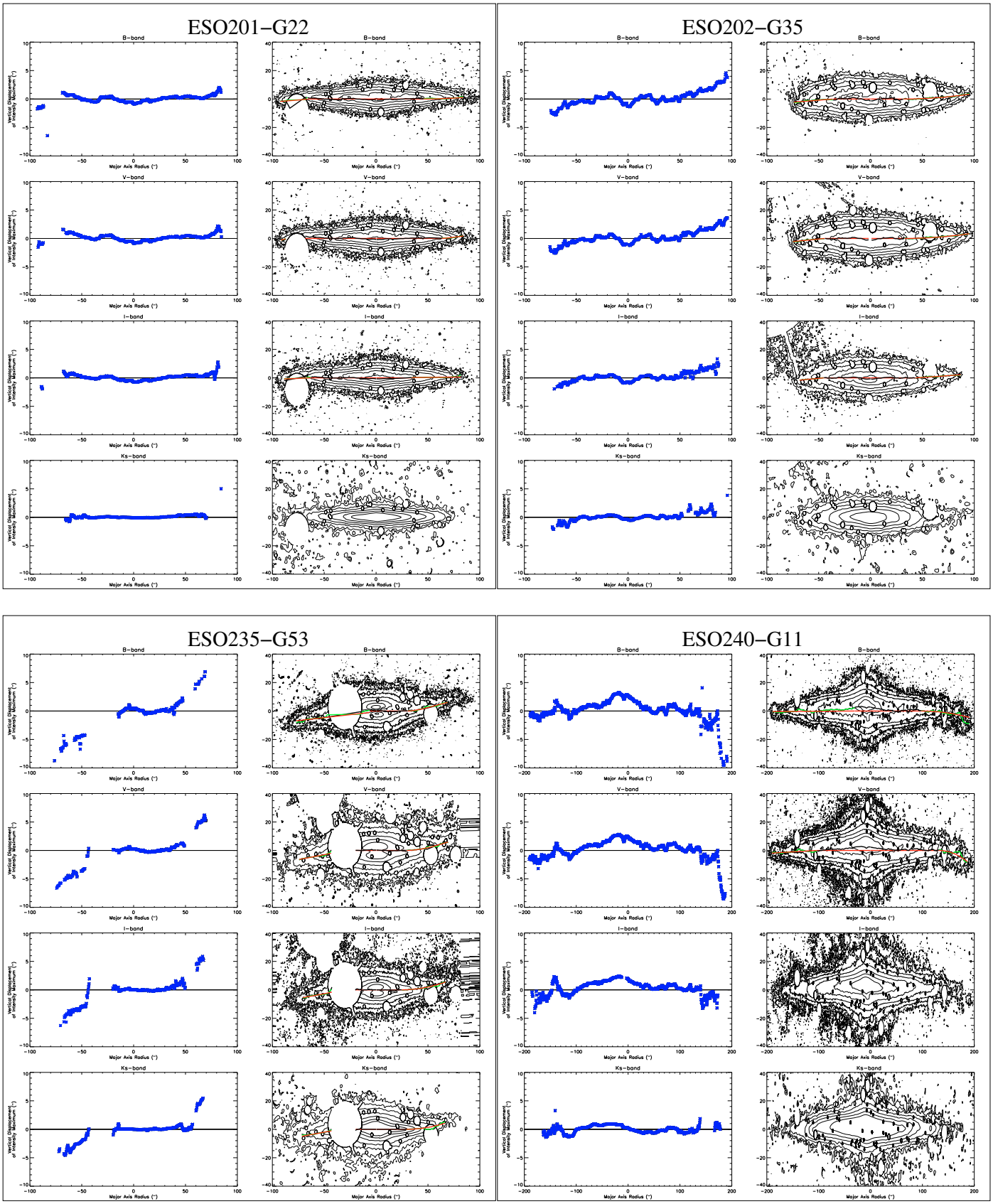

Fig. 3. continued.

in the Southern Hemisphere is an example of this type of behaviour (Porcel et al. 1997). Florido et al. (1991) also report such "elbow"-type warps. This effect may come from the presence of a more strongly warped dust lane (than the stellar disc) or be an intrinsic effect associated with warps. For such galaxies, a four-parameter fit would have provided a better description. However,

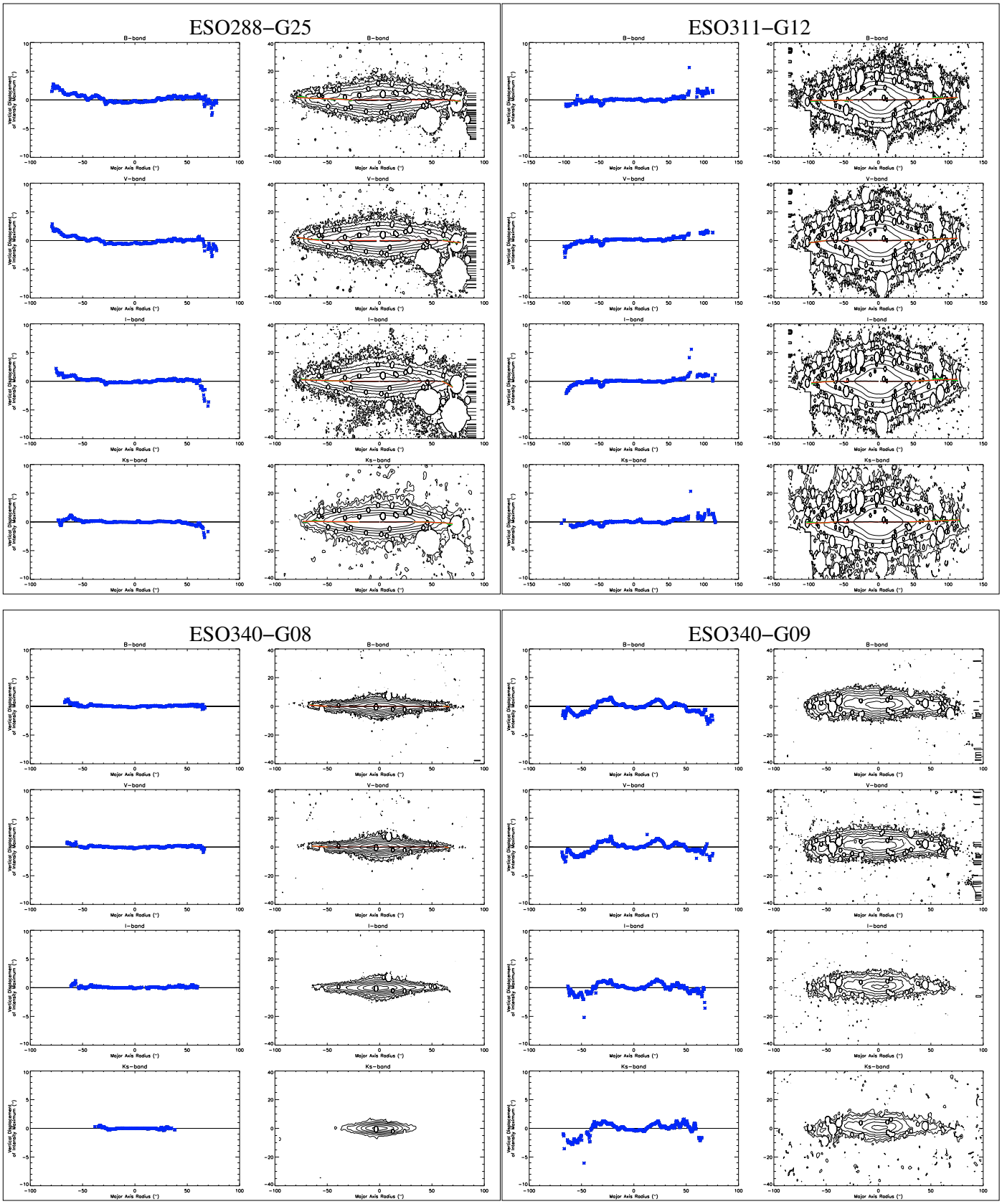

Fig. 3. continued.

since an excessive number of fit parameters renders any interpretation of simple warps unclear, we prefer to use three-parameter fits.

5. Analysis

We consider a galaxy as warped if it is warped (according to the definition in Sect. 4.2) in any of the four observed bands. Based

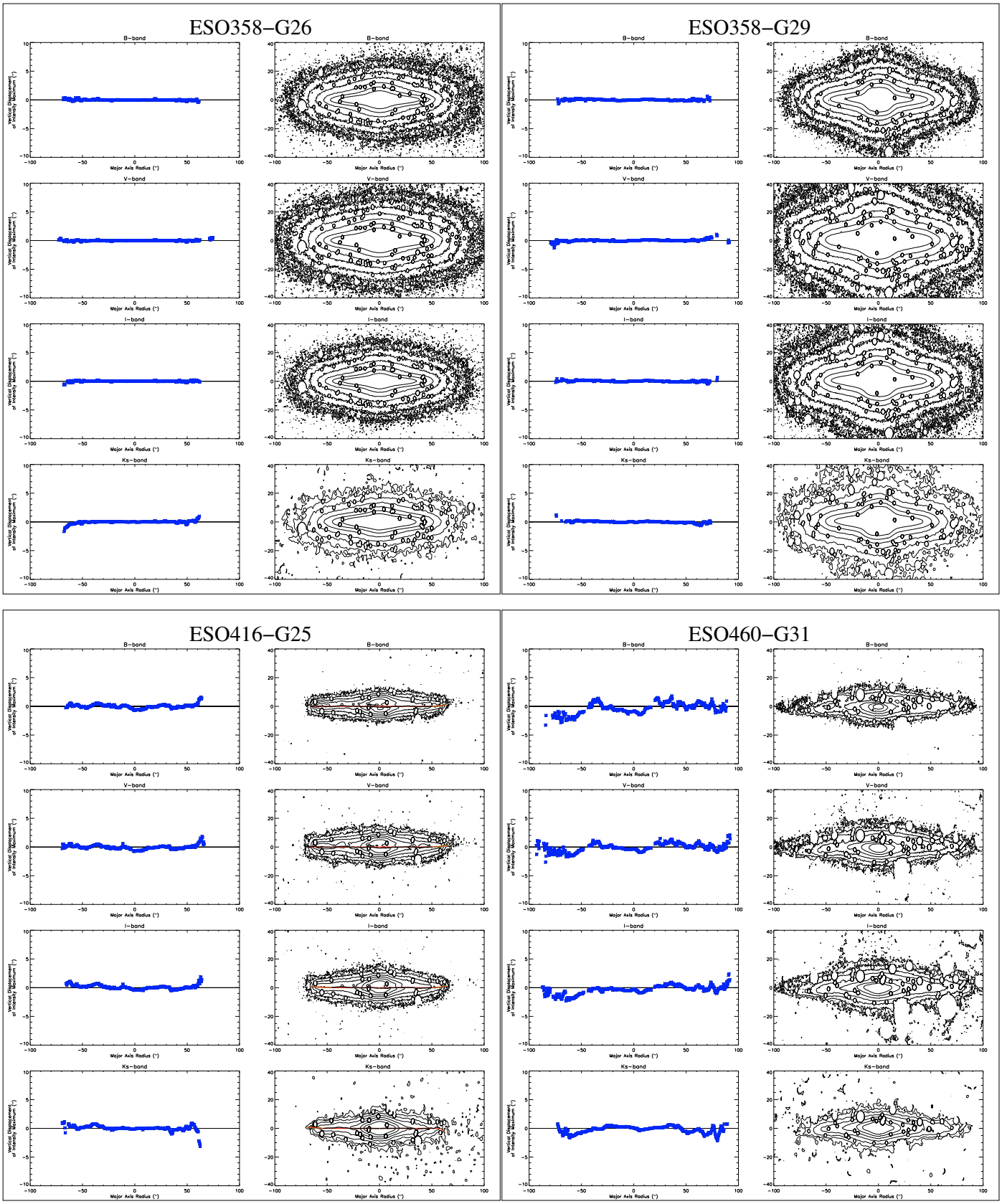

Fig. 3. continued.

on this assumption, we find that 13 of our 20 sample galaxies (65%) are warped. This fraction supports previous results based on larger galaxy samples with similar optical characteristics to our sample (Sánchez-Saavedra et al. 1990, 2003; Reshetnikov & Combes 1999). Given the difficulties of observing warps with their line of nodes perpendicular to the line of sight, this high fraction of warped discs indicates that essentially all spirals are warped. Optical warps are less perceptible than HI warps, but at

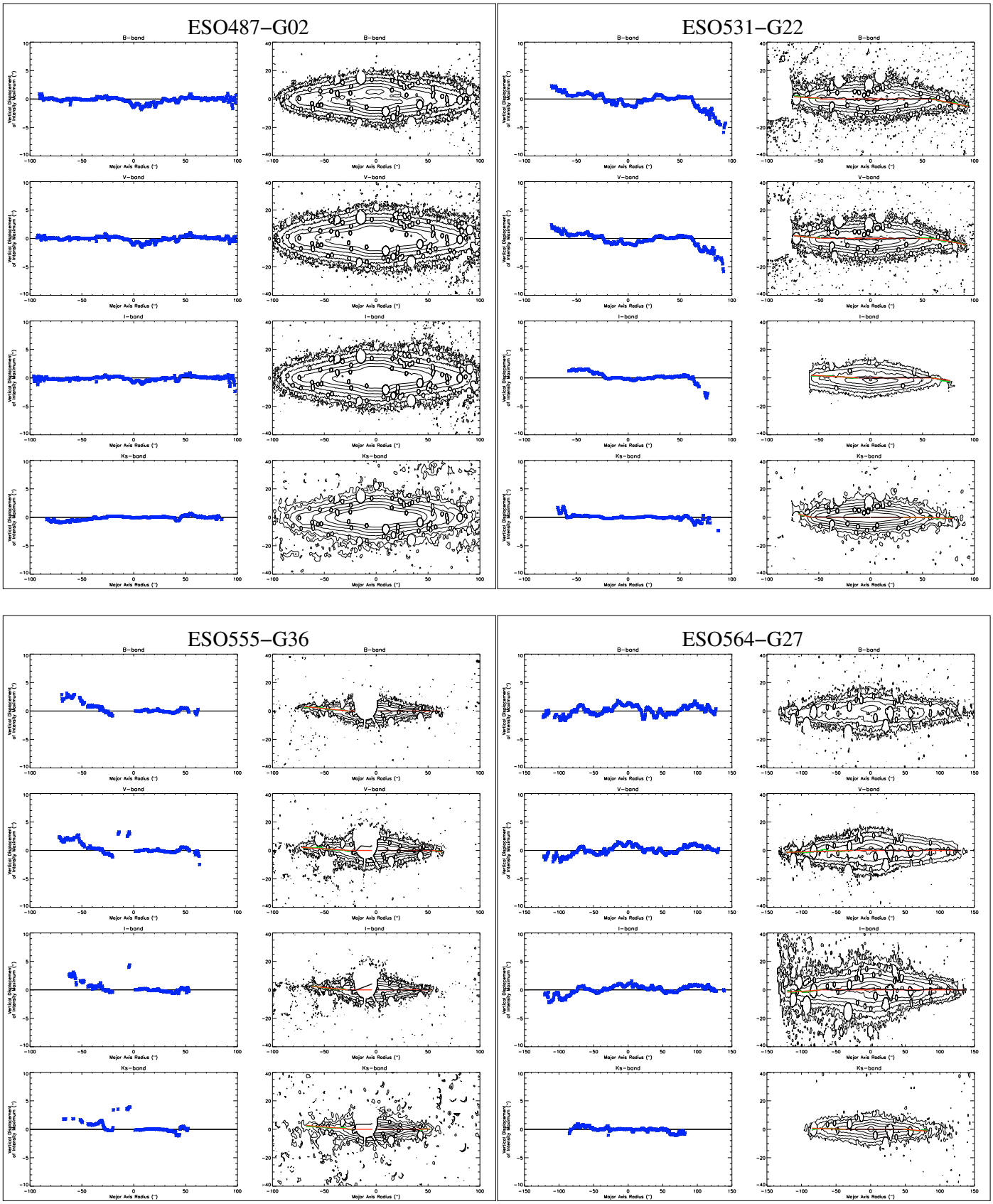

Fig. 3. continued.

both wavelengths the frequency of warps is the same, i.e., close to 100% (Sancisi 1976; García-Ruiz 2001; García-Ruiz et al. 2002b; van der Kruit 2007).

As expected, the N- and S-like warp frequencies are similar, since these characteristics depend on the observer rather than the galaxy. We observe six galaxies with N-like and four galaxies

Table 2. Warp parameters for our four filters ($\times 10^4$) and degree of asymmetry for each warped galaxy, with warp values listed in boldface.

Galaxy	B filter				V filter				I filter				K_s filter			
	ω	ω_R	ω_L	α_s	ω	ω_R	ω_L	α_s	ω	ω_R	ω_L	α_s	ω	ω_R	ω_L	α_s
ESO026-G06	1 ± 3	1 ± 3	−0 ± 3		0 ± 2	1 ± 2	−1 ± 2		2 ± 3	2 ± 3	1 ± 3		−3 ± 3	−2 ± 3	−1 ± 3	
ESO033-G22	−1 ± 4	0 ± 4	−1 ± 4		−3 ± 6	−1 ± 6	−2 ± 6		−1 ± 4	−1 ± 4	0 ± 4		3 ± 4	1 ± 4	1 ± 4	
ESO142-G24	**3 ± 2**	**4 ± 2**	−1 ± 2	1.0	**3 ± 2**	**4 ± 2**	0 ± 2	1.0	**4 ± 2**	**4 ± 2**	0 ± 2	1.0	2 ± 2	1 ± 2	0 ± 2	–
ESO157-G18	**−4 ± 3**	−2 ± 3	−1 ± 3	–	**−4 ± 2**	**−3 ± 2**	−1 ± 2	−1.0	0 ± 3	−1 ± 3	1 ± 3	–	1 ± 3	1 ± 3	0 ± 3	–
ESO201-G22	**4 ± 2**	**3 ± 2**	1 ± 2	1.0	2 ± 2	**3 ± 2**	−1 ± 2	1.0	2 ± 2	**3 ± 2**	−1 ± 2	1.0	2 ± 3	2 ± 3	1 ± 3	–
ESO202-G35	**17 ± 6**	**12 ± 6**	5 ± 6	1.0	**16 ± 3**	**12 ± 3**	**5 ± 3**	0.4	**11 ± 6**	**9 ± 6**	3 ± 6	1.0	4 ± 4	4 ± 4	2 ± 4	–
ESO235-G53	**29 ± 6**	**10 ± 6**	**19 ± 6**	0.3	**39 ± 7**	**16 ± 7**	**22 ± 7**	0.2	**28 ± 3**	**11 ± 3**	**17 ± 3**	0.2	**25 ± 2**	**10 ± 2**	**15 ± 2**	0.2
ESO240-G11	**−4 ± 3**	**−4 ± 3**	0 ± 3	−1.0	**−2 ± 1**	**−3 ± 1**	1 ± 1	−1.0	0 ± 2	−1 ± 2	0 ± 2	–	0 ± 2	0 ± 2	0 ± 2	–
ESO288-G25	**−6 ± 5**	1 ± 5	**−8 ± 5**	−1.0	**−7 ± 2**	−2 ± 2	**−5 ± 2**	−0.4	**−6 ± 3**	−1 ± 3	**−5 ± 3**	−1.0	**−5 ± 1**	**−3 ± 1**	**−2 ± 1**	−0.2
ESO311-G12	**5 ± 1**	**3 ± 1**	1 ± 1	0.5	**5 ± 1**	**3 ± 1**	**2 ± 1**	0.2	**5 ± 1**	**3 ± 1**	**2 ± 1**	0.2	**4 ± 1**	**2 ± 1**	1 ± 1	0.3
ESO340-G08	−1 ± 1	1 ± 1	**−2 ± 1**	−1.0	−1 ± 1	1 ± 1	**−2 ± 1**	−1.0	−1 ± 2	1 ± 2	−2 ± 2	–	−1 ± 1	−1 ± 1	−1 ± 1	0.0
ESO340-G09	−2 ± 7	−6 ± 7	4 ± 7		4 ± 5	−1 ± 5	5 ± 5		1 ± 8	−6 ± 8	7 ± 8		9 ± 9	2 ± 9	8 ± 9	
ESO358-G26	−1 ± 1	−1 ± 1	−1 ± 1		0 ± 1	0 ± 1	0 ± 1		0 ± 0	0 ± 0	0 ± 0		2 ± 2	1 ± 2	2 ± 2	
ESO358-G29	0 ± 1	0 ± 1	0 ± 1		1 ± 1	1 ± 1	1 ± 1		−1 ± 2	0 ± 2	0 ± 2		−2 ± 2	−1 ± 2	−1 ± 2	
ESO416-G25	0 ± 1	**2 ± 1**	−1 ± 1	1.0	0 ± 1	**2 ± 1**	−1 ± 1	1.0	−2 ± 2	1 ± 2	**−4 ± 2**	−1.0	**−4 ± 2**	−1 ± 2	**−3 ± 2**	−1.0
ESO460-G31	8 ± 9	1 ± 9	7 ± 9		4 ± 4	2 ± 4	3 ± 4		7 ± 8	1 ± 8	6 ± 8		0 ± 3	−3 ± 3	3 ± 3	
ESO487-G02	−1 ± 3	0 ± 3	0 ± 3		−1 ± 2	0 ± 2	−1 ± 2		1 ± 2	0 ± 2	1 ± 2		4 ± 4	0 ± 4	4 ± 4	
ESO531-G22	**−20 ± 6**	**−14 ± 6**	−6 ± 6	−0.4	**−16 ± 4**	**−11 ± 4**	**−5 ± 4**	−0.4	**−11 ± 4**	−4 ± 4	**−7 ± 4**	−0.3	**−6 ± 2**	**−2 ± 2**	**−4 ± 2**	−0.3
ESO555-G36	**−10 ± 4**	0 ± 4	**−11 ± 4**	−1.0	**−12 ± 8**	−1 ± 8	**−11 ± 8**	−1.0	**−12 ± 5**	−1 ± 5	**−11 ± 5**	−1.0	**−10 ± 5**	−2 ± 5	**−9 ± 5**	−1.0
ESO564-G27	3 ± 3	0 ± 3	2 ± 3	–	**4 ± 3**	2 ± 3	3 ± 3	1.0	**3 ± 2**	1 ± 2	2 ± 2	1.0	**−5 ± 1**	**−3 ± 1**	**−2 ± 1**	−0.2

Table 3. Warp parameters as a function of passband.

Galaxy name	Side	r_{last} ±1 (″)	y (±0.5)				A (±1)				C (±0.01)			
			B	V	I	K_s	B	V	I	K_s	B	V	I	K_s
		(3)	(4)	(5)	(6)	(7)	(8)	(9)	(10)	(11)	(12)	(13)	(14)	(15)
ESO142-G24	Right	110	−1	−1.5	1	0	108	106	103	–	0.17	0.12	0.27	–
	Left	103	0	0.5	0	0	−105	−103	−104	–	0.10	0.04	0.08	–
ESO157-G18	Right	90	−1.5	−2	−1	0	70	68	–	–	−0.06	−0.07	–	–
	Left	92	0.5	0.5	0	1	−81	−115	–	–	−0.05	0.04	–	–
ESO201-G22	Right	71	0	0.5	0.5	0	46	63	29	–	0.07	0.10	–	–
	Left	72	1	1	0.5	0	−66	−86	−63	–	0.05	0.21	0.02	–
ESO202-G35	Right	82	2	2	2	0	30	33	43	–	0.90	0.07	0.05	–
	Left	72	−2	−2	−2	−1.5	−41	−44	−45	–	0.07	0.07	0.09	–
ESO235-G53	Right	70	7	6	5	6	27	36	30	30	1.52	0.16	0.15	0.39
	Left	70	−7	−5	−6	−4	−11	−35	−35	−39	0.11	0.16	0.11	0.10
ESO240-G11	Right	180	−5.5	−5.5	−3	0	101	132	–	–	–	–	–	–
	Left	165	−0.5	−1.5	−1	0	–	−103	–	–	0.00	0.02	–	–
ESO288-G25	Right	67	−0.5	−1	−3.5	−2.5	65	60	60	43	−0.08	−0.09	−0.49	−0.04
	Left	73	2.5	2	1	0	−26	−28	−29	–	−0.03	−0.05	−0.02	–
ESO311-G12	Right	118	1.5	1	1	0	46	32	47	32	0.03	0.02	0.02	0.02
	Left	102	–	–	–	0	−49	−75	−63	−60	0.01	0.06	0.03	0.02
ESO340-G08	Right	37	0	0	0	0	64	59	–	–	−0.08	−0.12	–	–
	Left	39	0	0	0	0	−50	−50	–	–	−0.05	−0.05	–	–
ESO416-G25	Right	63	1.5	1.5	1.5	−3	51	51	51	59	1.00	0.68	0.61	−0.68
	Left	69	0	0	–	1	–	–	−46	−54	–	–	−0.04	−0.06
ESO531-G22	Right	88	−4	−3.5	–	−2.5	58	44	58	44	−0.14	−0.12	−0.11	–
	Left	69	2	1.5	–	2	−39	−48	−12	−57	−0.05	−0.04	−0.04	−0.14
ESO555-G36	Right	52	0	0	0	0	–	53	50	–	–	–	−0.07	–
	Left	69	2.5	2	–	1.5	−28	−25	−28	−21	−0.04	−0.02	−0.04	−0.02
ESO564-G27	Right	117	0	0.5	0.5	−1	–	–	–	48	–	–	−0.04	−0.04
	Left	83	0	−1	−0.5	−0.5	–	−25	−70	−37	–	0.01	0.02	−0.02

Notes. (3) Radius of the last measured point in K_s (arcsec); (4)–(7) y at the same point (arcsec); (8)–(11) warp starting points (arcsec); (12)–(15) asymptotic slope.

with S-like warps. The frequency of asymmetric warps is lower: ESO416-G25 exhibits a U-like warp, while ESO240-G11 and ESO555-G36 show L-like warps. Therefore, the most frequent warp morphologies are N- and S-like warps (see also Ann & Park 2006).

The distribution of warped galaxies as a function of morphological type is shown in Fig. 5, where the hatched area shows all galaxies and the cross-hatched area covers warped galaxies. The warp frequency does not seem to depend significantly on galaxy morphology, except for S0 and very-late-type galaxies, which both yield lower frequencies.

A noticeable result from Sánchez-Saavedra et al. (2003) was that S0 galaxies are generally not warped. This places strong constraints on any hypothesis proposed to explain warps. Among our sample galaxies, ESO311-G12 has a small warp in both the optical and the NIR, but both of the other S0 sample galaxies,

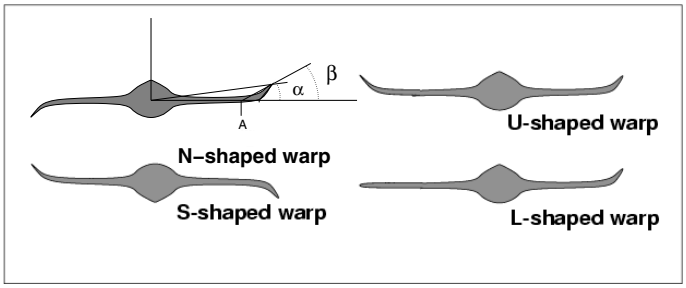

Fig. 4. Definitions of angles, parameters, and types of warps.

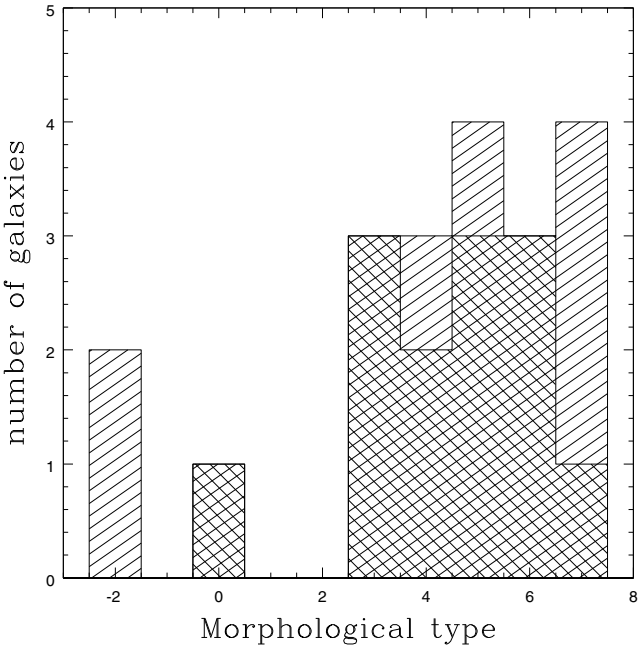

Fig. 5. Morphological-type distribution of our warped galaxies. Hatched area: all galaxies. Cross-hatched area: Warped galaxies.

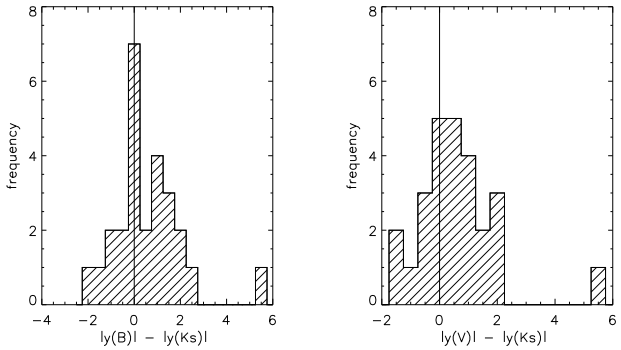

Fig. 6. Histogram of $y(B) - y(K_s)$ and $y(V) - y(K_s)$ at the last measured point in K_s.

ESO358-G26 and ESO358-G29, do not exhibit any detectable warps. Although our sample only contains three S0 galaxies, so that we cannot draw any statistical conclusions on that basis, our results are not in contradiction to previously published results.

Since we have data in both optical and NIR bands, we can compare both, enabling us to either detect or reject colour dependences in the warps. This comparison is difficult, however, because of inherent uncertainties and because the differences as a function of wavelength are not very large. Five of our galaxies (ESO235-G53, ESO288-G25, ESO311-G12, ESO416-G25, and ESO555-G36) show similar warp curves in all four observed bands, one galaxy (ESO531-G22) is warped in all four filters but exhibits a clearly weaker IR warp, one galaxy (ESO564-G27) is warped in the V, I, and K_s filters, and six galaxies (ESO142-G24, ESO157-G18, ESO201-G22, ESO202-G35, ESO240-G11, and ESO340-G08) are warped in the optical bands but not in the IR.

Since NIR profiles reach, in general, smaller radii than their optical counterparts, it is not straightforward to compare the warp distortion at different wavelengths. To do so, we compared the value of the fitted warp curve's y at the same radial distance in each band, for which we adopted the last measured point in K_s (i.e., the h parameter of Ann & Park 2006): see Table 3, Col.3. Based on this table, we appreciate that the optical B and V bands do not exhibit significant differences. However, we find a difference between V and K_s: $y(V)$ is usually greater than $y(K_s)$ (in 14 of 22 cases; see Fig. 6). On the other hand, $y(K_s)$ is greater than $y(V)$ for only six of the 22 cases. This difference can be quite large. The most extreme case is ESO240-G11 (right-hand side), where the $y(V) - z(K_s) = 5.5''$. We find a marginal tendency for NIR warps to have lower absolute values of the fit parameter C. Our attempts at statistically detecting a colour dependence of the observed warps are, therefore, inconclusive. A better understanding would require more studies of this type. If the colour dependence were eventually confirmed, mechanisms acting directly on the gas as the perturbing agent should be favoured. A colour difference has already been found by Florido et al. (1991). They also noticed that the dust lane in NGC 4013 is much more strongly warped than its optical disc. Recently, a study of 2MASS star counts in the Milky Way (Reylé et al. 2009) confirmed that the Galactic warp is less obvious in stars than in the gas and that the disc's shape is different at negative and positive longitudes. However, other authors have not been able to confirm such a difference (e.g., Momany et al. 2006, for the Milky Way).

Figure 7 shows the behaviour of the warp angle β as a function of passband. This angle represents the strength of the warp, i.e. how much the outer disc deviates from the plane defined by the inner (unwarped) disc. Its highest value is obtained for galaxies with revised Hubble type $T = 3$, corresponding to Sb. For these galaxy types, a tendency exists toward lower values of β in the NIR filter than in the B band. The starting point of the warp, A, does not appear to be a function of wavelength.

Kregel et al. (2002) analysed and used the same optical observations discussed here to study the flattening and truncation of the stellar discs. We take their measurements of the truncation radius (see van der Kruit 2007, for definition), R_{max}, in the I band for 11 of our warped galaxies. It would be very useful to compare this truncation radius with the starting radius of the warp (A), because the relation between warps and disc truncations in edge-on galaxies (van der Kruit 2007), if any, is unclear. Obviously we obtain from this comparison that the warp radius, A, is approximately equal to 0.8 R_{max}. Van der Kruit (2007) concludes that when an HI warp is present, it starts at approximately 1.1 R_{max}. Therefore it appears that optical warps always start earlier than HI warps (HI warps start at approximately 1.4 A), although we note that the low resolution of the HI data makes it difficult to detect low-amplitude warps.

Kregel et al. (2004) also presented HI synthesis observations of 15 edge-on galaxies. They have seven galaxies in common with our sample, of which ESO487-G02 was observed with insufficient sensitivity, and five galaxies are found to have a

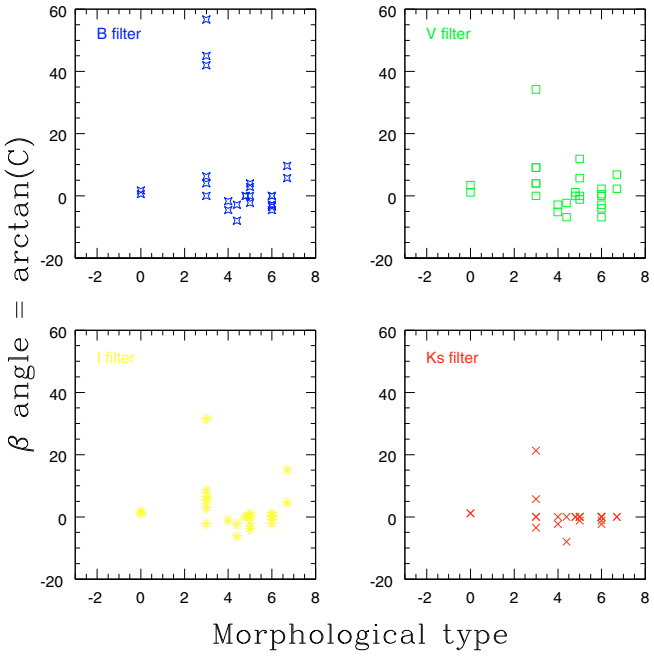

Fig. 7. Distribution of warp angle as a function of revised Hubble type.

warped HI disc. We now analyse the objects in common with Kregel et al. (2004) for which warps have been detected either by them, by us, or by both. They find that the neutral hydrogen distribution in ESO142-G24 appears warped on both sides of the galaxy, following a similar pattern to the stellar disc. In our optical observations, the warp starts at 106″ in the south and 104″ in the north, but on the basis of our NIR observations, we could not detect the same behaviour. Instead, we observe a corrugated disc.

Kregel et al. (2004) find that ESO157-G18 is lopsided, which may be related to the small companion, APMBGC157+052+052, although this galaxy had no previously determined redshift. They did not detect any clear HI warp. We also detected some differences between both sides of this galaxy. Our warp curves exhibit a similar behaviour in all optical bands, while in the NIR the warp is not clear.

ESO201-G22 shows a similar warp curve in HI and in all optical bands, but it is uncertain in the NIR, where the data are not as deep as in the optical. The K_s-band warp curve finishes at a smaller radius than in the optical bands. The bright star on the eastern (left-hand) side of the galaxy hinders our analysis of this region.

ESO240-G11 is very interesting because a region in the galaxy's northwest (right) is clearly warped in the *B* and *V* bands, but the warp is not as marked in the NIR. Kregel et al. (2004) detected warping of the HI layer and they point out that the HI warp can be traced by faint emission in the *I*-band image. In the optical bands, the dust lane is not completely coincident with the galactic plane, which means that this galaxy is either not perfectly edge-on or that it has a warped or asymmetric bulge, which also results in a rather large error bar. On the southeastern (left-hand) side, the warp radius is $103 \pm 2''$ with $\beta = -2.3°$, and on the northwestern side this radius is $132.3 \pm 0.6''$ and $\beta - 63.7°$, so this galaxy exhibits an L-like warp. The "elbow" where the warp begins in a given direction turns back to the mean plane and ends in the opposite hemisphere should show the beginning of the spiral arms. A more detailed study of corrugations in the galaxy's stellar and dust discs would also be very interesting.

The U-like type galaxy ESO416-G25 shows a similar warp curve in all bands, including in HI and the NIR.

The final galaxy also studied by Kregel et al. (2004) is ESO564-G27. This is a clearly corrugated Sc galaxy with some bright foreground stars projected onto the major axis, so it is very difficult to obtain robust conclusions about the stellar warp. Kregel et al. (2004) find that the neutral hydrogen is rather symmetric and extends further than the stellar disc. It is warped on both sides, with the warp apparently starting beyond the stellar disc. We cannot compare this with our results because of the large uncertainties.

Then we can conclude from this comparative study that 5 out of 6 galaxies have an HI warp (only ESO157-G18 does not show any clear HI warp), and these 5 galaxies have an optical warp, while in the NIR the presence of a warp is unclear or absent in all of them. This would indicate that the old star population is less warped than the gas and the more recently born stars.

We calculated α_s – see Eq. (3) – for all warped galaxies, and the results are shown in Table 2. The asymmetry in the warp angles seems related to the warp's intrinsic properties. García-Ruiz et al. (2002b) show that the largest asymmetries are observed in galaxies that display obvious tidal features. We can only show, based on our sample, that the three galaxies that exhibit asymmetries, ESO235-G53, ESO311-G12, and ESO531-G22, all show a large warp amplitude, which supports the positive correlation found by García-Ruiz et al. (2002b). However, none of the galaxies in our sample are involved in strong tidal interactions.

6. Discussion and conclusions

Are all warps produced by the same mechanism? For example, gravitationally driven warps should exhibit no differences between gaseous and stellar morphologies, as opposed to mechanisms acting on the gas (e.g., magnetically or accretion-driven warps). Are the warp curves the same for different colours; i.e., is there any difference in shape and magnitude at different wavelengths?

The present study suggests that, in some of the observed galaxies, the warp is smaller at NIR wavelengths than in the optical. This – combined with the important result of Sánchez-Saavedra et al. (2003) that lenticulars do not exhibit warps (which is also compatible with the results in this paper) – suggests that gas seems to be a necessary ingredient in the development of warps. We have not been able to robustly confirm the absence of warps in S0-type galaxies because our sample only contains three S0s. Therefore, we cannot draw any statistical conclusions on that basis, but our results (at least) do not contradict previously published results that most (if not all) lenticulars are not warped. This must be explained by some theoretical model. Models based on gravity alone might have significant difficulties to explain these observations. A recent study using 2MASS star counts in the Milky Way (Reylé et al. 2009) shows that the warp is less pronounced in stars than in the gas, and it also shows different disc shapes at negative and positive longitudes. The magnetic model of Battaner et al. (1990) is consistent with all of these observations.

Our results show that NIR warps exist with a frequency that is nearly the same as that of optical warps. This suggests that warps are long-lived structures that were formed in the early stages of the evolution of most galaxies. Since warps can be dissipated on a time scale close to the galaxy's rotation period, this indicates that the responsible mechanism, whatever it may

be, seems to be acting permanently. The intergalactic magnetic-field model remains an interesting possibility. It is well-known that a warp will disappear on a time scale of approximately 2 Gyr (Binney 1992). However, in the magnetic model of warps, the field configuration is not an initial condition but extragalactic fields act permanently. The extragalactic magnetic-field lines could be frozen in in the intergalactic medium, therefore corotating with galaxy clusters and presenting a relatively stable configuration of the field with respect to the warped galaxy.

The magnetic model was designed to explain N- and S-like warps ($m = 1$ modes), the most frequently occurring type (51% out of 73% of warped discs in the large sample of 325 edge-on galaxies of Ann & Park 2006). This model does not manage to explain $m = 0$ warps (U-shaped profiles). They should be interpreted as coming from gradients in the extragalactic field, with characteristic lengths close to a galaxy's size. Generations of asymmetric warps through other mechanisms have been considered by Saha & Jog (2006) and López-Corredoira et al. (2002). Other mechanisms have been proposed to induce warping. In fact, the variety of warp morphologies could come from different causes that may act differently from galaxy to galaxy. However, observations of NIR warps and direct comparison with their optical counterparts could provide some constraints.

The frequency of warped discs in our sample is very high (65%). Given the difficulty of detecting warps with their lines of nodes in the plane of the sky, this suggests a fraction of nearly 100% for the frequency of warps in spirals. We have also been able to confirm the finding by Reshetnikov & Combes (1999) that warps are equally present in all types of spirals, $T > 0$.

The abrupt break between the undisturbed inner disc and the warped region (with a roughly constant slope) suggests that these two regions have different formation and evolutionary histories (e.g., van der Kruit 2007). However, van der Kruit concludes that HI warps start at 1.1 $R_{\rm max}$. If this were the case, optical and NIR warps could not be observed. That they are indeed observed allows us to conclude that $R_{\rm max} > A$. Nevertheless, we cannot discard a possible relationship between truncations and warps. It appears that optical warps always start closer in than HI warps, although we note that the low resolution of the HI data makes it difficult to detect low-amplitude warps.

Acknowledgements. We are grateful for the helpful cooperation of the Ursuline Mothers during the period of this work. This paper has been supported by the "Plan Andaluz de Investigación" (FQM-108) and by the "Secretaría de Estado de Política Científica y Tecnológica" (AYA2000-1574).

References

Ann, H. B., & Park, J.-C. 2006, NewA, 11, 293
Battaner, E. 1996, Astrophysical Fluid Dynamics (Cambridge University Press)
Battaner, E., Florido, E., & Sánchez-Saavedra, M. L. 1990, A&A, 236, 1
Battaner, E., Garrido, J. L., Sánchez-Saavedra, M. L., & Florido, E. 1991, A&A, 251, 402
Battaner, E., Florido, E., Jiménez-Vicente, J., Porcel, C., & Sánchez-Saavedra, M. L. 1997, The Impact of Large Scale Near-IR Sky Surveys, ed. F. Garzón et al. (Dordrecht: Kluwer Academic Publishers), Series Astrophysics and Space Science, 210, 49
Binney, J. 1991, Dynamics of Disk Galaxies, ed. B. Sundelius, Goteborg, Sweden, 297
Binney, J. 1992, ARA&A, 30, 51
Bosma, A. 1978, Ph.D. Thesis, Rijksuniversiteit Groningen, Netherlands, http://nedwww.ipac.caltech.edu/level5/March05/Bosma/frames.html
Bosma, A. 1981, AJ, 86, 1791
Briggs, F. H. 1990, ApJ, 352, 15
Brinks, E., & Burton, W.B. 1984, A&A, 141, 195
Burke, B. F. 1957, AJ, 62, 90
Burton, W. B. 1988, Galactic and Extragalactic Radio Astronomy, ed. G. L. Verschuur, & K. I. Kellerman (Berlin and New York: Springer-Verlag), 295
Carter, B. S., & Meadows, V. S. 1995, MNRAS, 276, 734
Corbelli, E., Schneider, S. E., & Salpeter, E. E. 1989, AJ, 97, 390
Dekel, A., & Shlosman, I. 1983, in Internal Kinematic & Dynamics of Galaxies, ed. E. Athanassoula (Dordrecht: Reidel), IAU SYMP., 100, 187
de Grijs, R. 1997, Ph.D. Thesis, Rijksuniversiteit Groningen, Netherlands, http://dissertations.ub.rug.nl/faculties/science/1997/r.de.grijs/
de Grijs, R. 1998, MNRAS, 299, 595
Florido, E., Prieto, M., Battaner, E., Mediavilla, E., & Sanchez-Saavedra, M. L. 1991, A&A, 242, 301
García-Ruiz, I. 2001, Ph.D. Thesis, Rijksuniversiteit Groningen, Netherlands, http://dissertations.ub.rug.nl/faculties/science/2001/i.garcia-ruiz/
García-Ruiz, I., Kuijken, K., & Dubinski, J. 2002a, MNRAS, 337, 459
García-Ruiz, I., Sancisi, R., & Kuijken, K. 2002b, A&A, 394, 769
Hunter, C., & Toomre, A. 1969, ApJ, 155, 747
Jiménez-Vicente, J., Porcel, C., Sánchez-Saavedra, M. L., & Battaner, E. 1997, Ap&SS, 253, 225
Kahn, F. D., & Woltjer, L. 1959, ApJ, 130, 705
Karachentseva, V. E., & Karachentsev, I. D., 2000, Astron. Rep., 44, 501
Kerr, F. J. 1957, AJ, 62, 93
Kregel, M., van der Kruit, P. C., & de Grijs, R. 2002, MNRAS, 334, 646
Kregel, M., van der Kruit, P. C., & de Blok, W. J. G. 2004, MNRAS, 352, 768
Lauberts, A., & Valentijn, E. A. 1989, The Surface Photometry Catalogue of the ESO-Uppsala Galaxies, ESO (ESO-LV)
López-Corredoira, M., Betancort-Rijo, J., & Beckman, J. E. 2002, A&A, 386, 169
López-Corredoira, M., Florido, E., Betancort-Rijo, J., et al. 2008, A&A, 488, 511
Masset, F., & Tagger, M. 1997, A&A, 318, 747
Mathewson, D. S., Ford, V. L., & Buchhorn, M. 1992, ApJS, 81, 413
Momany, Y., Zaggia, S., Gilmore, G., et al. 2006, A&A, 451, 515
Porcel, C., Battaner, E., & Jiménez-Vicente, J. 1997, A&A, 322, 103
Reshetnikov, V., & Combes, F. 1998, A&A, 337, 9
Reshetnikov, V., & Combes, F. 1999, A&AS, 138, 101
Reshetnikov, V., Battaner, E., Combes, F., & Jiménez-Vicente, J. 2002, A&A, 382, 513
Reylé, C., Marshall, D. J., Robin, A. C., & Schultheis, M. 2009, A&A, 495, 819
Rogstad, D. H., Lockhart, I. A., & Wright, M. C. H. 1974, ApJ, 193, 309
Saha, K., & Jog, C. J. 2006, A&A, 446, 897
Sánchez-Saavedra, M. L., Battaner, E., & Florido, E. 1990, MNRAS, 246, 458
Sánchez-Saavedra, M. L., Battaner, E., Guijarro, A., López-Corredoira, M., & Castro-Rodríguez, N. 2003, A&A, 399, 457
Sánchez-Salcedo, F. J. 2006, MNRAS, 365, 555
Sancisi, R. 1976, A&A, 53, 159
Sparke, L. S. 1984, ApJ, 280, 117
Sparke, L. S., & Casertano, S. 1988, MNRAS, 234, 873
Thuan, T. X., & Gunn, J. E. 1979, PASP, 88, 543
Tubbs, A. D., & Sanders, R. H. 1979, ApJ, 230, 736
van der Kruit, P. C. 2007, A&A, 466, 883
Wainscoat, R. J., & Cowie, L. L. 1992, AJ, 103, 33
Weinberg, M. D. 1998, MNRAS, 299, 499
Weinberg, M. D., & Blitz, L. 2006, ApJ, 641, L33

Galaxy Disks and Disk Galaxies
ASP Conference Series, Vol. 230, 2001
J.G. Funes, S.J., and E.M. Corsini, eds.

Magnetic Fields are not Ignorable in the Dynamics of Disks

E. Battaner, E. Florido and A. Guijarro

Departamento de Física Teórica y del Cosmos, Universidad de Granada, Granada, Spain

Abstract. Magnetic fields are considered to be dominant when $\varepsilon_B \geq \varepsilon_K$, being $\varepsilon_B = B^2/8\pi$ the magnetic energy density and $\varepsilon_K = 1/2\rho\theta^2$ the rotation energy density, for a conventional moderate $B = 1\mu$G. They are considered to be negligible when $\varepsilon_B < \varepsilon_K$ for $B \sim 10\mu$G. With no assumption and no theoretical calculation, we show that magnetic fields cannot be ignored in the outer parts of a galaxy like the Milky Way and in the whole disk of a dwarf galaxy.

1. Introduction

Magnetic fields are of the order of $5 - 10$ μG in the interior of a spiral galaxy (e.g., see Beck 1991) and of the order of $1 - 3$ μG in the intergalactic medium (e.g., see Kronberg 1994). We therefore assume 1 μG in the outer region. This interpolated value is therefore a conservative one.

In Fig. 1 the kinetic energy density as a function of the galactocentric distance is plotted for the Milky Way and DDO 154. For the Milky Way, the density data have been taken from Diplas & Savage (1991, but see also Burton 1992). For the rotation curve we assumed a constant value of 200 km s^{-1} for $R \geq R_\odot$, as it results from the works by Homma & Sofue (1997), Merrifield (1992), and Olling & Merrifield (2000). For the typical irregular galaxy DDO 154, the surface density and the rotation data were taken from Gelato & Sommer-Larsen (1999). A typical thickness of 1 kpc was assumed.

A 1 μG magnetic field in the outer disk does not produce detectable synchrotron radiation, because (1) under equipartition $I \propto B^{7/2}$, i.e. the intensity I decreases much more faster than B does. (2) Some authors assume that the number density of relativistic electrons is proportional to the density (because their sources are supernova explosions, which are produced where density is larger). In this case, I decreases still faster, in an exponential way, or even faster as a result of the typical stellar truncation. Probably, B decreases much slower because the strength in the intergalactic medium is $\sim 1\mu$G. (3) The synchrotron spectrum suddenly steepens for large radii (Lisenfeld et al. 1996) what is easily interpreted as a truncation of relativistic electron sources.

2. Conclusions

When considering the rotation curve of spirals, magnetic fields are not at all negligible. They are particularly important in dwarf irregular galaxies where θ

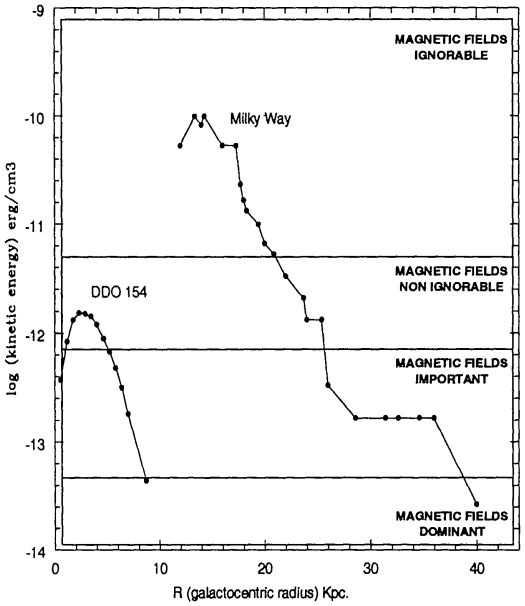

Figure 1. Kinetic energy density radial profile of the Milky Way and DDO 154. The ranges in which contribution of the magnetic fields is ignorable, non ignorable, important and dominant are also plotted.

is lower. Magnetic fields have similar values (see for instance, Beck 1991). Theoretical models by Nelson (1988), Battaner et al. (1992), Battaner & Florido (1995) and Battaner, Lesch & Florido (1999), have already explored this possibility. *Ignoring magnetic fields when interpreting rotation curves can be completely unrealistic.*

References

Battaner, E. & Florido, E. 1995, MNRAS, 277, 1129

Battaner, E., Garrido, J. L., Membrado, M. & Florido, E. 1992, Nature, 360, 652

Battaner, E., Lesch, H. & Florido, E. 1999, Anales Física, 94, 98

Beck, R. 1991, in ASP Conf. Ser. Vol. 18, The Interpretation of Modern Synthesis Observations of Spiral Galaxies, ed. N. Duric & P. C. Crane (San Francisco: ASP), 43

Burton, W.B. 1992, in SAAS-FEE Adv. Course 21, The Galactic Interstellar Medium, ed. D. Pfenniger & P. Bartholdi, (Berlin: Springer-Verlag), 126

Diplas, A. & Savage, B. D. 1991, ApJ, 470, L35

Gelato, S. & Sommer-Larsen, J. 1999, MNRAS, 303, 321

Honma, S. & Sofue, Y. 1997, PASJ, 49, 539

Kronberg, P. P. 1994, Rep. Prog. Phys., 57, 325

Lisenfeld, U., Alexander, P., Pooley, G. G. & Wilding, T. 1996, MNRAS, 281, 301

Merrifield, M. R. 1992, AJ, 103, 1552

Nelson, A. H. 1988, MNRAS, 233, 115

Olling, R. P. & Merrifield, M. R. 2000, MNRAS, 311, 361

Magnetic fields and the dynamics of the outer disk of spiral galaxies

Eduardo Battaner, Estrella Florido, Ana Guijarro, and Africa Castillo

Citation: AIP Conf. Proc. **784**, 784 (2005); doi: 10.1063/1.2077249
View online: http://dx.doi.org/10.1063/1.2077249
View Table of Contents: http://proceedings.aip.org/dbt/dbt.jsp?KEY=APCPCS&Volume=784&Issue=1
Published by the American Institute of Physics.

Magnetic fields and the dynamics of the outer disk of spiral galaxies

Eduardo Battaner*, Estrella Florido*, Ana Guijarro* and Africa Castillo*

*Dep. Física Teórica y del Cosmos. Univ. Granada. Spain

Abstract. Recent observations may support the hypothesis of magnetically driven rotation curves in spiral galaxies. Following this model three dynamical regions should be expected: 1) An inner region where magnetic fields are ignorable, 2) A region in which the magnetic strength decreases slower than 1/R, and 3) an outermost region where the strength reaches a slope proportional to 1/R. This radial variation is observed in the Milky Way and NGC 6946.

Keywords: Spiral galaxies, magnetic field
PACS: 95.30.Qd, 98.52.-b

The magnetic hypothesis to explain the flatness of the rotation curve of spiral galaxies assumes that the radial magnetic force given by

$$F_{mag} = -\frac{1}{8\pi R^2}\frac{\partial\left(R^2 B_\varphi^2\right)}{\partial R} \tag{1}$$

(where R is the galactocentric radius; B_φ the azimuthal component of $\vec{B}$) balances the centrifugal force at very large radius and is non-negligible at large radii (see Battaner et al. 1992; Battaner and Florido 1995, 2000). In this presentation we state that observed field strength does actually support this hypothesis, without comparison with any particular theoretical model.

We just take into account that from the point of view of magnetic influence a spiral galaxy could be divided into three regions:

1. An internal region in which $\vec{B}$ cannot compete with $\vec{g}$.
2. An external region in which $F_{mag} < 0$ (inwards), i.e.

$$\left|\frac{1}{B_\varphi}\frac{\partial B_\varphi}{\partial R}\right| < \frac{1}{R} \tag{2}$$

3. An outermost region in which $F_{mag}(R \to \infty) \to 0$, hence

$$\left|\frac{1}{B_\varphi}\frac{\partial B_\varphi}{\partial R}\right| \to \frac{1}{R} \tag{3}$$

because at very large radii $\rho(R \to \infty) \to 0$, too.

The R^{-1}-profile is called the "critical profile". If $\left|(1/B_\varphi)(\partial B_\varphi/\partial R)\right| < 1/R$ the profile is called "subcritical". A subcritical profile produces an inward force, hence the

CP784, *Magnetic Fields in the Universe: From Laboratory and Stars to Primordial Structures*
edited by E. M. de Gouveia Dal Pino, G. Lugones, and A. Lazarian

rotation velocity must be higher. A critical profile produces no net radial force. But at large radii the B_φ-profile must be very close to critical because the density is very low.

These facts are confirmed by precise observation of the magnetic field strength and energy density in the Milky Way and in NGC 6946 (Beck, 2004).

In the Milky Way the profile is subcritical for $R \geq 7$ kpc and becomes critical for $R \geq 10$ kpc. In NGC 6946 the profile is subcritical for $R \geq 4$ kpc; the critical region is not observed (or is absent). In the Milky Way it is observed that the magnetic radial scale length (~ 8 kpc) is much larger than the density radial scale length (~ 3 kpc). In M31 the strength at 25 kpc is nearly the same as in the inner disk (Han et al. 1998) therefore $\left|(1/B_\varphi)(\partial B_\varphi/\partial R)\right|$ is very low. In NGC 6946, at 8 kpc, the inward magnetic force is equivalent to the force by a central point mass of 5×10^9 $M_\odot$, which is not negligible as the stellar mass within $R < 8$ kpc is about 10^{10} $M_\odot$.

Therefore, magnetic forces cannot be ignored in the dynamics of galaxies. The magnetic model is a competitive one for explaining the flat rotation curve of spiral galaxies.

REFERENCES

E. Battaner, J.L. Garrido, M. Membrado, and E. Florido, *Nature*, **360**, 652 (1992).
E. Battaner, and E. Florido, *Monthly Notices of Royal Astron. Soc.*, **277**, 1129–1133 (2000).
E. Battaner, and E. Florido, *Fundamentals of Cosmic Physics*, **21**, 1–154 (2000).
R. Beck, *astro-ph/0310287* (2004).
S.L. Han, R. Beck, and E.M. Berkhuijsen, *Astronomy and Astrophysics*, **335**, 1117–1123 (1998).

MAGNETIC FIELDS IN GALAXIES

EDUARDO BATTANER[1,2] , ESTRELLA FLORIDO[1,2]
1 Departamento de Física Teórica y del Cosmos, Universidad de Granada, SPAIN
2 Instituto Carlos I, Universidad de Granada
ANA GUIJARRO [1,3]
3 Centro Astronómico Hispano Alemán, Almería, SPAIN
JOSE ALBERTO RUBIÑO-MARTÍN
Instituto de Astrofísica de Canarias, La Laguna, Tenerife, SPAIN
BEATRIZ RUIZ-GRANADOS[1,2]
ALMUDENA ZURITA[1,2]

Abstract: Magnetic fields not only provide a basic tool for observing galaxies but constitute an important clue to interpret many dynamic processes taking place in them, mainly in spiral and irregular galaxies. As in the Sun, magnetic fields become important where gravity becomes lower, i.e. in the outermost regions. Any peripheric feature should be explained taking into account magnetic fields, in particular warps, truncations of stellar systems, lopsidedness and so on. Of special cosmological interest is the role of magnetic fields in the rotation curve of spirals. All these questions are still insufficiently explored and the study of magnetic fields in the whole universe open wide areas of interpretation.

Keywords: Magnetic Fields – Galaxies

1 Introduction

The word magnetism has an Indo-European origin, coming from the root "magh" equivalent to "have power". From the same root are the words "magic" and the spanish "desmayarse" (to faint). In non-scientific forums "magnetism" is still connected to the meaning of "magic" and even with "hypnotic" power to "fascinate".

When magnetic fields lost their "magic power" to become a physical quantity? As we are aware the first scientific thought about magnetism being applied to a cosmic question was written in the logbook of a well known sailor around 1500:

"Fallo que de Septentrión en Austro, pasando cien leguas de las dichas islas [Azores], que luego en las agujas de marear, que fasta entonces noruesteaban, nordestean una cuarta de viento todo entero... Me puse a tener esto del mundo y fallé que no era redondo en la forma que escriben; salvo que es de la forma de una pera que sea toda

muy redonda, salvo all donde tiene el pezón, que allí tiene más alto, o como quien tiene una pelota muy redonda y en un lugar de ella fuese como una teta de mujer allí puesta...". This was written after the third journey to America by Columbus.

There is a recent excellent book in which an exhaustive review of most aspects of galactic magnetism are deeply considered. This is the book "Cosmic Magnetic Fields" edited by Wielebinski and Beck in 2005. This book provides a so extensive and intensive up-to-date of galactic magnetism that it is not noteworthy to repeat hear the most established facts of galactic magnetism. The reader is also addressed to other interesting reviews [1, 2]. We will then concentrate in complementary topics concerning magnetic effects.

In this review we will concentrate in those topics concerning a) large scale magnetic phenomena and b) peripheric ones. This aim is equivalent to deal with controversial and even speculative topics. We will consider also magnetic fields in the pregalactic medium, as a possible clue to many features found today in z=0 galaxies.

For other problems of galactic magnetic fields the reader is addressed to the cited book edited by Wielebinski and Beck. It is nevertheless interesting to briefly list some important topics at lower scale which will be here not considered, in which magnetic fields cannot be ignored or even are dominant, which are at present in phase of study, debate or promising development.

We will not consider the problem of AGN, radio lobes and optical and radio jets even if this is one of the chapters more insufficiently understood of galactic magnetism. Here, fields are not only the clue for explaining the ejection itself and the reacceleration of electrons but can provide an additional mechanism to feed the AGN [4]. The different dynamo mechanisms undoubtedly constitute one of the most important chapters, to explain how a regular field can arise as a consequence of turbulent motions, being a case where we "see" how chaos may produce order. Other small scale phenomena are as well important. Fields play a crutzial role in HI and molecular clouds as well as in the HI diffuse medium, not only as a passive magnitude being amplified, ordered and disordered by them, and not only as a dynamic force, but also as a direct heat productor, via reconnection [5] of magnetic field lines. This could be very important in other lower scale phenomena, such as in HII regions, bubbles and so on, in which the role of reconnection has just begun to be realized. Other phenomena as magnetic fields in bars and spiral arms, reversals and magnetic arms are not the objective here. Magnetic helicity can play an important role in our galaxy as well as in primordial magnetism. Finally, a considerable effort has been made in simulations in magnetized cosmic systems that will be not reviewed here [6, 3]. We will not consider the problem of the tools to observe and measure galactic fields. The synchrotron radiation constitues the most important source of information about magnetic fields, but observing this radiation in some galaxy simply tells us that magnetic fields are there, but obtaining their strength and directions is a more difficult question. The synchrotron brightness not only depends on the magnetic field but also on the number

LNEA III, 2008.
A. Ulla & M. Manteiga (editors).

density and energy spectrum of the relativistic electrons. Therefore, some assumptions are needed, for example, equipartition of energies. The polarized synchrotron continuum provides clear information about the direction of the field vector, but only of its component perpendicular to the line-of sight. Faraday rotation also needs an additional observing tool to know the number density of the thermal electrons and we as well need a large number of extragalactic radio sources behind the observed galaxies. In our own Galaxy the number of extragalactic sources and galactic pulsars is high but the existence of a random component of the magnetic fields renders difficult the estimation of the large scale distribution of the regular component. (See Section 6).

2 Why are magnetic fields non-ignorable in any peripheric phenomenon.

The reason by which magnetic fields can be important in peripheric phenomena is double: a) They decrease slowly for increasing radii and b) Order of magnitude arguments show that they are not ignorable. The situation is therefore similar to that in the Sun and magnetic stars. Magnetic fields could compite with gravitation at large radii in normal spiral galaxies and at all radii in dwarf spiral galaxies.

There are evidences for large field strengths in galaxies, even at large radii:

- The field strength of a sample of 74 spiral galaxies is 9 μG [7, 8]. Some galaxies, like M31, M83 and NGC6946 have a strength of the order of 15 μG [8]. Starburst galaxies like M82 reach 50 μG [9]. These are total fields but only the regular fields are able to produce magnetic forces at large-scale. Usually regular and random fields have similar orders, but at large radii the higher degree of polarization, and hence the field regularity, increases. At about 8 kpc the total field of NGC6946 is about 10 μG [8] and the regular field must be slightly lower.

- The magnetic energy density, $B^2/8\pi$ decreases very slowly with radius (Figure 1). For example, in NGC6946 (probably the best observed external galaxy [10]) the radial scale length of the magnetic energy density is very large, of the order of 16 kpc, compared with a radial scale of the density of this galaxy of only 3 kpc. The radial scale length of the regular field is probably larger than 16 kpc, as deduced from the higher degree of polarization at large radii.

- Faraday rotation of extragalactic sources behind M31 lead to magnetic strength similar to those found at lower radii [11].

- In our Galaxy the total field is 6 μG at 10 kpc (about 10 μG in the inner galaxy) [12, 13]. In Figure 2 we reproduce the radial profile [14] for our Galaxy. We

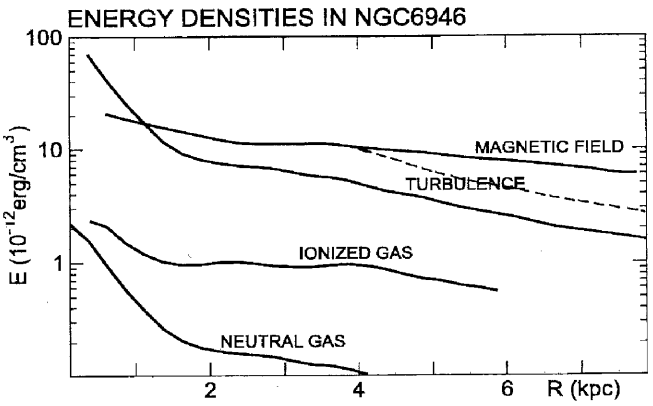

Figure 1: Energy densities in NGC6946 from [14]. The dotted line corresponds to a critical profile. The magnetic force is directed inwards. R is the galactocentric radius along the symmetry plane of the galaxy.

see that at 17 kpc the field strength of the total field is 4 μG. Therefore, the regular field should be only slightly lower.

- The order of magnitude of the strength outside galaxies, in the intra-cluster medium, is similar. Faraday Rotation of sources placed behind the Coma cluster were detected [15] and deduced to be 2 μG [16]; with much higher resolution it was obtained 7-8 μG [17]. Statistically it was deduced a value of 2-12 μG in a sample of 40 galaxies [18, 19, 20]. In addition, μG fields found everywhere, even in extracluster regions near Coma could suggest an equipartition of magnetic and CMB energy densities [21]. In this case, $B^2/8\pi = aT^4$, being T the CMB temperature and a is the radiation pressure constant; $a = 4\sigma/c$ where σ is the Stefan-Boltzmann constant. We should have for a widespread field, $B \approx 3\mu G$. That does nor mean that a cosmological aligned field exists, what would be incompatible with the Cosmological Principle and in desagreement with the absence of a correlation between Rotation Measure in quasars and preferred directions of this relation. It has been estimated 10^{-11}G as an upper limit for such homogeneous aligned cosmological field. However regular fields of the order of few microgauss are normal in clusters and may be present in large filaments and walls of the large scale structure [16]. Then, if the galactic magnetic field must connect with the intracluster field, and given the existence of an active turbulent magnetic diffusion, the regular magnetic field at large radii must be

as high as 1-5 μG in normal spiral galaxies .

Field strengths this magnitude cannot be ignored. Or, in other words, if gravitational forces decrease as $1/R^2$ (at large radii, and only due to the visible matter) and magnetic forces decrease much slower, the question is at what R the magnetic force becomes a substantial fraction of the gravitational one. Usually, the criterion for not neglecting a term is when it is at least one tenth of the dominant term. Hence

$$0.1\frac{GM}{R^2}\rho \approx \frac{1}{8\pi}\frac{1}{R^2}\frac{d(R^2B_\varphi^2)}{dR} \tag{1}$$

where M is the visible matter of the galaxy (seen at large radii as producing a central point potential), ρ is the density, B_φ is the azimuthal component of the magnetic field strength (the main component and the one that produces a radial force competing with gravity). For an order of magnitude estimate, and taking into account the above arguments, we assume B_φ independent of R, and consider $\rho = \rho_o e^{-R/R_o}$, then

$$Re^{R/R_o} = \frac{GM\rho_o}{B_\varphi^2} \equiv 4\times 10^4\frac{M\rho_o}{B_\varphi^2} \tag{2}$$

In the last term of this equation M is measured in $10^{11}M_\odot$, ρ_o in $10^{-23}gcm^{-3}$, B in μG and R in kpc. This transcendent equation would give us the radius at which magnetic fields cannot be ignored when compared with the visible mass of the galaxy.

We now take temptative values, $B_\varphi \approx 5$, $\rho_o \approx 1$, $M \approx 1$, $R_o \approx 3$ and obtain $R \approx 14kpc$. For some galaxies, the influence of magnetic fields can be very important, especially for dwarf spirals, if we take $M = 0.1$, $\rho_o = 0.1$, $B_\varphi = 5$ (as dwarf spirals have even higher strengths [8, 22]) in which magnetic fields should be non-ignorable at all radii.

3 Magnetic fields and rotation curve

The techniques and difficulties for obtaining rotation curves have been detaily reviewed [23]. The possible influence of magnetic fields in the large scale dynamics of a spiral galaxy was early claimed [24, 25]. Later, a substantially different model was presented [26, 27]. In this and a subsequent model it was argued that magnetic fields alone, i.e. without the need of the hypothesis of galactic dark matter, were able to be responsible of the paradoxical large and flat rotation curve of spiral galaxies at the rim. Before reviewing the magnetic hypothesis of the rotation curve, it is salutary to prevent the reader that assuming negligible the contribution of galactic dark matter does not imply at all to assume negligible the amount of cosmological dark matter. On the other hand we cannot disregard the existence of galactic dark matter,

LNEA III, 2008.
A. Ulla & M. Manteiga (editors).

but the fact that existing models are able to explain this noticeable rotation curve, must prevent us that trying to explain it, ignoring magnetic fields, can be completely unrealistic. The magnetic hypothesis of the rotation curve is still controversial and a clear example of how much the astronomical community is prone to reject alternative scenarios, even when they are based on classical concepts.

A reconsideration of these magnetic models is now necessary as some of the properties of magnetic fields, such as strengths and radial gradients, which were assumed in these early models, have been recently confirmed by observations.

In a first model [26], it was claimed that fields of the order of 6 μG in the outer parts could provide a centripetal force which together with the gravitational force of visible matter could balance the large centrifugal force. This "large" strength could produce a flaring higher than observed [28]. This important objection prompted us to develop a more detailed model [29]. In this two-dimension model that included horizontal and vertical motions and escape, only fields of $\sim 1\mu G$ at large radii, or slightly lower, were necessary. Today, with the development of measure techniques, it is not necessary to explain why an excessive flaring is not to be expected with fields of order 5 μG, just because this is actually the observed strength. If the hydrostatic equation in the vertical direction leads to an excessive flaring, this just indicates that this equation was not properly applied. It was shown [29] that vertical motions and escape are basic ingredients in the vertical component of the motion equation.

The Virial theorem inform us about the net expansive effect of magnetic fields and however they can produce a centripetal force. No objection can arise from this fact as our model integrated the equation of motion while the Virial theorem is obtained from this equation under some restrictive assumptions. It was shown [29] that this potential incompatibility vanishes when the vertical direction is included. Magnetic fields should have a net expansive effect but they could have a centripetal action in the radial direction compensated with an escape in the vertical one. This second model predicted a vertical escape flux of the order of 0.1 $M_{\odot} yr^{-1}$. Another recent work [30] argued against the hypothesis of magnetically driven rotation also revisiting the Virial theorem. Other arguments in favour or against have been discussed in [31] and will not be repeated here. Rotation curves under the interpretation of dark matter, MOND and magnetic field were analyzed and discussed [32]. These magnetically driven models [26, 29] were presented more than ten years ago. At that time several assumptions were made which have been clearly supported or confirmed by recent observations [31].

Magnetic forces arise from two different effects: the force due to the magnetic pressure gradients and the magnetic tension. The first one, $\nabla(B^2/8\pi)$, is usually centrifugal as B decreases for increasing R. The second one $(1/4\pi)\vec{B}\cdot\nabla\vec{B}$ is, in real galaxies, centripetal. In a pure ionized gas ring, with an azimuthal field, it can be easily demonstrated that this magnetic tension produces an inward force. Then, the direction of the magnetic force arises from the competing action of gradients in

LNEA III, 2008.
A. Ulla & M. Manteiga (editors).

the magnetic energy density and the magnetic tension. The most important radial magnetic action, taking into account both effects can be written as a radial force

$$F_{radial} = -\frac{1}{8\pi\rho}\frac{d(R^2B_\varphi^2)}{dR} \tag{3}$$

There are other forces but this represents the radial force produced by the azimuthal component of the field, which is the most important. We see that when $B_\varphi \propto 1/R$, there is no magnetic force. It is then expected that the B_φ-profile would asymptotically converge to a $B_\varphi \propto 1/R$ profile for very large R, as the force should become vanishing when the density tends to zero. A profile of the type of $B_\varphi \propto 1/R$, or:

$$-\frac{1}{B_\varphi}\frac{dB_\varphi}{dR} = \frac{1}{R} \tag{4}$$

is called the critical profile. When B_φ decreases slowly with R, slowly than the critical profile, then $d/dR(R^2/B_\varphi^2)$ becomes negative and the net force is centripetal. Such a profile is called sub-critical. On the other hand if B_φ decreases faster with R, the net magnetic force is centrifugal and the profile is called super-critical.

In the outer part of real galaxies we could identify three regions: A) An internal one where magnetic fields cannot compite with gravitation and therefore the shape of the B_φ-profile is unimportant, B) An intermediate zone where the B_φ-profile is subcritical and hence the net magnetic force is directed inwards, and C) An outermost region in which the B_φ-profile is critical, or better, asymptotically critical, in which the net magnetic force is null, corresponding to a density tending to zero.

There are at present only two galaxies for which we have data precise enough for this identification. These are NGC6946 and the Milky Way [14]. We reproduce the observational B_φ-profiles for both galaxies together with the critical slope (Figures 1 and 2 from [31]). In NGC6946 the profile is clearly subcritical for $R \geq 3kpc$ indicating a net centripetal force. In the Milky Way we see that the slope is critical for $R \geq 10kpc$, and subcritical for $7 \leq R \leq 10kpc$. For $R < 7kpc$, clearly, magnetic forces should be negligible.

These two plots are in noticeable agreement with the theoretical expectations from the magnetic model and encourage theoreticians and observers to appreciate how magnetic fields should be included in the study of rotation curves, mainly when we see that standard ΛCDM models do not satisfactorily explain them ([33, 34, 35]). Some elliptical galaxies permit the obtention of rotation curves too. As they are gas-poor magnetic fields cannot be important. Rotation curves in these galaxies seem to be keplerian [36, 37].

Other types of galaxies should be investigated for large magnetic dynamical effects:

- Some galaxies exhibit an outer ring (both ellipticals and spirals). An isolated ring should be much more affected by magnetic fields as the force arising from

LNEA III, 2008.
A. Ulla & M. Manteiga (editors).

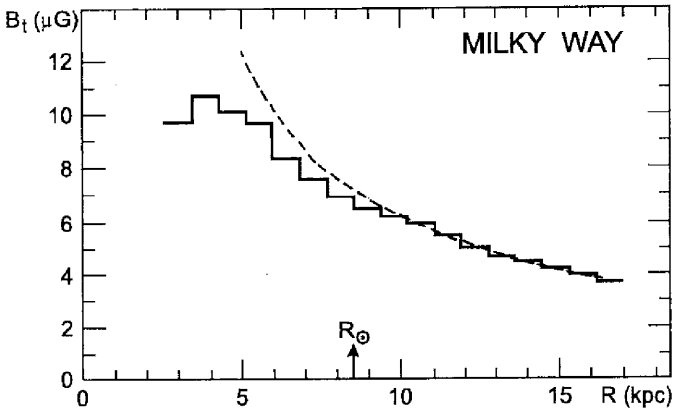

Figure 2: Total magnetic field strength in the Milky Way. A critical profile (dotted line) follows a region with magnetic force directed inwards. From [14] and [31].

the gradient of the magnetic energy density is absent. Therefore, the inwards magnetic force due to the magnetic force should be higher and easier to be identified. We include here polar ring galaxies, whatever was the origin of the ring.

- Dwarf irregular galaxies can be considered extreme late-type spirals. As they are small, according to the Tully-Fisher relation [38] the rotation velocity is low. With a low rotation velocity, dynamo models predict low magnetic fields strengths. However, observations show that these strengths are at least as high as in normal spirals, as above mentioned. Not only the peripheric regions could be influenced by magnetic fields, but the whole irregular galaxy. It should be stressed that magnetic fields also induce large vertical motions and that these galaxies exhibit especially vertical outflows as well as gas and field ejections. A good example is the galaxy DDO 154 [39]. Slowly rotating galaxies of the Local Group reveal strong total magnetic fields of more than 10 μG (in NGC4449 and in IC10) [40].

Other works also present analyses favoring the existence of dynamically non-negligible magnetic fields [36, 41]. For a more complete review the reader is addressed to [32, 31] where arguments in favor and against are analyzed in more detail.

Another complementary problem is the identification of the mechanism producing these fields. The first approach would be how to obtain critical profiles. The possibility of a turbulent magnetic diffusion of the z-component of the magnetic field, amplified and converted into azimuthal field in the central disk by differential rota-

tion to produce critical 1/R-profiles was considered [42, 32, 43, 44]. However the azimuthal component should vanish at z=0 in the galactic plane contrary to the observations [44, 45]. See, however [11]. Other dynamo-like mechanisms are able to produce critical profiles [32].

4 Truncations of stellar disks.

Truncations of stellar disks were discovered and studied by van der Kruit and Searle [46, 47, 48, 49]. Other more recent observations have been reported in [50, 51] and many others. We understand that "truncations" should be "complete". With the word "complete" we understand that beyond a certain radius, R_{max}, the density of the stellar system is null (within observational limits). This was the first description proposed by van der Kruit and Searle and this interpretation was followed and adopted by most astronomers [52, 53]. Clearly, truncations cannot be completely sharp, only relatively sharp [54]. Therefore, we can speak of a truncation curve , $T(R)$, defined as the difference between the observed light profile and the extrapolated exponential of the inner untruncated disk. Clearly, when we are observing edge-on galaxies what we observe is the surface brightness but the deprojected surface brightness should be proportional to the density of stars. We understand that truncations are peripheric, complete and not completely sharp.

From the observational point of view, several recent papers [55, 56, 57, 58, 59], have found that the "truncation" is not a good description of the phenomenon. They find that the correct description is a double exponential profile with a break in between. Sometimes, the second exponential is steeper, sometimes it is shallower and sometimes the profile is unbroken. This simple scheme proposed in [55] has been enriched in more recent papers where the authors divide these three types into a series of subtypes, often introducing a third exponential which can be either shallower or steeper than the second, rendering the initial classification more complex. When the second exponential is shallower they also use the word "untitruncation". Most of their analysis is based in face-on spirals and in the optical, but edge-on galaxies also in the optical have also been studied [59].

A description more in agreement with the early interpretation of van der Kruit and Searle and Binney and Tremaine has been observed [60, 61, 62]. Following these authors there is a real non-sharp complete truncation being the truncation curve given by a fitting formula proportional to $(R_{max} - R)^{-\alpha}$ where α is close to unity. Figure 3 shows a typical truncation profile and in Figure 4 we plot the truncation curve. As these authors work in the NIR and the formers in the optical, the first explanation would be that both wavelengths, tracing different populations, are intrinsically different. However, the galaxy NGC6504 was observed in the optical and in the NIR [63] with the best depth available and it was found that the optical profile is as well

LNEA III, 2008.
A. Ulla & M. Manteiga (editors).

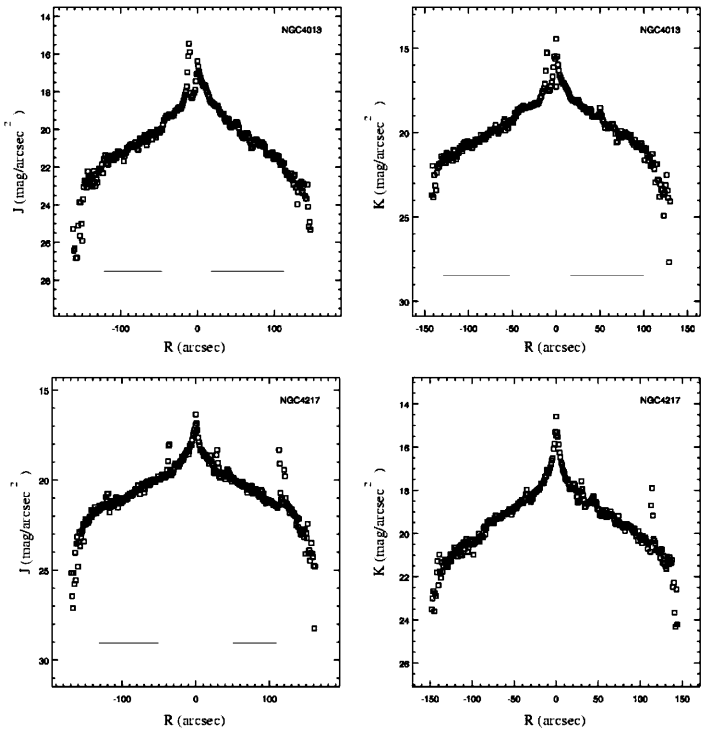

Figure 3: Truncation profile in the spiral galaxy NGC4013 and NGC4217 ([60]).

really truncated. They have reached 28.5 magnitudes per arcsec square with no trace of stars beyond $R_{max} = 82$ arcsec. Profiles in the optical and in the NIR have a slope continuously steeping without evidence of a double exponential. (See Figure 5).

The NIR profiles also confirm the existence of antitruncations such as that of NGC2654 [62] as shown in Figure 6.

We are here, however, more interested in the physical process responsible of truncations. This section is included in this review because magnetism is one of the proposed mechanisms [64]. The scenario is simple and connected with that of magnetically driven rotation (see last section). Suppose gas moving in circular orbits with gravity plus magnetic fields in balance with the centrifugal force. Suddenly (in a very short time compared with typical dynamic times) some stars are born from this rotating gas. Magnetic fields can no longer act on the stars. Therefore new born

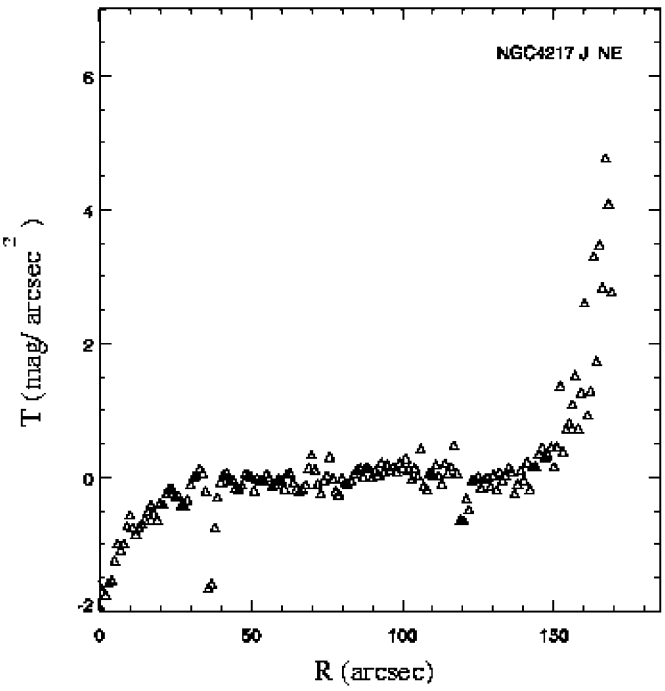

Figure 4: Truncation curve in the spiral galaxy NGC4217 ([60]).

stars are formed out of equilibrium of forces. Then, some stars migrate to larger radii orbits (producing antitruncations) and others escape from the galaxy in the radial direction (producing truncations).

This hypothesis has the "a priori" advantage that, qualitatively at least, is able to explain both antitruncations and truncations. For the case of truncations, we deduced [64] by means of our simpler model that

$$R_{max} = \frac{2GM}{\theta_o^2} \tag{5}$$

being M the visible mass of the galaxy and θ_o the asymptotic rotation velocity ($\theta_o = \theta\,(R \to \infty)$). Taking into account the Tully-Fisher relation $L \propto \theta_o^x$, where x is typically 3.5, we obtain either $R_{max} \propto \theta_o^{1.5}$ or $R_{max} \propto L^{0.7}$. The relation between R_{max} and $\theta_o^{1.5}$ is fully confirmed by observations. (See Figure 7 and [54] for edge-on galaxies). We also see that truncations should be more difficult to be detected in large galaxies, as R_{max} is higher. This is also confirmed by the observations.

There are other non-magnetic models for the explanation of truncations. If we assume that the initial gaseous disk was exponential without neither truncations nor

LNEA III, 2008.
A. Ulla & M. Manteiga (editors).

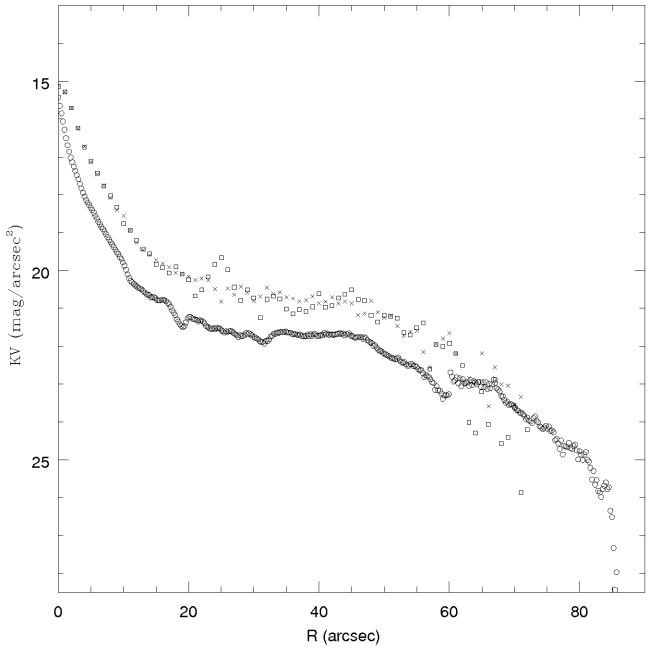

Figure 5: Truncation curves in the spiral galaxy NGC6504 in the optical and NIR ([63]).

breaks, and if the density of stars drop beyond an R_{max}, either, for some reason, the gas beyond R_{max} has no ability to form stars, or the stars once formed flow away. Below a density threshold, stars could be no longer formed out of gas. The threshold hypothesis [65, 66] is of the former type. The excess of angular momentum induced by a large differential rotation beyond R_{max}, could cause the inability to form stars too [67] . This explanation would also be of the former type. Clearly, magnetically driven truncations belong to the second type of explanations.

There is an interesting argument [68] against the scenarios inhibiting star formation. A sudden drop in the rotation curve takes place at R_{max}. This drop was also found in NGC5055 [69].

This drop indicates that there is a rather sharp decrease in the total mass (gas plus stars) not only of stars. Another argument favoring models which do involve large scale dynamics, is that the radial decrease of gas amount is due to a radial decrease in the number of molecular clouds, but the density in these outer clouds is not different when compared with the inner clouds.

Another interesting model, also involving large scale motions, has been proposed

LNEA III, 2008.
A. Ulla & M. Manteiga (editors).

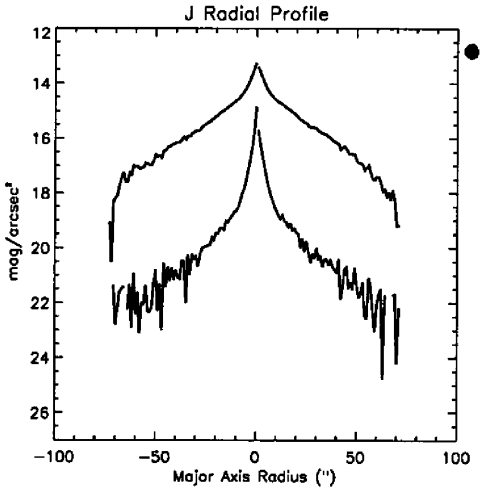

Figure 6: Antitruncation in the NIR (J band) in the galaxy NGC684.

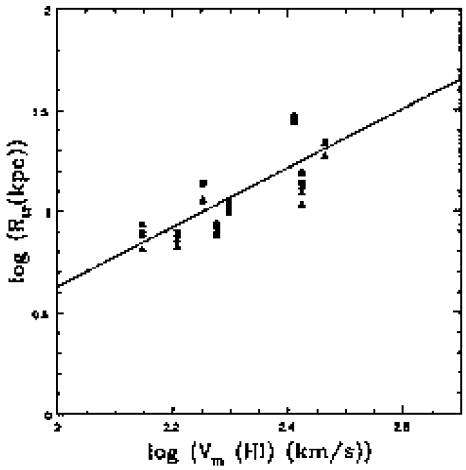

Figure 7: Relation between the truncation radius and the asymptotic velocity.

[68, 54], in which the disk was formed in two steps. In the first step the inner disk was formed with a size R_{max}. This finite size R_{max} was established by the maximum specific angular momentum. The extragalactic gas falling later, in the second step, produced the outer region.

With respect this model defended in [54] with the first settled truncated rigid disc and a warped external disc in a more recent step, relating R_{max} and the radius

LNEA III, 2008.
A. Ulla & M. Manteiga (editors).

at which the warp begins, we should have two comments: First, optical warps exist and even most galaxies have warped stellar systems [70, 71, 72]. Second, very early z=1 galaxies show optical warps and much larger than the present one [98].

An important observational fact is that R_{max} increases with the band wavelength used (see for instance Figure 7). This is another reason to use NIR to detect truncations. This is also a constraint that models must explain. It is interesting to note that breaks are also observed in large-z galaxies [74, 58].

5 Warps.

It is well known that most spiral galaxies have a warped plane when observed at 21 cm ([75, 76, 77] and others). The warps are also observed in the optical ([70, 72, 60, 71, 79]). The frequency of warped disk in spiral galaxies is very large. In contrast, no lenticular galaxy has been observed to be warped [72]. All the spiral galaxies with very extended HI-disk are warped. These facts suggest that the mechanism producing the bending acts directly on the gas and that the stellar warp is the consequence of being stars born in a warped disk. Therefore, we have searched for a magnetic scenario being in this case the extragalactic magnetic fields responsible of the warps.

There are other hypothesis (see [80, 81, 68], for instance). Tidal interaction [82] may explain some warps but not their high frequency: Near all spiral galaxies are warped. Sparke and Casertano [95] showed that some discrete modes can survive, but they did not take into account the reaction of the halo, what would destroy the warp in few orbit periods. Binney [80] considered the interesting possibility that the permanent accretion of material into the DM halo would produce a continuous redistribution of its angular momentum and the warps would be created by the reaction of the disk to this redistribution.

It seems that warping could be a natural response of the outer disk to a series of stimulations and that different mechanisms could be responsible in different galaxies. However the observation of large edge-on spiral galaxies could contribute to determine the dominant scenario. The intergalactic medium could play an important role [83] by interaction with extragalactic clouds [84, 85], by the flowing of galaxies in an intra-cluster medium [86] or by extragalactic magnetic fields [87].

The magnetic model of warps is an interesting possibility. It is known that a warp will disappear in a time of about 2 Gyr [80], or even shorter in the magnetic case. However, in the magnetic model of warps, the field configuration is not an initial condition but extragalactic fields are acting permanently. Any cause of warps must act permanently.

The intergalactic magnetic field must penetrate in the outer disk by some mechanism at work in the external region. Probably the intercharge of matter and fields between disk and intracluster medium is very active as vertical out and inflows are

very common, transporting these flows the frozen-in field lines. This intercharge can be very active mainly in the outer disk where the low surface density produces low gravitation enabling vertical motions. These flows could be considered as turbulent (even if they are not properly turbulent) and the mechanism of field transport could then be treated as a turbulent magnetic diffusion. The coefficient of turbulent magnetic diffusion, $\beta = (B'/B)v'l$, should not be constant but highly radial dependent. B' and B are the fluctuating and mean magnetic field strengths, v' a characteristic velocity of the fluctuations and l a typical eddy size (e.g. [88]). We take $B'/B \sim 1/3$, as the random component is slightly lower than the regular one [8] and $l \approx 1$ kpc is the size of the larger eddies, that can be identified with the thickness of the disk. It is difficult to assess values for v' but it must change very much with radius. Taking $v' \sim 1$ km/s in the inner disk we obtain β (inner) $= 10^{26}$ cm^{2}s^{-1}, which is even larger than currently adopted values [89, 90, 91].

The turbulent process producing the turbulent diffusion of magnetic fields is usually assumed to consist in bubbles arising massive type II supernovae which reach typical velocities of about 100 km/s and heigths around 1 kpc from the plane, usually raining back [92]. Observation of bubbles, holes or chimneys are more frequent in spiral arms, with a higher star formation rate. Their effects are more importat at large galactocentric radii with a lower vertical component of gravity. With these high values of v' we would obtain β (outer) larger than $= 10^{28}$ cm^{2}s^{-1} [93] following recent developments of the fountain model.

The diffusion time $\tau = l^2/\beta$ becomes τ (inner) $\approx 3 \times 10^9$ years and τ (outer) $\approx 3 \times 10^7$ years. The first one is larger than the rotation time, then the extragalactic B_r field could not effectively penetrate in the inner disk, but B_r should have the same extragalactic value in the warped region. Therefore, radial component of the vertical field gradient should very effective in producing warps.

The magnetic model was designed to explain S-warps (m=1) which is the most frequent type (68% in the large sample of 325 edge-on galaxies [79]). This model barely explain m=0 warps (U-shaped profile); they should be interpreted as arising from gradients in the extragalactic field, with characteristic length of the order of the galaxy size. The generation of asymmetric warps by other mechanisms have been considered [94, 84].

There seems to be a common orientation of warps in relative low-scale clusters. For example it was noticed [96] that in the Local Group the warps of the Milky Way, M31 and M33 show a very noticeable alignment. Also a common orientation of warps in the neighborhood of the Milky Way was found [87, 97]. This fact suggests an extragalactic origin.

It is interesting to notice too that warps are observed in high redshift galaxies [98]. The warps are even larger in these first steps in galaxy evolution. If warps are driven by extragalactic magnetic fields this fact would be interpreted as a result of past higher magnetic strengths. It should be taken into account that due to expansion

LNEA III, 2008.
A. Ulla & M. Manteiga (editors).

Ba^2= constant, being a the cosmological scale factor, $a^{-1} = z+1$, therefore at $z \sim 1$, in the Hubble Deep Field, the magnetic strengths were 4 times higher than today.

Intergalactic magnetic fields may produce warps, being the angle of 45^o between the rotation axis and the direction of the field, the angle of higher efficiency for bending the disk. When both directions are closer, a larger flaring of the disc would be expected. When the field direction lies close to the galactic plane it would produce lopsidedness, i.e. elliptical shapes in the outer isophotes with radial increase of eccentricity [99]. This could provide a basis of interpretation of observed lopsidedness ([100, 101, 102, 103]). In particular, it was found [101] found that about 50% of spiral galaxies exhibit lopsidedness and that about 20% of the galaxies have a lopsidedness magnitude $< A_1/A_o >\geq 0.19$ [102] . Also the lopsidedness of the young stellar population is greater than the old one [104]. This indicates that the gas is the first component suffering the distortion. An extragalactic magnetic field is therefore a temptative explanation of lopsidedness that should be explored.

6 Galactic magnetic fields.

A very promising field is the interpretation of the CMB taking into account primordial pre-recombination magnetic fields and even the possibility of finding observational traces of their existence with the great sensitivity of the space mission Planck. There is a wide Planck team interested on this topic [107]. A knowledge of primordial magnetic fields provides an understanding of their influence in galaxy birth and evolution.

Observations of CMB can not only provide information about the magnetized pregalactic medium. They also constitute the most complete direct information of the large scale magnetic field of the Milky Way and some other nearby galaxies. From the all-sky maps obtained at different wavelengths we may obtain the maps of the polarized synchrotron continuum emission and hence very important restrictions on the 3D-distribution of the galactic field.

Preliminary calculations can be obtained using WMAP data. The procedure is as follows: We can select different models proposed in the literature with different free parameters. We them obtain for each model and for each set of parameters of each model the best fit to the real data. We have considered five models and about 70000 sets of parameters per model. In Figure 8 we plot the polarization angle obtained at 22 GHz by WMAP and in Figure 9 the best fir model with the best set of parameters. The model coincides with that proposed in [108] even if different parameters better reproduce the observational map. Nevertheless, this type of approach does not permit the firm withdrawal of other models and we will must wait for Planck, with its much higher sensitivity for polarization to determine the 3D distribution of magnetic fields in our galaxy.

Other techniques [109, 110] to determine the large scale configuration of the

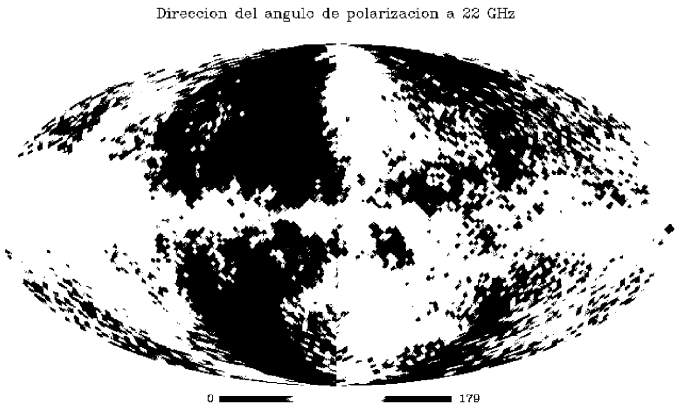

Figure 8: All sky polarization angle from WMAP at 22 GHz.

galactic magnetic field are based on Faraday Rotation of pulsars and extragalactic radio sources. Pulsars inform about the field near the plane and have the advantage of a null intrinsic Faraday Rotation. These techniques do not provide a common picture yet. Probably, the magnetic field of the Milky Way has an "axisymmetric spiral" distribution, distorted by spiral arms and random fluctuations.

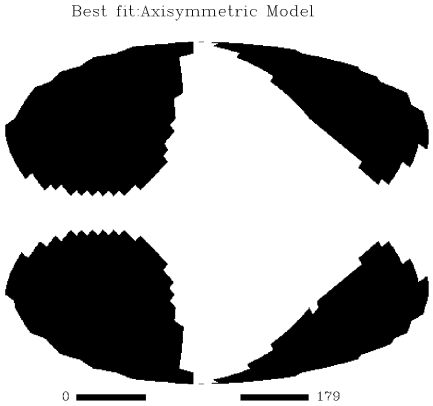

Figure 9: Best fit model of the all sky polarization angle.

References

[1] Valleée. J. 2004, New Astronomy 48, 763
[2] Widrow, L.M. 2002, Rev. Modern Phys. 74, 775
[3] Camenzind, M. 2005, in Cosmic Magnetic Fields, Lectures Notes in Physics, Springer, Ed. by R. Wielebinski and R. Beck
[4] Battaner, E., Isern, J., Florido, E. 1989, Astrophys. Space Sci. 162, 35
[5] Birk, G.T., Lesch, H., Neukirch, T. 1998, MNRAS 296, 163
[6] Dolag, K. 2006, Astron. Nach. 327, 575
[7] Niklas, S. 1995, PhD. Thesis, Univ. Bonn.
[8] Beck, R. 2005, in "Cosmic Magnetic Fields", Lectures Notes in Physics, Springer, Ed. by R. Wielebinski and R. Beck
[9] Klein, V., Wielebinski, R., Morsi, H.W. 1998, A&A 190, 41
[10] Beck, R. 2007, A&A 471, 93
[11] Han, J.L., Beck, R., Ehle, M. et al. 1999, A&A 348, 405
[12] Strong, A.W., Moskalenko, I.V., Reimer, O. 2000, ApJ 537, 763
[13] Beck, R. 2001, Sp. Sci. Rev. 99, 243
[14] Beck, R. 2004, Ap&SSci 289, 293
[15] Kim, K.T., Kronberg, P.P., Dewdney, P.E., Landecker, T.L. 1990, ApJ 355, 29
[16] Kronberg, P.P. 2005, in "Cosmic Magnetic Fields", Lectures Notes in Physics, Springer, Ed. by R. Wielebinski and R. Beck
[17] Feretti, L., Dallacas, D., Giovannini, G. et al. 1995, A&A 302, 680
[18] Kim, K.T., Tribble, P.C., Kronberg, P.P. 1991, ApJ 379, 80
[19] Clarke, T.E., Kronberg, P.P., Böhringer, H. 2001, ApJ 547, L111
[20] Vogt, C., Ensslin, T.A. 2003, A&A 412, 373
[21] Kronberg, P.P. 1994, Rep. Prog. Phys. 57, 325
[22] Battaner, E., Florido, E., Guijarro, A. 2001, in "Galaxy Disks and disks galaxies" ASP Conference Series 230,169, Ed. J.G. Funes, E.M. Corsini
[23] Sofue, Y., Rubin, V. 2001, ARAA 39,137
[24] Nelson, A.H. 1988, MNRAS 233,115
[25] Peratt, A.L. 1988, Laser and Particle Beams 6, 471
[26] Battaner, E., Garrido, J.L, Membrado, M. et al. 1992, Nature 360, 652
[27] Binney, J. 1992, Nature 360, 624
[28] Cuddeford, P., Binney, J. 1993, Nature 365, 20
[29] Battaner, E., Florido, E. 1995, MNRAS 277, 1129
[30] Sánchez-Salcedo, F.J., Reyes-Ruiz, M. 2004, ApJ 607, 247
[31] Battaner, E., Florido, E. 2007, Astron. Nach. 328, 92
[32] Battaner, E., Florido, E. 2000, Fund. Cosmic Phys. 21,1
[33] Navarro, J., Steinmetz, M. 2000, ApJ 538, 477
[34] Hayashi, E., Navarro, J.F. 2002, BAAS 34, 1270
[35] Abadi, M.G., Navarro, F., Steinmetz, M. et al. 2003, ApJ 591, 499
[36] Kutchera, M., Jalocha, J. 2004, AcPPB 35, 2493
[37] Romanovsky, A.J. et al. 2003, Science 301, 1696

LNEA III, 2008.
A. Ulla & M. Manteiga (editors).

[38] Swaters, R. 1999, PhD Thesis, Univ. Gröningen
[39] Battaner, E., Florido, E., Guijarro, A. 2001, in "Galaxy disks and disk galaxies", Ed. by J.G. Funes and E.M. Corsini, ASP Conference Series 230, 169
[40] Chyzy, K.T. et al. 2003, A&A 405, 513
[41] Nishikori, H., Machida, M., Matsumoto, R. 2006, ApJ 641, 862
[42] Battaner, E., Lesch, H., Florido, E. 1999, An. Fis. 94, 98
[43] Sofue, Y., Fujimoto, M., Wielebinski, R. 1986, ARAA 24,459
[44] Shukurov, A. 2005, in "Cosmic Magnetic Fields", Lectures Notes in Physics, Springer, Ed. by R. Wielebinski and R. Beck
[45] Kulsrud, R.M. 2005, in "Cosmic Magnetic Fields", Lectures Notes in Physics, Springer, Ed. by R. Wielebinski and R. Beck
[46] van der Kruit, P.C. 1979, AAS 38,15
[47] van der Kruit, P.C., Searle, L. 1981a, A&A 95, 105
[48] van der Kruit, P.C., Searle, L. 1981b, A&A 95, 116
[49] van der Kruit, P.C., Searle, L. 1982, A&A 110, 61
[50] Barteldrees, A., Dettmar, R.J. 1994, AAS 103, 475
[51] de Grijs, R., Kregel, M., Wesson, K.H. 2001, MNRAS 324, 1074
[52] Wainscoat, R., Cohen, M., Völk, K. et al. 1992, ApJSS 83, 111
[53] Binney, J., Tremaine, S. 1987, in "Galactic Dynamics", Princeton Series on Astrophysics.
[54] van der Kruit, P.C. 2008, in "Formation and evolution of Galaxy Disks", ASP Conference Series Ed. J.G. Funes and E.M. Corsini
[55] Erwin, P., Beckman, J.E., Pohlen, M. 2005, ApJ 626, L81
[56] Erwin, P., Pohlen, M., Beckman, J.E. 2008, AJ 135, 20
[57] Pohlen, M., Trujillo, I. 2006, A&A 454, 759
[58] Trujillo, I., Pohlen, M. 2005, ApJ 630, L17
[59] Pohlen, M., Zaroubi, S., Peletier, R. et al. 2007, MNRAS 378, 594
[60] Florido, E., Battaner, E., Guijarro, A. et al. 2001, A&A 378, 82
[61] Florido, E., Battaner, E., Guijarro, A. et al. 2006a, A&A 455, 467
[62] Florido, E., Battaner, E., Guijarro, A. et al. 2006b, A&A 455, 475
[63] Florido, E., Battaner, E., Zurita, A. et al. 2007, A&A 472, L39
[64] Battaner, E., Florido, E., Jiménez-Vicente, J. 2002, A&A 388, 213
[65] Kennicut, R.C. 1989, ApJ 344, 685
[66] Schaye, J. 2004, ApJ 609, 667
[67] Fall, S.M., Efstathiou, G. 1980, MNRAS 193, 189
[68] van der Kruit, P.C. 2007, A&A 466, 883
[69] Battaglia, G., Fraternali, F., Oosterloo, T. 2006, A&A 447, 49
[70] Sánchez-Saavedra, M.L., Battaner, E., Florido, E. 1990, MNRAS 246, 458
[71] Reshetnikov, V., Combes, F. 1998, A&A 337, 9
[72] Sánchez-Saavedra, M.L., Battaner, E., Guijarro, A. et al. 2003, A&A 399, 457
[73] Reshetnikov, V., Battaner, E., Combes, F. et al. 2002, A&A 382, 513
[74] Pérez, I. 2004, A&A 427, 47
[75] Sancisi, R. 1976, A&A 53, 159

[76] Briggs, F.H. 1990, ApJ 352, 15
[77] García-Ruiz, J., Sancisi, R., Kuijken, K. 2002, A&A 394, 769
[78] Florido, E., Prieto, M., Battaner, E. et al. 1991, A&A 242, 301
[79] Ann, H.B., Park, J.C. 2006, NewA 11, 293
[80] Binney, J.J. 1992, ARAA 30, 51
[81] Battaner, E., Florido, E., Jiménez-Vicente, J. et al. 1997 in "The impact of large scale near-IR surveys", 49, Ed. F.Garzón. Kluwer
[82] Weinberg, M.D., Blitz, L. 2006, ApJ 641L, 33
[83] Sánchez-Salcedo, F.J. 2006, MNRAS 365, 555
[84] López-Corredoira, M., Betancort-Rijo, J.A., Beckman, J.E. 2002, A&A 386, 169
[85] López-Corredoira, M., Betancort-Rijo, J.A., Beckman, J.E. 2008, astro-ph/07061550, in "Pathways through an eclectic Universe", Ed. by J. Knappen, T.J. Mahoney, A. Vazdekis, ASP Conference Series.
[86] Kahn, F.D., Woltjer, L. 1959, AJ 130, 705
[87] Battaner, E., Florido, E., Sánchez-Saavedra, M.L. 1990, A&A 236, 1
[88] Battaner, E. 1996, in "Astrophysical Fluid Dynamics", Cambridge Univ. Press
[89] Ruzmaikin, A.A., Sokoloff, D., Shukurov, A.M. 1989, MNRAS 241, 1
[90] Sokoloff, D., Shukurov, A.M. 1990, Nature 347, 51
[91] Ruzmaikin, A.A., Shukurov, A.M., Sokoloff, D.D. 1988, in "Magnetic fields in galaxies", Kluwer Ac.
[92] Norman, C., Ikeuchi, S. 1989, ApJ 345, 372
[93] Avillez, M.A., Breitschwerdt, D. 2004, A&A 425, 899
[94] Saha, K., Jog, C.J. 2006, A&A 446, 897
[95] Sparke, L., Casertano, S. 1988, MNRAS 234, 873
[96] Zurita, A., Battaner, E. 1997, A&A 322, 86
[97] Battaner, E., Garrido, J.L., Sánchez-Saavedra, M.L. et al. 1991, A&A 251, 402
[98] Reshetnikov, V., Battaner, E., Combes, F. et al. 2002, A&A 382, 513
[99] Battaner, E., Florido, E., Sánchez-Saavedra, M.L. 1992, A&A 253, 89
[100] Baldwin, J.E., Lynden-Bell, D., Sancisi, R. 1980, MNRAS 193, 313
[101] Richter, O.G., Sancisi, R. 1994, A&A 290, L9
[102] Rudnick, G., Rix, H.W. 1998, Astron.J 116, 1163
[103] Angiras, R.A., Jog, C.J., Omar, A. et al. 2006, MNRAS 369, 1849
[104] Heller, A.B., Brosch, N., Almoznino, E. et al. 2000, MNRAS 316, 569
[105] Chyzy, K.T., Beck, R., Kohle, S. et al. 2000, A&A 355, 128
[106] Grasso, D., Rubenstein, H.R. 2001, Phys. Rep. 348, 163
[107] Battaner, E. et al. 2007, poster in PLANCK Toulouse Meeting
[108] Page, L. et al. 2007, ApJSS 170, 335
[109] Wielebinski, R. 2005, in "Cosmic Magnetic Fields", Lectures Notes in Physics, Springer, Ed. by R. Wielebinski and R. Beck
[110] Wolleben, M., Landecker, T.L., Reich, W. et al. 2006, A&A 448, 411